On the atmospheric boundary layer over highly complex topography

A dissertation submitted to the

SWISS FEDERAL INSTITUTE OF TECHNOLOGY (ETH)
ZURICH

for the degree of

DOCTOR OF NATURAL SCIENCES

presented by

Andreas Hans Philipp Weigel

Dipl.-Phys., University of Munich
born on 9 October 1975
German citizen

accepted on the recommendation of

Prof. Dr. Atsumu Ohmura, examiner
PD Dr. Mathias W. Rotach, co-examiner
Prof. Dr. C. David Whiteman, co-examiner

2005

It's a dangerous business [...] going out of your door.
You step onto the Road, and if you don't keep your feet,
there is no knowing where you might be swept off to.

J.R.R. Tolkien (1954)

Acknowledgments

On the front cover of this thesis there is only one single name printed. However, I was not alone on my journey through the Riviera Valley. I was accompanied by many individuals who provided advice, guidance, encouragement and friendship, and who helped me to overcome all the difficulties and obstacles I came across on my trek. I would like to begin this dissertation by expressing my sincerest thanks to all these people.

First of all, I would like to acknowledge my advisor Mathias Rotach, who initiated this highly interesting project. Should I ever be asked to define *the perfect advisor*, unhesitatingly I would give his name as definition. While granting all the freedoms I wanted he also continuously provided all the guidance, support and encouragement I needed. I particularly enjoyed all those long and inspiring discussions we had, be it at the institute, be it during pleasant dinners at his home, or be it via email across the Atlantic. When frustrations were large he somehow always managed to transform them back into fresh enthusiasm, optimism and motivation. This not only refers to my scientific work, but also to other aspects of life. Thank you for everything!

I am equally indebted to Atsumu Ohmura, my doctoral supervisor at the IAC, for integrating me into his research group. By his immense range of interests and knowledge, he helped me to see my project in a wider context. I particularly appreciated that he had an open ear whenever I asked for it. Furthermore, I want to thank him for his generosity when financial support was needed for publications, conferences and summer schools.

Finally, I am grateful to my external co-examiner, Dave Whiteman, who provided many helpful comments and thoughts on my dissertation. His numerous publications on mountain meteorology were a permanent guide and companion on my journey through the Riviera. I particularly appreciated his invitation to Richland in 2003 and the good discussions we had there.

My efforts in evaluating MAP-Riviera measurement data were supported by several people. Marco Andretta and Eva van Gorsel are acknowledged for introducing me to the measurement sites and for providing the sonic anemometer data I needed for my evaluations. Also, I am very grateful to Marco Andretta and Pierluigi Calanca for their good advice on numerous aspects of time-series analysis, especially at the initial stages of my work. Martin Zingg helped to catalogue the flight legs of the aircraft measurements. Special thanks go to Bruno Neininger whose intensive and patient support with the processing, evaluation and interpretation of the airborne data was invaluable. Our joint efforts to identify systematic measurement errors were crucial to the progress of this work. I also want to thank him for demonstrating me his research aircraft during a flight over the Black Forest.

In the course of my doctoral work, a wonderful research collaboration developed with Fotini Katopodes Chow from Stanford University. This collaboration opened the world of numerical modeling to me, and I would like to express my sincerest thanks to Fotini. Without her, this

their support and friendship. These thanks include my flatmates (Anita Sandmeier, Peter Sche-lander and Alastair McClymont), who provided the friendly and harmonic home I needed, as well as to my friends from the "world outside".

Special thanks go to Will Sawyer, Fotini Katopodes Chow, Alastair McClymont, Oliver Fuhrer and Sebastian Eisele for carefully proof-reading parts of this dissertation.

My deepest thanks, however, go to my family for their constant love and support: to my siblings (Michael, Stephan, Tina, Ulrich), my nephews and nieces, my in-laws, and, most importantly, to my parents Ingeborg and Joachim. They provided encouragement, helpful advice and comfort when I needed it most. It is to them that I dedicate this work.

Abstract

The characteristics of turbulent processes over steep mountainous topography still belong to the most unexplored topics in the field of boundary layer meteorology. It cannot be taken for granted that classical scaling schemes and similarity relationships hold in such an environment. Nevertheless, for lack of better knowledge, most numerical weather and climate prediction models use subgrid-scale (SGS) parameterizations which are based on similarity relations from flat and homogenous terrain. This may have a major effect on the accuracy and performance of these models. However, a thorough evaluation of this problem has so far not been possible, simply because there is only sparse experimental evidence on subgrid-scale processes over highly complex topography.

As a first step in mitigating this unsatisfying data situation and improving the understanding of the atmospheric boundary layer over mountainous terrain, the Riviera Valley in southern Switzerland has been chosen for a detailed study on the thermal, dynamic and turbulence characteristics of the daytime atmosphere in a steep Alpine valley. This research focuses on clear-sky summertime conditions and combines the evaluation of measurement data from the MAP-Riviera field campaign (carried out from summer through autumn in 1999) with the application of a high-resolution large-eddy simulation code, the Advanced Regional Prediction System (ARPS), using horizontal resolutions as fine as 350 m.

In the first part of this work, aircraft measurements, radio soundings and sonic anemometer data are used to investigate and characterize the Riviera atmosphere. A pronounced valley wind system is observed. Temperature profiles show that the daytime growth of the well-mixed layer is consistently suppressed and that on days with strong valley winds, a stabilization occurs almost throughout the entire valley atmosphere. This stabilization appears to be due to a strong curvature-induced secondary circulation in the southern part of the valley. The turbulence structure differs from that over flat and homogenous terrain. For example, turbulent kinetic energy (TKE) is observed to be non-zero well above the mixed layer. Nevertheless, it has been possible to modify the classical convective scaling approach such that it can be applied in the steep Riviera topography.

In the second part of this work, the MAP-Riviera dataset is used to investigate the measures necessary to achieve accurate simulations of flow over steep, mountainous terrain. Excellent agreement of the aforementioned large-eddy simulations with observations is obtained, but only when high-resolution surface datasets are used and appropriate nested grid configurations are carefully chosen. The sensitivity of the results to initial soil moisture, land use data, grid resolution, topographic shading, and turbulence models is explored. In particular, the soil moisture initialization on the 1 km grid is found to be most crucial to the success of the finer resolution predictions.

Finally, ARPS is applied to evaluate the underlying physical processes determining the daytime evolution of the valley atmosphere structure. A heat budget analysis shows that the observed suppression of the well-mixed layer is caused by the combined effects of cold-air advection in the along-valley direction and subsidence of warm air from the free atmosphere

aloft. Averaged over the entire valley, subsidence - a result of overshooting slope winds - turns out to be one of the main heating sources of the valley atmosphere and appears to be an important driving mechanism for the onset of thermally driven up-valley winds. As far as the turbulence structure is concerned, ARPS underpredicts TKE. Nevertheless, the aforementioned scaling approach is confirmed by the model. An evaluation of the TKE-budget equation reveals that TKE is predominantly shear-induced, rather than buoyancy-driven, due to the interaction of cross-valley and up-valley flow. In a last step, the mass budget of the valley atmosphere is investigated. If the stratification is not too stable, a net vertical export of air mass is observed, which appears to be partially due to a narrowing of the valley cross-section. The associated export of moisture can significantly exceed surface evaporation, thus stressing the need for better SGS parameterizations of coarse atmospheric models.

In summary, this study shows that, even over highly complex topography, small-scale atmospheric processes, including turbulence, reveal consistent features which can be reproduced and understood with high-resolution large-eddy simulations. Thus, the basis is provided for further studies of this kind with the ultimate aim of assessing and improving the quality of SGS parameterizations of numerical weather and climate prediction models.

Zusammenfassung

Turbulente Prozesse in komplexer Gebirgstopographie gehören nach wie vor zu den am wenigsten erforschten Gebieten der Grenzschichtmeteorologie. Es ist fraglich, ob klassische Skalierungsregime und Ähnlichkeitsbeziehungen in solch einem Umfeld angewandt werden können; ihre Gültigkeit ist lediglich für homogene und flache Topographie erwiesen. Dennoch verwenden die meisten numerischen Wetter- und Klimamodelle auch in komplexem Terrain derartige Ähnlichkeitsfunktionen zur Parametrisierung nicht auflösbarer kleinskaliger Prozesse. Möglicherweise wird dadurch die Genauigkeit und Leistung solcher Modelle erheblich beeinträchtigt. Eine gründliche Untersuchung dieser potentiellen Problematik war bislang jedoch nicht möglich, was vor allem daran lag, dass kaum Messdaten zu Feinstrukturprozessen in gebirgiger Topographie existierten.

Das Riviera-Tal in der Südschweiz ist für eine detaillierte Studie der thermischen, dynamischen und turbulenten Eigenschaften einer typischen alpinen Talatmosphäre ausgewählt worden - dies mit dem Ziel, das Verständnis der atmosphärischen Grenzschicht in steilem Gelände zu erhöhen und die oben angesprochene schlechte Datenlage zu verbessern. Die vorliegende Arbeit befasst sich vor allem mit der Atmosphäre unter sommerlichen Schönwetterbedingungen. Dabei wird eine Methodik angewandt, die auf zwei Säulen basiert: Zum einen auf der Auswertung von Messdaten der MAP-Riviera Feldstudie (durchgeführt im Sommer und Herbst 1999), zum anderen auf sogenannten Grobstruktursimulationen (large-eddy simulations, LES) mit horizontalen Auflösungen von bis zu 150 m. Die Simulationen werden mit dem numerischen Wettervorhersagemodell ARPS durchgeführt.

Im ersten Teil dieser Arbeit wird die Riviera-Atmosphäre mit Hilfe von Flugzeugmessungen, Radiosondierungen und Sonic-Anemometerdaten untersucht und charakterisiert. Man kann ein ausgeprägtes Talwindsystem beobachten. Temperaturprofile zeigen, dass die Ausbildung einer tiefen Mischungsschicht stets unterdrückt ist. An Tagen mit besonders starken Talwinden stabilisiert sich die Atmosphäre sogar fast bis zum Talboden. Die Ursache hierfür ist eine ausgeprägte Sekundärzirkulation in der südlichen Talhälfte, die durch eine topographisch bedingte Krümmung der Stromlinien induziert wird. Die Turbulenzstruktur unterscheidet sich wesentlich von derjenigen über flacher und homogener Topographie. So beobachtet man zum Beispiel noch weit oberhalb der Mischungsschicht signifikante Werte von turbulenter kinetischer Energie (TKE). Trotzdem kann das klassische Skalierungsverfahren für konvektive Grenzschichten derart modifiziert werden, dass es in auch der steilen Riviera-Topographie anwendbar ist.

In einem zweiten Schritt wird anhand des MAP-Riviera-Datensatzes evaluiert, welche Maßnahmen notwendig sind, um Luftströmungen in steilem, gebirgigem Gelände exakt simulieren zu können. Dabei stellt sich heraus, dass die oben genannten Grobstruktursimulationen hervorragend mit den Beobachtungen übereinstimmen, sofern hochauflösende Oberflächendatensätze verwendet werden, und sofern die ineinander geschachtelten Simulationsgitter sorgfältig konfiguriert sind. Die Abhängigkeit der Ergebnisse von der Bodenfeuchte-Initialisierung, von

den Landnutzungsdaten, von der Gitterauflösung, von der Anwendung einer topographischen Schattierungsroutine sowie von der Wahl des Turbulenzmodells wird untersucht. Insbesondere die Bodenfeuchte-Initialisierung auf dem 1 km-Gitter erweist sich dabei als entscheidender Faktor für erfolgreiche Simulationen.

Schließlich wird ARPS dazu verwendet, die physikalischen Prozesse zu untersuchen, die die Struktur der Talatmosphäre bestimmen. Eine Analyse des Wärmehaushalts zeigt, weshalb das Wachstum der konvektiven Mischungsschicht unterdrückt ist: Grund hierfür ist der kombinierte Effekt von talaufwärtiger Kaltluftadvektion und von Subsidenz aus der potentiell wärmeren freien Atmosphäre. Diese Absinkbewegung wird durch die Wechselwirkung der thermischen Hangwinde mit der freien Atmosphäre induziert. Gemittelt über das gesamte Tal erweist sich Subsidenz als eine der Hauptursachen für die Erwärmung der Talatmosphäre, und damit als ein wichtiger Antriebsmechanismus für thermische Talaufwinde. Was die Turbulenzstruktur anbelangt, so produziert ARPS zu niedrige TKE-Werte. Dennoch kann das oben erwähnte Skalierungsverfahren mit Hilfe des Modells verifiziert werden. Eine Auswertung der TKE-Gleichung zeigt, dass TKE vor allem durch Windscherung produziert wird, die sich aus den thermischen Talwinden und -zirkulationen ergibt. Auftrieb ist in diesem Zusammenhang von geringerer Bedeutung. In einem letzten Schritt wird die Massenbilanz der Talatmosphäre untersucht. Im Falle nicht allzu stabiler Schichtung kann ein vertikaler Export von Luft beobachtet werden, der sich teilweise aus der topographischen Einengung des Tales ergibt. Der damit verbundene vertikale Feuchtetransport kann die Oberflächenverdunstung deutlich übertreffen, was den Bedarf für bessere Feinstrukturparametrisierungen in grob aufgelösten atmosphärischen Modellen unterstreicht.

Alles in allem zeigt die vorliegende Studie, dass kleinskalige atmospärische Prozesse - Turbulenz eingeschlossen - selbst in komplexer Gebirgstopographie wiederkehrende Strukturen aufweisen, die mit hoch auflösenden LES reproduziert und verstanden werden können. Damit ist die Grundlage für weitere Studien dieser Art geschaffen, die letztendlich dazu dienen können, die Feinstrukturparametrisierungen numerischer Wetter- und Klimamodelle zu verbessern.

Contents

Chapter 1

Introduction

1.1   A whirlpool in the mountains

Big whirls have little whirls that feed on their velocity,
And little whirls have lesser whirls and so on to viscosity.

This short verse of Lewis Fry Richardson (1922) illustrates one of the main features of turbulent atmospheric flows: energy is transferred among a wide range of interacting length scales, reaching from the kilometer scale down to millimeters, where energy is dissipated by viscous dissipation (e.g. Panofsky and Dutton, 1984). At the same time, the smallest fluctuations and perturbations can have a huge impact on the evolution of large-scale structures such as weather systems (e.g. Lorenz, 1993), i.e. the atmosphere is highly chaotic. This behavior is due to the non-linearity of the underlying Navier-Stokes equations and poses a fundamental limitation on the performance of numerical weather and climate models, because all scales need to be considered.

In 1922, almost twenty years before Konrad Zuse constructed the first computer, Richardson estimated that about 64,000 "human calculators" were necessary to predict the weather faster than it actually evolves. Fortunately, computer technology advanced much more rapidly than Richardson may have anticipated in his most optimistic dreams. However, the (truly hypothetical) numerical simulation of a typical weather system in full resolution would require about 10^{24} grid points (Voke and Collins, 1983), which is far beyond the capacities any computer will ever achieve (Härtel, 1996). On state-of-the-art computer systems, typical climate models (e.g. 'ECHAM') can nowadays run with a horizontal grid resolution of about $100\,\mathrm{km}$, global weather forecast models (e.g. the 'ECMWF forecast model') with $40\,\mathrm{km}$ grid spacing, and operational regional meso-scale models (such as the 'LM' and the 'aLMo') with resolutions as fine as $7\,\mathrm{km}$.

A common feature of all these models, whatever their resolution, is that they are not able to resolve boundary layer processes and turbulence. Parameterizations are required in order to estimate the impact of these sub-grid scale processes on the larger scale flow structure. To a considerable degree, such parameterizations employ empirical knowledge. For example, the description of the turbulent surface exchange processes of momentum, heat and moisture typically incorporates Monin-Obukhov similarity theory (Monin and Obukhov, 1954). The associated similarity relationships, however, are based on measurements over flat and homogeneous terrain. A very prominent field campaign in this context was the Kansas experiment (Haugen et al., 1971; Businger et al., 1971). But do the "laws of Kansas" also hold in Nepal or Switzer-

land? Can it be taken for granted that turbulent motion shows exactly the same characteristics over highly mountainous topography as it does over a plain? The answer proves to be 'no'. For instance, recent measurements of stress profiles in the surface layer of a steep valley slope have indeed revealed deviations from textbook knowledge: in contrast to flat topography, stress has a significant lateral component and varies with altitude (Andretta et al., 2000, 2001). Moreover, it is alarming that simulations of flow over the Pyrenees on a 10 km grid are shown to improve significantly if an unrealistically high "effective" roughness length is applied (Georgelin et al., 1994). Thus, it is possible that current numerical weather and climate models are inherently flawed because they use inappropriate turbulence parameterizations (Rotach, 1995).

This problem has never been quantitatively evaluated, simply because there is only very limited experimental evidence on the turbulence structure in steep terrain. At present, detailed field studies of the atmospheric boundary layer over non-flat topography have mainly been restricted to comparatively gentle hills (Mason and Sykes, 1979; Taylor and Teunissen, 1987; Coppin et al., 1994; Vosper and Mobbs, 1997; Vosper et al., 2002). The same applies to wind tunnel measurements (e.g. Finnigan et al., 1990; Gong and Ibbetson, 1989; Ross et al., 2004). Theoretical approaches (e.g. Jackson and Hunt, 1975; Mason and Sykes, 1979; Hunt et al., 1988a,b) require the linearization of the equations of motion and are therefore bound to fail in the case of steep slopes. While not being representative of 'real' mountain terrain, these studies showed that even a gentle hill can lead to highly complex phenomena such as separation bubbles and lee-side turbulent wakes. With increasing obstacle height and steepness, these effects can assume considerable dimensions. For example, Attié et al. (1999) measured turbulent wake zones in the lee of the Pyrenees with a horizontal extent of as much as 70 km. How much more complicated must the turbulence structure in a steep and narrow alpine valley be? It is all but certain that boundary layer scaling regimes (as summarized in Holtslag and Nieuwstadt, 1986) exist in such topography.

Yet, the situation is even more complicated. The exchange of momentum, heat, moisture, aerosols and pollutants is not only effected by turbulent transport, but also by mesoscale flows such as thermally and mechanically driven mountain winds, which can reveal a high degree of complexity. Overshooting slope winds, for example, have been shown to have a considerable and climatologically relevant impact on the exchange of heat (Noppel and Fiedler, 2001) and moisture (Henne et al., 2005). The characteristic length scales of such mesoscale fluxes are closely linked to the scales of the underlying topography. Given that the full resolution of complex mountainous topography may require a horizontal grid spacing of 100 m (Young and Pielke, 1983), it is clear that the effect of, say, mountain winds is not considered at all by typical weather and climate models and needs to be incorporated into their sub-grid scale parameterizations.

The examples mentioned above represent only a small fraction of the big 'whirlpool' of mountain-related small-scale processes with potential impact on weather and climate. There are many more important issues which will not be evaluated here. The countless number of implications associated with mountain waves (e.g. Durran, 1990) or with orographically induced cloud formation and rain (e.g. Banta, 1990; Fuhrer and Schär, 2005), for example, are not addressed. The focus of this work is the daytime atmosphere in a steep and narrow alpine valley under clear-sky summer conditions. In a dual approach, consisting of both the evaluation of measurement data and the application of high-resolution large-eddy simulations (LES), the impact of mountain winds and turbulence on the boundary layer is evaluated. For the first time, the turbulence structure of an entire valley atmosphere is considered and evaluated. It is my aim to show that, despite the complexity of the system, small-scale processes and turbulent motions

can be understood even in such an environment, and that attempts to find parameterizations are highly promising rather than inherently doomed to failure. Moreover, with a detailed description and evaluation of the model setup, guidelines for further studies on this topic shall be provided. Hopefully this dissertation contributes a few valuable drops to the comprehension of the big 'whirlpool in the mountains'.

The following sections contain short reviews of previous work relevant to this dissertation. First, to provide a reference for comparison, the characteristics of the atmospheric boundary layer over flat and homogenous topography are briefly sketched (Section 1.2). Then, Section 1.3 outlines the differing boundary layer conditions in complex and mountainous terrain with special consideration of thermally-driven mountain winds. In Section 1.4, recent experimental and numerical approaches to valley meteorology are summarized. Finally, this introductory chapter concludes with an outline of the research objectives of this dissertation.

1.2 The convective boundary layer over flat and homogenous topography

The atmospheric boundary layer (ABL) is the part of the troposphere that is directly influenced by the planet's surface. It governs the exchange of energy, momentum, water vapor, carbon dioxide and other scalars between the surface and the free atmosphere aloft. The properties of ABLs over flat and homogenous topography are well investigated and described. Comprehensive reviews can, for example, be found in Stull (1988), Garratt (1992, 1994) and Kaimal and Finnigan (1994).

One of the main characteristics of atmospheric boundary layers is the occurrence of turbulent motions. These can be triggered either by strong wind-shear ('mechanically induced') or by buoyancy effects ('thermally induced'). The structure of the ABL depends strongly on the properties of turbulence, and therefore on the local flow conditions, the surface characteristics and the stratification of the atmosphere. In the case of a highly stable stratification (e.g. over ice), the ABL is very thin with depths of less than 100 m; vertical transport of air is suppressed, and turbulence is maintained by mechanical forcing. At the other extreme are thermally induced convective boundary layers (CBLs), which can assume depths of several kilometers and generally develop over land under sunny summer conditions. As this study focuses on exactly such atmospheric conditions, stable and neutral boundary layers are not given further consideration.

The evolution of the CBL is determined by sensible surface heat flux and is thus closely linked to incoming solar radiation. Typically, the diurnal pattern of CBL growth proceeds as follows: In the early morning, the boundary layer is stably stratified. After sunrise, insolation at the ground drives turbulent heat fluxes that cause a CBL to grow upward from the ground into the nocturnal boundary layer. Once the inversion is destroyed, thermals can penetrate deeply into the 'residual layer' (RL), the neutrally stratified remnants of the CBL of the previous day. Eventually, the capping inversion on top of the RL is reached. CBL growth slows down and a second heating mechanism becomes effective: entrainment, i.e. the downward mixing of warm air due to overshooting thermals. After sunset, CBL growth ceases and a nocturnal inversion develops as the ground cools down. This diurnal cycle is schematically illustrated in Fig. 1.1. Due to its well-mixed nature, the CBL is characterized by constant potential temperature, specific humidity and aerosol concentrations. Convection typically occurs in organized structures: depending on wind shear, it can either have a cellular-type or a roll-like structure (Moeng and
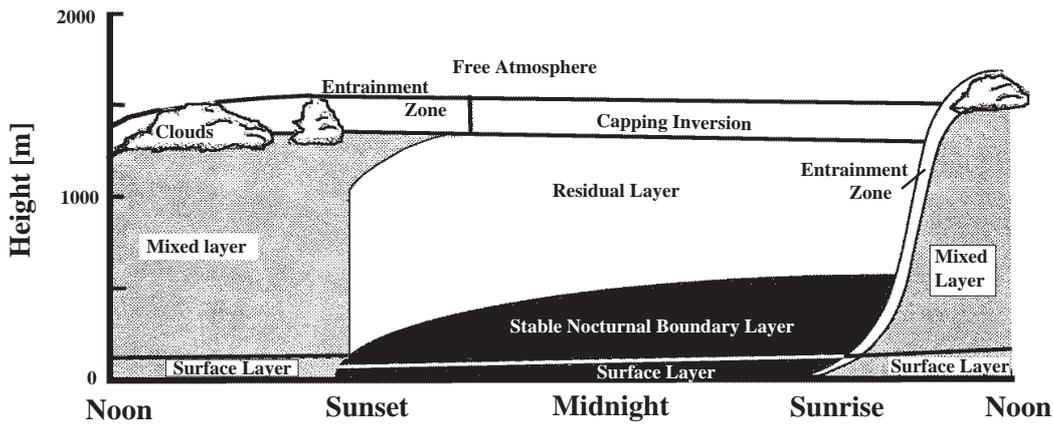
Figure 1.1: *Schematic illustration of the diurnal cycle of CBL evolution (adapted from Stull, 1988). Further explanation is given in the text.*

Sullivan, 1994).

Deardorff (1970) proposed a scaling approach for CBLs which is based on three fundamental variables: a buoyancy parameter g/θ (g = gravitational acceleration, θ = potential temperature), the surface turbulent sensible heat flux $\overline{w'\theta'}_0$ and the mixed layer depth z_i. From these, a convective velocity scale w_* and a convective temperature scale θ_* can be constructed with:

$$w_* = \sqrt[3]{\frac{g}{\theta} \cdot \overline{w'\theta'}_0 \cdot z_i} \qquad \text{and} \qquad \theta_* = \frac{\overline{w'\theta'}_0}{w_*} \ . \tag{1.1}$$

Subsequent model studies (Deardorff, 1972; Wyngaard and Coté, 1974) and measurements (Kaimal et al., 1976; Caughey and Palmer, 1979; Lenschow et al., 1980; Hunt and Carruthers, 1990) supported this scaling approach and led to the formulation of similarity relationships.

1.3 The convective boundary layer over steep and mountainous topography

Comparatively little is known about the CBL over steep and complex terrain. To the author's knowledge, no information is presently available on the turbulence structure and scaling approaches within a mountain CBL, and it is one of the objectives of this dissertation to provide a first step towards filling this gap of knowledge. However, some research has been carried out with respect to more 'global' characteristics, such as temperature profiles, aerosol concentrations and boundary layer growth rates, which will be briefly summarized at the end of this section. I first want to focus, in more detail, on the nature and properties of thermally-driven valley flows. Such air currents typically develop under the conditions considered in this study, and they directly affect the structure of valley boundary layers. More comprehensive reviews can be found in the books of Barry (1992) and Whiteman (2000) and in the monograph edited by Blumen (1990).

1.3.1 Thermally-driven mountain winds

Every mountain hiker is familiar with the phenomenon of thermally-driven mountain winds, with the nice refreshing breezes one can experience on a sun-exposed slope, or with the freezing gusts that rush down a mountain on a clear night. By the nineteenth century, these thermally-driven winds were already extensively described by explorers in all parts of the world, from the Himalayas to the Andes (summarized e.g. by J. von Hann, 1932). Generally, a distinction is made between *slope winds* and *valley winds*: Slope winds are directed up or down the underlying slopes normal to the contour lines, while valley winds blow along the valley axis. From numerous measurements made in the first half of the twentieth century, it is known that these air currents reveal a distinct diurnal pattern (e.g. Defant, 1951), which is illustrated schematically in Fig. 1.2. In the early morning, the valley wind blows in the down-valley direction (a). After sunrise, up-slope winds develop (b); the down-valley flow becomes weaker, ceases (c) and finally reverses to an up-valley direction (d). In the late afternoon, when incoming solar radiation decreases, the up-slope winds cease (e) and turn down-slope (f). Later in the evening, the valley winds become weaker and finally transition back to the down-valley direction (g,h). Due to mass conservation, up-slope winds and down-slope winds are accompanied by subsidence and lifting, respectively, in the valley center. In 1932, Wagner published a theory on these mountain winds which, in its core, is still valid today. In particular, he realized that different mechanisms are responsible for the forcings of slope and valley winds.

(i) *Slope winds.* Slope winds are driven by horizontal temperature gradients between the surface layer on a slope and the air at the same altitude over the valley center. During the daytime, the associated pressure gradient force points towards the (heated) slope, while it reverses at night when the surface is cooled by emission of longwave radiation. The resulting accelerations in the up-slope (day) and down-slope (night) direction are supported by buoyancy and gravity forces, respectively (see Fig. 1.3).

The basic flow features of slope winds and the underlying physical processes have been studied with conceptual models (reviewed by Egger, 1990). However, the applicability of such models to real cases is limited due to their simplifying assumptions. The famous slope flow model of Prandtl (1942), for example, does not consider the horizontal pressure gradient force. Sensitivity studies are therefore often carried out with the help of mesoscale models. By this method, Bader and McKee (1985) and Atkinson and Shahub (1994) showed that slope winds are weakened in the case of strong stability; and Zhong and Whiteman (2004) used a mesoscale model to evaluate the momentum budget of nocturnal drainage flows as a function of slope angle. One of the few experimental studies dealing with the dynamics of thermally-driven up-slope flow was carried out by Kossmann and Fiedler (2000). From a momentum budget analysis, they found that slope winds can only develop if an inversion is present above the heated slope; otherwise, the upward buoyancy force would not be deflected toward the up-slope direction. Slope winds are often mistakenly regarded as a steady and homogenous flow. However, the microscale structure of slope winds has been shown to be highly complex (Hunt et al., 2003; Van Gorsel et al., 2003). Moreover, slope winds react very rapidly to local changes of incoming radiation (Vergeiner and Dreiseitl, 1987), which leads to a high degree of spatial and temporal variability. Cloud shading, for example, can immediately decrease the speed of slope winds (Whiteman et al., 2000, p.182). Given the complexity of daytime radiation and energy budgets in a steep valley (Whiteman et al., 1989a,b; Matzinger et al., 2003), it is therefore clear that point measurements of slope winds are hardly representative for an entire valley, posing serious limitations to the experimental quantification of mass and heat transport due to these winds.
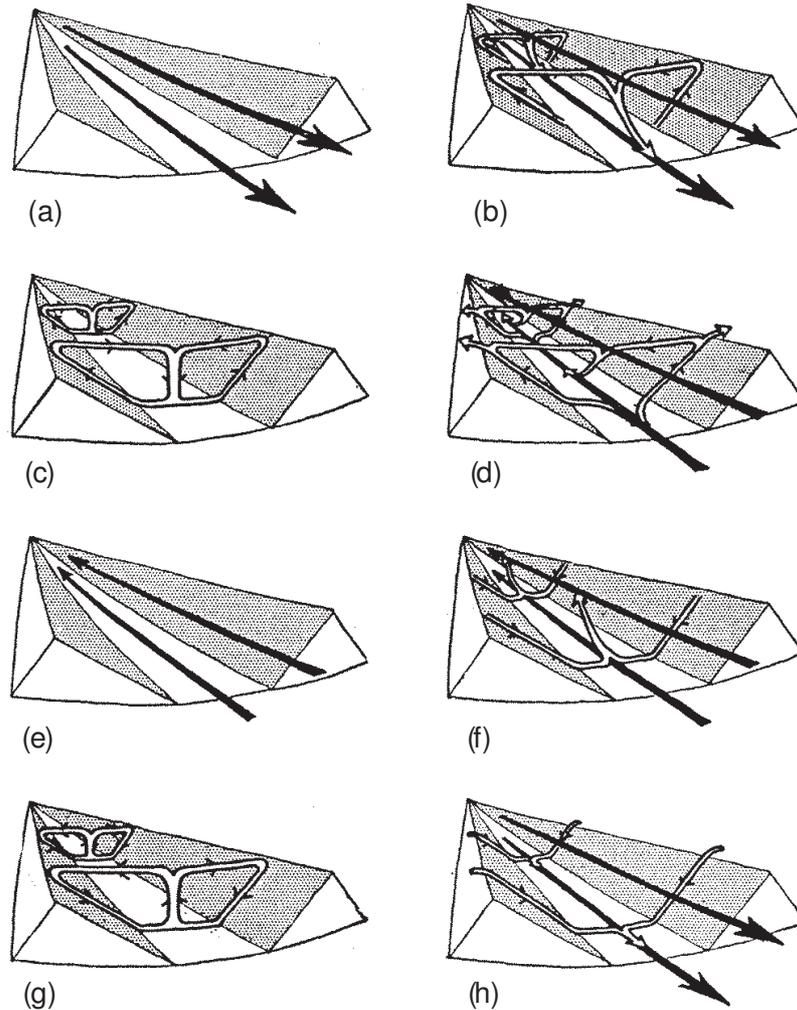
Figure 1.2: *Diurnal cycle of valley winds (after Defant, 1951). Explanations of the figures are given in the text.*

(ii) *Valley winds.* As has been shown in many studies, the diurnal cycle of potential temperature in a valley atmosphere reveals a higher amplitude than the corresponding cycle over an adjacent plain (e.g. Freytag, 1985; Vergeiner and Dreiseitl, 1987). The resulting along-valley gradients of hydrostatic pressure drive the valley winds. Wagner (1932a) introduced a volume argument to explain this phenomenon. To understand his idea, consider a volume V of air, which is supplied with an amount of heat Q. Applying the laws of thermodynamics, one obtains in good approximation that the resulting change in potential temperature, $d\theta$, is inversely proportional to V (e.g. Whiteman, 1990, p.10). Let V_{valley} be the volume of air which is contained in a typical valley, i.e. which is enclosed by the valley sidewalls and a horizontal area A_{xy} at ridgetop level. As a valley is typically U-shaped or V-shaped rather than rectangular, V_{valley} is smaller than a corresponding volume V_{plain} under an area A_{xy} at the same altitude over a plain (see Fig. 1.4). If the same amount of heat Q is supplied to these two volumes, the smaller V_{valley} heats faster than V_{plain} (because $d\theta \sim 1/V$). This leads to the along-valley temperature gradients necessary for valley winds. Wagner's concept was reinvestigated by Neininger (1982) and extended by Steinacker (1984). It is often referred to as the "topographic amplification factor" (TAF) concept. McKee and O'Neil (1989) further generalized the TAF
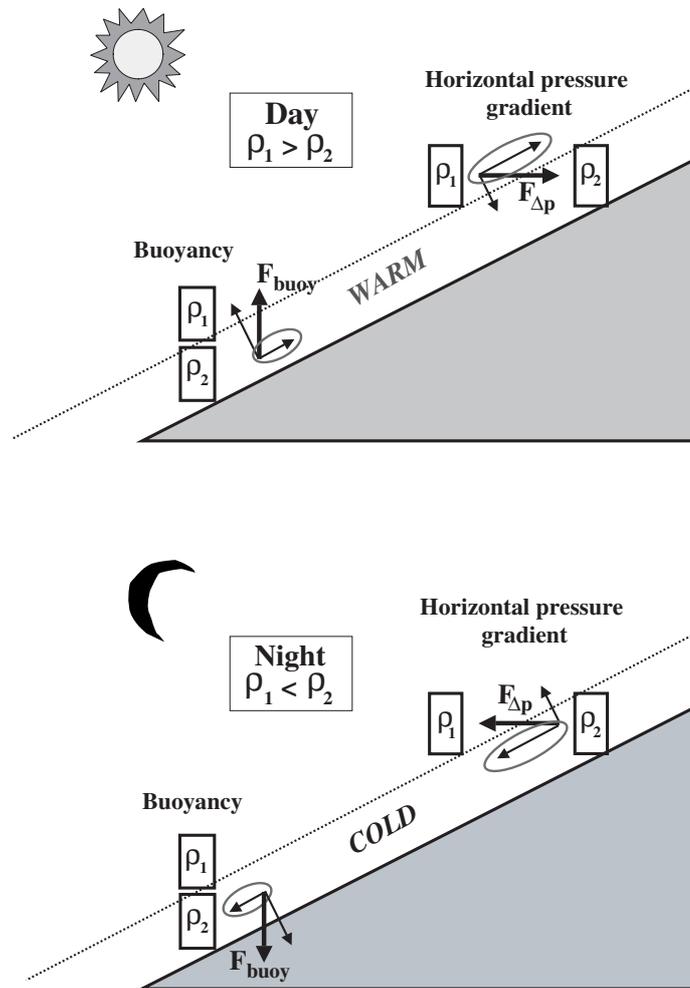
Figure 1.3: *Schematic illustration of the forcing mechanisms of thermally driven slope winds. The surface layer next to the slope acquires heat during the daytime and at night cools down further than does the air over the valley center. The arising density gradients induce buoyancy and horizontal pressure gradient forces. Their slope-parallel components (encircled) lead to the development of (a) daytime up-slope flow and (b) nocturnal down-slope winds.*

idea by showing that intra-valley variations in cross-sectional area can also introduce along-valley pressure gradients.

The TAF concept impresses by its simplicity, but it has two important constraints (Whiteman, 1990). Firstly, it requires some mechanism to efficiently transport the heat from the slopes to the valley center. Secondly, the TAF concept demands a 'rigid lid' on top of the valley to inhibit any exchange of energy with the free atmosphere aloft. This second assumption, in particular, needs to be taken with caution: Measurements show that a considerable amount of valley air can be transported into the free atmosphere by overshooting slope winds (e.g. Kossmann et al., 1998; Henne et al., 2004).

The phenomenology of slope and valley winds can be influenced and modified by a count-less number of external factors. Special topographic features can have a big impact. The
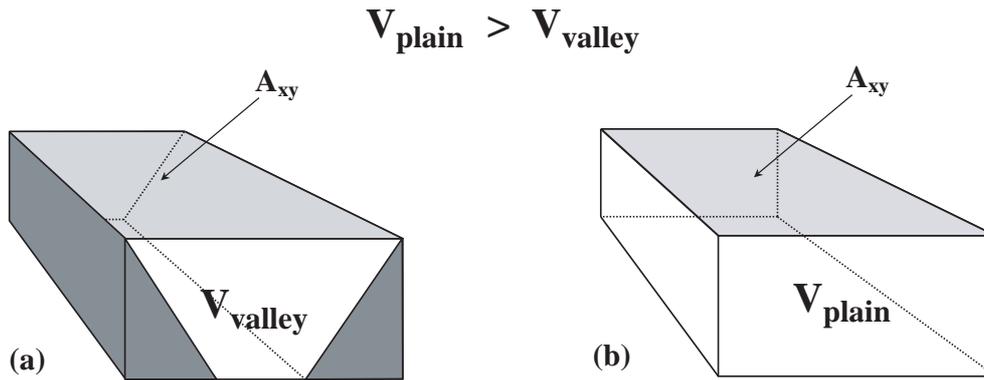
$$\mathbf{V_{plain}} > \mathbf{V_{valley}}$$

Figure 1.4: Illustration of the volume argument mentioned in the text. The volume V_{valley} (a), which is enclosed by two valley sidewalls and a horizontal area A_{xy} at ridgetop level, is smaller than a corresponding volume V_{plain} (b) under an area A_{xy} at the same altitude over a plain.

existence of tributaries, for example, has been shown to significantly enhance the strength of nocturnal drainage flows (Porch et al., 1989). Subbasins within a valley, on the other hand, can locally reverse valley winds to the opposite direction, as has been observed in the Colorado River Valley (Whiteman et al., 1999a). Further complications are imposed by valley bends (Sakiyama, 1990; Kossmann and Sturman, 2003; Weigel and Rotach, 2004; Weigel et al., 2005), which can result in unexpected cross-valley flow or lead to local zones of flow divergence or convergence. Lakes in a valley can produce their own local wind system and alter the superimposed mountain winds (Kossmann et al., 2000; Zawar-Reza et al., 2004). Another important impact source is, of course, the external meteorology. Cloud cover and moisture, for example, weaken night-time drainage flows (Barr and Orgill, 1989). Channeling effects can further influence the valley currents, either by the synoptic-scale pressure gradient or by transport of momentum (Whiteman and Doran, 1993; Whiteman et al., 1999b; Weigel and Rotach, 2004). Finally, variations in insolation can induce local flow modifications. For instance, cross-valley currents can develop when the two valley sidewalls are heated differentially, as is typically the case in the morning (Whiteman, 1989; Bader and Whiteman, 1989).

1.3.2 Thermal characteristics and other aspects of convective boundary layers over complex terrain

Measurements of temperature profiles have enhanced our knowledge of the thermal characteristics of valley atmospheres. The breakup of morning inversions in a deep valley, for example, is comparatively well investigated. Whiteman (1982) undertook observations in several Colorado Valleys as well as simulations with a thermodynamic model (Whiteman and McKee, 1982). He discovered that only a part of the incoming solar radiation is used for CBL growth in the classical sense. The rest of the available energy is used to drive up-slope winds; this upward mass flux is compensated by subsidence of the stable core of the residual nocturnal layer. This results in temperature profiles which show a sinking morning inversion and simultaneously a growing mixed layer until the inversion is eventually broken. The same pattern of morning inversion breakup has been observed in closed sinkholes (Whiteman et al., 2004), thus proving that valley winds are not responsible for this breakup pattern. Nevertheless, strong valley winds can have a direct impact on the boundary layer structure. Thermally-driven up-valley winds, for example, advect potentially cooler air; thus, surface heating may be reduced and CBL growth

slowed down (Kalthoff et al., 2000). Strong gap flows such as foehn in the Alpine Rhine Valley have the potential to make mixed layers highly heterogeneous with sudden increases of depth and multiple sublayers (Baumann-Stanzer and Groehn, 2004). Another effect, which is often observed in the early afternoon, arises from strong subsidence due to a thermally-induced cross-valley circulation: The downward advection of potentially warmer air from aloft can lead to a stabilization in the upper part of the valley CBL (Kimura and Kuwagata, 1995; Kuwagata and Kimura, 1995, 1997; Rampanelli et al., 2004; Weigel and Rotach, 2003, 2004).

At present, very little is known about the CBL structure over ridges. There is still controversy on whether a CBL typically follows the orography (Dayan et al., 1988) or not (Nyeki et al., 2000). Measurements in the Black Forest suggest that both patterns can occur (Kossmann et al., 1998). Another unanswered question is whether or not CBL and 'aerosol layer' (AL) are identical over steep terrain. Recent measurements and simulations in the Jungfraujoch region in Switzerland suggest that CBL and AL height differ significantly due to the effect of mountain venting (De Wekker et al., 2004).

1.4   Recent experimental and numerical approaches to valley meteorology

Much of the work cited above has been gained during extensive measurement campaigns. The ASCOT (Advanced Studies in Complex Terrain) program, for instance, was dedicated to the investigation of nocturnal drainage flows in several North American valleys (Clements et al., 1989). Other studies, such as TRACT (Transport of air pollutants over complex terrain) in the Upper Rhine Valley (Kossmann et al., 1998; Kossmann and Fiedler, 2000) or VOTALP (Vertical Ozone Transport in the Alps, Furger et al., 2000) in the Mesolcina Valley in Switzerland focused on the ozone and pollutant transport by valley and slope flows. VTMX (Vertical Transport and Mixing, Doran et al., 2002) was a recent study in the Salt Lake Valley region which attempted to study nighttime mixing over urban areas in complex terrain. Finally, the Mesoscale Alpine Program (MAP, Bougeault et al., 2001) was dedicated to the investigation of mesoscale processes occurring over Alpine topography, such as foehn, gravity wave breaking and orographically induced precipitation (Binder and Schär, 1996). One of the eight MAP sub-projects focused on boundary layers in complex terrain. A field study within the framework of this sub-project, the so-called "MAP-Riviera" measurement campaign (Rotach et al., 2004), provides the experimental basis of this dissertation.

There have been many more important and insightful field studies in recent decades, which are not explicitly mentioned here. A summary can be found in Whiteman (1990, pp. 6-8).

While such measurement campaigns are invaluable and irreplaceable for the investigation of valley atmospheres, they all have the inevitable deficiency of being case-studies. As shown above, mountain flows and valley boundary layers can appear in myriads of variations. This complicates a generalization of the findings obtained in one specific valley to other valley topographies. For the same reason, it can be dangerous to "extrapolate" information from a single-point measurement to an entire valley or basin, for instance to calculate a valley heat budget (Fast et al., 1996). In recent years, high-resolution numerical models have become a very helpful tool in this context.

Historically, the implementation of such models in complex topography was not only hampered by the limited computational power. A major problem arose from the fact that, on resolu-

tions of less than 10 km, vertical accelerations cannot be neglected relative to buoyancy, i.e. the application of the commonly used hydrostatic approximation is not justified (Kalnay, 2003, pp. 24–25). This led to the development of techniques to deal with unwanted non-hydrostatic effects, such as sound waves, and to make non-hydrostatic models computationally competitive to hydrostatic ones (e.g. Klemp and Wilhelmson, 1978; Durran and Klemp, 1983; Skamarock and Klemp, 1992). In the 1990s, several non-hydrostatic mesoscale models emerged. Examples include the Penn-State/NCAR Mesoscale Model Version 5 (MM5, Dudhia, 1993), the Regional Atmospheric Modeling System (RAMS, Pielke et al., 1992), the Coupled Ocean/Atmosphere Mesoscale Predicition System (COAMPS, Hodur, 1997) and the Advanced Regional Prediction System (ARPS, Xue et al., 2000, 2001).

With modern computer systems, such models can now be used in sub-kilometer resolution. In several real-case studies, their performance has been evaluated by comparisons to measurement data. Already in 1996, Fast et al. applied RAMS with a resolution of 250 m to evaluate measurements of Whiteman et al. (1996) in a canyonland basin and to estimate the heat budget. Zängl et al. (2001) used MM5 at 800 m resolution to simulate the Earth's deepest valley (5000 m), the Kali Gandaki Valley in Nepal, and could reproduce several measured features such as very strong daytime valley winds (Egger et al., 2000). However, the former authors experienced initialization problems due to the steep slopes. Zhong and Fast (2003) presented the first intercomparison of three state-of-the-art mesoscale models (RAMS, Meso-Eta, MM5). They simulated the Salt Lake Valley and compared the output to measurement data from the VTMX campaign, using a grid spacing of less than 1 km. All three models were able to reproduce the complicated flow patterns, but they also revealed quantitative deficiencies such as a cold bias and an underestimation of net radiation and mixed layer depth. Zängl et al. (2004) used MM5 to simulate a foehn event in the lower part of the Alpine Rhine Valley at 1 km resolution. A similar event was investigated in the smaller Wipp Valley by Gohm et al. (2004) at 267 m resolution. The breakthrough of the foehn was well reproduced, but the model additionally predicted a shallow foehn phase which was not found in the observations. Finally, De Wekker et al. (2005) applied RAMS on a 333 m grid in the Riviera Valley, which is also the valley of interest in this dissertation. They were successful in reproducing measured temperature profiles, but the simulated flow structure showed significant deviations from the observations.

All these studies commonly show that the qualitative features of the investigated flows are well reproduced, while quantitative comparisons, if carried out at all, still reveal considerable deficiencies. The evaluation and improvement of such high-resolution models over complex topography is an area of ongoing research and is also part of this work.

A particularly interesting perspective is provided by the concept of large-eddy simulations (LES; pioneered by Deardorff (1970) and reviewed among others by Härtel (1996) and Ferziger (1996)). In contrast to the commonly used Reynolds averaging approach, the Navier-Stokes equations are spatially filtered on a well defined length scale, i.e. the larger scales of the turbulence spectrum are explicitly resolved. Thus, by assuming that only these 'large eddies' are directly affected by the mean flow, and by assuming that the (parameterized) small scales show a rather universal behavior, the uncertainties with respect to the turbulence structure over complex terrain can be partlially circumvented with LES. Therefore, the method of LES has been chosen as a basis for the simulations carried out in this dissertation.

1.5   Objectives and outline

This dissertation focuses on the summertime atmospheric boundary layer in a steep and narrow Alpine valley under clear-sky weather conditions. Not only are 'classical' aspects such as air currents and thermal characteristics considered but also, for the first time ever, the turbulence characteristics of the bulk valley atmosphere are explored. This study is based on the evaluation of measurement data and the application of a high resolution LES model. Using these tools in unison, the physical processes determining both the characteristics of a valley atmosphere and its "communication" with the free atmosphere aloft are evaluated and quantified.

The measurements used in this research have been obtained from the MAP-Riviera field campaign, which was carried out from summer through autumn in 1999 in the Riviera Valley in southern Switzerland. The data-set includes radio soundings and aircraft measurements as well as sonic anemometer and profile measurements at various surface stations, making it a data-set of unprecedented completeness with respect to boundary layer studies in such a complex topography. A detailed description of the campaign was published by Rotach et al. (2004). The numerical simulations were undertaken with the Advanced Regional Prediction System (ARPS Xue et al., 2000, 2001) using a one-way nesting scheme with horizontal resolutions as fine as 150 m. A short description of the model specifications is given in Appendix A.

The following research questions are addressed in this work:

❑ What is the mean dynamic and thermal structure of the daytime atmosphere in a steep and narrow Alpine valley such as the Riviera?

❑ What steps are necessary to accurately simulate flow in a steep valley? Which are the most sensitive parameters?

❑ What impact does a sharply curved valley have on the flow structure? How are the thermal characteristics affected?

❑ How can turbulence be characterized in such a valley? What are the production mechanisms? Can promising scaling approaches be found?

❑ How does the valley atmosphere interact with the free atmosphere? What are the exchange processes?

❑ How is the valley heated? What are the dominant processes? To what extent do the TAF assumptions of valley heating hold?

These questions are analyzed and discussed in five chapters. The first three of these chapters (Chapters 2-4) have already been published or submitted for publication and are therefore presented in the form of self-contained scientific papers. The outline is as follows:

➠ **Chapter 2** (Weigel and Rotach, 2004) characterizes the mean flow and thermal structure of the Riviera Valley on the basis of measurement data, in particular airborne and radiosonde data. The impact of external factors such as the synoptic-scale flow or curvature of the valley is investigated. Moreover, the turbulence structure is evaluated. Profiles of turbulent kinetic energy (TKE) and stress are presented and scaling approaches discussed.

➠ **Chapter 3** (Chow, Weigel, Street, Rotach and Xue, 2005, submitted) describes the steps which are necessary to achieve accurate simulations of flow over steep terrain (partially already presented in Weigel et al. (2004a) and Chow et al. (2004)). The model, ARPS, is applied to the Riviera Valley with horizontal resolutions as fine as 150 m. Its performance is evaluated by quantitative comparisons to measurement data. In particular, the sensitivity of the model to soil moisture, surface characteristics, grid resolution, topographic shading and turbulence closure are evaluated.

➠ **Chapter 4** (Weigel, Chow, Rotach, Street and Xue, 2005, submitted) investigates the three-dimensional flow structure as obtained from model simulations. Comparisons are made to airborne data. The model is then applied to understand the thermal structure of the valley atmosphere, to calculate the valley heat budgets, and to identify the dominating heating mechanisms. The role of heat exchange processes between the valley atmosphere and the free atmosphere aloft is evaluated in this context.

➠ **Chapter 5** again deals with the turbulence structure. TKE values are extracted from the model output and compared to the airborne measurements presented in Chapter 2. In particular, the scaling behavior is evaluated and discussed. Moreover, the dominant TKE production mechanisms are determined by analyzing the TKE budget equation.

➠ **Chapter 6** focuses on the exchange of mass and moisture between the valley and the free atmosphere. The importance of the individual exchange mechanisms is quantified and put in context to the valley wind strength, the surface turbulent moisture fluxes and the stratification of the valley atmosphere.

➠ **Chapter 7** summarizes the results of this work and provides final conclusions. Suggestions for future research are made. The appendices provide a summary of the main features of ARPS and an outlook on the application of semi-idealized simulations.

Chapter 2

Flow structure and turbulence characteristics of the daytime atmosphere in a steep and narrow Alpine valley

Flow structure and turbulence characteristics of the daytime atmosphere in a steep and narrow Alpine valley[*]

Andreas P. Weigel[1] and Mathias W. Rotach[2]

Abstract

Aircraft measurements, radiosoundings and sonic anemometer data - obtained during the MAP-Riviera field campaign in autumn 1999 in southern Switzerland - are used to investigate the flow structure, temperature profiles and turbulence characteristics of the atmosphere in a steep and narrow Alpine valley under convective conditions. On all predominantly sunny days of the intensive observation periods, a pronounced valley wind system develops. In the southern half of the valley, the daily up-valley winds have a jet-like structure and are shifted towards the eastern slope. These up-valley winds advect potentially colder air, a process which appears to be balanced by vertical warm air advection from above. The profiles of potential temperature show that, with the onset of up-valley winds, the mixed layer consistently stops growing or - on days with very strong up-valley winds - even stabilizes almost throughout the entire valley atmosphere. This is probably due to a pronounced secondary circulation in the southern part of the valley, which induces advection of warm air from above. The secondary circulation appears to be a consequence of sharp curvature in the along-valley topography.

Turbulence variables are calculated from flight legs in the along-valley direction. Turbulent kinetic energy (TKE) scales surprisingly well (i) if a TKE criterion (TKE > 0.5 $m^2 s^{-2}$) is employed as a definition of the boundary layer height and (ii) if the 'surface fluxes' - which exhibit a substantial spatial variability - from the slope sites are used rather than those from directly beneath the profile considered. Significant site-to-site differences in incoming solar radiation seem to be the reason for this characteristic behaviour. Profiles of momentum flux - scaled with a surface friction velocity - reveal more scatter than the TKE profiles, but still show a consistent behaviour. A surprisingly strong shear in the cross-valley direction can be observed and is probably a result of the secondary circulation.

2.1　Introduction

The atmosphere over mountainous terrain is characterized by a high degree of complexity. Dynamic aspects, such as local circulation patterns and the structure of mountain winds, have been investigated and comprehensively described in numerous publications (e.g. Wagner, 1938; Vergeiner and Dreiseitl, 1987; Barry, 1992; Whiteman, 1990, 2000). Moreover, conceptual and numerical models have been developed and employed in order to explain these mechanisms (e.g. Egger, 1990; Bader et al., 1987). Generally, a distinction is made between 'slope winds' and 'valley winds'. Slope winds are directed normal to the valley axis and parallel to the slopes. They are driven by horizontal density gradients between the surface layer on the slopes and the air over the centre of the valley. Under clear-sky daytime conditions, a symmetric double-circulation is expected to develop, with air rising along the heated slopes and subsiding in the valley centre. In the case of significant temperature differences between the two valley side-walls, this circulation pattern degenerates to a simple cross-valley circulation with upslope winds at the warmer side and downslope winds at the colder side. Thermal valley winds, on the other hand, are parallel to the valley axis. They are due to along-valley temperature gradients, which may be understood with the 'topographic amplification factor' concept as described by Steinacker (1984). Therefore, they do not require the valley floor to be sloped. On days with convective conditions, the valley winds are usually in up-valley direction.

Local circulations in a valley have been shown to directly influence the growth of the atmospheric boundary layer (e.g. Whiteman, 1982; Kossmann et al., 1998) and to play an important role in the transport of heat and moisture in such complex environments (Kimura and Kuwagata, 1995). Noppel and Fiedler (2001) estimated the heat flux due to slope winds to be even big enough to be considered in global circulation models. An understanding of the flow structure in mountainous terrain is, however, not only important to weather and climate aspects, but also to other fields such as pollutant transport (e.g. Clements et al., 1989) and atmospheric chemistry in Alpine valleys (e.g. Furger et al., 2000).

In contrast to local circulation systems, only very little is known about the turbulence structure over highly complex terrain. This is the more remarkable as the effect of turbulence on the transport of momentum, heat, water vapour, pollutants, greenhouse gases, etc. is at least of comparable importance. Some knowledge about turbulent flows over gentle hills has been gained from wind-tunnel experiments (e.g. Finnigan et al., 1990) and field measurements (e.g. Taylor and Teunissen, 1987; Vosper et al., 2002). Linear theory (Jackson and Hunt, 1975; Hunt et al., 1988b) provides further understanding, though it may fail in the lee side of a mountain ridge, where turbulent wakes can develop (Vosper et al., 2002, and references therein). However, no predictions can so far be made about the turbulence structure in a deep and steep Alpine valley. If anything, it can be expected to be highly complicated, as it lies simultaneously in the wake region of the upwind ridge and in the upslope region of the downwind ridge. It cannot be taken for granted that scaling regimes (as summarised in Holtslag and Nieuwstadt, 1986) and similarity relationships exist at all for such an environment. On the contrary, the validity of traditional boundary layer schemes, which have been developed and verified for flat and homogeneous terrain, seems to be rather unlikely. Nevertheless, numerical weather and climate models apply exactly such schemes in their parameterizations of subgrid-scale processes also over complex terrain, simply because no more is known about the real turbulence state (Rotach, 1995). This may have a major effect on the accuracy and performance of such models (Rotach et al., 2004). Therefore, in order to make a first step towards filling this gap of knowledge, an intensive measurement campaign has been carried out in a typical Alpine valley - the so-called MAP-Riviera project, a sub-project within the framework of the Mesoscale Alpine Program

Table 2.1: *Location of the sonic anemometers*

Site	Name	Location	Height (m above msl)	Measurement (m above ground)	Surface characteristics
A1	Bosco di Sotto	Valley floor	250	4	Mixed agriculture
B	Rored	Eastern slope	760	24	Forest
E1	Maruso-Roasco	Eastern slope	1060	13	Meadow
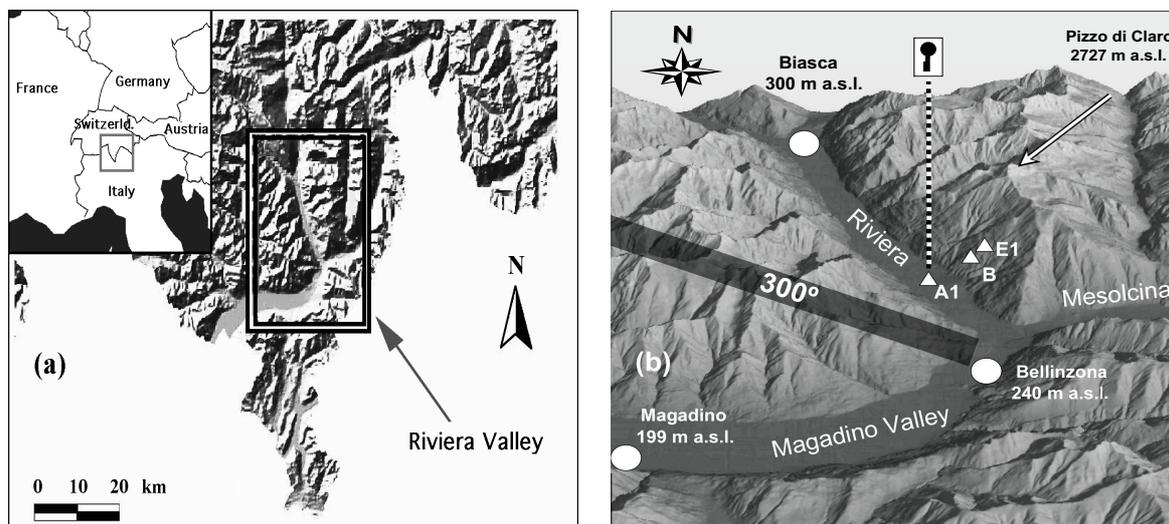
Figure 2.1: *(a) location and (b) topography of the Riviera Valley, showing location of the three surface stations A1, B and E1 (see Table 2.1). The grey bar in (b) indicates the bisecting line (≈300°) of the angle enclosed by the Riviera Valley and the Magadino Valley (see Section 2.3.1).*

(MAP Bougeault et al., 2001).

This contribution focuses on the mean structure and turbulence characteristics of the valley atmosphere under sunny, convective conditions. In the next section, a brief description of the set-up and location of the MAP-Riviera project is provided. The observed mean dynamic and thermal structure of the valley atmosphere is described in section three and discussed in section four. Section five gives an account of the turbulence structure.

2.2 Observations

A comprehensive description of the MAP-Riviera project can be found in Rotach et al. (2004). The declared aim of the project was to investigate in detail both the atmospheric and the hydro-logical processes occurring in a typical U-shaped Alpine valley. The observational campaign was carried out in the Riviera Valley in southern Switzerland (Fig. 2.1a) from August through October 1999. The Riviera Valley has a length of approximately 15 km and an orientation from north-north-west to south-south-east. The valley floor is about 1.5 km wide and only slightly sloped ($\approx 0.2°$). The southern end of the valley, which will from now on be referred to as the 'valley entrance', has an elevation of 240 m*, while the northern end ('valley exit') is at 300 m. The surrounding peaks reach altitudes of more than 2700 m, giving the valley an average depth of 2–2.5 km. The valley floor is characterized by agricultural land, with a freeway and

---

*All altitudes are above mean sea level in this chapter
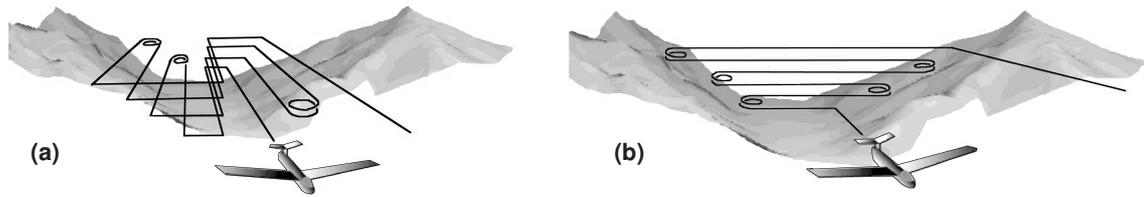
Figure 2.2: *Aircraft measurement patterns, showing typical flight paths (a) along the valley, and (b) across the valley.*

a railroad line running through the valley. The side walls have an inclination of 30–35° and are mainly covered with forest of height 10–15 m. Above 1800 m, alpine meadows and rocks dominate.

Eleven towers with a total of twenty sonic anemometers, placed along the valley bottom and on the eastern slope up to the ridge, provided continuous measurement of temperature, wind, moisture, pressure and radiation as well as turbulent quantities over the whole period. In this study, data from three sonic anemometers are used, one on the valley floor (station A1) and two on the eastern slope (stations B and E1). Their locations are shown in Fig. 2.1b and described in Table 2.1. In addition to these permanent observations, eight days were chosen as intensive observation periods (IOPs), during which the vertical and spatial structure of the valley atmosphere was investigated in detail. This was done by means of a light research aircraft (Neininger et al., 2001) and radiosoundings (launched at three-hourly intervals), tethered balloon ascents (half-hourly) and a microwave temperature profiler (with temporal resolution of twenty minutes). The aircraft was equipped amongst others with a five-hole pressure probe, a thermocouple and an infrared gas analyser allowing for the high-frequency (10 Hz) sampling of wind speed, temperature and moisture. The eight IOP days included both overcast and sunny days, i.e. days with predominantly mechanical forcing and days with convective conditions. This contribution focuses on the four mainly sunny IOP days, namely 21, 22, 25 August and 1 October 1999; the latter two were completely cloud-free, and the former two showed some transient cumulus clouds along the mountain ridges.

The flight pattern consisted of relatively long flight-legs (10–15 km) in the along-valley direction as well as short flight legs (1–4 km) normal to the valley axis. A typical along-valley flight path (AVFP) consisted of legs in 4–5 levels of elevation (from 500 m up to a maximum of 2000 m) with three legs per level: one next to the eastern slope, one next to the western slope, and one in the valley centre (Fig. 2.2a). The high sampling resolution of 10 Hz allowed for the calculation of turbulence variables (Section 2.5). The along-valley flight paths which were carried out on the afternoons of the convective IOP days are listed in Table 2.2. As with all time data in this contribution, flight times are given in UTC (local daylight-saving time = UTC + 2 hours). The cross-valley flight legs were carried out in a vertical plane approximately 3.5 km north of the valley entrance (where the surface stations and the radiosoundings were also located) and gave 'snapshots' of the structure of the valley atmosphere. A typical cross-valley flight path (CVFP) is illustrated in Fig. 2.2b.

Table 2.2: Overview of the along-valley flight paths.

No.	Date	Time (UTC)	No.	Date	Time (UTC)
1	21 Aug. 1999	1330-1445	5	25 Aug. 1999	1230-1330
2	21 Aug. 1999	1500-1620	6	25 Aug. 1999	1345-1500
3	22 Aug. 1999	1230-1330	7	1 Oct. 1999	1130-1230
4	22 Aug. 1999	1400-1500			
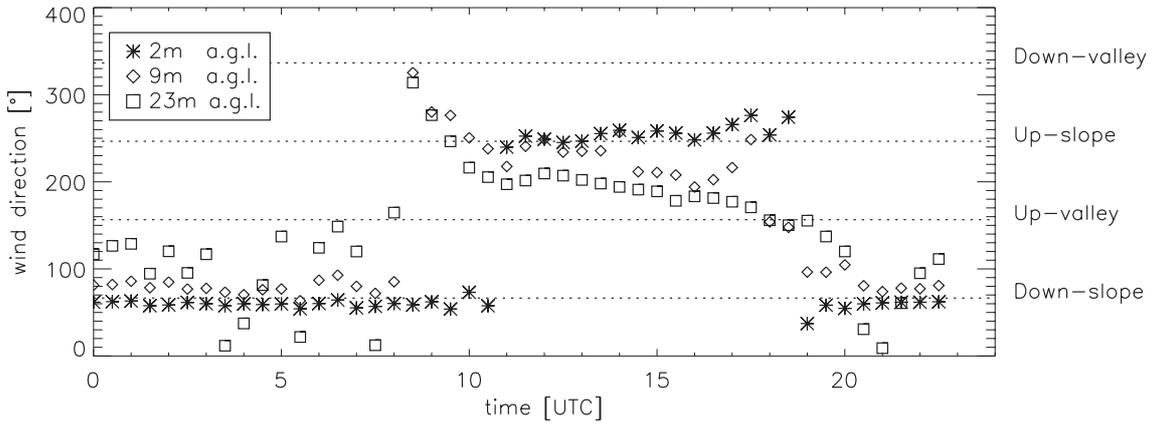
Figure 2.3: Time series (half-hourly averages of 10 Hz sonic anemometer data) of the surface wind direction on the eastern slope on 21 August in three heights above ground level. The data were obtained at a tower situated 500 m away from station E1 (at the same altitude, but in forest canopy). Inside the canopy (height ≈ 13m), a clear diurnal pattern with down-slope winds at night and up-slope winds during the day is observable. Outside the canopy the daytime winds reveal a strong up-valley component.

2.3 Mean observed structure of the valley atmosphere

2.3.1 Wind system

(i) Slope winds. During all convective IOP days of the measurement campaign, thermally driven slope winds were detected at the towers along the eastern slope of the valley. Generally, the following pattern can be observed. Winds in the canopy change from downslope to upslope at about 0900 UTC, and turn back to the downslope direction in the evening. In the afternoons, above the canopy, the upslope winds are overlain by up-valley winds. Fig. 2.3 shows a typical example of this characteristic diurnal pattern (measured on the eastern slope). A detailed account of the slope-wind observations in the Riviera Valley is given by Van Gorsel et al. (2003).

(ii) Channelling of the synoptic-scale flow. Whiteman and Doran (1993) showed that the direction of the synoptic-scale flow can influence the direction of the valley winds. In this subsection, the role of the synoptic-scale flow on the winds in the Riviera Valley is investigated for all eight IOP days, including the overcast days. In order to obtain the mere channelling contribution and to minimize the potential impact of thermally induced along-valley pressure gradients, measurements from the morning hours have been used. If available, winds have been determined from radiosoundings launched around 0800 UTC at station A1. On 28 September and 1 October, no radiosondes were launched at 0800 UTC and data from the 1100 UTC soundings have been used instead. On 21 and 22 August, the soundings entirely failed to measure winds. On these days the valley wind has been estimated from aircraft measurements

Table 2.3: Evaluation of the impact of the synoptic-scale flow on the wind direction in the Riviera Valley. The synoptic-scale winds were determined at 4000 m and the valley winds at 2000 m. If available, data were obtained from the morning soundings in the Riviera Valley (RS). Otherwise, aircraft measurements (AC) and soundings in Milan (MS) were used. 'UV' (up-valley) is approximately 155° and 'DV' (down-valley) 335°.

Date	Synoptic-scale wind (°, m s^{-1})	Valley wind direction and speed (m s^{-1})	Source and time (UTC) for synoptic-scale wind	Source and time (UTC) for valley wind
21 Aug. 1999	270 9	UV 2	MS 0600	AC 0730-0800
22 Aug. 1999	300 10	(no wind)	MS 0600	AC 0730-0800
25 Aug. 1999	300 10	DV 2	RS 0739	RS 0739
21 Sept. 1999	230 9	UV 3.5	RS 0809	RS 0809
22 Sept. 1999	230 8	UV 3	RS 0758	RS 0758
28 Sept. 1999	300 15	DV 7	RS 1055	RS 1055
29 Sept. 1999	290 17	UV 2.5	RS 0758	RS 0758
1 Oct. 1999	320 19	DV 2	RS 1055	RS 1055

(from CVFPs carried out between 0730 and 0800 UTC) and the synoptic-scale wind from the 0600 UTC soundings in Milan (about 90 km south-south-east of the Riviera Valley). Generally, the valley winds have been determined at an altitude of about 2 km (i.e. 1750 m above the valley floor), and the synoptic-scale wind at 4 km.

The results of these comparisons are listed in Table 2.3. While a synoptic-scale flow from directions further north than 300° seems to be channelled to a down-valley wind ($\approx 335°$), a flow from further south than 300° results in an up-valley wind ($\approx 155°$). This critical angle of 300° is approximately equal to the bisecting line of the angle which is enclosed by the Magadino Valley and the Riviera Valley (indicated in Fig. 2.1b). Thus, the impact of the synoptic-scale flow on the valley wind in the Riviera Valley needs to be seen as the combined effect of channelling in the Riviera Valley as well as in the adjacent Magadino Valley.

On sunny days, valley winds are predominantly driven by along-valley gradients in potential temperature. Due to the channelling effect, the magnitude of these thermally driven valley winds can then be expected to be either amplified or weakened by the synoptic-scale flow, depending on its direction.

(iii) Thermally driven valley winds. From now on, the focus is on the four IOP days with convective conditions. On all these days, significant up-valley winds have been observed at the surface station A1. As can be seen in Fig. 2.4, they begin in the late morning (between 0800 and 1100 UTC) and last until 1600–1800 UTC. This pattern is typical for thermally driven up-valley winds. Interestingly, on all 'valley wind days' of the MAP-Riviera campaign, the nocturnal down-valley winds are comparatively weak with magnitudes rarely exceeding 1 m s^{-1}. The reasons for this asymmetric behaviour have not been investigated.

The spatial structure of the up-valley winds has been obtained from aircraft measurements. Fig. 2.5 shows two examples from CVFPs at 1500 UTC on 21 August and at 1200 UTC on 25 August. These up-valley winds (and those on the other convective IOP days) consistently have a jet-like structure. The 'jets' are shifted towards the eastern slope[3] and have a depth of about 700–1500 m. A bird's-eye view on the wind structure (Fig. 2.6) reveals that this surprising pattern is restricted to the southern half of the Riviera Valley. Further north, the up-valley winds are spread out over the entire valley width. Measurements of an operational surface

---

[3]Cyclists living in the Riviera Valley region are familiar with this phenomenon. When cycling down the valley, the western side is preferred in order to minimize annoying headwinds [M. Buzzi, personal communication].
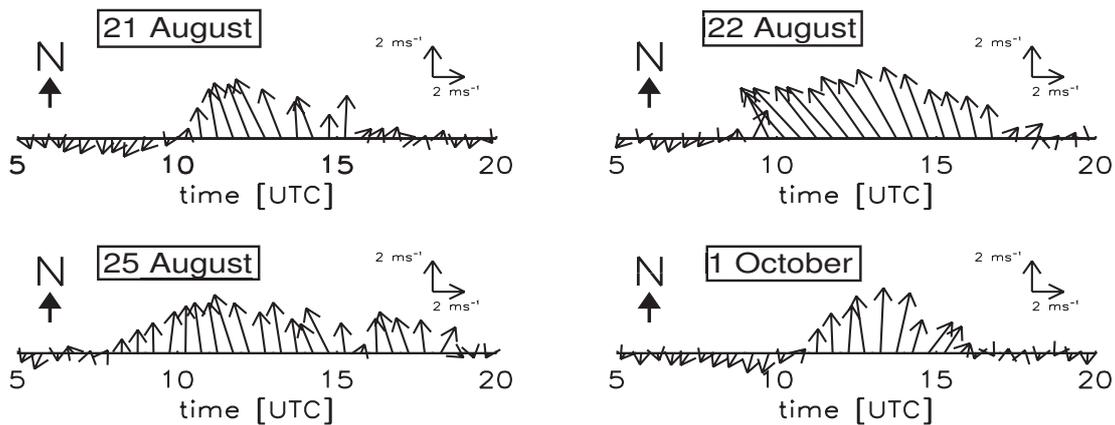
Figure 2.4: *Time series (half-hourly averages of 10 Hz sonic anemometer data) of surface winds measured at station A1. On all four convective IOP days, significant up-valley winds develop in the late morning and prevail throughout the afternoon.*

station in Magadino (not shown) indicate that the up-valley wind in the Riviera Valley is a continuation of a westerly (up-valley) flow in the Magadino Valley. It is very likely that, in the Bellinzona area, a flow-splitting occurs with some of the Magadino flow also continuing eastward into the smaller Mesolcina Valley.

In order to get into the Riviera Valley, the air from the Magadino Valley has to flow around a sharp edge of roughly 90°. Due to its inertia, the air is pushed towards the eastern slope, which could explain the jet-like flow structure in the valley entrance region. In Section 2.4.3, the effect of this curvature in the along-valley flow will be further elaborated.

Maximum speeds of the up-valley jet in the Riviera Valley vary from day to day. They are relatively high on 21 August with $9 \ \mathrm{m\,s^{-1}}$ and on 22 August with $11 \ \mathrm{m\,s^{-1}}$, and weaker on 25 August and 1 October with velocities not exceeding 7 and $6 \ \mathrm{m\,s^{-1}}$, respectively. The synoptic-scale flow in the afternoons of 21 and 22 August comes from 270° and 290° (i.e. 'less' than 300°), whereas on 25 August and 1 October it has a direction of 310° (i.e. 'more' than 300°). This can partly explain the significant differences in the observed velocities of the up-valley winds, because in agreement with the arguments at the beginning of Section 2.3, the thermally driven up-valley winds can be expected to be amplified by the synoptic-scale flow on 21 and 22 August and to be weakened on 25 August and 1 October.

2.3.2   Potential temperature

Fig. 2.7 shows the profiles of potential temperature of the four convective IOP days as obtained from the radiosoundings at station A1. On 21 August, a well-mixed layer develops and grows to a thickness of about 650 m by 1200 UTC. In the afternoon, however, the profiles reveal a stabilization of the air down to the valley floor with a potential temperature lapse rate of roughly $0.001 \ \mathrm{K\,m^{-1}}$. A similar and even more pronounced pattern can be observed on 22 August. A well-mixed layer with a depth of about 600 m is already developed at 0920 UTC. By 1200 UTC, a stabilization occurs and the profiles show a lapse rate of about $0.002 \ \mathrm{K\,m^{-1}}$. Measurements with the microwave temperature profiler (not shown) reveal that, after this stabilization, a shallow well-mixed layer of less than 350 m depth temporarily reoccurs. All in all, on both these days the afternoon temperature profiles are characterized by a more or less uni-
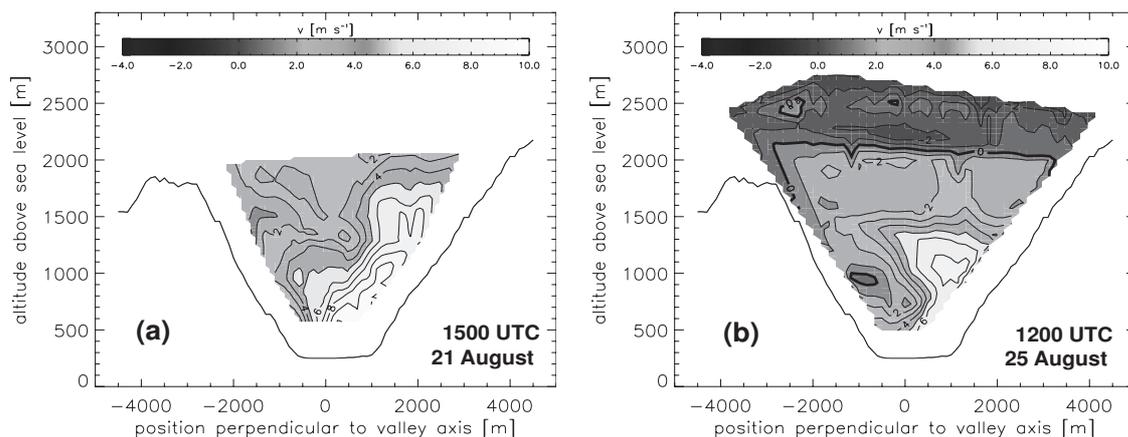
Figure 2.5: *Aircraft measurements of the along-valley wind component. The measurements were carried out (a) at around 1500 UTC on 21 August and (b) at around 1200 UTC on 25 August. The strong up-valley jet on the eastern side of the valley can be clearly seen. The legs were flown in a slice approximately 3.5 km north of the valley entrance.*

form stable stratification up to 3500-4000 m – a level significantly higher than the surrounding ridges and peaks.

The profiles of 25 August, which have already been described by De Wekker et al. (2005), behave differently. They are characterized by a three-layer structure, which becomes apparent by 0900 UTC: at the bottom (below 700 m) a well-mixed layer, in the middle (up to about 2000 m) a stably stratified layer (roughly 0.007 K m^{-1}), and above that – beginning at the level of the surrounding topography – an almost neutral layer. The mixed layer, which grows to a thickness of about 500 m by 0915 UTC, does not stabilize or decrease in the afternoon (in contrast to 21 and 22 August), but it does not continue to grow, either. A qualitatively similar pattern can be observed for 1 October. Here, the well-mixed layer has a depth of only about 200 m at 1100 UTC. Tethered balloon measurements reveal that the mixed layer does not become thicker than 300 m in the afternoon (not shown). At around 1400 UTC, the valley floor becomes shaded and the well-mixed layer begins to collapse. As on 25 August, the well-mixed layer is covered by a stable layer (up to about 1200 m with a lapse rate of about 0.004–0.005 K m^{-1}) and an almost neutral layer aloft (up to 3200 m).

The diurnal development of the valley atmosphere of the four convective IOP days can be categorized into two patterns. One pattern is represented by 21 and 22 August ('type I'), when a mixed layer of considerable depth develops by noon. In the afternoon, the up-valley winds become very strong, and the valley atmosphere stabilizes. A relatively shallow mixed layer can, if at all, only prevail temporarily. The other pattern is defined by 25 August and 1 October ('type II'), which exhibits weaker afternoon valley winds and a mixed layer that stops growing by noon, but does not decrease or disappear as in type I.

2.4   Discussion of the mean atmospheric structure

2.4.1   Possible explanations of the temperature profiles

According to current textbook knowledge, the morning inversion in a valley atmosphere is destroyed by the combined effect of turbulent heating from the bottom and subsidence of the stable core of the residual nocturnal layer as a consequence of upslope winds (Whiteman,
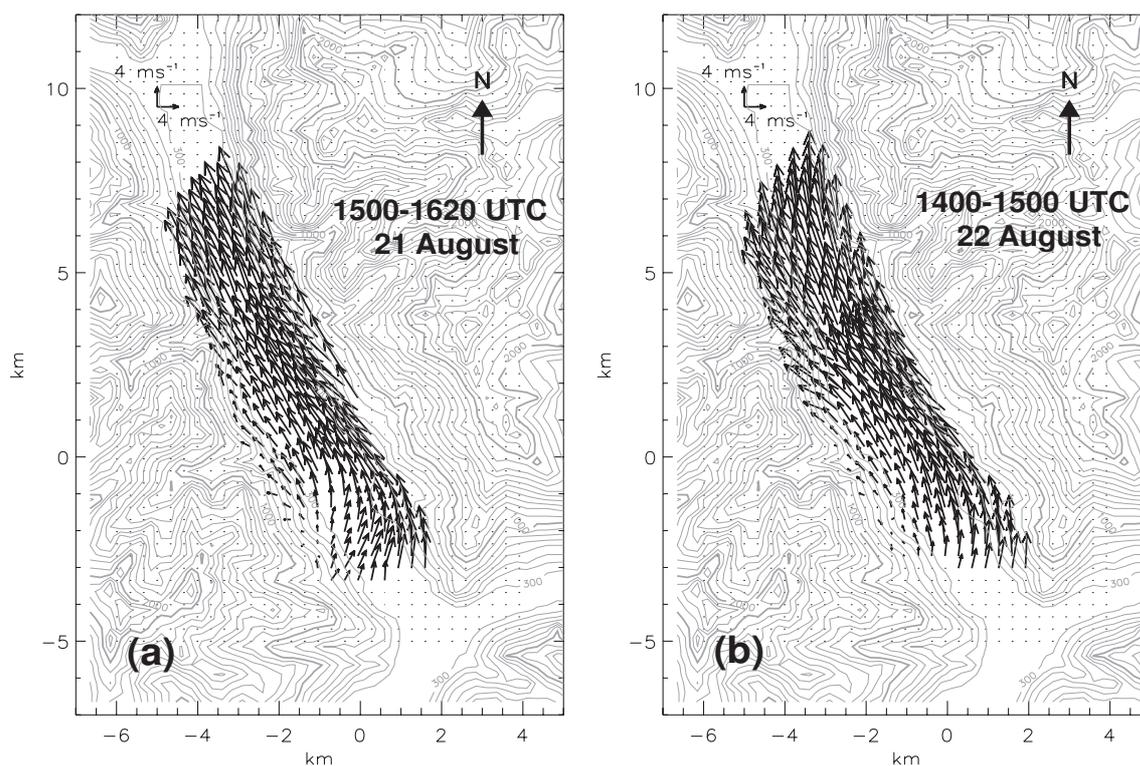
Figure 2.6: *Aircraft measurements of the valley wind on (a) 21 August (AVFP 2) at ≈830 m altitude and (b) 22 August (AVFP 4) at ≈940 m. The curvature of the flow in the southern part of the valley is quite apparent. In each case, data were obtained and interpolated from three along-valley flight legs (eastern slope, valley centre, western slope). The axes are labelled in km with respect to an arbitrary origin at 46.27°N, 9.02°E.*

1982). This results in temperature profiles which show a sinking morning inversion and a simultaneously growing mixed layer until the inversion is eventually broken. However, neither observed development type I nor type II is compatible with this concept.

For type II, two explanations have been proposed in the literature. De Wekker et al. (2005) suggest, from their numerical simulations of 25 August in the Riviera Valley, that the heating of the middle layer and its stable stratification are a result of horizontal advection of heat from the slopes to the valley centre. Another hypothesis has been described by Kuwagata and Kimura (1995, 1997), who observed and simulated similar temperature profiles in the Ina Valley in Japan. They attribute the structure of the temperature profiles to the subsidence of potentially warmer air, as part of a 'standard' thermal cross-valley circulation with air rising along the slopes and subsiding in the valley centre.

Neither of these mechanisms, however, is general enough to explain the type I cases. As described in Section 2.3.1, the mean flow has maximum velocity over the eastern slope at the valley entrance and then spreads over the whole valley width. Thus, advection of heat from the slopes to the valley centre as proposed by De Wekker et al. (2005) can only occur from the eastern side. However, on 21 and 22 August, the isentropes in the valley-cross section (discussed further in Section 2.4.3) are inclined such that an advection scheme would result in cooling rather than heating. Subsidence of warm air in the valley centre due to a 'standard' thermal circulation, on the other hand, cannot alone be responsible for the sudden stabilization of the boundary layer either, as shall be demonstrated here for 22 August. Typical afternoon surface heat fluxes were of the order of 70 W m^{-2}. Taking a maximum mixed-layer depth of about 350 m, this corresponds to a heating rate of approximately 0.0002 K s^{-1}. If a vertical
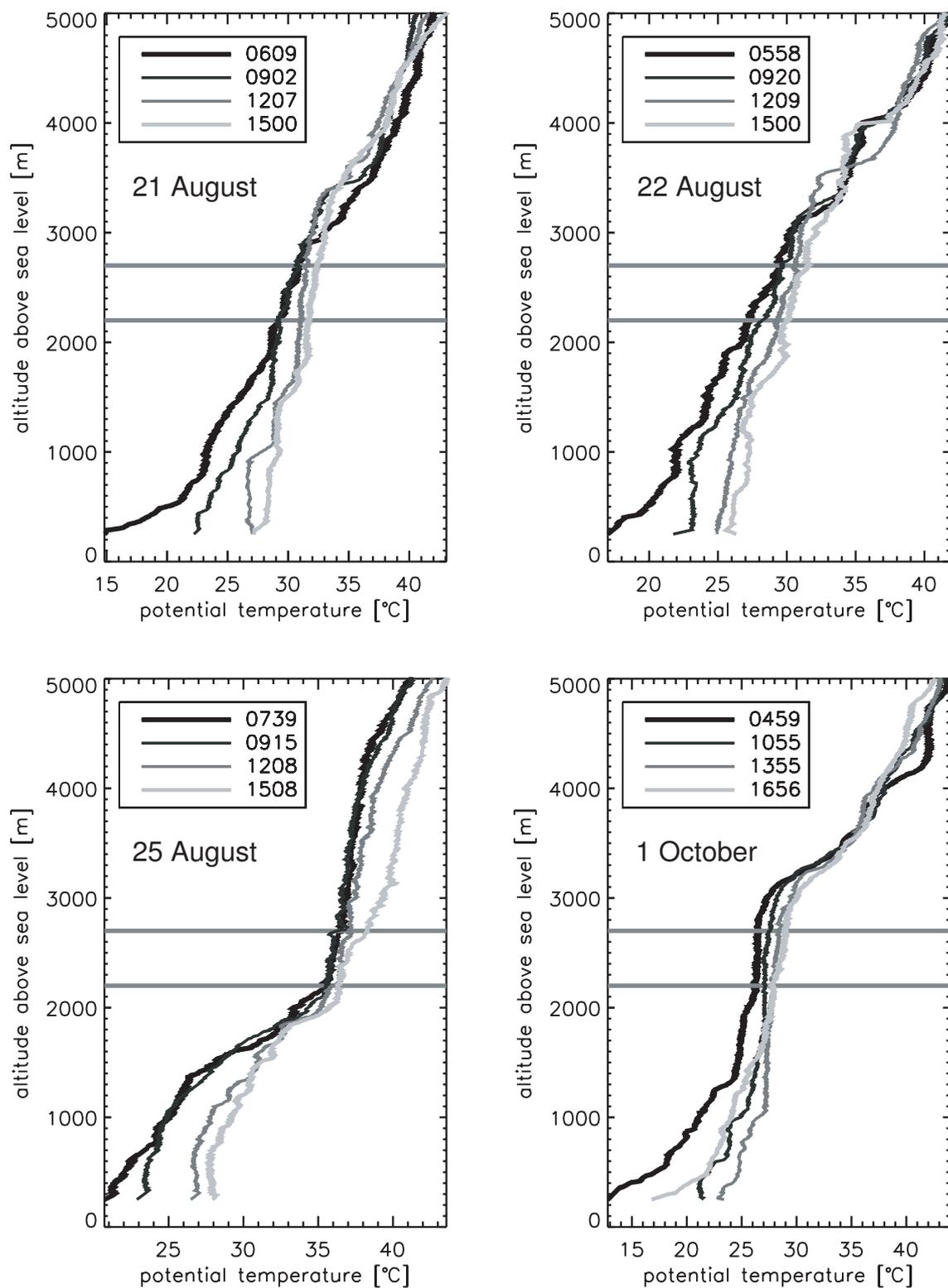
Figure 2.7: *Profiles of potential temperature as obtained from radiosoundings on the four convective IOP days. The soundings were launched next to surface station A1 at the indicated times* UTC. *The grey bars indicate the range of elevation of the ridges next to the valley.*
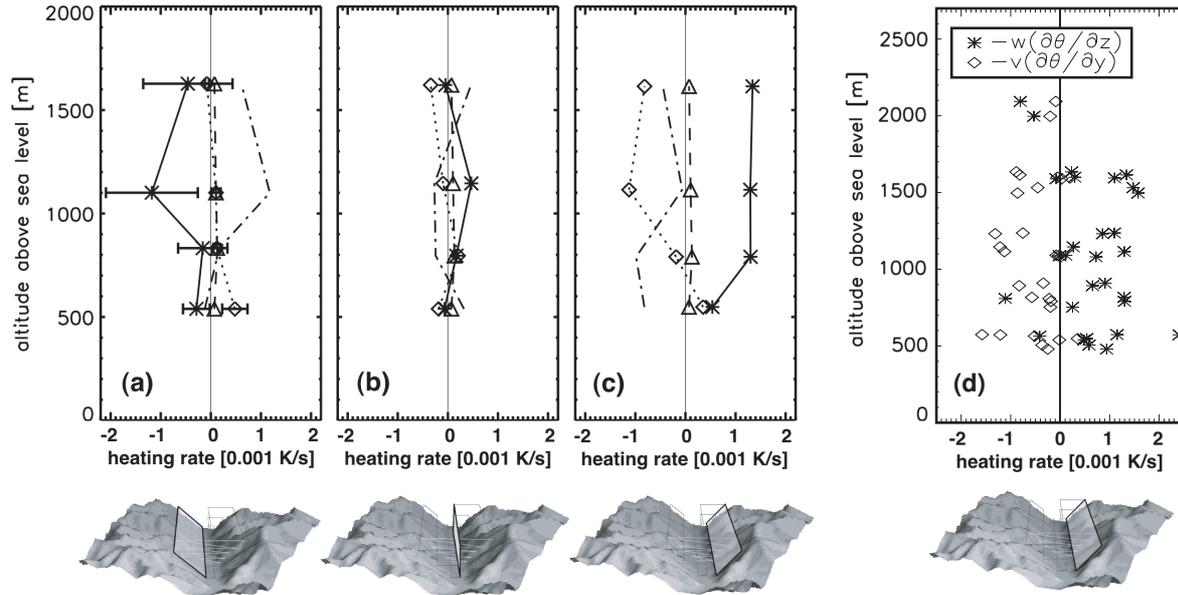
Figure 2.8: *Profiles of heating and cooling terms in the thermal budget. (a)-(c) have been derived from along-valley flight legs on 22 August (AVFP 3) in a plane (a) parallel to the western slope, (b) in the valley centre and (c) parallel to the eastern slope. The plots display the contribution of vertical advection of potential temperature (solid line with asterisks) and along-valley advection (dotted line with diamonds) to the overall heating rate (dashed line with triangles). The other terms of the budget equation (cross-valley advection and divergence of turbulent heat flux) are treated as a residual (dot-dashed line). Error-bars have been included in (a) to indicate the level of variability. (d) shows vertical advection (asterisks) and along-valley advection (diamonds) of potential temperature next to the eastern slope for* all *afternoon along-valley flights on the convective IOP days.*

potential temperature gradient of $0.002 \, \mathrm{K\,m^{-1}}$ is assumed, air would have to subside with a velocity of at least $0.1 \, \mathrm{m\,s^{-1}}$ in order to prevent a further growth of the mixed layer. With a valley width of more than $2 \, \mathrm{km}$ at $350 \, \mathrm{m}$ above ground and a typical upslope-wind speed of $1 \, \mathrm{m\,s^{-1}}$ (as observed on site E1), mass conservation would require the upslope wind layers on both sides of the valley to be about $100 \, \mathrm{m}$ thick. This, however, is very unrealistic, because already at canopy height (10–15 m) the upslope winds strongly interact with the mean flow and begin to turn into the up-valley direction (Fig. 2.3). As stated earlier, on 21 and 22 August the valley was temporarily shaded by cumulus clouds, resulting in short-time dips of turbulent surface heat flux. However, even in this regime of reduced surface heat fluxes, the 'standard' circulation cannot explain the observed profiles, as in the case of shading the slope winds and thus the subsidence in the valley centre would instantly cease (Vergeiner and Dreiseitl, 1987). We believe that another mechanism is involved, at least on 21 and 22 August, and begin with a look at the heat budget.

2.4.2 Heat budget and circulation pattern

Under the assumption of a negligible latent heat and radiation flux divergence, the tendency equation of potential temperature θ can be written as

$$\frac{\partial \theta}{\partial t} \;=\; -u\frac{\partial \theta}{\partial x} - v\frac{\partial \theta}{\partial y} - w\frac{\partial \theta}{\partial z} - \nabla \mathbf{H} \qquad (2.1)$$

where **H** is the turbulent kinematic heat flux. The coordinate system is oriented such that the x-axis points normal to the valley axis (roughly east-north-east) and the y-axis is aligned with the valley axis (roughly north-north-west). The horizontal wind components u and v are defined analogously. The left-hand side of this equation is the overall heating rate. The terms on the right-hand side represent heating due to cross-valley advection of potential temperature, along-valley advection, vertical advection and turbulent heat flux divergence.

The overall heating rate can be obtained from the profiles of potential temperature as measured by the radiosoundings. The contributions of along-valley advection and vertical advection have been estimated from the along-valley flight legs. A determination of the cross-valley advection appears to be very error-prone because of the high heterogeneity and generally low magnitude of the cross-valley wind component. Due to a noise problem in the high-frequency airborne temperature measurements, a calculation of the turbulent heat flux divergence has not been possible. Cross-valley advection and turbulent heat flux divergence therefore have to be treated as a residual.

The relative error of the along-valley and particularly the vertical advection terms is on the order of 100%, and often even larger. Therefore, only qualitative information can be extracted from these measurements. In Figs. 2.8a–2.8c, profiles of the heating (cooling) terms are plotted for an AVFP on 22 August. The profiles have been obtained from three stacks of along-valley flight legs, one next to the western slope, one in the valley centre and one next to the eastern slope. The overall heating rate turns out to be negligibly small on all three planes compared to the advection terms. At the western slope, the vertical advection is balanced by the residual term. In the valley centre, the advective contributions are generally very small. At the eastern slope, vertical advection is balanced by along-valley advection. Due to the large relative error in the estimates of the advection terms, only those features will be regarded as significant which can consistently be observed on the other afternoon flights of the four convective IOP days. In this sense, neither the profiles of the western slope nor those in the valley centre reveal a clear pattern (not shown). However, the eastern slope profiles consistently show the same behaviour; significant heating due to vertical advection, which seems to be balanced by the advection of colder air in the along-valley direction (Fig. 2.8d).

Thermally driven up-valley winds are a result of along-valley gradients in potential temperature and therefore advect potentially colder air. As these up-valley winds are shifted towards the eastern slope in the southern part of the valley (Section 2.3.1), the significant cooling contribution of along-valley winds in Fig. 2.8d is plausible. More astonishing, however, is the strong heating due to vertical advection, which implies a downward transport of warm air next to the eastern slope.

In order to get further insight into this heating mechanism, the spatial structure of the mean cross-valley wind has been investigated. Illustrative cross-sections are plotted for afternoon flights on 21, 22 and 25 August in two planes of 3 km width each: one about 3.5 km and one about 10 km north of the valley entrance (Fig. 2.9). The wind velocities have been obtained from AVFPs and interpolated over the valley cross-section by means of Delaunay triangulation (described, for example, in Watson, 1992). As each of the flight paths took about an hour, local non-stationarities cannot be ruled out, resulting in some discontinuities in the interpolated flow field (particularly evident, for example, in Fig. 2.9b). Nevertheless, an interesting and consistent pattern emerges: in the southern plane, clearly negative vertical winds in the eastern part of the valley and simultaneously positive winds in the valley centre and in the western part can be observed, together with a significant negative cross-valley wind component close to the surface (up to about 4 m s^{-1}). This indicates the existence of a clockwise circulation. On 21 and 22 August this circulation is much stronger than on 25 August. In the northern plane, no

pronounced downward flow is present next to the eastern slope. The vertical wind component is generally much weaker. Here, the flow structure is more consistent with a 'standard' valley circulation with air rising at the slopes and subsiding in the valley centre. It should be added, that also in the southern plane a slope wind layer does exist on the eastern slope, but it is too shallow to be observed by the aircraft (see Fig. 2.3).

In the light of these observations, the strong heating contribution due to vertical advection at the eastern slope (Fig. 2.8d) can now be understood. The clockwise circulation in the southern part of the valley seems to be strong enough to dominate the heat budget of the whole valley.

2.4.3 The mechanism of the secondary circulation

The observation of a clockwise circulation pattern with a downward flow next to the eastern slope is - at first sight - relatively surprising. In the afternoons, the eastern side of the valley is completely sun-exposed and therefore receives more short-wave radiation than the other side of the valley (Matzinger et al., 2003). If anything, one would expect an upward movement at this side due to thermally driven upslope winds.

In the 'standard' picture, slope winds exist on both sides of a valley, accompanied by a zone of subsidence in the valley centre. One could interpret the observed clockwise circulation pattern as a degenerate valley circulation with the subsidence region being pushed towards the eastern slope by the predominantly westerly synoptic-scale flow. Alternatively, this circulation could be due to a rotor flow, induced for example by a trapped lee-wave as described by Doyle and Durran (2002).

Neither of these hypotheses, however, can explain why this clockwise circulation in the Riviera Valley is only observable in the southern part of the valley. We therefore suggest another mechanism, which is associated with the curvature of the up-valley flow in the valley entrance region (Fig. 2.6). We start by noting that the flow of water in a curved channel develops a secondary circulation in a plane perpendicular to the flow direction (e.g. Rozovskii, 1957; Kalkwijk and Booij, 1986). This is due to two counteracting forces which act in a direction normal to the curved streamlines: an outward directed centrifugal force (causing an inclination of the water surface) and an inward directed hydrostatic pressure gradient force (as a consequence of the inclined water surface). Averaged over the flow depth, the two forces are in balance. However, while the pressure gradient force is height-independent, the stream-wise velocity and thus the centrifugal force increase with height (due to friction on the ground). Consequently, local imbalances arise. While the pressure gradient force dominates close to the ground and drives an inward flow, the centrifugal force dominates close to the water surface, resulting in an outward flow there. Mass conservation then leads to subsidence next to the outer wall of the curved channel and upwelling next to the inner wall. In nature, this phenomenon can be observed, for example, in rivers (Bathurst et al., 1977) and in tidal flows around headlands (Geyer, 1993). We think that the situation of a strong up-valley flow entering the Riviera Valley from the Magadino Valley (Fig. 2.1b) may also be seen as a curved channel flow. Due to the centrifugal acceleration, the colder air of the up-valley flow is pushed towards the eastern slope of the valley resulting in an inclination of the isentropes. Cross-sections of the potential temperature structure - measured on 21 and 22 August - show that this is indeed the case in the Riviera Valley (Fig. 2.10). In direct analogy to the secondary circulation in a curved channel flow, a gradient of hydrostatic pressure then builds up between the two sides of the valley and a secondary circulation develops. The adaption of this mechanism for the Riviera Valley is illustrated schematically in Fig. 2.11.

Kalkwijk and Booij (1986) estimated the maximum velocity of a curvature-induced sec-
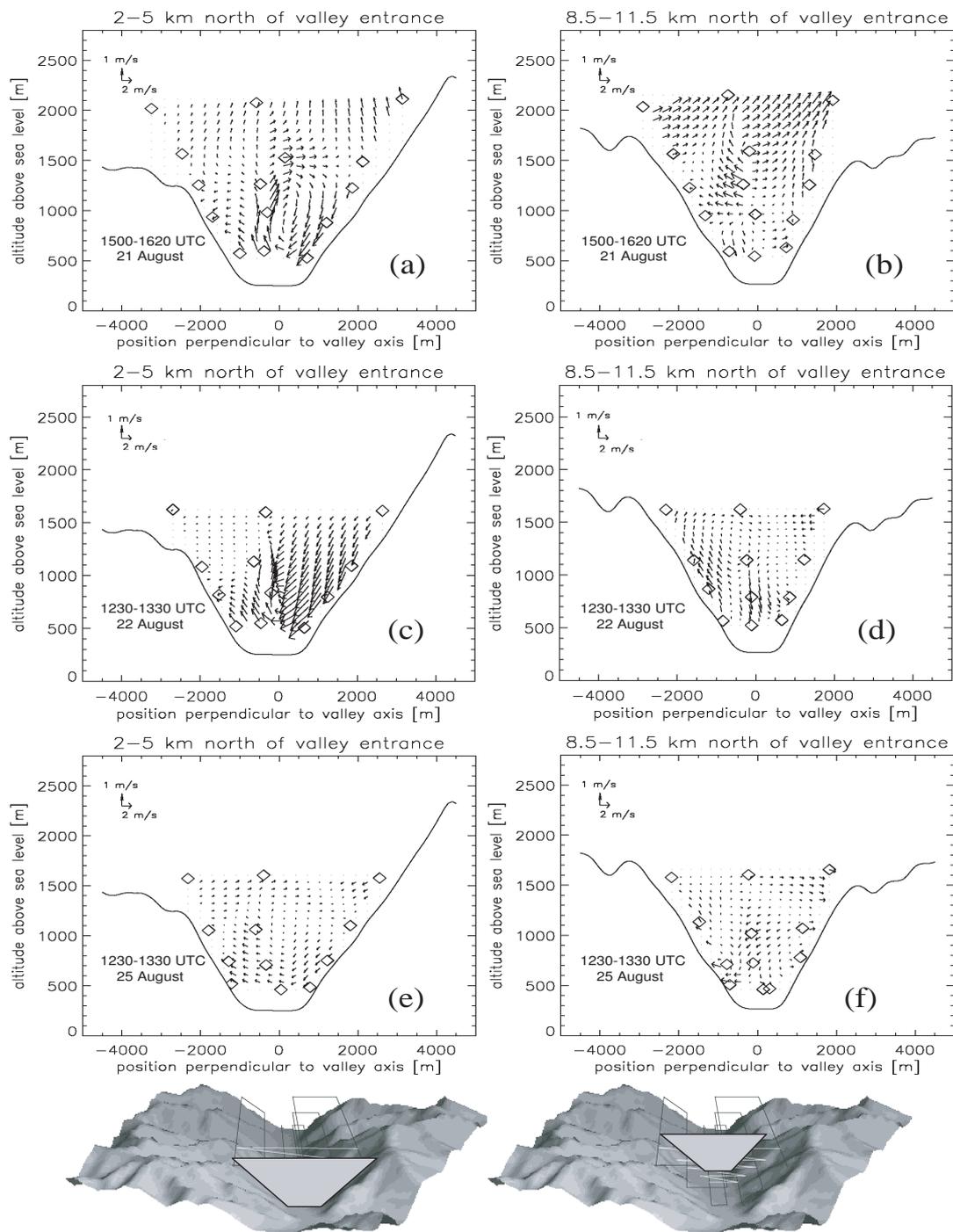
Figure 2.9: *Interpolated cross-valley flow fields in slices of 3 km thickness (a) about 3.5 km and (b) about 10 km north of the valley entrance on 21 August 1999. The wind speeds have been obtained from along-valley flight legs, whose projected positions are indicated by diamonds, and averaged over a distance of 3 km centred on the plane representing the slice. (c) and (d) are as (a) and (b), but for 22 August, and (e) and (f) are for 25 August.*
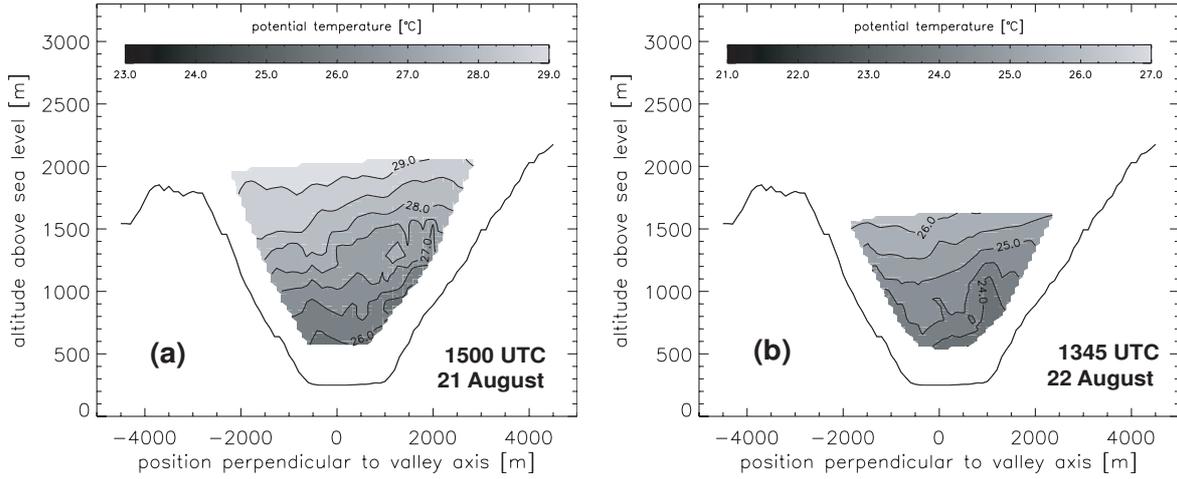
Figure 2.10: *Aircraft measurements of potential temperature, carried out on (a) 21 August around 1500* UTC *and (b) 22 August around 1345* UTC *in a slice approximately 3.5 km north of the valley entrance. The isentropes are clearly inclined, with the eastern side of the valley being colder than the western side.*

ondary circulation for a water flow in a curved channel. Even though their idealized assumptions certainly do not hold in the Riviera Valley in general, their calculation can give an idea of the order of magnitude of the cross-valley wind speed to be expected. They assume a rectangular channel cross-section, incompressibility, a logarithmic velocity profile, a parabolic eddy viscosity and a cross-channel velocity which is small compared to the average stream-wise velocity. Friction in vertical planes is neglected. If one furthermore assumes stationarity and neglects the Coriolis acceleration, the equation of momentum in the direction perpendicular to the main flow can be written as

$$u_s \frac{\partial u_n}{\partial s} - \frac{\partial}{\partial z} \left(K_m \frac{\partial u_n}{\partial z} \right) - \frac{u_s^2}{R} + \frac{1}{\rho} \frac{\partial p}{\partial n} = 0 \qquad (2.2)$$

This formulation is in curvilinear coordinates: u_s is the velocity in the *s*-direction (along the streamlines, i.e. in the up-valley direction) and u_n is the velocity in the *n*-direction (normal to the streamlines, i.e. in cross-valley direction). R is the curvature radius of the streamlines, ρ the density of the fluid, p the pressure and K_m the eddy viscosity. The terms in Eq. 2.2 represent the stream-wise advection and frictional dissipation of cross-channel flow, the centrifugal acceleration and the cross-channel pressure gradient.

Starting with this equation and following the calculations of Kalkwijk and Booij (1986), an estimate of the maximum cross-valley flow $u_{n,\max}$ can be obtained. With typical values from our measurements for the height-averaged up-valley wind speed ($\langle u_s \rangle = 7$ m s^{-1}) and the stream-wise Reynolds shear stress at the bottom ($\overline{u_s' w'}_0 = -0.6$ m^2 s^{-2}), an upper limit can be estimated at $u_{n,\max} \approx 30 \cdot (h/R)$ m s^{-1}, with h being the depth of the flow. Taking $h \approx 1000$ m and $R \approx 5000$ m, we get $u_{n,\max} \approx 6$ m s^{-1}. This value exceeds our measurements, which show $u_{n,\max}$ to range between approximately 1 and 4 m s^{-1} (Figs. 2.9a, 2.9c and 2.9e), but the order of magnitude is the same.

2.4.4 Influence of the secondary circulation on the temperature profiles

The clockwise secondary circulation is very pronounced on 21 and 22 August and much weaker on 25 August. This is plausible, because the strength of the circulation is proportional to the
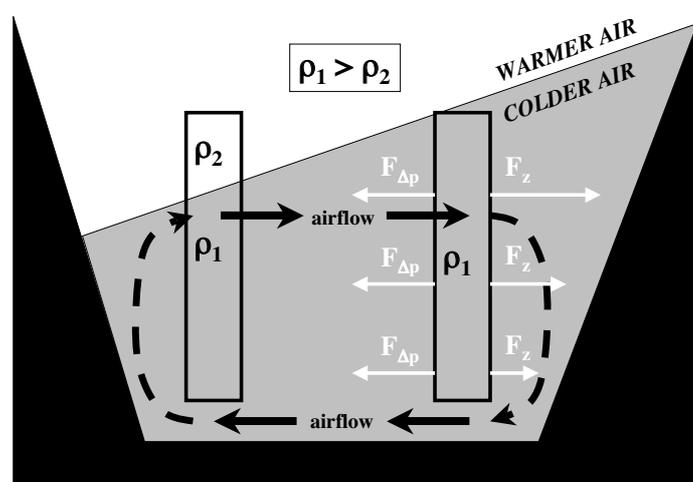
Figure 2.11: *Mechanism of the curvature-induced secondary circulation in the Riviera Valley entrance region. The centrifugal acceleration pushes the potentially colder air of the up-valley flow towards the eastern slope, resulting in an inclination of the isentropes. Due to different air densities ρ, a hydrostatic pressure gradient force $F_{\Delta p}$ emerges between the two sides of the valley, which - averaged over the flow depth - balances the centrifugal force F_z. However, local imbalances occur, as the pressure gradient force is height-independent (in this simple model) while the centrifugal force increases with height (due to frictional flow deceleration close to the ground). These imbalances drive a westward flow close to the ground and an eastward flow close to the upper boundary of the up-valley flow. Due to mass conservation, a clockwise secondary circulation finally develops.*

up-valley wind speed, which is lower on 25 August. On 1 October, the convective IOP day with the weakest up-valley wind, no secondary circulation has been observed at all. If a secondary circulation existed on that day, its effect would have been very small, possibly beyond the measurement accuracy of the aircraft.

This finally leads us to a possible explanation of the difference between the temperature profiles of type I and type II: on days with strong up-valley winds (21 and 22 August), the curvature-induced secondary circulation effectively transports warm air down towards the ground, which results in a stabilization of the valley atmosphere. Only a very shallow mixed layer can - temporarily - exist. On days with weaker up-valley winds (25 August and 1 October), the circulation is not strong enough, and a comparatively thicker well-mixed layer can prevail, though it does not grow in the afternoons.

As the mechanism of the proposed secondary circulation is quite general, similar results should be observable elsewhere, when a sharp curvature in the valley topography is present. A more detailed evaluation of the conditions leading to such a secondary circulation by means of large-eddy simulations is intended for a future paper.
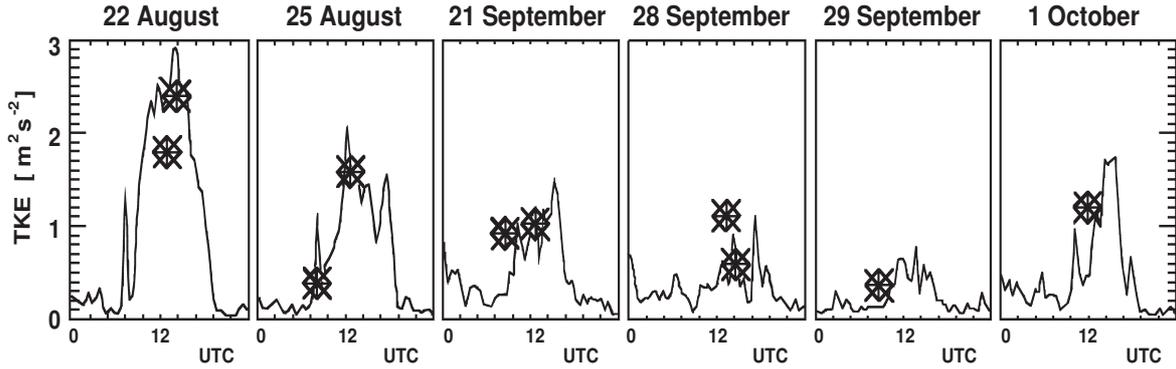
Figure 2.12: *Comparison of aircraft and tower data on six days of the measurement campaign. The solid line is the time series of turbulent kinetic energy (TKE), as obtained from station B on the eastern slope. The asterisks show airborne TKE-values from flight legs which passed station B at a distance of less than 75 m.*

2.5 Turbulence structure

The flow structure on convective days in the Riviera Valley has been shown to be highly complex. It is therefore not certain whether or not the turbulence in such an environment reveals a consistent, 'reproducible' pattern. This section focuses on this question.

2.5.1 Filtering

The high sampling frequency of 10 Hz and the aircraft flight pattern with along-valley flight legs of approximately 10–15 km length allows the calculation of profiles of turbulence statistics by means of eddy correlation. A recursive low-pass filter as described by McMillen (1988) has been applied to extract the turbulent fluctuations from the measured signals. In order to make the filter symmetric, it has been applied twice, once in the forward direction and once in the backward direction, and the two resulting filtered time-series have then been averaged. This procedure is carried out in order to avoid the phase lag which is inherent in this filter (De Franceschi and Zardi, 2003).

For the investigation of scaling characteristics to be discussed in the next subsection, the turbulence values from the aircraft measurements have to be compared to those obtained from the surface stations. It is thereby important that approximately the same length-scales of turbulent motion are included in both observation systems. De Franceschi and Zardi (2003) showed that a filter time constant, τ, results in an effective cut-off period of $2\pi\tau$. If v_0 is a typical wind speed at a surface station, v_a the velocity of the aircraft and τ_0 the filter time constant applied to the surface data, then the aircraft data need to be filtered with a time constant $\tau_a = \tau_0 v_0 / v_a$ in order to include comparable length-scales. In our measurements, v_0 was typically around 4 m s^{-1} (in the afternoons) and v_a approximately 50 m s^{-1}. τ_0 has been set to 300 s, requiring a filter constant for the aircraft data of $\tau_a = 24$ s. The success of this approach has been evaluated by means of flight legs, which were carried out very close (less than 75 m) to surface station B. Fig. 2.12 shows the very good correspondence between turbulent kinetic energy (TKE) values obtained from these flight legs and the respective data from the tower.
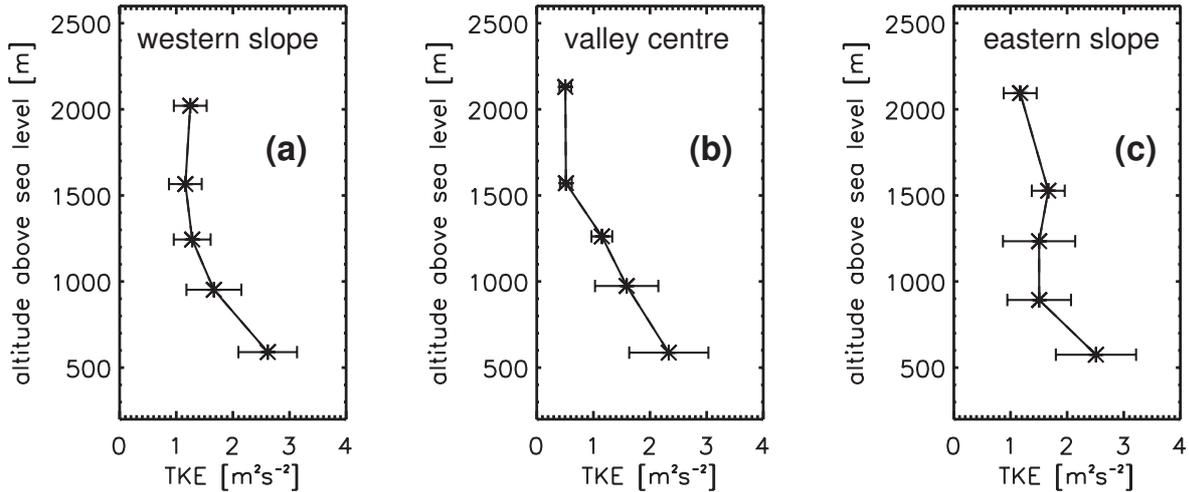
Figure 2.13: *Typical profiles of turbulent kinetic energy (TKE), as obtained from along-valley flight legs on 21 August (a) parallel to the western slope, (b) in the valley centre and (c) parallel to the eastern slope. The error bars indicate the level of TKE variability within each flight leg (standard deviation of TKE from subintervals of 350 m length).*

2.5.2 Observations

In Fig. 2.13, typical profiles of TKE are shown (here AVFP 2). The values have been obtained from along-valley flight legs parallel to the western slope, in the valley centre and parallel to the eastern slope. In the valley centre, TKE decreases with increasing height from approximately $2.5 \, \mathrm{m}^2 \, \mathrm{s}^{-2}$ continuously down to $0.5 \, \mathrm{m}^2 \, \mathrm{s}^{-2}$, while the values remain higher close to the slopes (at altitudes above 1000 m). Similar behaviour is observed on the other afternoons (not shown), leading to the assumption that the profiles might exhibit some sort of similarity. Convective conditions and the observation of a (shallow) mixed layer at least on some of the convective IOP days would suggest mixed-layer scaling according to Deardorff (1970), where the mixed layer height, z_i, and the convective velocity scale, $w_*(= \{(g/\overline{\theta_0}) \cdot \overline{w'\theta'_0} \cdot z_i\}^{1/3}$, with $\overline{w'\theta'_0} =$ surface heat flux, $\overline{\theta_0} =$ surface potential temperature), are the characteristic variables. However, due to the vertical warm-air advection as discussed in Section 2.4.2, neither has the 'well-mixed' property been observed on all the days (despite positive surface heat fluxes), nor is there always a clear inversion which could provide a useful estimate for z_i. We therefore try and apply a modified Deardorff scheme, in which the definition of the length-scale z_i has slightly changed: z_i is defined as the height of the turbulent layer, based on a TKE threshold criterion ($\mathrm{TKE} > 0.5 \, \mathrm{m}^2 \, \mathrm{s}^{-2}$), which is applied to the TKE profiles in the valley centre. This criterion is based on our observation that in the Riviera Valley the decrease of TKE with height often stagnates once TKE has fallen below $0.5 \, \mathrm{m}^2 \, \mathrm{s}^{-2}$ (as in Fig. 2.13b).

Fig. 2.14 shows the scaled profiles of TKE (z/z_i vs. TKE/w_*^2) which were measured during the four convective IOP days from along-valley flight legs in the valley centre. In Fig. 2.14a the velocity scale w_* has been obtained using the surface heat flux from station A1, i.e. directly beneath the TKE profile. With this w_*, the scaled TKE profiles exhibit some overall similarity but they do not fall on one single curve at all. The correspondence becomes much better when using w_* as obtained from surface site B at the eastern slope at 760 m (Fig. 2.14b). A further improvement can be seen with w_* taken from site E1 (Fig. 2.14c) at 1060 m. Note that in all three panels of Fig. 2.14, the same observed values of TKE and z_i are used and only w_* has been varied by using surface heat fluxes from different sites. This indicates that the turbulence structure of the valley atmosphere (in our example the centre part of the valley) is to a high
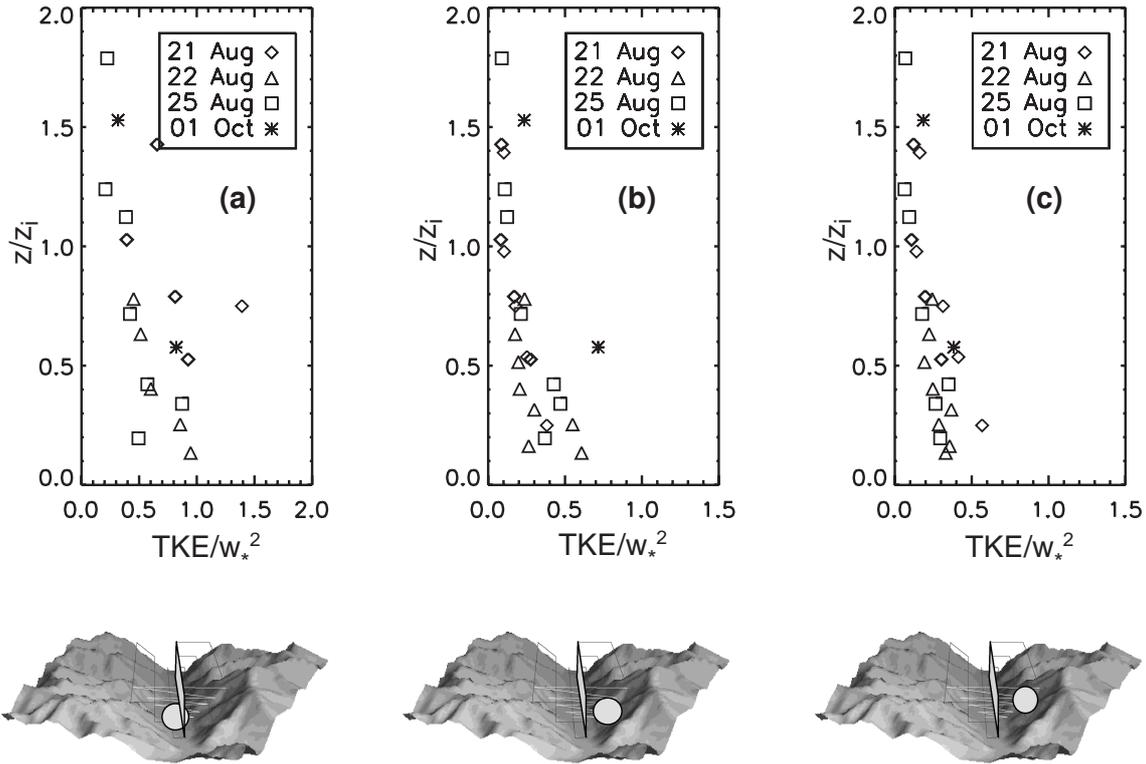
Figure 2.14: *Profiles of turbulent kinetic energy (TKE), derived from flight legs in the along-valley direction in the valley centre on four convective days. Each plot displays the same TKE values, but scaled with different values of w_*^2 derived from surface heat fluxes: (a) from the valley floor at station A1 (values with close-to-zero surface heat flux due to temporary cloud shading have been omitted here), (b) from the eastern slope at station B and (c) from the eastern slope at station E1.*

degree related to the surface processes on the eastern slope rather than those on the valley floor.

Concerning the choice of the surface site for the scaling of Reynolds stress components (cross-valley stress $\overline{u'w'}$ and along-valley stress $\overline{v'w'}$), similar results - though less pronounced - have been obtained. Here, only results of scaling with a surface friction velocity $u_* = (\overline{u'w'}_0^2 + \overline{v'w'}_0^2)^{1/4}$ from site E1 are shown (Fig. 2.15). Though there is much more scatter than in the TKE profiles, some consistent features become evident: (i) cross-valley stresses are positive for $z/z_i < 0.5$ over the eastern slope and predominantly negative over the western slope, (ii) along-valley stresses are negative over the eastern slope, whereas no consistent sign can be attributed to the central and western profiles, and (iii) the magnitudes of the along-valley and cross-valley stresses seem to be comparable.

2.5.3 Discussion

Significant values of TKE have been observed on the afternoons of the convective IOP days, even when the stratification was slightly stable (on type I days sometimes down to the ground). This demonstrates that the boundary layer thickness in such an environment apparently cannot be extracted from the temperature profiles. The application of a TKE-threshold criterion, however, proves to be very successful: the profiles of TKE reveal surprisingly good scaling characteristics, taking into consideration the complexity of the environment and the heterogeneity of the flow field.

The strong dependence of the scaling behaviour on the location of the surface station is
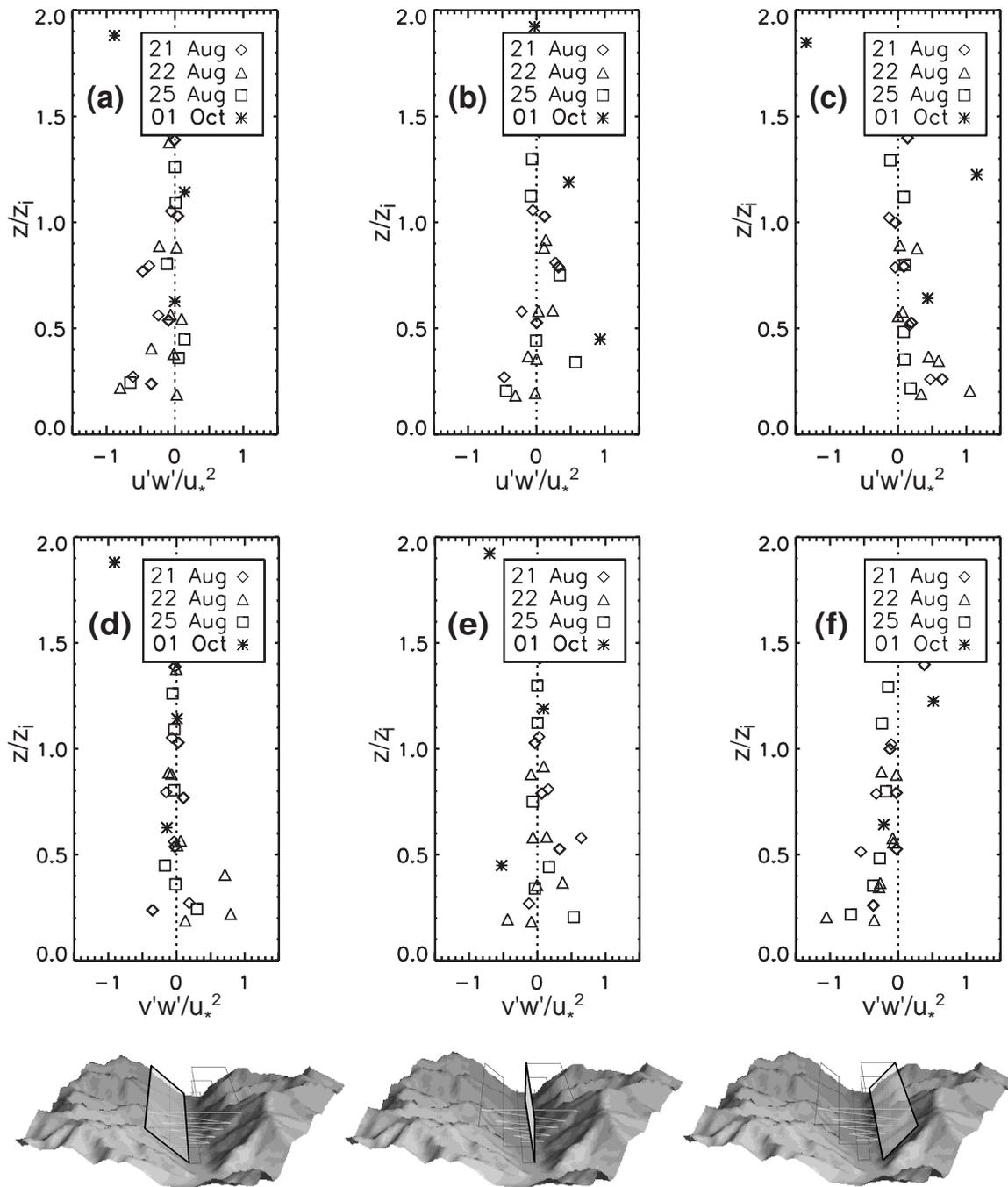
Figure 2.15: *Profiles of cross-valley stress, scaled with a friction velocity u_*^2 obtained at station E1, from flight legs (a) parallel to the western slope, (b) in the valley centre and (c) parallel to the eastern slope. (d)-(f) are as (a)-(c), but for along-valley stress.*
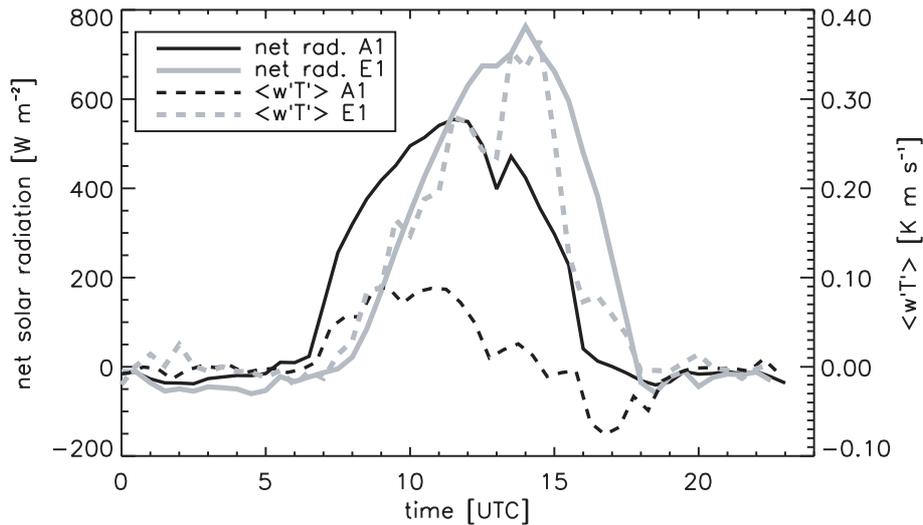
Figure 2.16: *Net radiation flux and kinematic surface heat flux at two different sites on 25 August. The maxima of the curves measured at the eastern slope (station E1) are much higher and occur later than those on the valley floor (station A1).*

astonishing. The big site-to-site differences in incoming solar radiation are probably the reason, with the east slope receiving much more radiation than the valley floor (Matzinger et al., 2003). Consequently, the slope is characterized by much higher surface heat fluxes than the valley floor (Fig. 2.16). Apparently, the strongly turbulence-producing slope surfaces have a dominating influence on the turbulence structure in large parts of the valley atmosphere. The interaction of the observed secondary circulation (Section 2.4.3) with the slope possibly plays an important role in this context, but a detailed explanation is subject to further research.

An attempt to scale turbulent stresses with the friction velocity u_* yields more scatter than the TKE profiles. This is not surprising, as the generation of stress is usually very complex and can be attributed to a combination of several factors (Kaimal et al., 1976). Moreover, the accuracy of stress measurements from flight legs as short as 10–15 km is very limited from a theoretical point of view (Lenschow and Stankov, 1986). Nevertheless, it can clearly be seen that the along-valley stress is strongest at the eastern side of the valley and has a negative sign. This is consistent with our observation that the up-valley wind is pushed towards the eastern slope (at least in the southern half of the valley, see Section 2.3.1), where consequently a maximum in friction occurs. Noteworthy is the behaviour of the cross-valley stress, with positive values at the eastern side and negative values in the centre and on the western side. In an 'ideal' convective boundary layer, the stress normal to the flow direction is expected to vanish (Kaimal et al., 1976). The non-vanishing cross-valley stress in our measurements - it has the same order of magnitude as the along-valley stress - can be seen as another manifestation of the secondary circulation. Consider an air parcel rising from the eastern side of the valley ($u_{\mathrm{parcel}} = 0$, $w_{\mathrm{parcel}} > 0$) and entering the secondary circulation ($u_{\mathrm{circ}} < 0$, $w_{\mathrm{circ}} < 0$), then the air parcel has a positive cross-valley wind component and a positive vertical wind component with respect to the secondary circulation. This is consistent with a positive cross-valley stress. Equally, air parcels in the boundary layer of the western side enter a flow structure which is directed vertically upward and westward, resulting in a negative cross-valley stress.

2.6   Summary and conclusions

In this paper, results are presented from the MAP-Riviera measurement campaign, which was carried out to investigate the mean structure and turbulence characteristics of the atmosphere in a typical U-shaped alpine valley. Data were obtained from a light research aircraft, radiosoundings, tethered balloon ascents and a microwave temperature profiler as well as sonic anemometers at several surface stations on the valley floor and along the eastern slope.

The focus of this contribution lies on the afternoons of four days with fair weather conditions. On all these days, a pronounced thermally driven valley wind system develops. Due to a strong curvature of the flow in the valley entrance region, the up-valley winds are pushed towards the eastern slope and reveal a jet-like structure in the southern half of the valley with wind speeds of up to about $10 \, \text{m s}^{-1}$. Moreover, a pronounced clockwise secondary circulation can be observed, which is not compatible with 'standard' valley circulation schemes. We believe that it is induced by the curvature of the up-valley flow in the southern part of the valley. The cold-air advection due to the up-valley winds seems to be balanced by vertical warm-air advection as a consequence of this secondary circulation.

The daily development of the profiles of potential temperature in the valley atmosphere follows two patterns: (i) temperature profiles with a well-mixed layer that stabilizes almost (sometimes even entirely) down to the valley floor in the afternoons ('type I'), and (ii) temperature profiles with a well-mixed layer that stops growing by noon, but does not disappear in the afternoon ('type II'). Days of type I are characterized by stronger up-valley winds, probably because of a 'supportive' synoptic-scale flow. Consequently, on those days the secondary circulation is also more pronounced, resulting in more advective heating from above. On type I days, this heating is apparently strong enough to stabilize the atmosphere more or less over the entire depth of the valley, while on type II days a well-mixed layer can prevail, but not grow. This behaviour of the thermal stratification indicates that profiles of potential temperature may not be a good indicator for the boundary-layer thickness in mountainous terrain, especially if the topography (e.g. the valley axis) is not ideally straight.

Turbulence profiles have been shown to scale astonishingly well if (i) the boundary-layer height is defined by applying a TKE-threshold criterion, and (ii) the surface heat fluxes from the sunlit, eastern slope are used rather than those from the surface station directly under the flight leg. Thus, the turbulence structure in large parts of the valley atmosphere seems to be closely related to (perhaps even determined by) the sun-exposed slope, which reveals a surface layer with larger turbulent heat fluxes than the valley floor. The success of the scaling for the TKE profiles leads to the (at first sight puzzling) result that on warm, convective and predominantly sunny days with positive surface turbulent heat fluxes, the mean temperature profile can be stable throughout but nevertheless a form of Deardorff scaling works. This paradox with the stable stratification is resolved through the presence of the secondary circulation. Similarly, the scaled Reynolds stresses are consistent with this circulation, which is due to the curvature of the along-valley flow.

Overall, the MAP-Rivera project was one of the first campaigns of this kind in such complex topography. Despite the steep terrain, the mean flow and particularly the turbulence structure proved to be much less 'random' than one might have anticipated. Further data analysis as well as large-eddy simulations are expected to deepen our understanding of the atmospheric processes in the Riviera Valley and Alpine terrain in general.

Acknowledgments

Chapter 3

High-resolution large-eddy simulations of flow in a steep Alpine valley. Part I: Methodology, verification and sensitivity experiments

High-resolution large-eddy simulations of flow in a steep Alpine valley. Part I: Methodology, verification and sensitivity studies[*]

Fotini K. Chow[1], Andreas P. Weigel[2],
Robert L. Street[1], Mathias W. Rotach[3] and Ming Xue[4]

Abstract

This paper investigates the steps necessary to achieve accurate simulations of flow over steep, mountainous terrain. Large-eddy simulations of flow in the Riviera Valley in the southern Swiss Alps are performed at horizontal resolutions as fine as 150 m using the Advanced Regional Prediction System (ARPS). Comparisons are made to surface station and radiosonde measurements from the MAP-Riviera project field campaign of 1999. Excellent agreement between simulations and observations is obtained, but only when high-resolution surface datasets are used and the nested grid configurations are carefully chosen. Simply increasing spatial resolution without incorporating improved surface data gives unsatisfactory results. The sensitivity of the results to initial soil moisture, land use data, grid resolution, topographic shading, and turbulence models is explored. Even with strong thermal forcing, the onset and magnitude of the up-valley winds are highly sensitive to surface processes in areas which are well outside the high-resolution domain. In particular, the soil moisture initialization on the 1 km grid is found to be crucial to the success of the finer resolution predictions. High-resolution soil moisture and land use data on the 350 m resolution grid also improve results. The use of topographic shading improves radiation curves during sunrise and sunset, but the effects on the overall flow are limited because of the strong lateral boundary forcing from the 1 km grid where terrain slopes are not well resolved. The influence of the turbulence closure is also limited because of strong lateral forcing and hence limited residence time of air inside the valley, and because of the stable stratification which limits turbulent stress to the lowest few hundred meters near the surface.

[1]Environmental Fluid Mechanics Laboratory, Stanford University, Stanford, CA, USA
[2]Institute for Atmospheric and Climate Science ETH, Zurich, Switzerland
[3]Swiss Federal Office for Meteorology and Climatology, MeteoSwiss, Zurich, Switzerland
[4]School of Meteorology and Center for Analysis and Predicition of Storms, University of Oklahoma, USA

3.1   Introduction

Increases in available computational power now allow high-resolution simulations of flow over complex terrain, but the appropriate numerical and physical parameters required by such simulations are not generally known. The influence of parameterizations such as those used for turbulence, soil moisture, solar radiation, surface roughness, the configuration of initial conditions, lateral boundary conditions, and the choice of numerical grids is highly situation dependent. Simulations are generally performed with "the best available" information and datasets. This paper investigates the steps necessary to achieve accurate large-eddy simulations of flow in highly complex terrain. Specifically, we examine the flow and temperature fields in the Riviera Valley, located in the Alps in southern Switzerland. The simulation results are verified through comparisons to surface and radiosonde observations in the Riviera Valley, obtained during the Mesoscale Alpine Programme (MAP) Riviera Project (Rotach et al., 2004). We also evaluate the model sensitivity to changes in parameterizations such as those listed above. The boundary layer processes in our simulated valley are described in Part II of this work (Weigel et al., 2005)[*], which includes comparisons to aircraft flight data, descriptions of along-valley wind transitions and secondary cross-valley circulations, and a heat budget analysis.

Obtaining accurate simulations of flow in highly complex terrain has been the object of much research. At relatively coarse resolution, a large domain can be used, but steep mountains and valleys cannot be resolved. Benoit et al. (2002), for example, performed 14 km and 3 km resolution real-time simulations of the entire European Alps during the MAP special observing period. Lu and Turco (1995) and Jacobson (2001) simulated flow over complex terrain in California at approximately 5 km resolution. Many studies point to increased grid resolution as a means to achieve better agreement with observations (see e.g. Revell et al. (1996); Gronas and Sandvik (1999); Grell et al. (2000)). At finer resolution, the topography is better resolved but the slopes become steeper and the domain often has to be smaller, both of which create new computational problems. The simulations of Gronas and Sandvik (1999) of a narrow valley in Norway and of Revell et al. (1996) of the New Zealand Alps region, for example, used resolutions down to about 250 m, but failed to reproduce the winds observed in the field, likely because they did not incorporate synoptic information or land surface data. More recently, Zhong and Fast (2003) compared simulations of the Salt Lake Valley region from three mesoscale models initialized with synoptic data. All three models (RAMS and MM5 at 0.56 km horizontal resolution, and Meso ETA at 0.85 km) were able to capture the general features of the valley flows as seen from observations. However, the details of the local circulations and vertical structure of the flow were not sufficiently well reproduced despite the relatively fine resolution used by these mesoscale models. The authors suggested that improvements in parameterizations of surface fluxes, vertical mixing, and radiation might further improve results.

Indeed, while the debate continues on whether increased resolution always increases the skill of weather forecasts (Hart et al., 2004; Cairns and Corey, 2003), it must be recognized that merely increasing grid resolution does not necessarily address all deficiencies in numerical models or in model configuraton. Chen et al. (2004) found that increasing the horizontal resolution (to 250 m) brought the most improvement to ARPS simulation results in the Salt Lake Valley region when the domain size was enlarged at the same time. Hanna and Yang (2001) suggested that errors in wind speed and direction in their simulations with four different mesoscale models were due to errors in the representation of turbulent motions, as well as to subgrid features in the topography and land use. Further examples are found in Zängl et al.

---

[*]Chapter 4 of this thesis

(2004) and Gohm et al. (2004), who simulated Foehn winds in the Wipp and Rhine Valleys, respectively, with MM5. Despite using resolutions as fine as 267 m in the horizontal and two-way grid nesting to incorporate synoptic data, Gohm et al. (2004) found discrepancies between the simulations and observations; e.g., the model predicted a shallow Foehn wind occurrence that was not observed. The authors pointed to the need for higher-resolution representation of the topography outside of the fine resolution domain, because the coarse grids were unable to provide accurate lateral boundary condition forcing for the fine grids. Zängl et al. (2004) found that the effect of the horizontal computational mixing was larger than the effect of increased resolution. Their model performed better with an improved computational mixing scheme at coarse resolution (3 km) than at fine resolution (1 km) with the traditional mixing scheme.

Previous simulations in the Riviera Valley region have been few. Grell et al. (2000) simulated a southern part of the Swiss Alps which included the Riviera Valley, using MM5 and RADM2 (for chemistry) with a horizontal resolution of 1 km to examine the advection of pollutants into Alpine valleys. Their focus was not on the Riviera, but on the neighboring Mesolcina Valley. Detailed comparison to observation data was not presented, and the authors stated that higher spatial and temporal resolution is needed to represent the atmospheric chemistry processes accurately. Simulations of the Riviera Valley, for the same time period as studied here, were performed by De Wekker et al. (2005) with the RAMS model (in Reynolds-Averaged Navier-Stokes, RANS, mode). Two-way grid nesting with grid spacings down to 333 m gave relatively good agreement with the observed potential temperature fields, but the numerical model did not to capture the wind structure of the valley very well. Consistent up-slope and up-valley winds were not apparent. Our simulation setup has many similarities to that of De Wekker et al. (2005), as discussed below.

In this paper, we use large-eddy simulation (LES) to describe the flow structure over the highly complex terrain in the Riviera Valley with very fine resolution (as fine as 150 m horizontal spacing). Our simulation tool is the Advanced Regional Prediction System (ARPS), a non-hydrostatic, compressible large-eddy simulation code written for mesoscale and small-scale atmospheric flows (Xue et al., 2000, 2001, 2003). All the studies mentioned above used RANS formulations, not LES closures for their simulations. LES separates resolved and turbulent motions using a physical length scale, the width of the explicit spatial filter (Chow et al., 2005a). RANS, on the other hand, applies a time average, usually with a very broad averaging period so that only very large scales are resolved. The traditional concept of LES is often associated with high-resolution simulations where most of the wavenumber range is resolved. The methodology of LES, however, does not prohibit its application to less well-resolved flows (Wyngaard, 2004). The coarser grids in our nested domain setup are more typical of mesoscale simulations, but can use the same LES equations. The differences between LES and RANS become small when similar space and time resolutions are used; often the only difference in implementation is the formulation of the turbulence model. The LES formulation is preferred for studies of turbulent flows because it is clear which physical features (length scales) are resolvable and which must be modeled. Wyngaard (2004) suggests the use of a more general tensor eddy-diffusivity model for coarser LES experiments; we have included a much more general dynamic reconstruction model (DRM) in our sensitivity experiments.

Simulations of the Riviera Valley are complicated by the complex terrain, the need for high-resolution surface datasets, and the presence of numerical discretization and lateral boundary condition errors, among other issues. The next section describes the flow conditions in the Riviera Valley on the days of interest, followed by a detailed description of our numerical setup (Section 3.3), and comparison of results to observation data (Section 3.4). We then perform sensitivity experiments to evaluate the relative impact of various configurations for soil
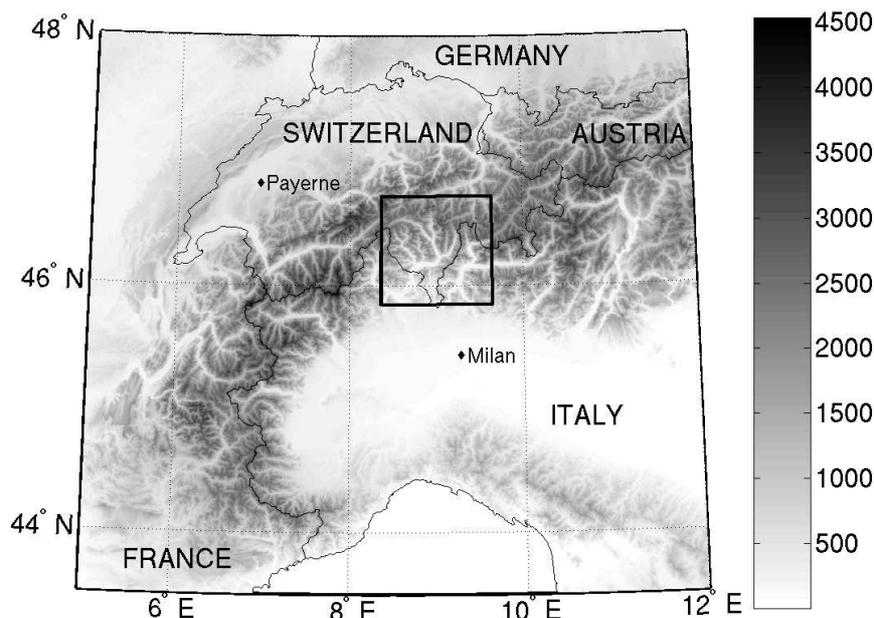
Figure 3.1: *Location of the Riviera Valley in the Alps, with elevation contours (m asl). The box outlines the 1 km grid for the Riviera region, shown in detail in Fig. 3.2a.*

moisture and temperature, land use data, grid resolution, topographic shading, and turbulence closure models (Section 3.5). We seek to answer several questions in the course of our study. Does increased grid resolution provide improved simulations? What are the effects of using high-resolution data for land use and soil properties? How are the results changed when topographic shading is included, or when different turbulence models are used? And finally, how do the nested grid parameters, such as size and resolution, affect the simulation results and/or the choice of physical parameterization schemes?

3.2 Flow conditions during the MAP-Riviera project

The Riviera Valley is a medium-sized valley located between the towns of Biasca and Bellinzona in the province of Ticino in southern Switzerland (see Figs. 3.1 and 3.2). The valley is about 15 km long and about 1.5 km wide at the valley floor, which is approximately 250 m asl at the southern entrance. Valley side walls have slopes of 30-35° and the surrounding peaks reach altitudes of up to 2700 m asl. The valley was the focus of an extensive field campaign, the MAP-Riviera Project (Rotach et al., 2004), which was part of the larger Mesoscale Alpine Programme (MAP) conducted in the fall of 1999 (Bougeault et al., 2001). The field data include measurements from surface stations, radiosondes, and aircraft flights, among others.

The focus of the simulations in this work is on fair-weather days that are dominated by thermal forcing. On such "convective" days, a slope- and valley-wind system will develop within the valley and will be sensitive to the local surface conditions that determine heating and cooling. Inclusion of synoptic forcing is also necessary, however, especially because in the Alps, the flow is channeled along valleys that connect over a large domain. We have simulated the convective days of August 21, 22 and 25, 1999. We focus on August 25, 1999 in this paper because it was the most cloud-free day of the measurement campaign, and because wind data were missing from radio soundings on August 21 and 22. After determining the best
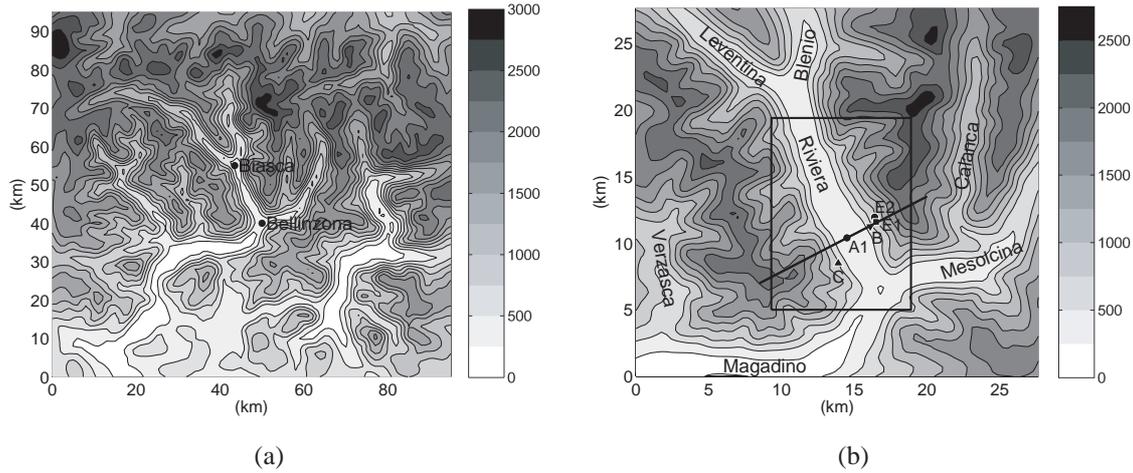
Figure 3.2: Riviera Valley elevation contours (m asl) for (a) the 1 km grid and (b) the 350 m grid with the 150 m grid shown within. Locations of surface stations (defined in Table 3.4) and vertical cross-section are also shown.

simulation setup for August 25, where quantitative comparisons could be made for both wind and temperature fields, simulations of August 21 and 22 were performed. The results from August 21 and 22 and further analysis of the flow structure and the heat budget of the valley wind system for all three cases are given in Part II of this work (Weigel et al., 2005).

3.3 Numerical simulation setup

This section describes the procedures used to achieve accurate simulations of atmospheric flow in the Riviera Valley. The steps taken include the use of high-order numerical methods, carefully selected nested grids, high-resolution land surface data, modifications to the radiation model, and improved turbulence closure models. A standard procedure, with grid nesting, but without refined surface characteristics or soil moisture initialization, provides a reference against which enhanced simulations and sensitivity experiments are compared. Table 3.1 lists the configuration for various simulations.

3.3.1 Large-eddy simulation code

ARPS was developed at the Center for Analysis and Prediction of Storms at the University of Oklahoma, and is formulated as an LES code that solves the three-dimensional, compressible, non-hydrostatic, filtered Navier-Stokes equations. ARPS is described in detail by Xue et al. (1995, 2000, 2001, 2003), so we only mention the relevant settings for this application.

Fourth-order spatial differencing is used for the advection terms. Temporal discretization is performed using a mode-splitting technique to accommodate high-frequency acoustic waves. The large time steps (Δt) use the leapfrog method. First-order forward-backward explicit time stepping is used for the small time steps ($\Delta \tau$), except for terms responsible for vertical acoustic propagation, which are treated semi-implicitly. Simulations were performed in parallel (with message passing) on IBM SP Power4 processors.

Table 3.1: *Riviera Valley simulation configurations. ECMWF and WaSiM soil moisture data have 0.5 degree (∼60 km) and 100 m resolution, respectively. The coarse USGS land use data is at 30 s (∼1 km) spacing as opposed to the 100 m GEOSTAT data. REF is the reference run using low-resolution surface data. REF-ST initializes soil temperature (ST) as an offset from the air temperature as opposed to using interpolation from ECMWF values. The LU-SM run name indicates the use of high-resolution land use (LU) and high-resolution soil moisture (SM) data, in addition to the soil temperature offset from REF-ST. Other run names are constructed similarly and represent variations from the LU-SM configuration. See text for details.*

Run name	Soil moisture		Soil temp.	Land use	Topo.	Turbulence
	1 km grid	350 m grid	350 m grid	350 m grid	shading	350 m grid
REF	ECMWF	ECMWF	ECMWF	1 km	Yes	TKE-1.5
REF-ST	ECMWF	ECMWF	offset	1 km	Yes	TKE-1.5
LU-SM	3-level	WaSiM	offset	100 m	Yes	TKE-1.5
LU-SM2	WaSiM/3-level	WaSiM	offset	100 m	Yes	TKE-1.5
LU-SM3	3-level	3-level	offset	100 m	Yes	TKE-1.5
SM	3-level	WaSiM	offset	1 km	Yes	TKE-1.5
LU-SM-NOSHADE	3-level	WaSiM	offset	100 m	No	TKE-1.5
LU-SM-NOTURB	3-level	WaSiM	offset	100 m	Yes	None
LU-SM-DRM	3-level	WaSiM	offset	100 m	Yes	DRM

3.3.2 Grid nesting and topography

Five one-way nested grids were used to simulate flow in the Riviera Valley at horizontal resolutions of 9 km, 3 km, 1 km, 350 m, and 150 m. The one-way nesting procedure used by ARPS allows adjustments in vertical resolution between grids, which we found to be necessary to accommodate the steep Riviera terrain; currently available two-way nesting schemes (in other codes) do not allow for vertical resolution changes, but the effect of two-way nesting should be explored in the future work. The valley first becomes reasonably well resolved at 350 m resolution (see the wavelet analysis of De Wekker, 2002). Details of the simulation domains are listed in Table 3.2. Figure 3.2 shows the topography for the 1 km, 350 m, and 150 m subdomains. All grids are centered on the Riviera Valley at 46.2881 N, 9.002 E, except for the 150 m resolution grid which is centered at 46.275 N, 9.005 E. Thus the boundaries are placed as far as possible from our region of interest, minimizing contamination by errors at the lateral boundaries that are magnified when the boundaries cross through complex terrain (Warner et al., 1997). A Lambert conformal map projection is used with the "true" latitude and longitude chosen very close to the center of the domain to minimize grid distortion, particularly for the smaller domains.

Table 3.2: *Nested grid configurations, with dimensions and time step sizes. In the vertical direction, the minimum grid spacing is Δz_{min} at the surface, and the averaging spacing is Δz_{avg}. Δt denotes the large time step and $\Delta\tau$ the small time step, selected such that $2\Delta t = n\Delta\tau$, where $n = 1, 2, \ldots$.*

Grid size (nx, ny, nz)	$\Delta x, \Delta y$	Δz_{min}	Δz_{avg}	Domain height	$\Delta t/ \Delta\tau$
$103 \times 103 \times 53$	9 km	50 m	500 m	25 km	10 s /10 s
$103 \times 103 \times 53$	3 km	50 m	500 m	25 km	2 s / 4 s
$99 \times 99 \times 63$	1 km	50 m	400 m	24 km	1 s / 1 s
$83 \times 83 \times 63$	350 m	30 m	350 m	21 km	1 s / 0.2 s
$67 \times 99 \times 83$	150 m	20 m	200 m	16 km	0.5 s / 0.05 s

Topography for the 9 km through 1 km grids was obtained using USGS 30 arc second topography datasets. The 350 m and 150 m resolution terrain data were extracted from a 100 m dataset available for all of Switzerland (Volkert, 1990). The terrain is smoothed near the boundaries of each nested subdomain to match the elevations from the surrounding coarser grid.

3.3.3 Vertical resolution and grid aspect ratio

ARPS uses a generalized terrain-following coordinate system. The grid is stretched using a hyperbolic tangent function from a vertical grid spacing of Δz_{min} at the surface to yield an average spacing of Δz_{avg} and a domain height of $\Delta z_{avg}(nz - 3)$ (see Table 3.2). The grid configurations are determined based on numerical considerations. High vertical resolution is needed to resolve the vertical structure of the atmosphere, especially near the earth's surface, but if the grid aspect ratio ($\Delta x/\Delta z$) becomes too large, numerical errors become large, particularly in the horizontal gradient terms (Mahrer, 1984). Poulos (1999) and De Wekker (2002) also found that the grid aspect ratio had to be small, especially for steep terrain. Increasing the vertical resolution too much, for example, leads to instabilities. Finally, LES also requires a small aspect ratio so as to avoid distortion of resolved eddies (Kravchenko et al., 1996).

Unfortunately, one or more of the above guidelines must be compromised because of the large domain sizes used here. At 9 km horizontal resolution, a good aspect ratio would require

vertical resolution on the order of 1 km, but this would severely degrade the representation of the vertical structure of the atmosphere. Our chosen aspect ratio for the 9 km grid is 180 at the surface; with $\Delta z_{min} = 50$ m the vertical structure is reasonably well captured. For the fine grids, we have more flexibility because the horizontal resolution approaches the vertical resolution and we can construct a grid much more favorable for LES; therefore, our 350 m resolution grid has a much reduced aspect ratio of about 10.

3.3.4   Initialization and lateral boundary conditions

To obtain realistic initial and boundary conditions, data from the European Centre for Medium-Range Weather Forecasts (ECMWF) were used to force ARPS simulations at the lateral boundaries of the coarsest resolution (9 km) grid. ECMWF analyses are given at six-hour intervals with 0.5 degree (approximately 60 km) horizontal resolution and 50 vertical levels. The ECMWF initialization data compare fairly well with nearby soundings, e.g. in Milan, Italy and Payerne, Switzerland, located outside the Alps (see Fig. 3.1, soundings not shown), but because of poor vertical resolution cannot capture the pronounced inversion observed in the radio soundings on August 25 (see Fig. 3.8 later). The ECMWF data are applied at six-hour intervals and are linearly interpolated in between. Relaxation towards the boundary condition values is applied to a 5-10 grid-cell zone around the edge of the domain, depending on the grid. Simulations continued for 30 hours beginning at 1800 UTC August 24. Output at hourly intervals was used to provide initial and boundary condition files for subsequent nested grid simulations.

3.3.5   Surface characteristics

The characteristics of the land surface strongly influence sensible and latent heat flux exchanges with the atmosphere. Surface fluxes are particularly important for predicting thermally-forced flows such as slope winds and along-valley winds. The ARPS land-surface soil-vegetation model solves soil temperature and soil moisture equations, as described in detail in Xue et al. (1995, 2001). ARPS normally uses 13 soil types (including water and ice), and 14 vegetation classes (following the United States Department of Agriculture classifications). Land use, vegetation, and soil type data for the 1 km and coarser grids are obtained from USGS 30 second global data. The soil data pre-processing program of ARPS was modified to handle this finer resolution data.

For the 350 m and 150 m resolution grids, we enhanced the ARPS surface data classes to incorporate land use and soil type at 100 m resolution, available for all of Switzerland from the land use and digital surface type data from the Swiss Federal Office of Statistics (GEOSTAT service). The dataset includes 69 land use categories; these have been mapped to a new set of 30 vegetation and 14 soil types (see Table A.1 in Appendix A and Tables 8.3 and 8.4 and Fig. 8.4 in Chow, 2004), as was done by De Wekker (2002) for RAMS. Different values, however, have been assigned in ARPS for the roughness length, leaf area index and vegetation fraction. A new soil type was added to represent bare rock, which makes up a significant portion of the mountain tops.

The soil-vegetation model must also be initialized with soil moisture and temperature data. Two soil layers of depths 0.01 m and 1.0 m for the surface and deep soil are used by the soil model. Soil temperature on the 9 km grid was initialized from ECMWF data. The soil temperature values at 9 km resolution are then interpolated to the 3 km and 1 km resolution grids. For the REF simulations (see Table 3.1), these ECMWF data are further interpolated to the 350 m grid. All other 350 m grids were initialized with a constant offset from the near-
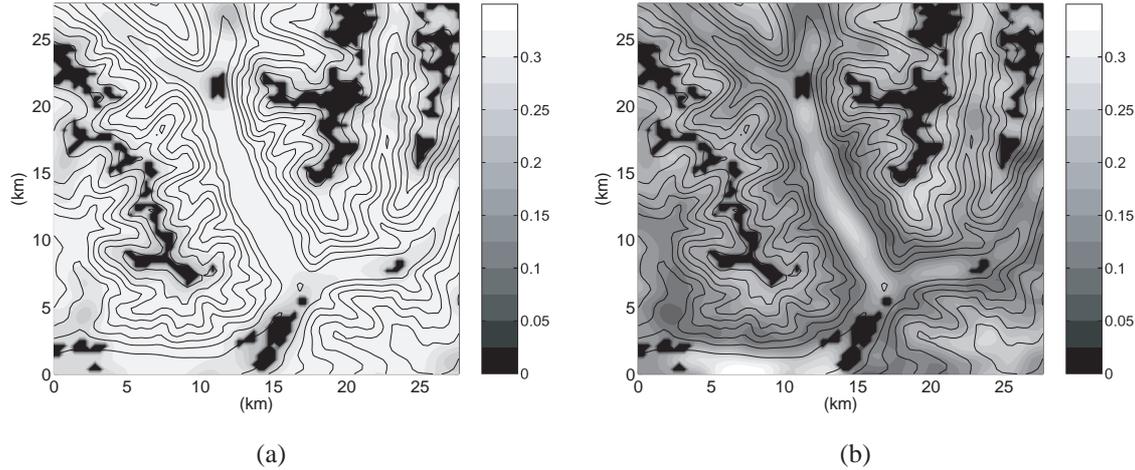
Figure 3.3: Contours of WaSiM soil moisture initialization (m³/m³, shaded) at (a) surface and (b) deep soil levels at 350 m resolution. Topography contours are shown at 250 m intervals.

surface air temperature: 0.6 K for the top layer and -2.1 K for the deep soil. These offsets are based on field observations in the Riviera Valley.

The soil moisture initialization can be particularly important for thermally forced flows (Eastman et al., 1998). Soil moisture on the 9 km resolution grid was initialized from ECMWF data, which in the Alps range from 0 (rocky and glacial areas) to 0.37 m^3m^{-3}, with the deep soil slightly wetter than the top layer for this time period. The area near the Riviera Valley has values of about 0.35 m^3m^{-3} (surface) and 0.366 m^3m^{-3} (deep), except for the rocky outcroppings which are close to zero. As for the soil temperature, the ECMWF soil moisture values are interpolated to the 3 km grid. These ECMWF data are further interpolated to the 1 km and 350 m resolution grids for REF and REF-ST (see Table 3.1).

For LU-SM and other simulations (see Table 3.1), high-resolution soil moisture initialization data were obtained to represent the spatial variability in the Riviera Valley better. We followed De Wekker et al. (2005) and used the Water Flow and Balance Simulation Model (WaSiM-ETH) (Jasper, 2001) to obtain soil moisture information. This hydrologic model is driven by meteorological data such as air temperature and precipitation and provides 100 m resolution for the catchment region of the Riviera. Figure 3.3 shows the distribution of soil moisture for the two layers used at the 350 m grid level on August 24 at 1800 UTC. The soil moisture is highest on the valley floor, significantly lower on the steep surrounding slopes, and zero on the rocky peaks of the mountains and in urban areas (e.g. in Bellinzona and Biasca). In the upper soil level, the WaSiM moisture values are comparable to the ECMWF data ($\sim$ 0.32 m^3m^{-3}). At the deep soil level, where there are no plant roots to hold water, the WaSiM moisture on the steep slopes is very low (0.08-0.12 m^3m^{-3}), but on the valley floor it is still relatively high ($\sim$ 0.25 m^3m^{-3}).

The soil moisture measurements taken at a few sites in the Riviera Valley during the field campaign (Zappa and Gurtz, 2003) compare quite well with the WaSiM values. For example, at 1200 UTC, measurements at site A1 (see Fig. 3.2b) showed the soil moisture to be 0.318 m^3m^{-3} at the surface and 0.293 m^3m^{-3} at 25 cm depth. In contrast, site B showed 0.306 m^3m^{-3} at the surface, and 0.212 m^3m^{-3} at 25 cm depth. This near-constant moisture with depth on the valley floor and the significant decrease with depth on the slope also appear in the WaSiM data.

Given ECMWF data for the 9 km resolution grid and WaSiM data for the 350 m and 150 m

grids, the question remains as to what the best values are at the intermediate resolutions of 3 km and 1 km. De Wekker et al. (2005) set the soil moisture to be constant on their coarser grids and found that the specific value did not significantly affect the results on the finest grid level. In contrast, our sensitivity studies in Section 3.5 show that soil moisture is a parameter to which the results are very sensitive, particularly at the 1 km grid level. We therefore incorporated a semi-empirical three-level soil moisture initialization, which is used for LU-SM on the 1 km grid. The soil moisture was set to 0 at altitudes above 2200 m where the soil type rock dominates. Between 2200 m and 500 m, moisture was initialized at 0.18 m^3m^{-3}, and below 500 m at 0.28 m^3m^{-3}. The same values were used at the surface and deep soil levels. These soil moisture values are intermediate values between the WaSiM deep and surface layer values, and can be seen as a compromise between the WaSiM and ECMWF data. The specific values were selected on a trial and error basis to obtain the best results. In addition to using interpolated ECMWF and three-level soil moisture initializations, we investigated the use of WaSiM data outside the Riviera catchment area in the LU-SM2 setup. The three choices for soil moisture initialization for the 1 km grid are summarized in Table 3.3 and are discussed further in Section 3.5.1.

Table 3.3: *Typical soil moisture values (m^3m^{-3}) for each dataset in the surface and deep layers. All have close to zero soil moisture at the rocky outcroppings and in urban areas. The surface layer does not vary as much as the deep layer so the differences between the valley and slope are not given. The 3-level data are constant in each elevation range.*

	Surface (0.01 m)	Deep (1.0 m)	
		Valley floor (< 500 m asl)	Slopes (500 - 2200 m asl)
ECMWF	0.35	0.37	0.37
WaSiM	0.32	0.25	0.10
3-level	same as deep	0.28	0.18

3.3.6 Radiation model

In steep valleys, "topographic shading" from shadows cast by neighboring topography can be important. ARPS normally only includes the effect of surface inclination when calculating incoming solar radiation. This "self-shading" accounts for much of the required modification to the incoming radiation in complex terrain, but topographic shading must be included to properly represent surface heating during sunrise and sunset. We use the topographic shading method of Colette et al. (2003), which is included in the latest version of ARPS. Colette et al. (2003) found that the inclusion of topographic shading could delay the morning inversion layer breakup in idealized simulations with steep valleys by approximately half an hour. The field study of Matzinger et al. (2003) emphasized the importance of the topographic shading in the Riviera Valley, where the delay in local sunrise significantly alters the net radiation balance. We evaluate the effect of topographic shading in Section 3.5.4. The complete treatment of short- and long-wave radiation in ARPS is described in Xue et al. (2001).

3.3.7 Turbulence and computational mixing

The standard closure models in ARPS include 1.5-order TKE (Deardorff, 1980; Moeng, 1984) and static Smagorinsky-Lilly models (Smagorinsky, 1963; Lilly, 1962). The TKE-1.5 model

solves an equation for the turbulent kinetic energy to determine the velocity scale for use in an LES-type eddy-viscosity formulation. The model can be used for LES as long as the chosen length scale is proportional to the filter width, as is done in ARPS (Deardorff, 1980; Moeng, 1984). The TKE approach is especially useful when a large fraction of the velocity scales is contained in the subfilter scales, as for coarse resolution grids (Pope, 2000, Chapter 13).

The TKE-1.5 closure is used in most of our simulations, but the dynamic reconstruction model (DRM) of Chow et al. (2005a) has also been applied at the 350 m grid. The DRM is a mixed model, combining a high-order scale-similarity term with a dynamic eddy-viscosity model. Here we use the Bardina scale-similarity term together with the dynamic model of Wong and Lilly (1994). Further details about the model and its implementation over complex terrain can be found in Chow (2004, Chapter 8). Simulations of neutral boundary layer flow using DRM over flat terrain were able to accurately represent the expected logarithmic layer near the bottom boundary, unlike standard eddy-viscosity models (Chow et al., 2005a). Applications to flow over an isolated hill (Askervein Hill, Scotland) were also successful (Chow and Street, 2004). Here, the DRM is also applied to the transport equation for potential temperature.

In addition to the turbulence model, fourth-order computational mixing is used to damp high-frequency motions that can build up due to nonlinear interactions; this can be considered a type of hyper-viscosity and is applied in computational space (and, in the case of potential temperature, to the perturbations from the homogeneous base state). ARPS also includes a divergence damping term to control acoustic noise. The impact of both of these damping terms has been investigated and the coefficients have been set to give the minimum amount of mixing required for stability.

3.4 Verification and comparison with observation data

Detailed results comparing the REF and LU-SM simulations with observation data for August 25, 1999 are given in this section. All results are from the 350 m resolution grid unless otherwise noted. The 150 m grid data are used in Part II to calculate profiles of the heat budget components over the valley base (Weigel et al., 2005).

3.4.1 Surface wind and temperature observations

Typical thermally-driven valley wind patterns include the onset of up-slope winds on the valley walls in the morning and the development of up-valley winds during the day. In the evening, the winds transition to down-slope and down-valley directions. The heating mechanisms which drive the Riviera Valley wind transitions are evaluated in detail in Part II (Weigel et al., 2005). A comprehensive discussion of slope and valley winds can be found in Whiteman (2000). The winds in the Riviera exhibit some aspects of typical valley flow patterns, as described further below.

Figure 3.4 shows the evolution of the surface potential temperature (θ) on August 25 at site A1 (Bosco di Sotto, see Table 3.4 and Fig. 3.2b) near the center of the simulation domains. Surface and radiosonde observations were collected at this location during the field campaign. The observations are compared to the REF, REF-ST, and LU-SM results.

Table 3.4: *Surface station locations, shown in Fig. 3.2b.*

Site	Name	Location	Elevation asl	Measurement height agl
A1	Bosco di Sotto	Valley floor (46.265 N, 9.012 E)	250 m	15.9, 28 m
B	Rored	Eastern slope (46.263 N, 9.031 E)	760 m	22, 28 m
C	Pian Perdascio	Western slope (46.238 N, 9.005 E)	340 m	5 m
E1	Roasco	Eastern slope (46.267 N, 9.037 E)	1060 m	2,12.7 m
E2	Monte Nuovo	Eastern slope (46.271 N, 9.036 E)	1030 m	16.8,22.7 m

To further quantify the comparison, the first three rows of Table 3.5 show the root-mean-square errors (rmse) and mean errors (bias) between simulations and surface observations at site A1. They are defined:

$$\text{bias} \;=\; \frac{1}{M}\sum_{j=1}^{M}\frac{1}{N}\sum_{i=1}^{N}(A_{i,j}-B_{i,j}) \tag{3.1}$$

$$\text{rmse} \;=\; \sqrt{\frac{1}{M}\sum_{j=1}^{M}\frac{1}{N}\sum_{i=1}^{N}(A_{i,j}-B_{i,j})^2} \tag{3.2}$$

where M is the number of time steps, N is the number of grid points, and $A_{i,j}$ and $B_{i,j}$ are the values of the datasets being compared.

From Fig. 3.4, we see that REF strongly underpredicts surface temperatures by up to 6 K (with an rmse of 3.20 K) while LU-SM stays within less than about 1 K from the observations (rmse of 0.69 K). After further investigation at the suggestion of one of the reviewers, the difference between the surface temperature in REF and LU-SM was found to be mostly due to the soil temperature initialization. REF uses soil temperature fields interpolated from ECMWF data, which are almost uniform over the 350 m Riviera Valley domain. LU-SM, on the other hand, uses an offset from the air temperature to initialize the soil temperature on the 350 m grid, and thus has elevation-dependent values which are more realistic and provide improved agreement with the observations. This hypothesis was verified by REF-ST, which uses the REF setup except that we initialized the soil temperature with an offset like in LU-SM, giving a reduction in rmse from 3.20 K (REF) to 1.60 K (REF-ST). The REF-ST setup required a simple code modification from the standard initialization options available in ARPS and showed the importance of spatial variability in soil temperature in complex terrain. All simulations except REF use the temperature offset to initialize the soil temperature (see Table 3.1). Because of the large temperature bias in REF, subsequent comparisons are made between REF-ST (rather than REF) and LU-SM, so as to isolate further differences in the model runs.

Figure 3.5 shows the evolution of surface wind speed (U) and direction (ϕ), also at site A1. During the first 6-7 hours on August 25, the dominant winds were down-valley (about 330°). Between 0600 and 0800 UTC (local time is CEST (Central European Summer Time) = UTC + 2 hours), winds shift to up-valley (about 150°). Local sunrise is at approximately 0700 UTC at the valley floor, but is earlier on the east-facing slopes and in the Magadino Valley (see Fig. 3.2). Sunset is at approximately 1600 UTC, and the winds shift to down-valley starting at about 1800 UTC. The surface winds are generally weak at night and become stronger with the onset of the up-valley flow during the day.

Comparisons with observations are now only shown for REF-ST and LU-SM for simplicity (the wind speed for REF-ST is similar to REF), but the rmse and bias values in Table 3.5 also include REF. The LU-SM predictions of the wind speed in Fig. 3.5 show the onset of up-valley

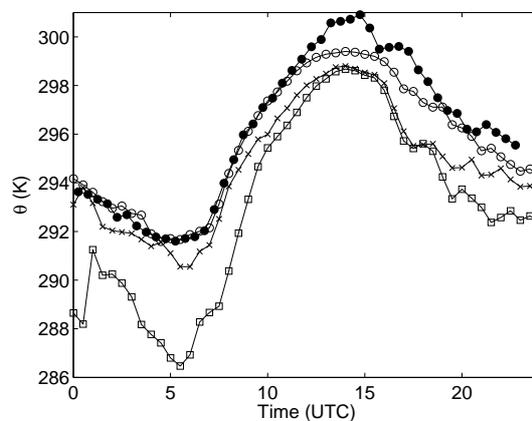**Figure 3.4:** *Surface potential temperature time series at Bosco di Sotto (site A1).* —●— *Observations;* —○— *LU-SM;* —×— *REF-ST;* —□— *REF*

(a)   (b)
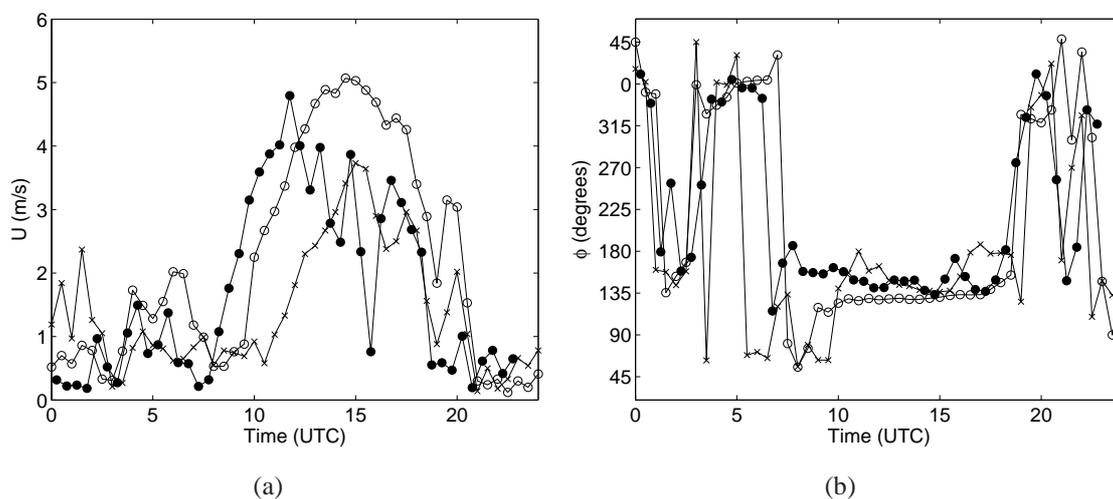
Figure 3.5: *Surface data time series comparisons at Bosco di Sotto (site A1, valley floor) for (a) wind speed and (b) wind direction.* —●— *Observations (averaged from 15.9 and 28 m agl);* —○— *LU-SM;* —×— *REF-ST*

winds about 1 to 2 hours later than observed at site A1, but this is significantly better than both REF-ST and REF. While the surface wind speed rmse values at site A1 are similar for all three simulations, the rmse does not reflect the fact that the wind transition delay in up-valley winds is 3-4 hours for REF-ST and 4-5 hours for REF. The ARPS data in the surface time series are from the lowest model level, which for the horizontal winds and temperature is at $\Delta z_{min}/2$ (15 m for the 350 m grid; see Table 3.2). Comparison is usually made to the closest observation level, but there can be surface layer effects due to the plant canopy, which are not represented in the model, so comparisons to a higher measurement level are often better. At site A1 we take an average of the observations at 15.9 and 28 m agl. The wind direction is not representative of the diurnal valley flows when winds are weak, making comparisons with LES results difficult. Nevertheless, the surface wind direction and speed are reproduced quite well by LU-SM. The results of De Wekker et al. (2005) showed a 2-hour delay in the onset of the up-valley winds and did not capture the evening transition to down-valley winds.

Overall, the errors between the observations and the simulated fields at site A1 from LU-SM are quite small in the Riviera Valley (e.g. rmse of $\sim$0.7 K for potential temperature and $\sim$1.3 m s^{-1} for wind speed), especially when compared to the results of other typical simulations (Zängl et al., 2004; Zhong and Fast, 2003). LU-SM significantly reduces all the errors except the wind direction bias, where REF-ST exhibited more fluctuations and hence a lower overall bias. Wind direction errors are large because of the fluctuations present at low wind speeds.

The most likely reason for the delayed along-valley wind transitions in the ARPS simulations is poor representation of surface soil conditions. Soil moisture controls the partitioning of surface heat fluxes into sensible and latent fluxes, thus determining the heating and cooling of the surface and ultimately the strength of along-valley and slope winds. Sensitivity tests in Section 3.5.1 confirm that changes in the soil moisture can significantly change the onset of valley wind transitions. Sensitivity to the soil temperature offset used for initialization in all runs except REF was small, and therefore was not investigated further.

The surface observations at the valley floor provide a simple reference for evaluating the simulation results, but we compare results at additional sites because the complex topography can lead to different wind transitions at different locations. Figures 3.6 and 3.7 show observed and simulated winds at surface stations at site C (Pian Perdascio, east-facing slope) and site E2 (Monte Nuovo, west-facing slope) (see Fig. 3.2b). Quantitative errors are given in Table 3.5 for these and two other sites on the eastern slope (B, E1). Note that the measured and simulated wind directions indicate the up-slope and down-slope transitions along the slopes and not the up-valley/down-valley directions as at site A1. Comparisons along the slopes are often difficult because of the effect of the plant canopy (Van Gorsel et al., 2003), and can be very sensitive to the exact location chosen on the grid; moving 100 m to the east or west can change the elevation by almost 100 m.

3.4.2 Vertical profiles

Figure 3.8 compares the potential temperature, wind speed, wind direction, and specific humidity (q) simulated by REF-ST and LU-SM with radiosonde data from site A1. The temperature structure of the atmosphere early in the morning (0739 UTC) is characterized by a stable layer below 1.5 km asl, a very stable layer between 1.5 and 2.2 km asl, and a mixed or slightly stable layer above that extends to about 4.5 km asl. The strong capping inversion at about 2 km asl is also present in the synoptic flow and is likely due to large-scale subsidence near a regional high pressure system; soundings well outside of the Alps in Milan, for example, also exhibit this inversion. Typical valley inversion layer breakup theory predicts that the mixed layer will con-

(a)   (b)
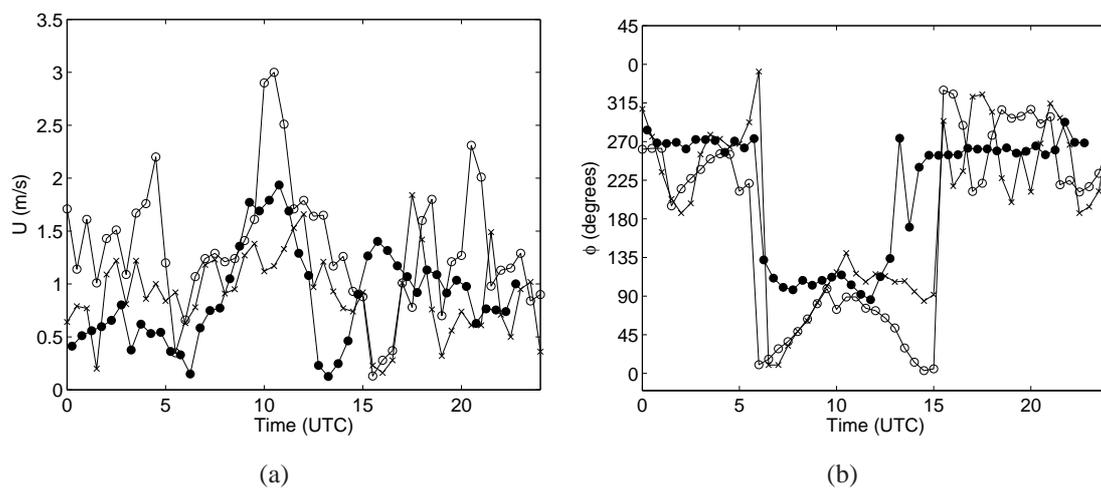
Figure 3.6: *Surface data time series comparisons at Pian Perdascio (site C, on western slope) for (a) wind speed and (b) wind direction. —•— Observations at 5 m agl; —○— LU-SM; —×— REF-ST*

(a)   (b)
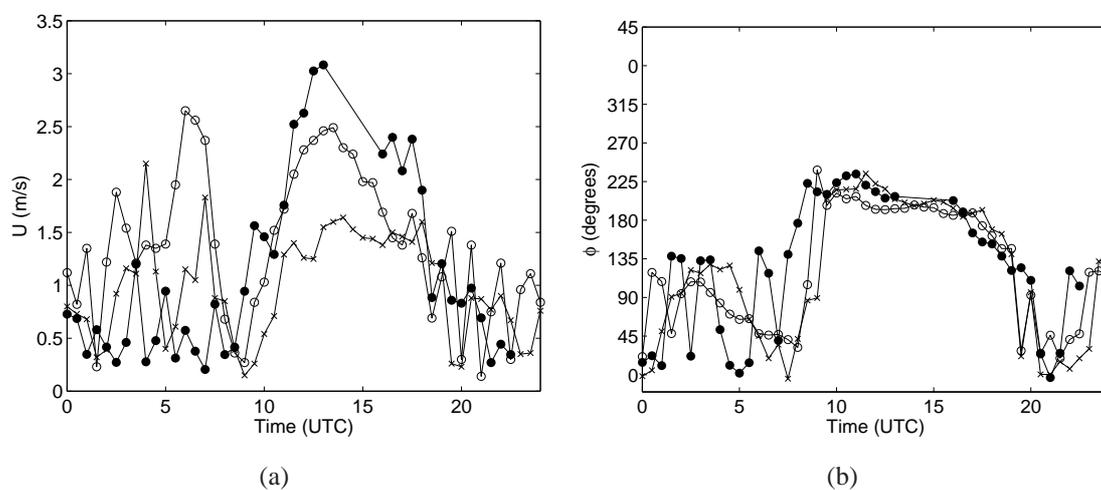
Figure 3.7: *Surface data time series comparisons at Monte Nuovo (site E2, on eastern slope) for (a) wind speed and (b) wind direction. —•— Observations at 22.7 m agl; —○— LU-SM; —×— REF-ST*

Table 3.5: *Root-mean-square errors (rmse) and mean errors (bias) for potential temperature, wind speed, and wind direction, for simulations compared to observations at site C (western slope) at 5 m agl, at site A1 using the average of 15.9 and 28 m values, and at sites B, E1, and E2 on the eastern slope using data from measurements at 22 m, 12.7 m, and 22.7, respectively; see Table 3.4. Note that the measurements at 5 m agl for site C do not agree as well with the simulations because of the low measurement height, where the influence from the vegetation canopy is large.*

Site	Run	θ (K)		U (m/s)		ϕ (deg)	
		rmse	bias	rmse	bias	rmse	bias
A1	REF	3.20	-3.04	1.47	-0.53	86.42	-1.50
	REF-ST	1.60	-1.39	1.25	-0.26	70.92	-9.33
	LU-SM	0.69	-0.41	1.28	0.57	63.21	-11.05
B	REF	1.00	-0.05	0.70	0.14	93.24	-10.92
	REF-ST	0.89	0.06	0.85	0.27	77.06	-9.63
	LU-SM	1.08	0.75	1.24	0.77	88.21	-27.19
C	REF	4.88	4.40	0.68	0.16	69.97	-35.79
	REF-ST	5.03	4.57	0.53	0.04	65.26	-23.42
	LU-SM	5.44	5.20	0.79	0.47	69.57	-3.17
E1	REF	1.04	-0.38	1.56	-0.99	56.17	14.95
	REF-ST	0.96	-0.37	1.53	-1.01	57.65	11.11
	LU-SM	0.60	0.12	1.44	-0.61	53.14	11.98
E2	REF	1.29	-1.17	0.97	0.22	57.72	-9.94
	REF-ST	1.32	-1.22	0.84	-0.25	61.79	-14.93
	LU-SM	0.81	-0.74	0.85	0.16	54.52	-11.83

tinue to grow while there is surface heating, as on such a "convective" day, and will eventually extend over the entire valley depth (Whiteman, 2000). The radiosonde observations, however, only show an 800 m mixed layer near the ground at 1208 UTC. The valley atmosphere above remains stable. The fact that the evolution of the vertical structure is atypical can be seen further from the sounding at 1508 UTC, when the surface temperature has increased by another degree but the mixed layer depth has decreased to about 500 m. This indicates the presence of other processes which act to inhibit mixed layer growth. The persistence of the stable layer throughout the day may be due to the presence of a strong secondary circulation and subsidence warming in the valley; these features are particularly evident on August 21 and 22, and have been discussed by Weigel and Rotach (2004)[*] and are analyzed in more detail in Part II (Weigel et al., 2005).

The agreement between LU-SM and the observed profiles in Fig. 3.8 is much better than REF-ST which does poorly near the ground. In particular, the potential temperature from REF-ST exhibits a cold bias below 1 km asl. The REF-ST wind direction also fails to exhibit the observed up-valley flow at 0915. Our simulated profiles are taken from one instant at the hour or half hour closest to the radiosonde ascent time, and are interpolated horizontally to the launch location. In the afternoon, the observed wind profiles corroborate the measurements at the surface stations which show increased wind speeds during the up-valley wind period. Both simulations, however, fail to match the observed surface warming during the afternoon, particularly at 1508 UTC. The wind speed profiles are especially difficult to compare because observed winds depend on fluctuations of the radiosonde's position as it rises. We cannot expect the LES results to provide exactly the same instantaneous profiles, but rather to represent the "mean" or resolved-scale structure (Germano, 1996). Another significant discrepancy between the observations and the simulation results is found at 2118 UTC, when the inversion at 2 km asl sharpens; the simulations do not resolve this feature in the temperature or humidity profiles. Wind data at 2118 UTC are missing near the surface, but the simulations indicate that the winds have reversed to down-valley, in agreement with the surface station time series observations (Fig. 3.5).

Table 3.6 shows the rmse and bias errors for LU-SM for each profile, including data up to about 6 km asl; the errors are quite small (e.g. ~ 2 m s^{-1} for wind speed) and confirm the good agreement between simulations and observations seen visually. Table 3.6 also gives the rmse and bias over all sounding times for REF and REF-ST, showing the overall improvement for LU-SM (e.g. θ rmse decreases from 1.43 to 0.94 K, and U rmse decreases from 2.29 to 2.04 m s^{-1}, from REF to LU-SM). The results of De Wekker et al. (2005) showed good surface temperature agreement at 0915, 1208 and 1508 UTC, but further above the ground the modeled profiles were too smooth and did not compare as well with observations as our LU-SM results. Specific humidity is also better reproduced in our simulations. It is difficult to compare wind predictions directly as De Wekker et al. (2005) presented vector profiles instead.

Table 3.6 shows the rmse and bias errors for LU-SM for each profile, including data up to about 6 km asl; the errors are quite small (e.g. ~ 2 m s^{-1} for wind speed) and confirm the good agreement between simulations and observations seen visually. Gohm et al. (2004), for example, found wind speed rmse errors from vertical profiles of about 5 m s^{-1} and a bias of $\pm$ 1.5 m s^{-1} for simulations in the Alps at 800 m resolution. Table 3.6 also gives the overall rmse and bias for all sounding times for REF, showing the large improvement for LU-SM over REF.

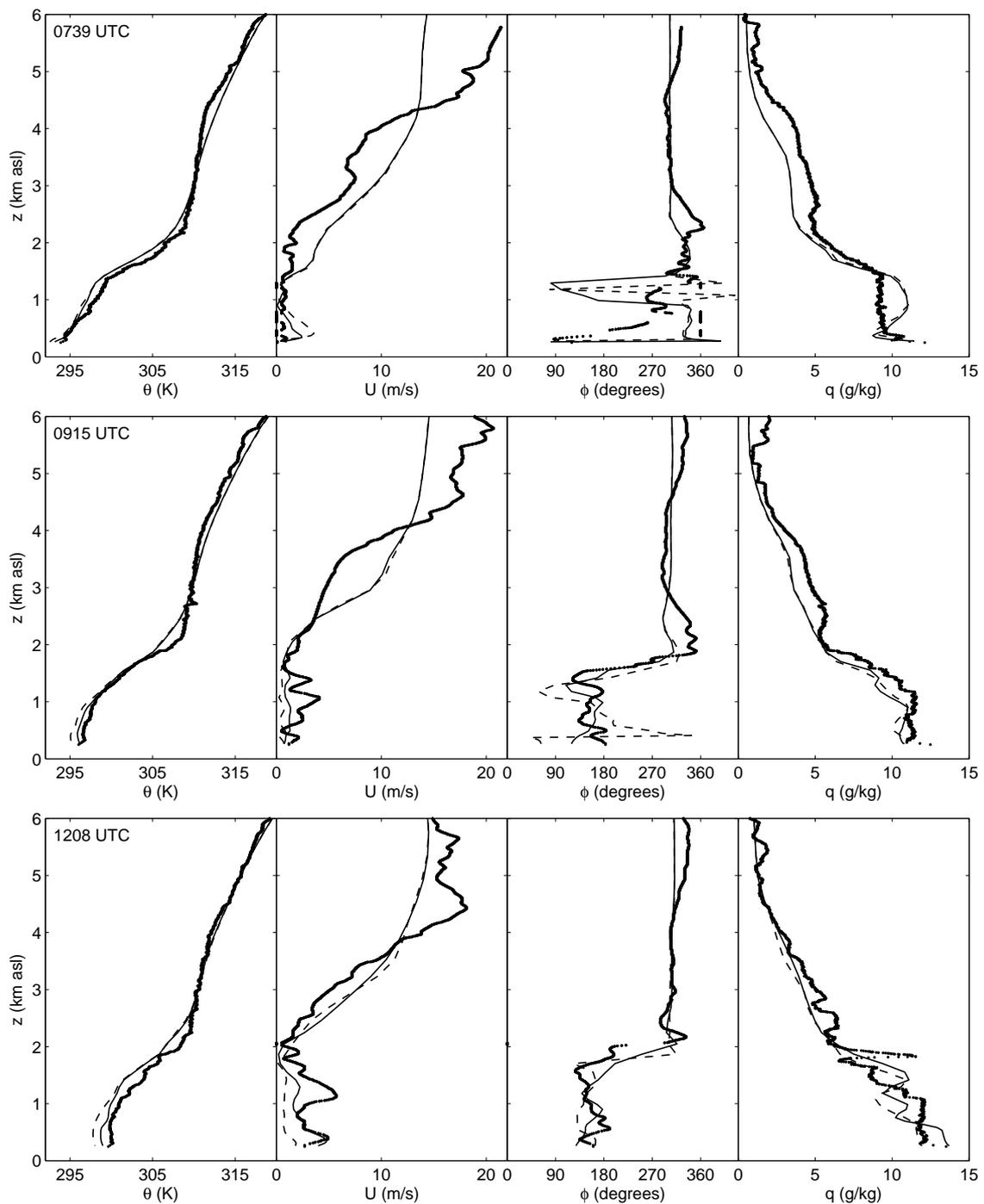[*]Chapter 2 of this thesis

Figure 3.8: *0739, 0915, and 1208* UTC *radiosonde observations compared to simulations at Bosco di Sotto (site A1) of potential temperature, wind speed, wind direction, and specific humidity on 25 August, 1999. Note that ϕ is equivalent to $\phi + 360$.* •••••• *Observations;* ——— *LU-SM;* ---- *REF-ST*
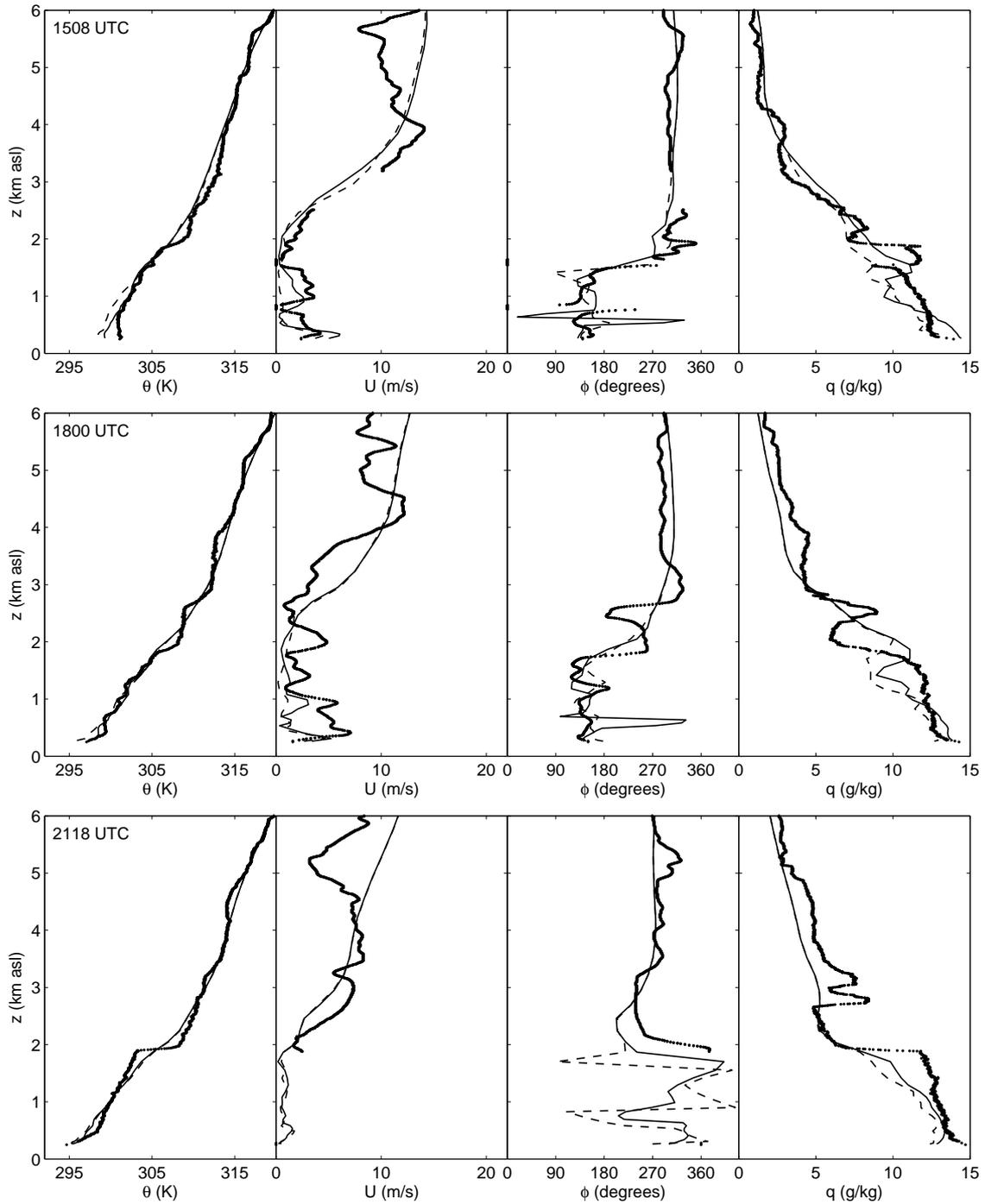
Figure 3.8: *Continued for 1508, 1800, and 2118* UTC.

Table 3.6: *Root-mean-square errors and mean errors (bias) for potential temperature, wind speed, wind direction, and specific humidity, for each radiosonde launch for LU-SM. The summary of all radiosonde launches is given in the column labeled "All"; comparisons to the REF and REF-ST results are also shown. Wind observation data were not available (NA) for 0600 UTC. ARPS data were taken from output at nearest half hour.*

Site	Run	θ (K) rmse	θ (K) bias	U (m/s) rmse	U (m/s) bias	ϕ (deg) rmse	ϕ (deg) bias	q (g/kg) rmse	q (g/kg) bias
LU-SM	0001	1.17	0.21	1.94	-0.05	38.00	-16.33	1.02	0.28
	0600	1.26	0.48	NA	NA	NA	NA	1.16	-0.35
	0739	0.82	-0.38	2.35	0.93	65.88	-7.10	1.15	-0.15
	0915	0.66	-0.34	1.99	-0.38	31.74	-11.30	0.93	-0.79
	1208	1.06	-0.80	1.75	-0.41	24.26	-4.27	1.24	0.04
	1508	0.99	-0.77	1.81	-0.09	61.29	-8.71	1.21	0.08
	1800	0.56	0.00	2.77	-0.90	54.09	16.13	1.33	-0.06
	2118	0.75	-0.15	2.29	0.20	23.96	-10.36	1.26	-0.95
LU-SM	All	0.94	-0.22	2.04	-0.12	45.73	-5.99	1.17	-0.24
REF	All	1.43	-0.73	2.29	-0.35	55.47	3.96	1.45	-0.75
REF-ST	All	1.14	-0.52	2.26	-0.34	44.80	-3.17	1.27	-0.56

3.4.3 Surface heat and momentum fluxes

Surface fluxes in ARPS are calculated from similarity theory, and they provide the necessary surface heating and cooling to drive valley winds. Figure 3.9 shows the modeled and observed time series of the sensible heat flux at surface stations A1 (valley floor) and B (eastern slope) for REF-ST and LU-SM; these stations are chosen to highlight differences between fluxes on the valley floor and slopes and because data were available and of good quality. The heat flux is the kinematic heat flux defined as $\overline{w\theta}$, where the overbar denotes spatial averaging. The heat fluxes from LU-SM compare quite well to the observations, especially considering the high spatial variability observed in the valley due to local slope variations (De Wekker, 2002, Fig. 2.10). The REF-ST results predict less than half the peak magnitude of the observed heat fluxes, thus reflecting the influence of soil moisture on surface heating and the consequently delayed onset of the up-valley winds. Station B on the east slope exhibits stronger negative heat fluxes at night than station A1 (0000 to 0700 UTC). Significant positive heat fluxes are observed during the day at both sites, with the simulations giving higher values at the valley floor than observed during the latter half of the afternoon. The peak heat flux is delayed on the east slope relative to the valley floor because the slope does not receive direct sunlight until later in the morning, and is heated until later in the afternoon. The peak magnitude is also much larger at site B because of the surface inclination and exposure of the site in the afternoon.

3.4.4 Radiation budget

The simulated surface heating depends on accurate representations of the incoming and outgoing radiation. Figure 3.10 shows the surface radiation balance throughout the day from LU-SM as compared to measurements at surface station A1. (Differences for REF-ST are quite small and therefore not shown.) The model slightly overpredicts incoming shortwave radiation, probably due to aerosols present in the Riviera atmosphere that are not accounted for by the model. The dip in the observations at 1300 UTC was due to a brief period of clouds which was not captured in the simulations. The net radiation is slightly underpredicted day and night, which
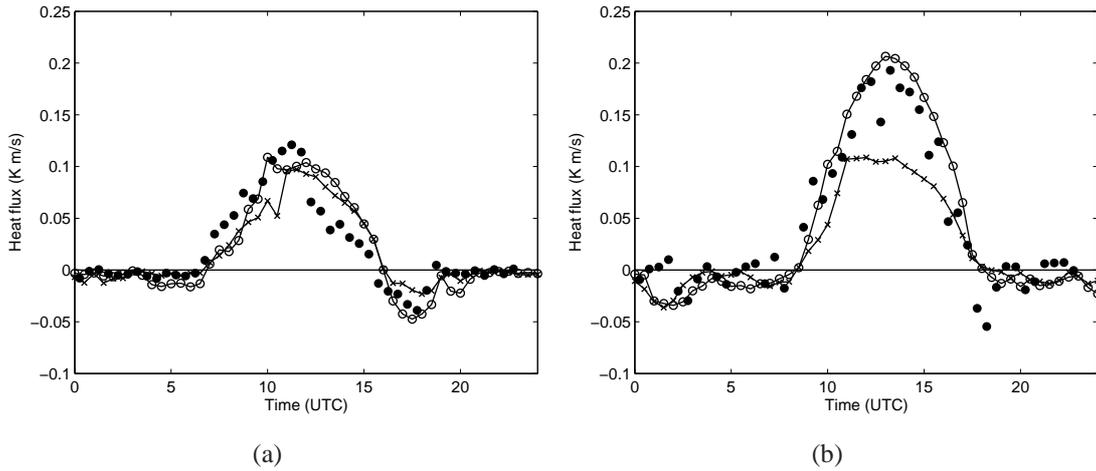
Figure 3.9: *Time series of kinematic sensible heat $(\overline{w\theta})$ flux at (a) site A1 (valley floor) and (b) site B (eastern slope).* ● *Observations;* —○— *LU-SM;* —×— *REF-ST.*

implies that the longwave radiation balance is at fault. Zhong and Fast (2003) found that night-time net radiation was also too low in their simulations of Salt Lake Valley. The net longwave radiation is often thought to be underestimated in valleys because the radiation models are one-dimensional (in the vertical); the models do not account for the incoming longwave emissions from the valley walls at night and therefore allow too much cooling.

The bias in our model values may be due to a combination of effects. Surface radiation measurements in the Riviera Valley showed that incoming longwave radiation was about 20-50 W m^{-2} larger on the valley floor as compared to on the ridge of the valley (Matzinger et al., 2003), indicating the effect of heating from the side walls. There were also particularly high daytime concentrations of aerosols on 25 August which could affect the downward longwave radiation. Finally, the choice of the constant surface emissivity in ARPS (0.995) may be too high (e.g. compared to the value used by Whiteman et al., 2004); we leave this to further investigations. Zhong and Fast (2003) also suggest that the absence of topographic shading in their simulations caused discrepancies; this effect is examined in Section 3.5.4.

3.4.5 Vertical turbulence structure

Figure 3.11 shows vertical cross sections of the resolved and subfilter-scale (SFS) turbulent stress contributions from LU-SM for vw averaged from 1300 to 1500 UTC at 300 s intervals. The vertical slice is perpendicular to the valley axis at site A1 (see Fig. 3.2). The velocities have been rotated to be aligned with the valley axes so that u is cross-valley (to the north-east) and v is along-valley (to the north-west); the uw stresses (not shown) have a somewhat lower magnitude. The resolved stress is computed from $< vw >_{res} \equiv < \overline{v}\,\overline{w} > - < \overline{v} >< \overline{w} >$ where the brackets denote time averaging. The plotted SFS stress is $< \tau_{23} >$, which contributes significantly only below about 500 m; here, the SFS stresses are several times larger than the resolved stresses, as also seen in the vertical profiles at the valley floor in Fig. 3.12. Profiles from the REF-ST simulations (not shown) are considerably lower in magnitude because of the reduced surface fluxes (Fig. 3.9). The atmosphere in the Riviera is stably stratified throughout the day except very near the surface (see Fig. 3.8), and the TKE-1.5 closure will not produce SFS turbulence when the flow is stable (as measured by the Richardson number) or when the
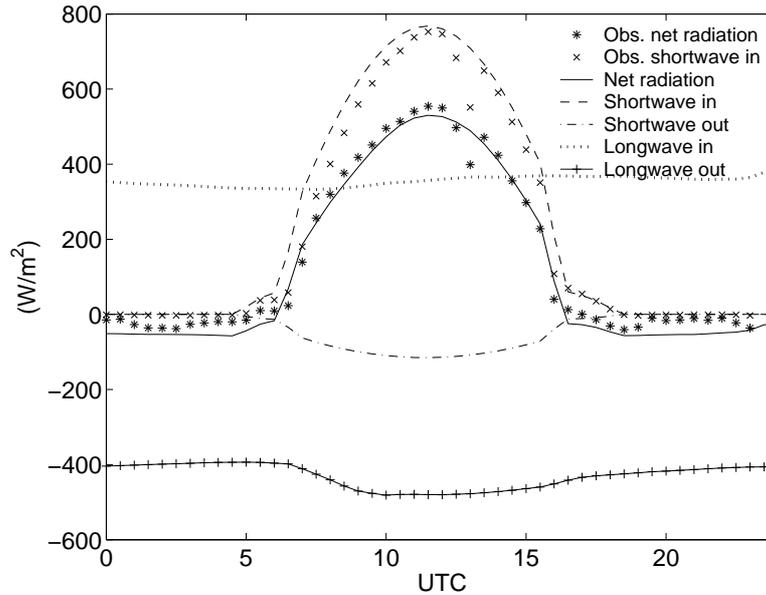
Figure 3.10: *Radiation budget components from LU-SM compared to observations at site A1.*

shear is too weak. That the SFS stress contributions are not large outside the near-surface layer perhaps explains why using different turbulence models does not have very large effects (see Section 3.5.5).

3.5 Sensitivity tests

The comparisons in Section 3.4 contrasted the improved results from LU-SM with those from REF which used a standard procedure with standard initial conditions and surface datasets. The LU-SM setup includes all the components found necessary to give the best agreement with observations. We now examine the effects of individual pieces used in LU-SM to determine the significance of each. We also attempt to provide some general recommendations for future simulations over complex terrain.

3.5.1 Soil moisture

Several studies have found sensitivity of simulation results to soil moisture (e.g. Eastman et al., 1998; Chen et al., 2001). The improved results from the use of high-resolution WaSiM soil moisture data have been shown in Figs. 3.5-3.8 which compare REF-ST and LU-SM. REF-ST used ECMWF soil moisture data; the result was that the up-valley wind transition occurred too late (by 3-4 hours) throughout the entire nested set of grids. Banta and Gannon (1995) found that increased soil moisture decreases the strength of katabatic winds; this is due to slower cooling caused by the increased thermal conductivity of moist soil and increased downward longwave radiation (because the air near the surface has higher humidity). Ookouchi et al. (1984) showed that increased soil moisture decreases up-slope winds because the wetter soil does not heat as quickly and hence produces smaller horizontal pressure gradients. Accordingly, with wetter soil (REF-ST), the transition to up-valley winds begins later, while the slightly drier soil (LU-SM) better reproduces the transition. This simple explanation is complicated, however, by the complexity in the topography of the Riviera Valley and its tributaries (the Magadino,

(a)   (b)
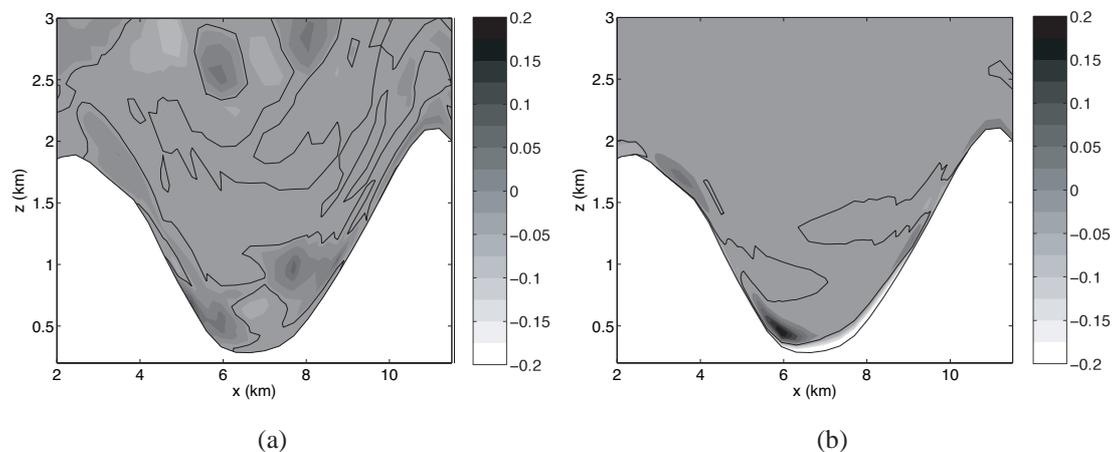
Figure 3.11: *Vertical cross-sections of (a) resolved vw and (b) SFS τ_{23} stress ($m^2\,s^{-2}$) perpendicular to valley axis at site A1 for LU-SM. Time averaged between 1300 and 1500 UTC at 300 s intervals. The black contour line marks the zero contour.*
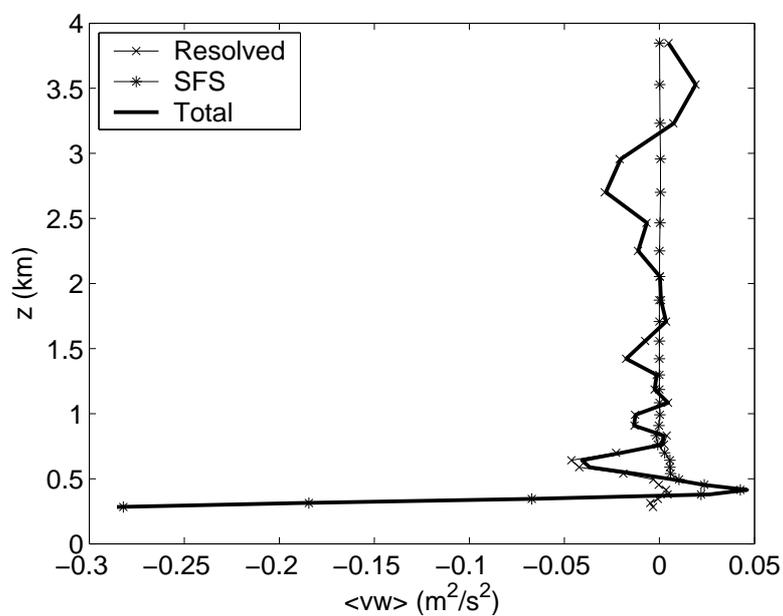
Figure 3.12: *Vertical profile of resolved, subfilter-scale, and total stress for vw located on valley floor for LU-SM. Time averaged between 1300 and 1500 UTC at 300 s intervals.*

(a)   (b)
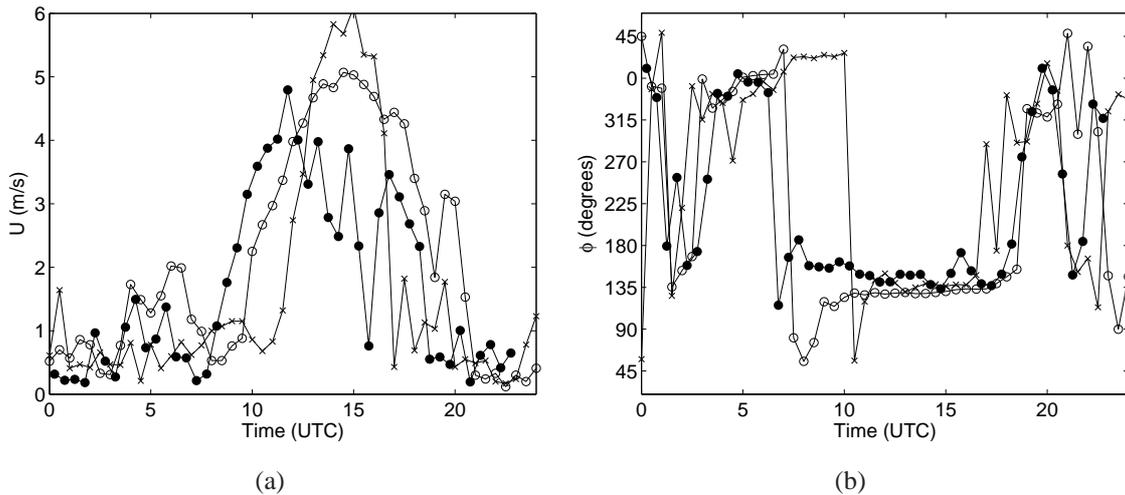
Figure 3.13: *Surface wind speed and direction at Bosco di Sotto (site A1) using different soil moisture initializations.* —•— *Observations;* —○— *LU-SM;* —×— *LU-SM2*

Mesolcina, Leventina and Blenio Valleys), because the effect of soil moisture will be different in each valley. Strong down-valley winds from the Mesolcina Valley, for example, could block the entrance of up-valley winds from the Magadino Valley into the Riviera Valley.

That the soil moisture effect is not straightforward is demonstrated by another experiment in which we use the WaSiM data at coarse resolutions as well. The WaSiM data cover only the Ticino and Verzasca river catchment areas, i.e., only the immediate vicinity of the Riviera. In the LU-SM2 simulations, however, we have applied the WaSiM soil moisture values over the 1 km grid where data are available. Over the rest of the domain, we use elevation-dependent values at three levels determined from averages of the WaSiM data (similar to the LU-SM setup, see Table 3.3). Thus, we "extrapolate" the values from the center of the domain, where the WaSiM data are available, to the rest of the Alpine region covered by the 1 km grid. The wind speed and direction from LU-SM and LU-SM2 in Fig. 3.13 differ significantly, although there is not as much difference in the temperatures (not shown). The onset of the valley winds sees a greater delay (by about two hours) in the morning (Fig. 3.13); the up-valley winds also die out about two hours too soon in the evening. Vertical profiles (not shown) indicate that these wind shift differences are present throughout the valley atmosphere and not just at the surface.

The effects of differences in soil moisture variability can also be seen by examining time series of surface fluxes. Figure 3.9 showed that the REF-ST surface fluxes are severely underpredicted, confirming the lack of adequate heating and the delay in the predicted onset of valley winds. Between LU-SM and LU-SM2, the differences in the heat and momentum fluxes (not shown) are much smaller but reflect the discrepancies in the valley winds predicted by LU-SM2 shown in Fig. 3.13.

The results of comparisons among LU-SM, LU-SM2 and REF-ST indicate that the soil moisture outside the fine-grid (350 m) domain is crucial for accurately predicting the wind transitions. In fact, using the three-level elevation-dependent soil moisture from the 1 km grid on the 350 m grid (LU-SM3) yields results almost equivalent to LU-SM. The effect of using the WaSiM data in LU-SM is small, improving the onset of the up-valley winds by approximately half an hour; Fig. 3.14 shows the surface wind time series for LU-SM and LU-SM3. Note that
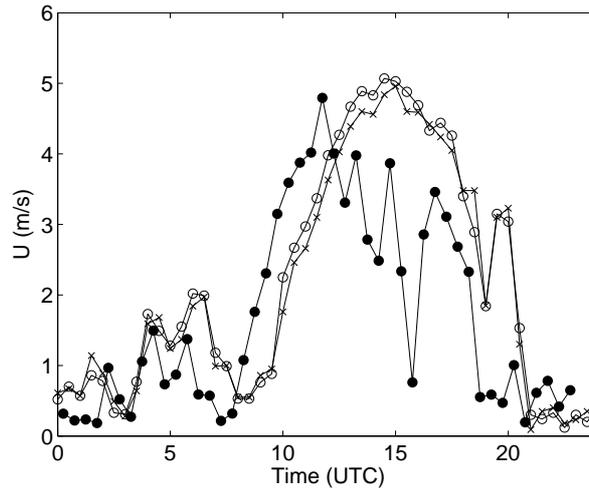
Figure 3.14: *Surface wind speed at site A1 using different soil moisture initializations.* —●— *Observations;* —○— *LU-SM;* —×— *LU-SM3*

WaSiM data are needed to obtain the three-level soil moisture values, so the LU-SM3 setup provides no practical advantage, but emphasizes the significance of the 1 km grid soil moisture initialization.

In summary, the LU-SM setup has the best possible initial soil moisture information. The simulations deteriorate in quality when we assume the large-scale ECMWF soil moisture distribution holds on the 1 km domain (REF-ST). Likewise, assuming that the local WaSiM soil moisture distribution in the Riviera Valley holds over the larger 1 km domain (LU-SM2) also yields poorer results than the three-level soil moisture used at 1 km resolution in LU-SM. This points to the need for high-resolution soil moisture measurements over a broader region (such as all of the Alps) to provide accurate input to large-eddy simulations. In our case, the sensitivity to soil moisture is highlighted in the 1 km grid, which is the first grid which can resolve the complex topography (albeit coarsely) while containing the entire valley system (i.e. the valleys surrounding the Riviera) responsible for forcing the thermal flow.

3.5.2   Land use data

We introduced 100 m resolution land use data for the 350 m grid level, as described previously in Section 3.3.5. To measure the impact of the increased number of vegetation and soil classes and increased spatial variability, we performed simulations with interpolated low-resolution land use data and the original vegetation and soil types (results are denoted SM) instead of the 100 m data. The SM wind direction in Fig. 3.15 shows erratic behavior during the morning valley-wind transition, and the wind speed time series shows an additional half hour delay in the up-valley winds relative to LU-SM. Differences in vertical sounding profiles are quite small except near the surface (not shown). Nevertheless, the overall results indicate that the high-resolution land use representation brings improvements.

3.5.3   Grid resolution

High grid resolution is particularly important over complex terrain like the Riviera Valley, where the terrain features that channel the flow must be well resolved. The width of the Riviera
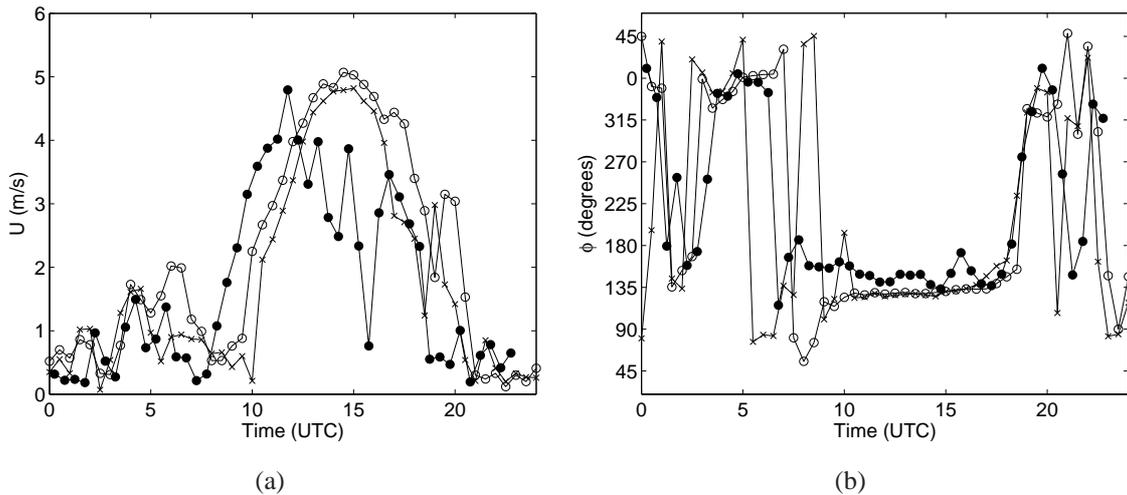
(a)

(b)

Figure 3.15: *Surface wind speed and direction at Bosco di Sotto (site A1) using different land use data.* ―●― *Observations;* ―○― *LU-SM;* ―×― *SM*

Valley floor is approximately 1.5 km. Given that the minimum well-resolved eddy for LES is $4\Delta x$, a horizontal resolution of 400 m barely resolves the valley floor. Coarse resolutions also do not represent the terrain elevation accurately. For example, the elevation of site A1 is 1123 m, 794 m, 334 m, and 263 m asl on the 9 km, 3 km, 1 km, and 350 m resolution grids, respectively. These are enormous height differences from the true elevation of 250 m asl and they greatly affect the representation of near-surface flow.

It may seem obvious that increasing resolution will improve results, but this is still debated in the literature (see e.g. Cairns and Corey, 2003; Hart et al., 2004). The comparisons here show the significant improvements that can be obtained at finer resolutions when the appropriate surface data are used. Figure 3.16 shows comparisons of the potential temperature results from 3 km, 1 km, and 350 m horizontal resolutions from LU-SM. The plotted surface values on the coarse grids (i.e. at the first grid level) are at much higher elevation than the real valley floor; thus, the potential temperature for the 3 km and 1 km grids is too high at the surface, especially during the night. A height-correction has not been carried out, as the choice of a suitable lapse rate would have been arbitrary and would not have improved the amplitude error in the temperature curve. The wind transition predictions on the 3 km and 1 km grids are also crude in comparison to the good agreement seen at the 350 m grid level (not shown). Fig. 3.17 shows an example where the finer vertical resolution of the 350 m grid (see Section 3.3.2) can capture strongly stratified layers (though not perfectly), unlike the 3 km and 1 km grids. These near-surface inversions are influenced by shallow down-slope wind layers and are responsible for the cooling seen during the night at the valley floor. The coarse grids are not able to capture such shallow stable layers because of the poor representation of the terrain slopes and the coarse near-surface resolution (Fig. 3.16).

The differences between the 350 m and 150 m results (not shown) are small. This is likely due to the lateral boundary forcing and the limited domain sizes; the 150 m grid is strongly forced by the 350 m results. The increased resolution up to 350 m is, however, clearly necessary for an accurate representation of this complex flow. The general results (e.g. wind transitions) are influenced strongly by the solution on the 1 km grid, so it is important to have good soil moisture values on this grid (see Section 3.5.1). Finer resolution allows a larger range of flow
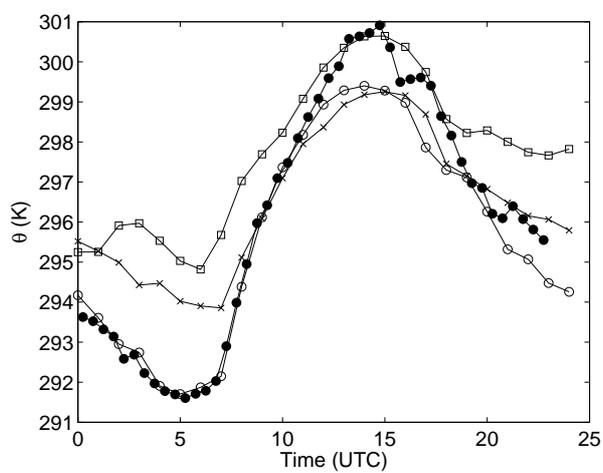
Figure 3.16: *Surface potential temperature at site A1 at various grid resolutions for LU-SM.* —•— *Observations;* —□— *3 km;* —×— *1 km;* —○— *350 m*
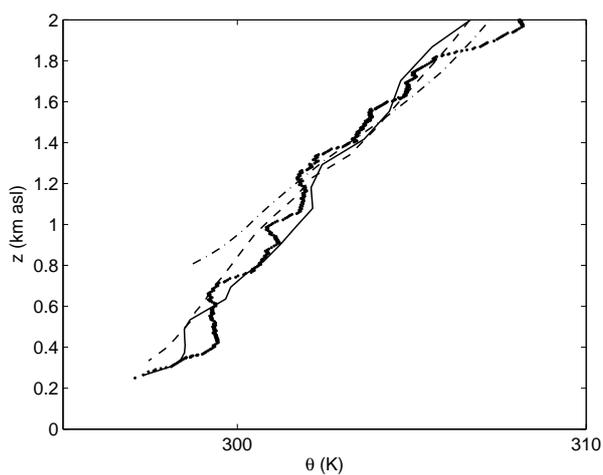

Figure 3.17: *Close-up of potential temperature soundings at 1800* UTC *and various grid resolutions for LU-SM.* •••••• *Observations;* —·— *3 km;* ---- *1 km;* —— *350 m.*
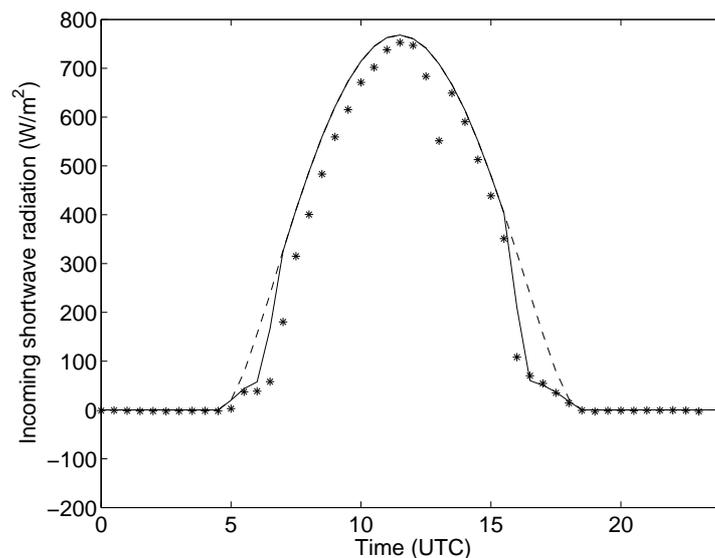
Figure 3.18: *Incoming solar radiation, with and without topographic shading, at site A1.* ∗ *Observations;* ——— *LU-SM;* - - - - *LU-SM-NOSHADE*

structures to be resolved, thereby better representing near-surface features (e.g. stratification), and relying less on the SFS turbulence models. At the same time, the unsatisfactory REF results (using interpolated low-resolution surface data) show that high-resolution surface data are necessary in addition to fine grid resolution.

3.5.4 Topographic shading

A series of simulations was performed without topographic shading for the entire set of simulations (LU-SM-NOSHADE) to investigate the influence of this modification to the radiation model. Figure 3.18 shows the incoming shortwave radiation with and without topographic shading, at site A1. The incoming shortwave radiation is significantly reduced around sunrise and sunset when topographic shading is included, and therefore compares better with the measurements. Figure 3.19 shows the spatial variation of differences in incoming shortwave radiation at 0600 UTC when topographic shading is included. The east-facing slopes are shaded while the sun is low on the horizon, resulting in nearly 300 W m^{-2} less insolation. The topographic shading model does not affect the longwave radiation balance at night.

The differences in the radiation curves and flow fields are insignificant at the coarser resolutions, because terrain slopes are smaller, but on the 350 m grid, surface temperatures are slightly warmer without shading ($\sim$ 0.5-1.0 K) during sunrise and sunset, as expected. Figure 3.20 shows a time series of the absolute value of differences at surface station A1 for LU-SM and LU-SM-NOSHADE. It is clear that the largest changes from topographic shading occur during sunrise and sunset. The influence of topographic shading in the comparisons of the vertical profiles is quite small.

Experiment LU-SM-NOSHADE shows increased up-slope winds along the east-facing slope of the Riviera as expected; however, differences are only on the order of 0.1 m s^{-1}, occasionally up to 0.5 m s^{-1} (not shown). Larger differences from topographic shading were observed in the idealized simulations of Colette et al. (2003), which did not include along-valley winds. Another reason why the impact of topographic shading is weaker here may be that the

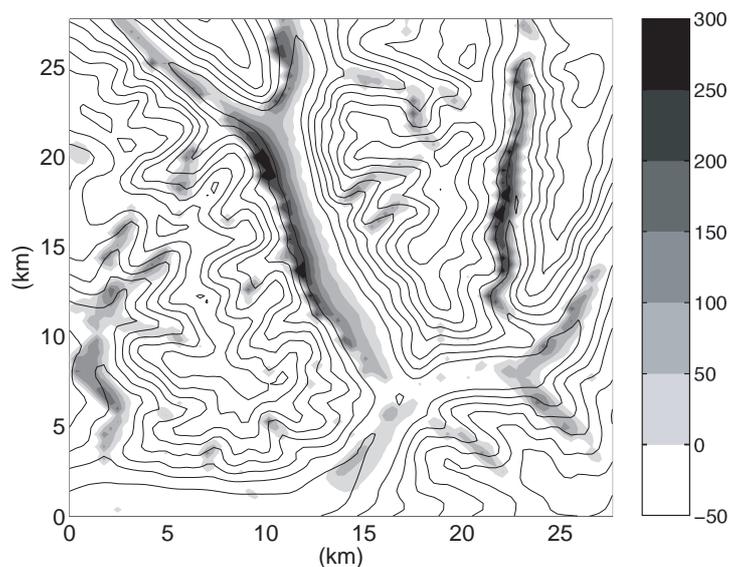**Figure 3.19:** *Difference in shortwave incoming radiation (filled contours, $W\,m^{-2}$) with and without shading (LU-SM-NOSHADE minus LU-SM) for the 350 m grid at 0600 UTC. Elevation contours (lines) shown at 250 m intervals.*
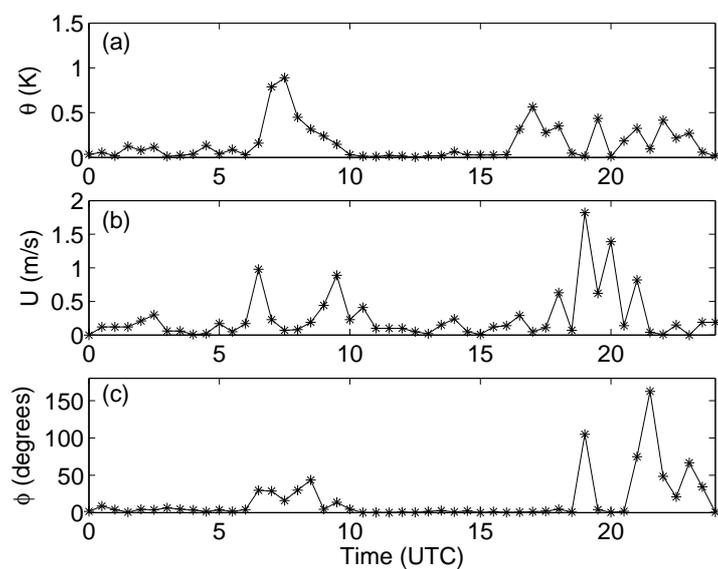

Figure 3.20: *Time series of the absolute difference between LU-SM and LU-SM-NOSHADE surface variables at site A1 for (a) potential temperature, (b) wind speed, and (c) wind direction.*

(a)   (b)
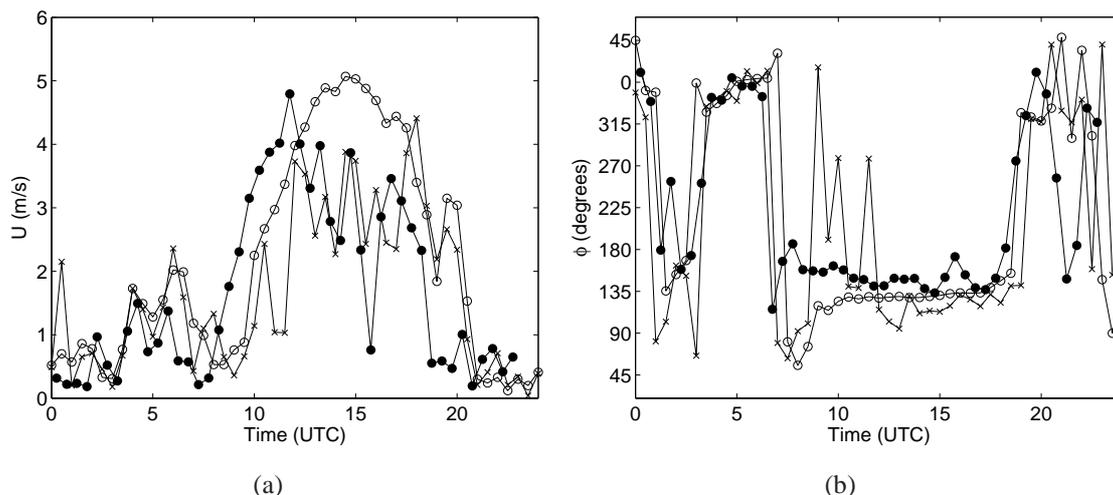
Figure 3.21: *Surface wind time series comparisons with and without a turbulence model at Bosco di Sotto (site A1) for (a) wind speed and (b) wind direction.* —•— *Observations;* —∘— *LU-SM;* —×— *LU-SM-NOTURB*

valley winds are forced by a pressure gradient over the entire valley wind system (i.e. from the Magadino Valley up to the Leventina Valley; see Fig. 3.2b). The beginning and end portions of this larger-scale valley are oriented more nearly east-west and are thus less affected by shading in the morning. In addition, the Magadino and Leventina Valleys are not entirely included in the 350 m domain. While the differences between LU-SM and LU-SM-NOSHADE are small, the improvement in the radiation curves in Fig. 3.18 is significant. The computational cost of adding the shading effect is negligible (Colette et al., 2003).

3.5.5 Turbulence closure

Little is known about the appropriate choice of turbulence models for LES in complex terrain. One measure of the influence of the turbulence model is the effect of turning the turbulence model on or off, as seen in Fig. 3.21 for LU-SM and LU-SM-NOTURB. The "no turbulence" simulations clearly do not perform as well as LU-SM. The surface wind predictions have significant differences; for example, the surface winds show more oscillations, as expected for a simulation with less dissipation.

The difference in the results is limited, however, to the near-surface region, because the SFS stress contribution is large only in the lowest 500 m, as shown in Figs. 3.11-3.12. This is due to the strong stable stratification in the valley atmosphere, with only a shallow mixed layer at the surface (Fig. 3.8). Accordingly, vertical profiles from LU-SM and LU-SM-NOTURB only show differences in the near-surface region (not shown). Intermittent turbulence may be important in stable layers above, but this is hard to capture with current turbulence models (Cederwall, 2001). All of the simulations also include fourth-order computational mixing, which acts like a hyper-viscosity term and may dominate the turbulence model effect at 350 m resolution. Numerical errors from finite-difference schemes also contribute to the dissipation of energy from large to small scales.

Simulations are also performed using the dynamic reconstruction model (DRM) of Chow et al. (2005a) (LU-SM-DRM). The differences in the TKE-1.5 and DRM predictions of the
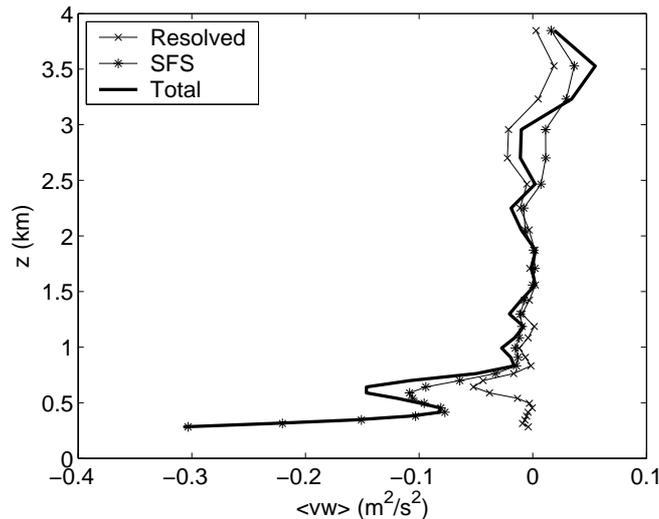
Figure 3.22: *Vertical profile of resolved, subfilter-scale, and total stress for vw at the valley floor for LU-SM-DRM (using the DRM turbulence closure). Time averaged between 1300 and 1500* UTC *at 300 s intervals.*

temperature and winds are not large, so they are not shown here. Details of the models and comparisons are given in Chow (2004). The most noticeable change is in the prediction of momentum fluxes. Figure 3.22 shows vertical profiles of time-averaged resolved and SFS stresses in the vw plane from LU-SM-DRM. Compared to Fig. 3.12, the DRM results give a significantly larger contribution from the SFS terms. This is consistent with the findings in Chow et al. (2005a) where the SFS stresses using DRM were larger (than those from an eddy-viscosity model used alone) due to the resolved subfilter-scale (RSFS) contribution, and hence gave better comparisons to stresses extracted from higher-resolution simulations. Here, the stress is also larger higher up in the valley atmosphere because the DRM is not as easily damped by stratification when the RSFS stress is included.

The simulation results show relative insensitivity to the turbulence model because differences are confined to the near-surface region. (In contrast, the sensitivity to soil moisture initializiation was high, where differences extended throughout the valley atmosphere and affected wind transitions, as seen, for example, in Figs. 3.5-3.8.) The limited influence of the turbulence model is due to the role of the strong stratification and also the strong lateral boundary forcing. The lateral boundary conditions are time dependent, but are only updated hourly. Intermediate values are linearly interpolated. Simulations of flow over Askervein Hill (Chow and Street, 2004) showed that realistic turbulent inflow conditions were necessary for satisfactory predictions of wind speed over the hill. The lateral forcing in the Riviera is not fully turbulent because of the linear time interpolation, so the turbulence must develop as the flow progresses through the domain and is influenced by the complex topography. Small-scale turbulent motions are present in the simulations, but the afternoon winds are quite strong, yielding a relatively short effective residence time of air parcels in the valley when compared to the 30-hour simulation time. Thus, small differences that arise due to different turbulence models (or topographic shading and other parameterizations) do not have time to manifest themselves especially when along-valley winds are strong.

Figure 3.23 shows that differences do occur on shorter time scales, comparing results from one-hour simulations using identical initial and boundary conditions but different turbulence
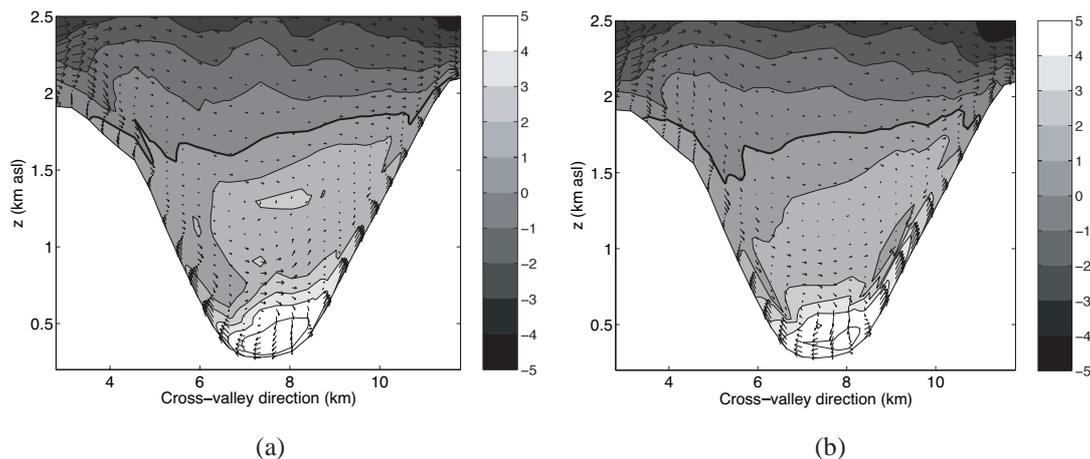
Figure 3.23: *Cross-valley winds (vectors) and along-valley winds (m s^{-1}, shaded) at 1300 UTC from the 350 m grid for (a) LU-SM with TKE-1.5 and (b) LU-SM-DRM with the DRM turbulence closure. Simulations start at 1200 UTC using identical initial and boundary conditions. Cross-valley distance measured along line shown in Fig. 3.2b. The zero contour line is shown in bold.*

models (the TKE-1.5 and the DRM). It is clear that the shape of the up-valley flow contours is different, and hence that the effect of the turbulence closure is not completely negligible, even though the performance of the models is difficult to quantitatively evaluate because of the lack of high-resolution observation data. Simulations over the entire day are more strongly influenced by lateral boundary conditions and surface characteristics, but the finer details are affected by the turbulence model.

3.6   Summary and conclusions

We have shown that ARPS can accurately reproduce the valley wind patterns observed under convective conditions in complex terrain. Comparisons to surface station and radiosonde measurements from the MAP-Riviera project field campaign of 1999 gave rmse values of less than 1 K for potential temperature and of about 2 m s^{-1} for wind speed. This success required careful initialization with high-resolution land use and soil moisture datasets, among other considerations. In contrast, increasing resolution without using high-resolution surface datasets did not yield satisfactory results. It was found that even with strong local thermal forcing, the onset and magnitude of the valley wind transitions are highly sensitive to surface fluxes in areas which are well outside the high-resolution domain. These processes directly influence the flow structure in the high-resolution domain via its lateral boundary conditions, but are inadequately resolved on the coarser grid of the previous nesting level. The three-dimensional structure and evolution of the valley boundary layer is investigated in detail in Part II (Weigel et al., 2005).

Our findings can be summarized as follows:

(i) Increased grid resolution provides improved numerical simulations, but only when surface and soil model fields are properly initialized. While 3 km horizontal spacing is often considered to be high resolution, it is not until we reach 350 m resolution that the wind transitions and vertical structure of the atmosphere become very well represented in a narrow valley. Even higher grid resolution will allow the representation of finer-scale motions and may improve the

ability of SGS turbulence models to contribute appropriately under stable stratification.

(ii) High-resolution soil moisture data proved to be necessary to obtain the most accurate predictions of wind transitions and surface fluxes. Improved soil moisture data (three-level elevation dependent values, motivated by WaSiM data) were crucial at the 1 km grid level, where the entire Riviera Valley is included in the domain and valley winds are generated over the whole valley network. High-resolution initial soil moisture data (100 m, obtained from the hydrologic model WaSiM), gave further improvement at the 350 m grid. All in all, the distribution of soil moisture was one of the most sensitive parameters in our simulations. The 100 m land use data provided detailed local land coverage and also improved simulation results, as did initializing the soil temperature with an offset from the air temperature, but the sensitivity to these modifications was not as large as for the soil moisture initialization.

(iii) Topographic shading improved the radiation curves measured at the valley floor and along the slopes, with the largest differences occurring during sunrise and sunset. The influence of topographic shading was only significant at the 350 m and finer grids where the steep topography is well resolved. The overall impact of topographic shading on the flow dynamics is small (see Fig. 3.18) because the fine-resolution flow is driven through grid nesting by the coarser resolution grid which is not sensitive to the shading.

(iv) The effect of different turbulence models in the Riviera Valley is unclear. Simulations without a turbulence model performed poorly in comparisons with surface observations. Results with the dynamic reconstruction approach, however, did not differ appreciably over the simulation period from the standard TKE-1.5 closure, perhaps because the turbulent stresses were only significant in the lowest 500 m near the surface (due to strong stratification) and because of strong lateral boundary forcing. There are visible effects on near-surface eddy structures but quantitative verification data are not available.

(v) The lateral boundary forcing is largely responsible for driving the flow transitions at the 350 m and 150 m grids. Thus the valley wind transitions are strongly influenced by the 1 km grid where the entire Riviera Valley is included in the domain. Unfortunately at 1 km resolution, the topography is not well resolved and surface data are sparser so errors are larger. The strong lateral boundary forcing limits our ability to fully evaluate the sensitivity of the topographic shading and turbulence closure models; the grid nesting effectively constrains the influence of these model components to the finest grids because of poor resolution on the larger grids.

The sensitivity to surface conditions points to a need for better surface characterization data. Extensive field campaigns and remote sensing developments are needed to obtain the necessary input data for forecast models. Accurate soil moisture data at 1 km resolution, for example, was found to be necessary for the success of the Riviera Valley flow simulations, but most field campaigns include at best a handful of soil moisture measurement locations. The design of such field campaigns could be greatly improved by examining model results like those obtained here for the Riviera Valley. Much research is also needed to construct radiation models that include the influence of neighboring terrain on local radiative heat fluxes that are important in steep terrain. Grid nesting techniques at the lateral boundaries also need further exploration. The transmission of turbulent fluctuations from the coarse to the fine grid at the lateral boundaries is currently severely limited by the grid resolution and the frequency at which lateral boundary condition data are available. More frequent boundary condition updates and two-way nesting techniques should be investigated.

Acknowledgments

Chapter 4

High-resolution large-eddy simulations of flow in a steep Alpine valley. Part II: Flow structure and heat budgets

High-resolution large-eddy simulations of flow in a steep Alpine valley. Part II: Flow structure and heat budgets[*]

Andreas P. Weigel[1], Fotini K. Chow[2],
Mathias W. Rotach[3], Robert L. Street[2] and Ming Xue[4]

Abstract

This paper analyzes the three-dimensional flow structure and the heat budget in a typical medium-sized and steep Alpine valley, the Riviera Valley in southern Switzerland. Aircraft measurements from the MAP-Riviera field campaign reveal a very pronounced valley-wind system, including a strong curvature-induced secondary circulation in the southern valley entrance region. Accompanying radio soundings show that the growth of a well-mixed layer is suppressed, even under convective conditions. Our analyses are based on the MAP-Riviera measurement data and the output of high-resolution large-eddy simulations using the Advanced Regional Prediction System (ARPS). Three sunny days of the measurement campaign are simulated. Using horizontal grid-resolutions of 350 m and 150 m (with a vertical resolution as fine as 20 m), the model reproduces the observed flow features very well. The ARPS output data are then used to calculate the components of the heat budget of the valley atmosphere, first in profiles over the valley base, then as averages over almost the entire valley volume. The analysis shows that the suppressed growth of the well-mixed layer is due to the combined effect of cold-air advection in the along-valley direction and subsidence of warm air from the free atmosphere aloft. It is further influenced by the local cross-valley circulation. This had already been hypothesized on the basis of measurement data, and is now confirmed through a numerical model. Averaged over the entire valley, subsidence turns out to be one of the main heating sources of the valley atmosphere and is of comparable magnitude to turbulent heat flux divergence. On the mornings of two out of the three simulation days, this subsidence is even identified as the only major heating source and thus appears to be an important driving mechanism for the onset of thermally driven up-valley winds.

4.1 Introduction

On fair-weather days, complicated thermally-driven flow patterns can develop in mountain valleys and affect the atmospheric boundary layer evolution. Such flow patterns are typically a superposition of several scales of motion, including local *slope winds* (directed normal to the valley axis and along the slopes), channeled and thermally-induced *valley winds* (parallel to the valley axis) as well as mountain-plain winds on the regional scale. The phenomenology of these flows has been well investigated and is comprehensively described in numerous reviews (e.g. Wagner, 1938; Barry, 1992; Whiteman, 1990, 2000). Slope winds are understood to arise as a consequence of horizontal density gradients between the surface layer over the slopes and the air over the center of the valley. Their physics can be reproduced by relatively simple conceptual models (Egger, 1990). As far as valley winds are concerned, however, there is still some controversy regarding the driving mechanisms. This paper uses large-eddy simulation of flow in a steep, Alpine valley to investigate the nature of along-valley wind formation using the heat budget as an analysis tool.

It is known that the diurnal cycle of potential temperature in a valley atmosphere reveals a higher amplitude than the corresponding cycle over an adjacent plain (e.g. Neininger, 1982; Vergeiner and Dreiseitl, 1987). While it is plausible that the resulting gradients in hydrostatic pressure drive winds in the along-valley direction, it is not yet clear why valleys heat more during the day and cool more at night than adjacent plains. Often, this is explained by means of the simple TAF (topographic amplification factor) concept (e.g. Wagner, 1938; Steinacker, 1984; McKee and O'Neil, 1989). It is based on a volume argument, stating that (in the daytime case) a given amount of incoming solar radiation applied over a mountain valley heats a smaller volume of air than if applied over a plain, resulting in a larger heating rate of the valley atmosphere. Analogously, the nocturnal cooling rate (driven by the emission of longwave radiation from the surface) is stronger in a valley than over flat terrain. The main limitation of the TAF concept is its assumption that the control volume must be thermodynamically closed, i.e. that no heat must be exchanged with the synoptic-scale flow in the free atmosphere above the valley. Moreover, it fails in the case of rectangular valleys. Another concept, which has been developed on the basis of idealized simulations, suggests subsidence heating as an important driving mechanism (Rampanelli et al., 2004): due to a thermally induced cross-valley circulation, which extends well above the valley top, warm air of the free atmosphere is forced to subside, thus warming the valley. So far, however, there have been very few estimates of the heat budget terms in a daytime valley atmosphere from measurements (e.g Hennemuth, 1987; Kalthoff et al., 2000; Weigel and Rotach, 2004), and they lack the spatial and temporal resolution to quantitatively assess the underlying heating mechanisms.

With the advances of computer technology, high-resolution numerical simulations have become an important tool in the investigation of small-scale processes and the flow structure over mountainous terrain (e.g. De Wekker et al., 2005; Gohm et al., 2004; Zängl et al., 2004, to mention only very recent studies). Such simulations can be used for heat budget analyses. Fast et al. (1996), for example, used the Regional Atmospheric Prediction System (RAMS, Pielke et al., 1992) to investigate the night time heat budget of the Sindbad Basin in Colorado and were able to partly confirm the measurements of Whiteman et al. (1996).

We have chosen the Riviera Valley in southern Switzerland (base width: 1.5 km, length: 15 km, depth: 2-2.5 km) to investigate the daytime flow structure, thermal characteristics and, ultimately, the heat budget in a typical medium-sized Alpine valley. In our approach, we combine measurements from the MAP-Riviera field campaign (Rotach et al., 2004) with the output of high-resolution large-eddy simulations (LES). For the modeling, we use the Advanced Re-

gional Prediction System (ARPS, Xue et al., 2000, 2001, 2003). In Part I of this work (Chow et al., 2005b)[5], an optimal model setup for simulating flow in the Riviera Valley with ARPS is described and results for one of the three days are evaluated by means of comparisons to radiosonde and surface data. Here, we use this setup to simulate and analyze three days of the measurement campaign (21, 22 and 25 August 1999) with fair-weather conditions. The experimental and numerical context is briefly described in the next section. Section 4.3 characterizes the three-dimensional flow structure in the valley and compares model results with aircraft measurements. The thermal structure is elaborated in Section 4.4, including a heat budget analysis of profiles over the valley base. Finally, the heat budget of the entire valley is analyzed in Section 4.5 and put into the context of the TAF and subsidence concepts of valley warming.

4.2 The field experiment and numerical simulations

The experimental setup of the MAP-Riviera Project has been extensively described by Rotach et al. (2004). The dataset obtained during the measurement campaign includes radio soundings and sonic and profile measurements, among others, at various surface stations. A light research aircraft (Neininger et al., 2001) was also employed. Focusing on both the mean and turbulence structures, the dataset is of unprecedented completeness with respect to boundary layer studies in such complex topography. In Part I (Chow et al., 2005b), radiosonde and surface measurements are used to evaluate the performance of ARPS in the Riviera Valley for the August 25 case. Here we focus primarily on the assessment of the three-dimensional flow-structure in the daytime Riviera atmosphere. The model performance in this aspect can be qualitatively evaluated by means of the airborne measurements (Weigel and Rotach, 2004)[6].

Chow et al. (2005b) have described the numerical context for the simulation of the Riviera atmosphere in detail. Simulations were quantitatively evaluated for 25 August 1999, as data quality and synoptic conditions were most 'ideal' on this day. The setup which has proven to yield the best results for 25 August is the so-called "LU-SM"-setup (Chow et al., 2005b)[7]. In this setup, ARPS is run in a one-way nesting mode. A grid of 9 km horizontal resolution is initialized from ECMWF analysis data and then successively nested down to grids of finer horizontal resolutions (3 km, 1 km, 350 m and 150 m). All simulations start at 1800 UTC of the previous day (local daylight saving time = UTC + 2 hours).

The best setup for the simulation of 21 and 22 August has turned out to be almost identical to the "LU-SM" setup. The only major difference is that on 21 and 22 August the model fields of the first nesting level (9 km resolution) are additionally nudged over the entire simulation period to the respective interpolated ECMWF fields, yielding some further improvement of the model output. This step has been necessary due to the more complicated synoptic conditions on 21 and 22 August: while 25 August was almost entirely cloud-free in all nesting-domains, the Alps were partially cloud-covered on 21 and 22 August. On 20 August - the day of initialization for the simulation of 21 August - there is even rainfall over the larger part of the Swiss Alps, making the model-initialization particularly error-prone and the nudging process important.

Unless otherwise stated, data from model runs on the 350 m grid (finest vertical resolution of 30 m) are used in this paper, as the 350 m grid is the finest domain still containing the entire Riviera Valley. The 150 m grid (finest vertical resolution of 20 m) which does not cover the

---

[5]Chapter 3 of this thesis
[6]Chapter 2 of this thesis
[7]see Section 3.5.1 of this thesis
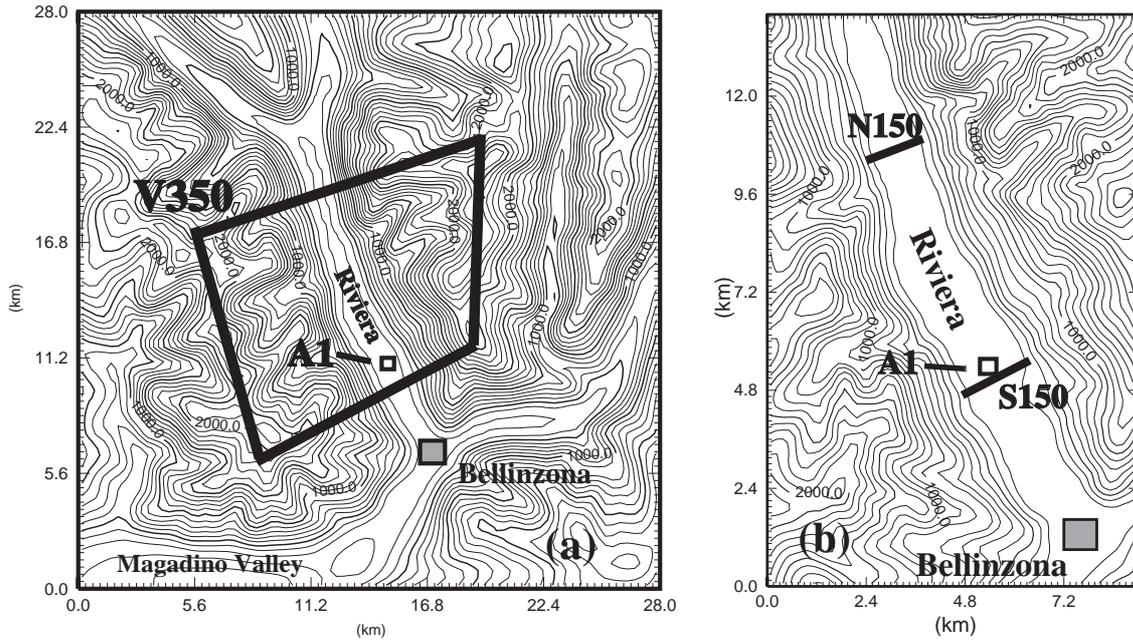
Figure 4.1: *Topography of (a) the 350 m grid and (b) the 150 m grid. 'A1' denotes the location of a surface measurement station (Bosco di Sotto). Data extracted from slices 'S150' and 'N150' are used in Section 4.4.2. 'V350' indicates the integration volume used in Section 4.5.*

whole valley, has been used in Section 4.4.2, where profiles of heat budget components over the narrow valley floor are assessed. The two high-resolution domains (350 m and 150 m) are shown in Fig. 4.1.

Regarding the choice of initial soil moisture distribution - one of the most sensitive parameters - the "LU-SM"-setup of Chow et al. (2005b)[8] has proven to give the best results as before. Following this setup, ECMWF soil moisture values are used on the 9 km and 3 km grids, a semi-empirical three-level initialization on the 1 km grid, and output data of the Water Flow and Balance Simulation Model (WaSiM-ETH, Jasper, 2001) for the ARPS runs on the 350 m and 150 m grids. For the three-level soil moisture initialization of the 1 km grid, the same values are used as on 25 August (see Table 3.3).

In Fig. 4.2, the diurnal cycle of measured and simulated surface winds and potential temperatures at measurement site A1 (Bosco di Sotto, see Fig. 4.1) are displayed for 21 and 22 August [for 25 August see Figs. 3.4 and 3.5). Table 4.1 shows the corresponding root-mean-square-errors (rmse) and mean errors (bias) for comparisons of the modeled surface wind speed, wind direction and potential temperature to the measurements. Bias and rmse are calculated in the same manner as described by Chow et al. (2005b)[9]. The ARPS data used in these comparisons are extracted from the lowest model level (i.e. 15 m agl), while the observational data are averages of measurements at 15.9 m and 28 m agl. The measurement level at 28 m has been included because the lower level (15.9 m) is influenced by surface layer effects from the plant canopy which are not captured in the model. On both days the diurnal cycles of potential temperature and surface winds are well reproduced by the model. On 21 August, however, the surface valley-wind magnitude is generally too large (on average by about 2.5 m s^{-1}), and simulated night-time surface temperatures are about 3-4 °C too warm. This warm bias is due to a shallow nocturnal near-ground inversion, which is observed from the radiosonde measure-

---

[8]see Section 3.5.1 of this thesis
[9]see Section 3.4.1 (Eqs. 3.1 and 3.2, respectively) of this thesis
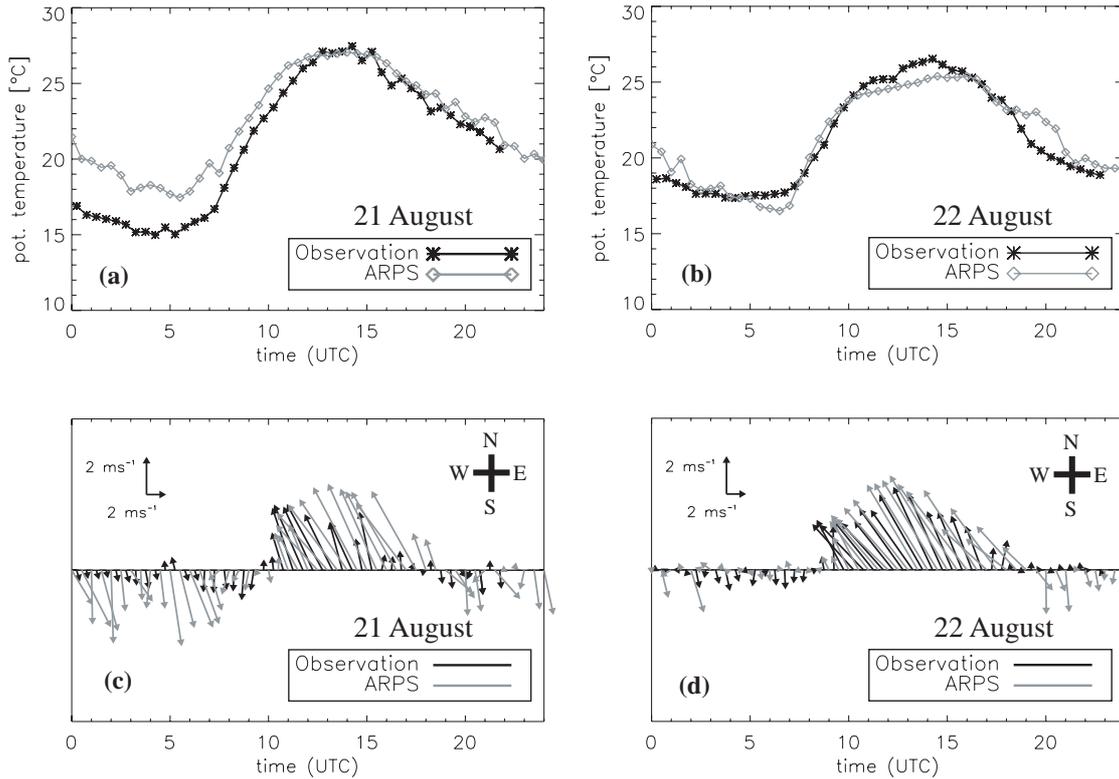
Figure 4.2: *Measured (black) and simulated (grey) time-series of potential temperature (upper panels) and surface winds (lower panels) at observation site A1 on 21 August (left hand side) and 22 August (right hand side). The comparisons for 25 August are shown in Figs. 3.5 and 3.4.*

ments (not shown) but not reproduced by the model. A reason for this model failure may be that the near-surface valley wind speeds are overestimated by the model in the first place, thus producing too much vertical mixing on the surface. Bias and rmse of these simulations at surface site A1 are listed in Table 4.1. It can be seen that the scores of wind speed and particularly potential temperature are better on 22 August than on 21 August. We believe that this is due to the difficult initialization situation on 20 August, as mentioned above. Compared to other recent modeling studies over terrain of similar complexity (e.g. Zängl et al., 2004), the bias and rmse of 21 August are still of comparable if not better quality. Moreover, in this paper our focus is on the daytime atmosphere, where the errors are lower than the 24-hour-averages given in Table 4.1.

In Fig. 4.3, modeled vertical profiles of potential temperature are compared to radiosondes launched at site A1. A comparison of wind profiles is not possible due to a failure in the measurements. Bias and rmse have been calculated using data up to an altitude of 6 km (see Table 4.2). Again, 21 August shows a worse average rmse than 22 August, namely 1.23 K vs. 0.85 K, but this is still considered low. Given the more complicated synoptic conditions on 21 and 22 August, the results are surprisingly good and justify the use of the 'LU-SM'-setup from 25 August on 21 and 22 August, at least for the evaluation of the daytime atmosphere. While the model fails to reproduce the mid-level inversions mostly seen between 3 and 4 km altitude, this shortcoming does not influence the following analyses, as this paper focuses on processes occurring within the valley atmosphere, i.e. at altitudes lower than 3 km.
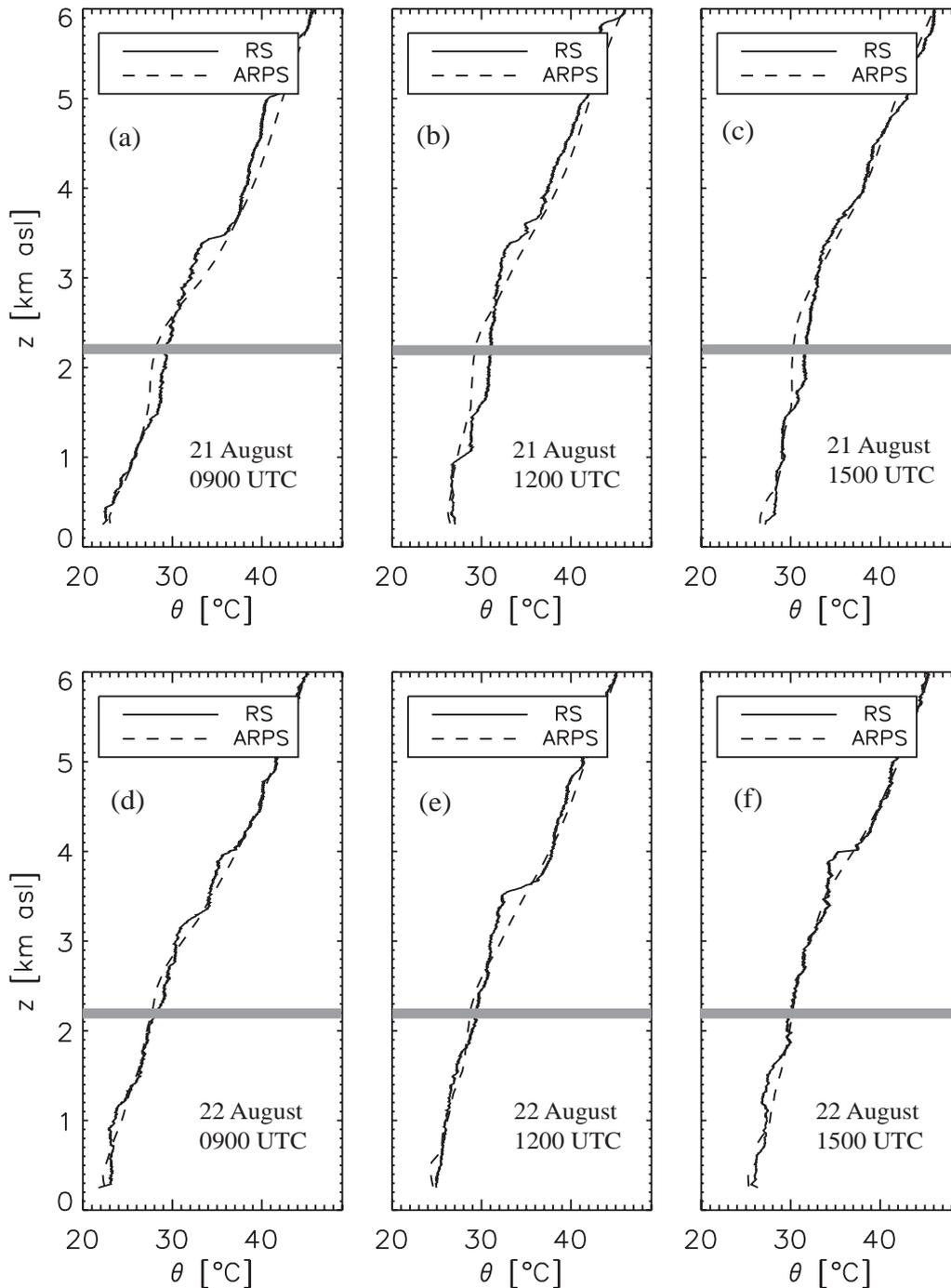
Figure 4.3: *Observed radiosonde (solid line, 'RS') and simulated (dashed line, 'ARPS') profiles of potential temperature on 21 (upper panels) and 22 August (lower panels) at 0900* UTC*, 1200* UTC *and 1500* UTC*. The grey bar indicates the crest height next to site A1. The corresponding profiles of 25 August are shown in Fig. 3.8.*

4.3   Flow patterns of the valley atmosphere

Weigel and Rotach (2004) identified several unexpected features in the three-dimensional flow structure of the Riviera Valley from the MAP-Riviera observations, particularly from the aircraft measurements. Here, we describe the flow structure as obtained from ARPS and compare the results to these measurements.

Table 4.1: *Root-mean-square-errors (rmse) and mean errors (bias) for simulations compared to measurements at surface station A1. θ is the potential temperature, U the wind speed and Φ the wind direction. 46 half-hourly values (beginning at 0015 UTC) have been used to calculate bias and rmse. The high values in Φ rmse are primarily due to light night-time winds, leading to large directional fluctuations.*

Date	θ rmse (K)	θ bias (K)	U rmse (m s^{-1})	U bias (m s^{-1})	Φ rmse (°)	Φ bias (°)
21 August	2.18	-1.76	2.41	-1.67	54.82	3.01
22 August	0.88	-0.19	1.80	-1.03	90.44	-7.93

Table 4.2: *Root-mean-square-errors (rmse) and mean errors (bias) for potential temperature θ for radio soundings up to 6 km from surface station A1.*

Sounding time (UTC)	0000	0600	0900	1200	1500	1800	2100	All
21 Aug: θ rmse (K)	2.12	1.47	0.78	0.91	0.76	1.19	1.36	1.23
21 Aug: θ bias (K)	0.73	0.73	0.17	-0.14	-0.49	0.50	0.42	0.28
22 Aug: θ rmse (K)	1.44	1.05	0.61	0.73	0.65	0.53	0.97	0.85
22 Aug: θ bias (K)	0.66	0.62	-0.06	0.04	0.02	0.41	0.65	0.32

4.3.1 Valley-wind structure

The modeled and measured time-series of surface winds at station A1 (21 and 22 August in Fig. 4.2; 25 August in Fig. 3.5) show a pronounced valley-wind system with weak nocturnal down-valley flows (about 330°) and stronger up-valley winds (about 150°) during the day, a pattern which is typical for thermally driven valley winds. Moreover, the simulations reveal potential temperature gradients in the along-valley direction of the Riviera Valley system (not shown), supporting the notion that the valley winds are of thermal origin. Aircraft observations show that the three-dimensional structure of the up-valley winds has a very distinct shape: in the southern half of the valley, the up-valley wind-speed has its maximum next to the west-facing slope, while further north the up-valley flow is uniformly spread over the valley diameter (Weigel and Rotach, 2004)[10]. This pattern is well-reproduced by the model, as demonstrated for 21 August in Fig. 4.4, which shows the modeled afternoon wind-vectors from a bird's-eye view at an altitude of 900 m asl and the corresponding airborne observations. Simulations and measurements of 22 and 25 August reveal the same flow pattern (not shown).

A vertical cross-section through the asymmetric valley flow in a slice approximately 3.5 km north of the southern valley mouth shows a jet-like flow structure with a distinct wind speed maximum on the order of 10 m s^{-1}, both in the airborne measurements and the simulations (Fig. 4.5). Weigel and Rotach (2004) attribute this behavior to centrifugal forces: the air coming from the Magadino Valley in the southwest has to flow around a sharp bend at the town of Bellinzona to enter the Riviera Valley (see Fig. 4.1a). Due to its inertia the air is pushed towards the west-facing slope. Similar behavior has also been observed in other curved valleys such as the Wipp Valley in Austria (e.g. Fig. 16 in Gohm et al., 2004).

---

[10]see Section 2.3.1 of this thesis
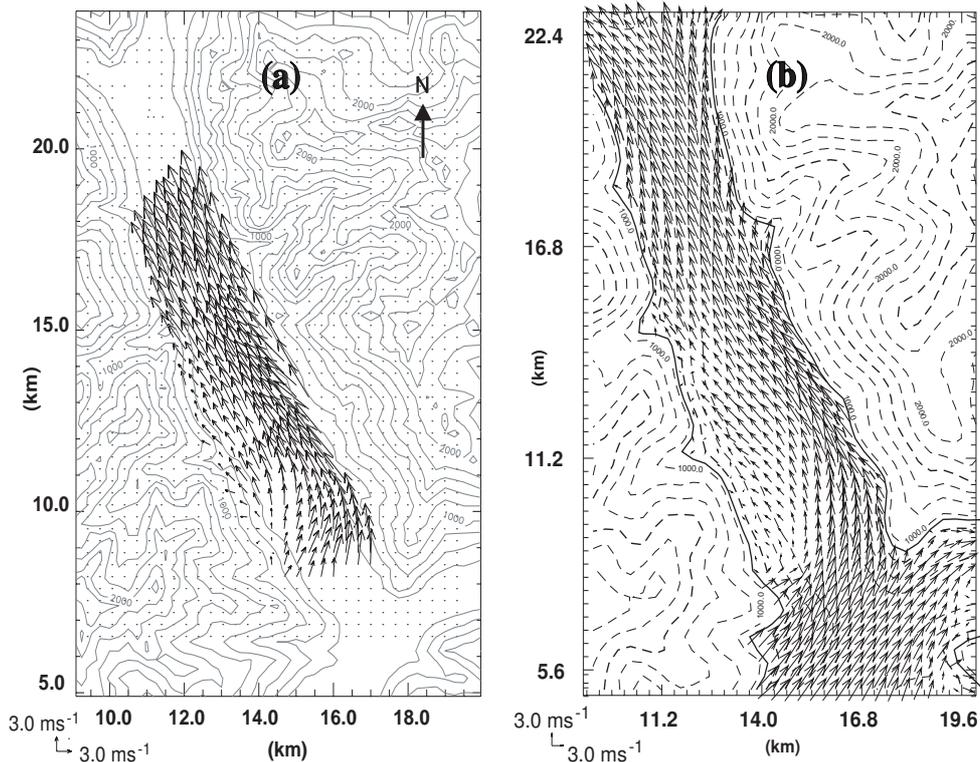
Figure 4.4: *Up-valley wind vectors at an altitude of 900 m on 21 August (a) as measured by the aircraft and (b) as simulated with ARPS. The airborne data are interpolated from three along-valley legs flown between 1500 UTC and 1620 UTC. The simulated flow structure is from the model output at 1530 UTC. The background elevation contours in (b) show the smoothed topography on the 350 m model grid and therefore look slightly different from those in (a). In both plots, the elevation contours are in 200 m intervals.*

4.3.2   Cross-valley circulations

In the 'classical' textbook picture (Whiteman et al., 2000), the atmosphere in a sun-lit valley is expected to develop a symmetric double-circulation with air rising along the heated slopes and subsiding in the valley center. In the case of significant temperature differences between the two valley side-walls, this circulation structure transitions to a simple cross-valley circulation with air rising along the warmer side and subsiding next to the colder side. Figure 4.6 shows the simulated cross-valley flow in two slices through the valley on 22 August: one in the northern part of the valley, and one close to the southern valley entrance (at the positions of slices 'S150' and 'N150' in Fig. 4.1b). At 0830 UTC, both cross-sections show a shallow layer of up-slope flow next to the east-facing slope, which is sun-exposed at that time. The rest of the valley atmosphere is characterized by slow subsidence (on the order of 0.3 m s^{-1}). Two hours later, when both slopes are exposed to direct shortwave solar radiation, the west-facing wall also develops a slope flow layer (not shown). The model output is thus consistent with the 'classical' picture of a symmetric double-circulation. Confirmation with aircraft data, however, is not possible, as the slow subsidence motion is beyond measurement accuracy.

At 1230 UTC the situation changes significantly: the two slices reveal very pronounced circulation patterns of different type. The cross-valley circulation rotates in the counter-clockwise sense in the northern cross-section, and in the clockwise sense in the southern valley entrance region. At this time, the west-facing side is already more sun-exposed than the east-facing slope (Matzinger et al., 2003), meaning that the counter-clockwise circulation pattern of Fig. 4.6c
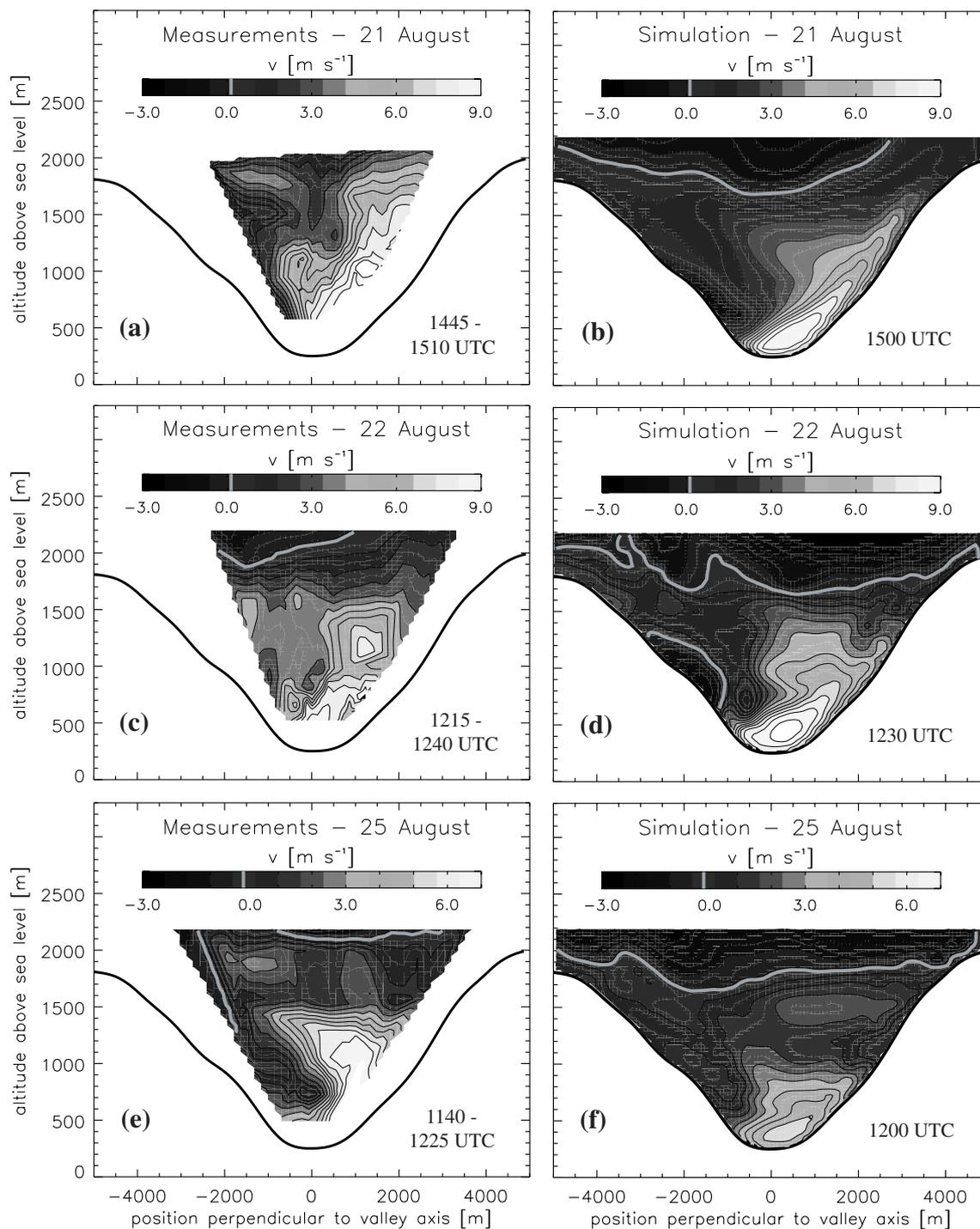
Figure 4.5: *Measured and simulated up-valley wind component in a valley cross-section about 3.5 km north of the southern valley entrance on 21, 22 and 25 August. The panels on the left hand side show airborne data and the panels on the right the corresponding simulation results. The measurement data have been obtained and interpolated from cross-valley flight legs in 8-11 levels of elevation. The grey line is the contour of zero along-valley velocity. Note the different grey scale on 25 August.*
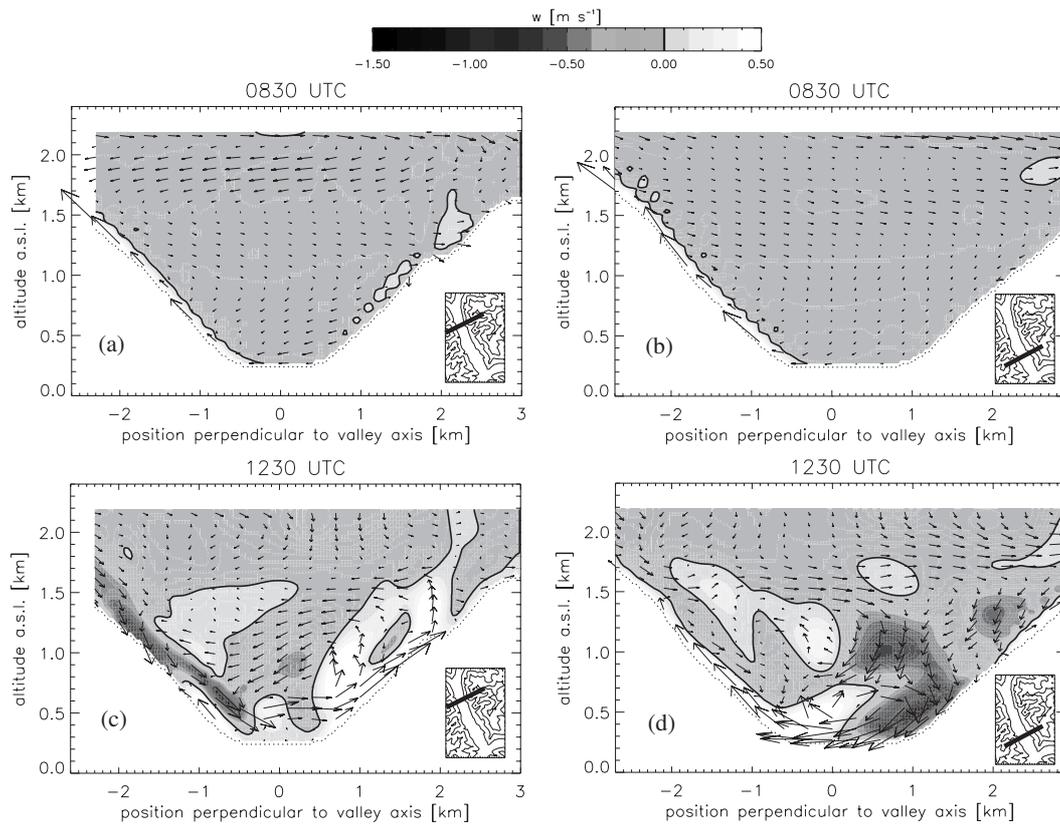
Figure 4.6: *Simulated cross-valley wind vectors on 22 August in two slices across the Riviera Valley (as indicated on the small topography panels): one in the northern half of the valley (a,c), and one close to the southern valley mouth (b,d). The upper panels show the cross-valley flow at 0830 UTC, the lower ones at 1230 UTC. The shading indicates vertical wind velocity. The black line is the contour of zero vertical velocity.*
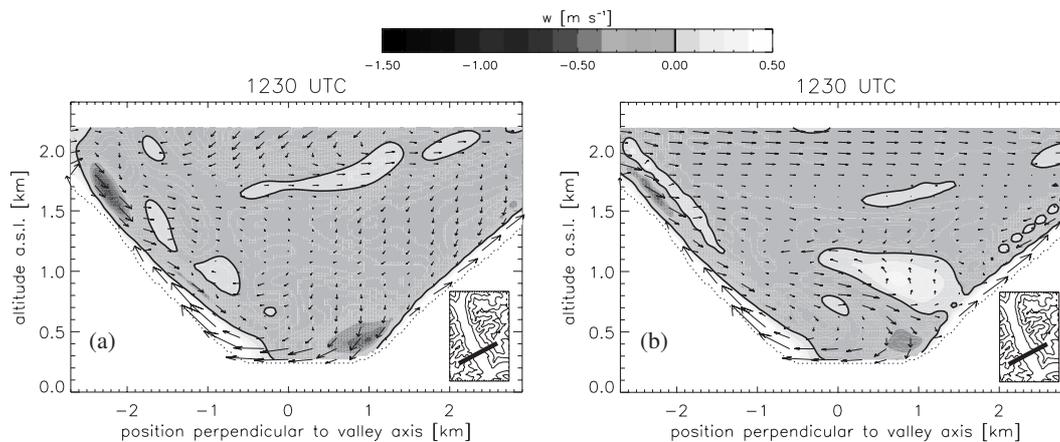
Figure 4.7: *Simulated cross-valley wind vectors in a slice close to the southern valley mouth on 21 August (a) and 25 August (b) at 1230 UTC. The shades of grey indicate vertical wind velocity. The black line is the contour of zero vertical velocity.*
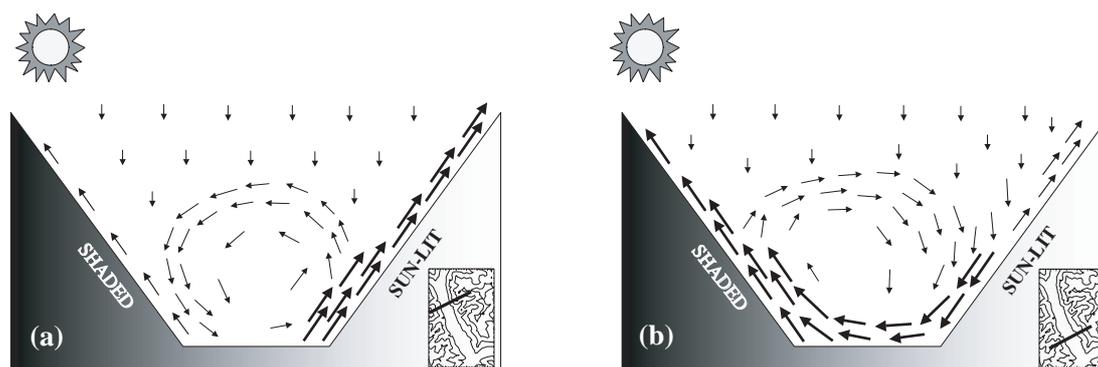
Figure 4.8: *Schematic representation of the afternoon cross-valley flow in two cross-sections in the Riviera Valley (as indicated in the small topography-panels). (a) shows the thermally driven counter-clockwise circulation observed in the northern half of the valley, while (b) displays the curvature-induced clockwise secondary circulation of the southern valley entrance region.*

is the expected thermally driven flow, with air rising along the heated west-facing slope and subsiding on the cooler east-facing side. Interestingly, the situation at the southern slice is reversed, with a strong downward motion on the sun-exposed slope. Fig. 4.7 shows that this surprising phenomenon of an 'anti-thermal' clockwise circulation in the southern valley entrance region is also found on 21 August and 25 August, but on the latter two days a shallow layer of up-slope flow persists on the west-facing wall next to the subsiding air. On all three days, the 'anti-thermal' circulation is very pronounced with vertical velocity magnitudes on the order of 0.5–1 m s^{-1}. Weigel and Rotach (2004)[11] have also identified this structure in the aircraft measurements. They attribute it to the sharp curvature of the streamlines in the valley entrance region, where the up-valley winds flow around a sharp bend to enter the Riviera Valley (see Fig. 4.1a). As is known from curved flows of channeled water (e.g. Rozovskii, 1957; Kalkwijk and Booij, 1986; Geyer, 1993), and as described by Weigel and Rotach (2004), curvature induces a 'secondary circulation' due to local imbalances between counteracting pressure-gradient and centrifugal forces. In the Riviera Valley, the secondary circulation is apparently strong enough to dominate over a counter-clockwise thermally driven circulation which would develop otherwise. The observed coexistence of two distinct and opposed circulation patterns within one valley is schematically summarized in Figure 4.8. A full quantitative evaluation of the momentum budget within these two circulation schemes is intended for a future paper.

4.4 Temperature structure

4.4.1 Profiles of potential temperature over the valley floor

The diurnal evolution of temperature profiles in the Riviera Valley is different from what is typically expected in a convectively forced boundary layer (Weigel and Rotach, 2004). The growth of the well-mixed layer has been observed to consistently cease by noon; sometimes, the valley atmosphere even re-stabilizes almost down to the valley floor despite positive surface heat fluxes. This is, for example, the case in the profiles of Figs. 4.3c and 4.3e - both in the measurements and the simulations. The difference between the atmosphere in the Riviera Valley and a 'normal' convective boundary layer becomes particularly apparent in Fig. 4.9,

---

[11]see Section 2.4.3 of this thesis
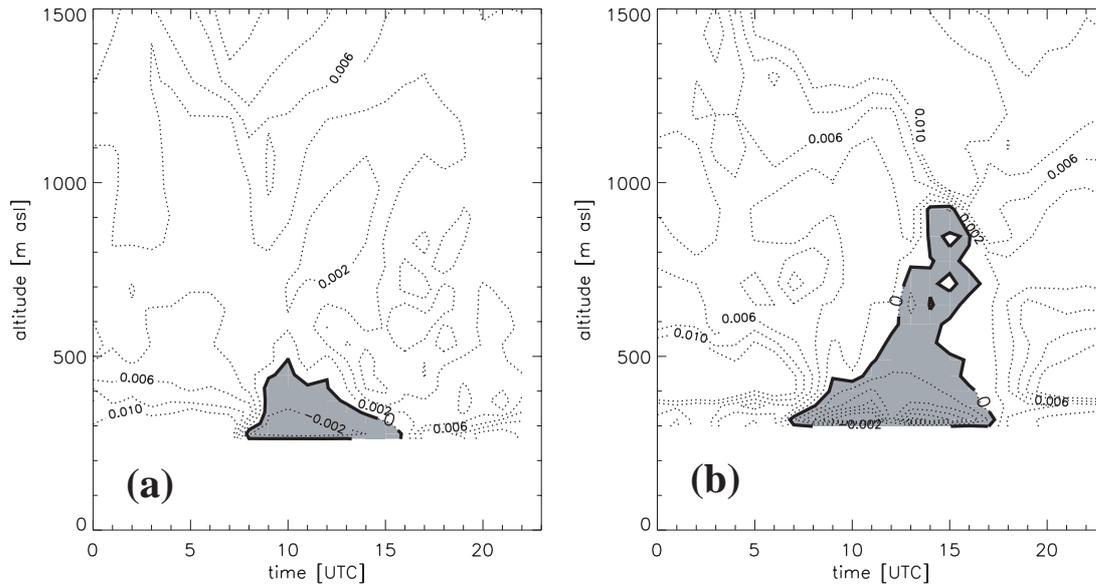
Figure 4.9: *Time-height plots of simulated vertical gradients of potential temperature on 25 August (contours labeled in $K\,m^{-1}$). The shading indicates neutral to super-adiabatic stratification. (a) is in the Riviera Valley (at site A1) and (b) at a location approximately 50 km southwest of the Riviera Valley (45.93° N, 8.77° E), i.e. at the beginning of the foothills of the Alps (obtained from the 1 km grid).*

where time-height plots of modeled gradients of potential temperature on 25 August are shown for soundings in the Riviera Valley and at a location approximately 50 km southwest of the Riviera Valley, i.e. at the beginning of the foothills of the Alps (data obtained from the 1 km grid). While the well-mixed layer stops growing in the Riviera Valley by noon (1000 UTC) and then continuously shrinks, outside the Alps it keeps growing until about 1500 UTC, becoming almost three times as deep as in the Riviera Valley.

Kuwagata and Kimura (1995, 1997) measured and simulated similar behavior in the Ina Valley, Japan, and Rampanelli et al. (2004) observed the same phenomenon in their idealized simulations. In both studies this was attributed to subsidence of warm air from the free atmosphere. From aircraft measurements, Weigel and Rotach (2004) were able to confirm strong heating due to subsidence[12], but the limited temporal and spatial resolution in the observation data did not allow a thorough analysis of the processes leading to the observed thermal structure. This deficiency can now be overcome with ARPS, which has been shown to reproduce well both the general feature of a suppressed mixed layer growth and the complicated flow and circulation structure. The model output can thus be used to analyze the heat budget of the atmosphere over the valley floor and to evaluate the processes which lead to the stabilization of the temperature profiles.

4.4.2   Profiles of heat budget components over the valley floor

To investigate the physical reasons for the inhibited mixed layer growth, the terms of the potential temperature (θ) equation are extracted from the model and analyzed. Neglecting heating due to moist processes (on all three days the simulated valley atmosphere is basically cloud-free on the 350 m grid), this equation reads:

---

[12]see Section 2.4.2 of this thesis

$$\frac{\partial \theta}{\partial t} = -u\frac{\partial \theta}{\partial x} - v\frac{\partial \theta}{\partial y} - w\frac{\partial \theta}{\partial z} - T - R \, . \tag{4.1}$$

The coordinate system is oriented such that the x-axis points cross-valley (normal to the valley axis) and the y-axis is along-valley (aligned with the valley axis). The horizontal wind components, u and v, are defined accordingly. The left hand side of this equation is the overall heating rate. The terms on the right hand side are heating (cooling) due to cross-valley advection of potential temperature, along-valley advection, vertical advection, subfilter-scale turbulent heat flux divergence (T) and radiation flux divergence (R). For greater readability, 'subfilter-scale turbulence' is henceforth simply referred to as 'turbulence'. The overall heating rate, total advection, T and R are directly obtained from the model, and the individual advection components in the valley coordinate system are calculated from the output fields of velocity and potential temperature.

Figure 4.10a shows the profiles of the heating (cooling) contribution terms of Eq. (1) on the late morning of 21 August. The profiles are averaged over 90 minutes (centered at 0945 UTC) over the valley floor width in slice 'S150' (shown in Fig. 4.1b; 'S' refers to the location of the slice in the southern valley half, and '150' to data with horizontal grid spacing of 150 m). The individual contributions of the three advection components in the valley coordinate system are shown in Fig. 4.10b. Radiation flux divergence is not plotted, as its contribution to the total heat budget was found to be negligibly small. It can be seen that the valley atmosphere experiences a net warming over the whole valley depth and up to about 2500 m. The warming is almost entirely due to vertical advection, apart from the lowest 100 m where turbulent heat flux divergence is the dominant heating source. The net heating rate has its maximum ($5 \cdot 10^{-4}$ K s^{-1}) close to the ground. On the mornings of the 22nd and the 25th of August, the profiles of the heat budget components reveal the same behavior (not shown). Analogous calculations have been carried out in a second slice in the northern half of the valley ('N150', see Fig. 4.1b), yielding equivalent results (not shown). This is not surprising, because the different circulation patterns illustrated in Fig. 4.8 are not yet established in the late morning, i.e. S150 and N150 are characterized by similar flow conditions.

Afternoon profiles (averaged over 90 minutes, centered at 1245 UTC) of the heat budget components in slice S150 on the three simulation days are displayed in Fig. 4.11 together with the corresponding advection components. As in the morning profiles, the valley atmosphere experiences a relatively homogenous net heating rate through almost the entire valley depth. Its magnitude is on the order of $2 \cdot 10^{-4}$ K s^{-1}, but in contrast to the morning situation, the heating rate is lower rather than higher close to the ground (on the order of 0.5-1.5 $\cdot 10^{-4}$ K s^{-1} in the lowest 200 - 300 m above surface). Turbulent heat flux divergence dominates as a source of heating in this close-to-surface layer, which hereafter will be referred to as the TFDL (turbulent flux divergence layer). The strong turbulent heating in the TFDL is almost entirely balanced by advective cooling, resulting in a comparatively small net heating rate. The advective cooling in the TFDL is mainly due to vertical advection, partially also due to along-valley advection (Figs. 4.11d-4.11f). Above the TFDL, the sign of the vertical advection changes, and it becomes the main contributor to the net heating rate, strong enough to offset the cooling effect of horizontal (mainly along-valley) advection. This is particularly evident in Fig. 4.11e. Except for on 22 August, cross-valley advection is mostly negative and of smaller magnitude than the other advection components.

Through most of the valley atmosphere, the corresponding profiles of the heat budget components in slice N150 reveal characteristics similar to those in S150. This is shown here for the example of 22 August (Fig. 4.12). As in S150, heating due to turbulent flux divergence is re-

S150: HEAT BUDGET   **S150: ADVECTION**

Figure 4.10: *Simulated profiles of (a) the heat budget contributions and (b) the respective advection terms in the valley coordinate system on the **late morning** of 21 August. The profiles are 90-minutes averages (centered at 0945 UTC) over the valley base width in slice **S150** (see Fig. 4.1b). The grey bar indicates the crest height.*

stricted to a shallow TFDL at the surface, and vertical advection is the dominant heating source through the rest of the valley atmosphere, i.e. above the TFDL, balancing the strong advective cooling in the along-valley direction. In the TFDL, however, all three advection components have opposite sign between N150 and S150, and the net heating rate at N150 is about twice as large as at S150 ($2 \cdot 10^{-4}$ K s^{-1} instead of $1 \cdot 10^{-4}$ K s^{-1}). The same behavior is observed on 21 and 25 August (not shown). The larger overall heating rate in the TFDL of slice N150 compared to S150 appears to be primarily due to the fact that in N150 vertical advection does not become negative and thus does not contribute to the net advective cooling.

4.4.3   Discussion

One of the most notable features of the heat budget analysis is the almost uniform heating rate through the upper three quarters of the valley atmosphere. In the morning (Fig. 4.10) the air next to the surface experiences the highest heating rate, eventually leading to destabilization and thus to the growth of a well-mixed layer. In the afternoon, the net heating rate at the ground is significantly reduced compared to the morning. It is still positive, but its magnitude is comparable to, and in the southern valley half even lower than, the relatively uniform 'background' heating through the rest of the valley atmosphere (Fig. 4.11 and 4.12). In such a situation, further destabilization of the surface air which would further enhance convective mixing is not possible. Our observation of a suppressed mixed-layer growth in the afternoons (Section 4.4.1) is thus reflected in the profiles of net heating rate. To understand this behavior, two aspects

S150:   HEAT BUDGET

net heating rate ———
total advection +·········+
turbulent flux div. ✳– – –✳

(a) 21 August 1245 UTC

(b) 22 August 1245 UTC

(c) 25 August 1245 UTC

heating rate [10^{-3} K s^{-1}]

S150:   ADVECTION

along–valley adv. ◇———◇
cross–valley adv. ✕·········✕
vertical advection △– – –△

(d) 21 August 1245 UTC

(e) 22 August 1245 UTC

(f) 25 August 1245 UTC

heating rate [10^{-3} K s^{-1}]

Figure 4.11: *Simulated profiles of the heat budget contributions (upper row) and the respective advection terms in the valley coordinate system (lower row) on the* **afternoons** *of 21 August (a,d), 22 August (b,e) and 25 August (c,f). The profiles are 90-minutes averages (centered at 1245* UTC*) over the valley base width in slice* **S150** *(see Fig. 4.1b). The grey bar indicates the crest height.*

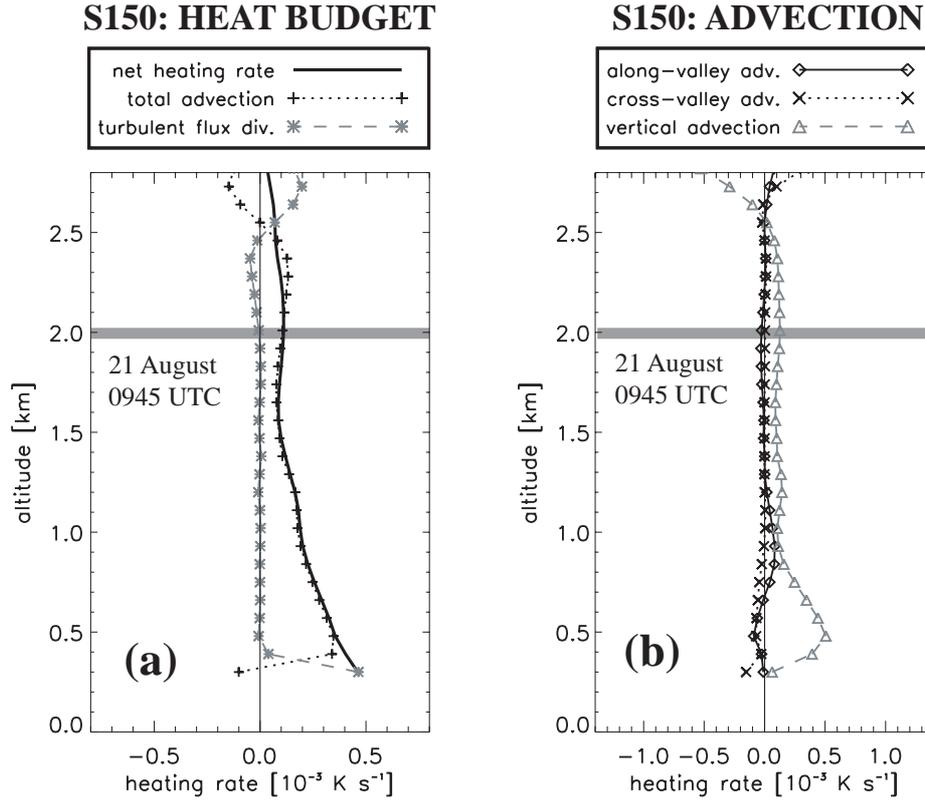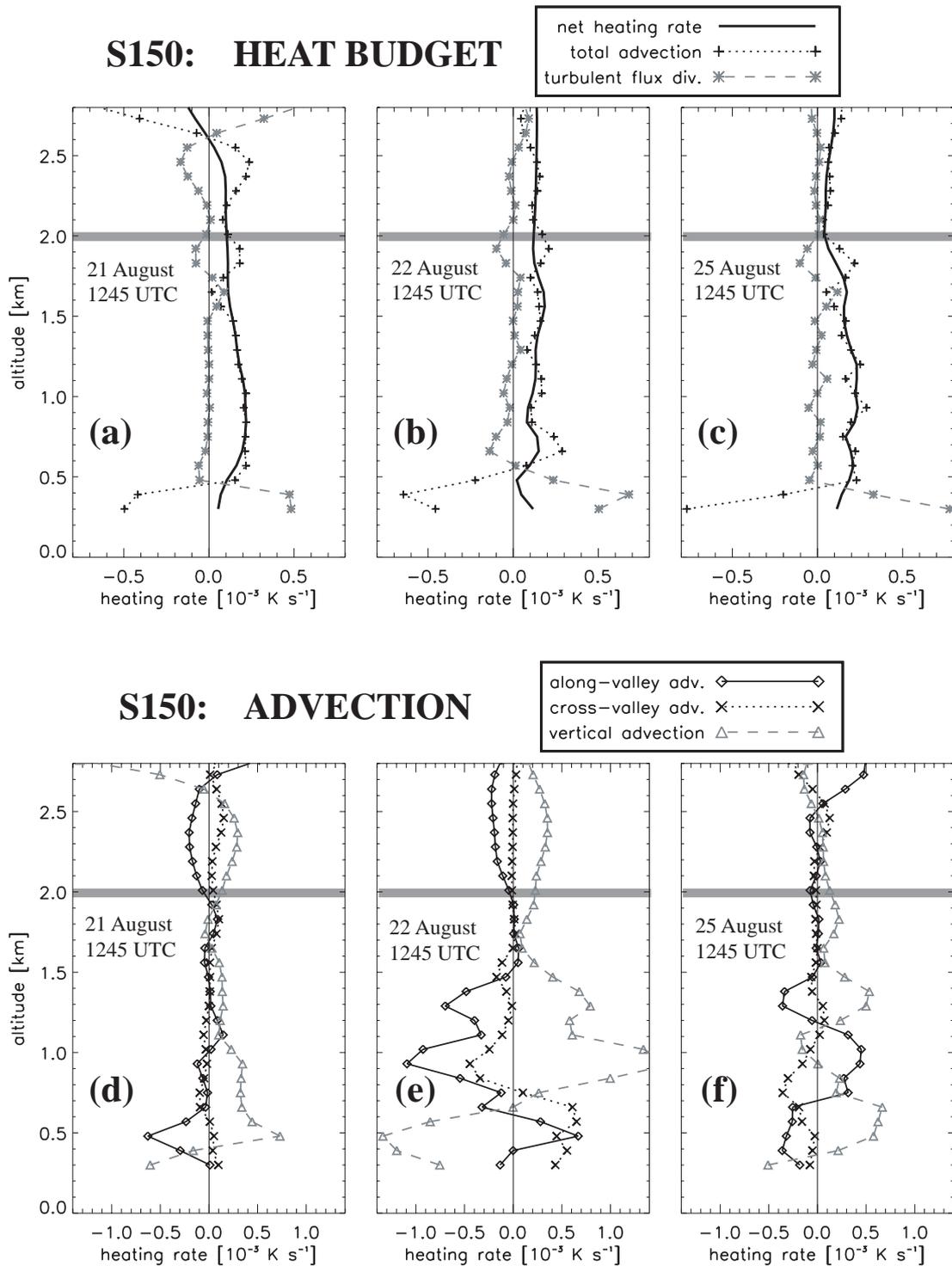**N150: HEAT BUDGET**   **N150: ADVECTION**
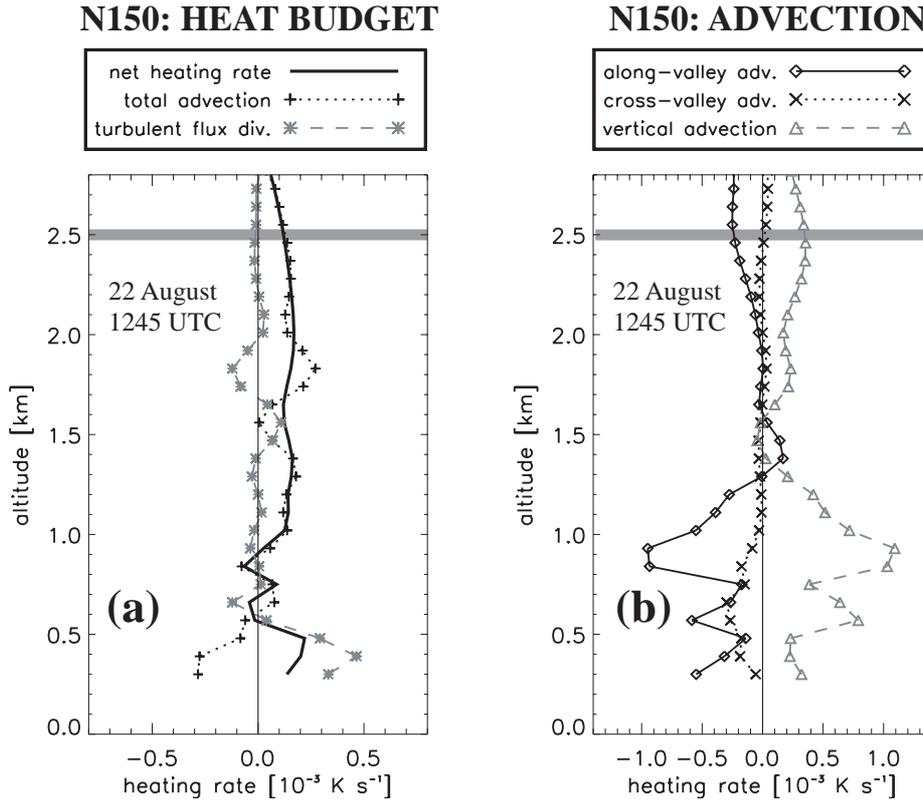
Figure 4.12: *Simulated profiles of the heat budget contributions (a) and the respective advection terms in the valley coordinate system (b) on the **afternoon** of 22 August. The profiles are 90-minutes averages (centered at 1245 UTC) over the valley base width in slice **N150** (see Fig. 4.1b). The grey bar indicates the crest height.*

need to be considered: (a) the positive uniform heating rate over almost the entire valley depth, and (b) the reduced heating rate on the surface despite positive surface heat fluxes.

The first aspect is clearly attributed to the subsidence of potentially warmer air (i.e., air with a higher potential temperature). Consistent with the idealized simulations of Rampanelli et al. (2004), this can be explained by the existence of slope winds. Air is carried out of the valley along the slopes and replaced by subsiding air in the valley center. The slope winds actually overshoot into the free atmosphere. This is shown for 21 August in Fig. 4.13, which shows contours of vertical velocity in a slice across the ridge east of surface station A1. Boundary layer air is vented into the free atmosphere in the manner described for example by Kossmann et al. (1999) or Henne et al. (2004). This explains why the subsidence heating dominates well above the crest height. Mountain venting begins in the morning hours, which is consistent with the observations of De Wekker et al. (2004) in the Jungfraujoch region in central Switzerland.

The other aspect leading to the observed stabilization of the valley atmosphere is the reduced net surface heating, which becomes effective in the afternoon once the strong up-valley winds have started. Being thermally driven, these winds advect potentially colder air up the valley axis. Above the TFDL, subsidence is strong enough to balance the cooling effect of the valley winds, resulting in a net positive advective heating contribution. Within the TFDL, the process appears to be more complicated, and a distinction needs to be made between the effects of the different flow and circulation patterns described in Section 4.3.

In slice N150, the up-valley wind is uniformly spread over the valley floor. The wind speed and thus the cooling next to the ground are relatively large (on the order of $5 \cdot 10^{-4}$ K s^{-1}
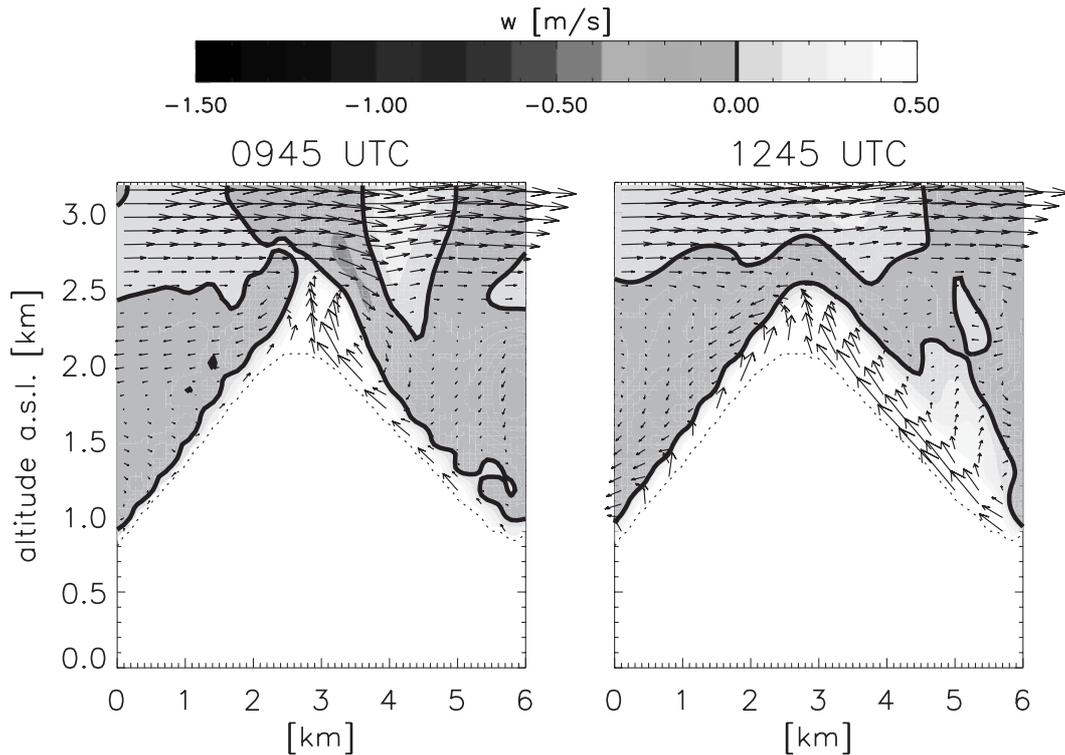
Figure 4.13: *Simulated flow structure in a vertical slice across the ridge east of surface station A1, showing the venting of boundary layer air into the free atmosphere on 21 August at (a) 0945* UTC *and (b) 1245* UTC. *The contours indicate vertical wind velocity, with the black line being zero vertical velocity.*

on all three simulation days). Moreover, the thermally-driven cross-valley circulation carries near-surface air from the shaded east-facing slope to the sunlit west-facing side, thus providing additional cooling. Close to the surface, subsidence heating is not strong enough to balance these cooling contributions. In slice S150, the situation is different: as has been explained in Section 4.3, the core of the valley wind is pushed from the valley center to the right over the sunlit heated west-facing slope. Thus, in the valley center, the cooling due to along-valley advection is reduced compared to N150. It can even be of opposite sign (Fig. 4.11e), because north of S150 the cold up-valley jet tends to meander back towards the valley center, leading to locally negative gradients in potential temperature in the along-valley direction. The curvature-induced clockwise secondary circulation, if strong enough, can lead to cross-valley advective heating, as the near-surface cross-valley flow comes from the west-facing sunlit slope (Figs. 4.11d,e). Moreover, this circulation advects potentially colder air from the 'lifted' core of the up-valley jet down to the ground (Fig. 4.6d and 4.7), resulting in the strong negative vertical advection which is observed on all three days in the TFDL (Figs. 4.11d-4.11f).

The lower surface heating rates in slice S150 compared to N150 show that the secondary circulation is a strong mechanism for surface-cooling, stronger than the 'undisturbed' along-valley advection of potentially colder air in slice N150. Consequently, the depth of the atmospheric boundary layer in the Rivera Valley is highly dependent on the exact position in the valley and the local circulation structure. Figure 4.14 shows the variation of well-mixed layer thickness in the along-valley direction, as obtained on 22 August at 1245 UTC on the 350 m grid. The position-dependent differences between the southern and the northern part of the valley are apparent. In the northern part of the valley, the well-mixed layer (shaded area) is only about 200 m thick; however, in the southern part, under the influence of the curvature-induced
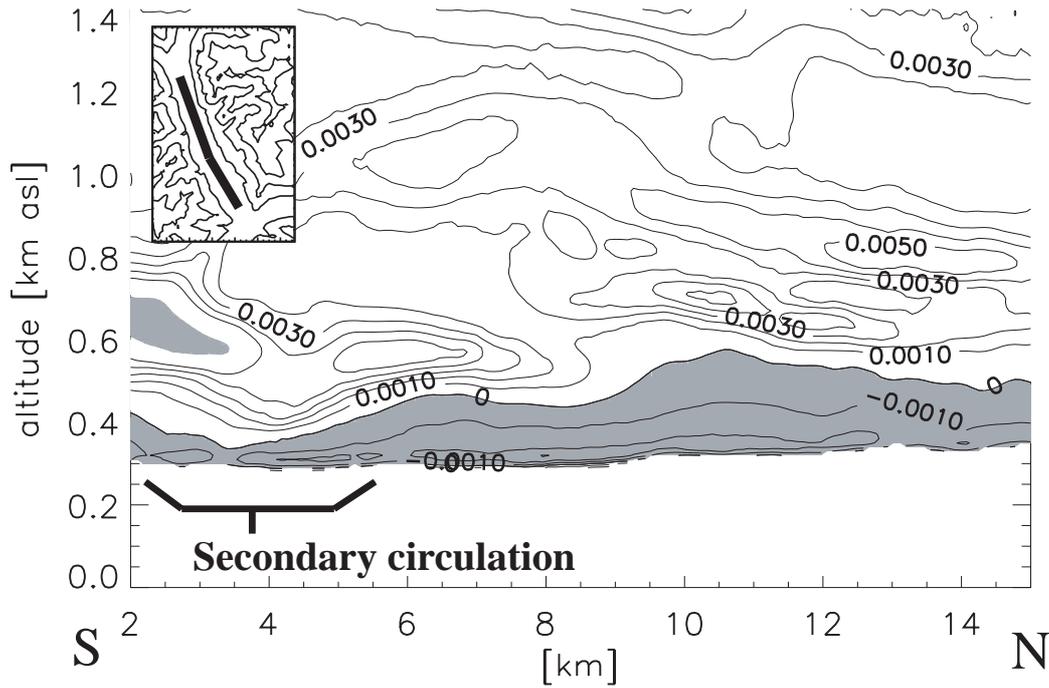
Figure 4.14: *Variation of well-mixed layer thickness in the along-valley direction on 22 August at 1245* UTC *as simulated with ARPS. The contours (labeled in $K\,m^{-1}$) show the vertical gradient of potential temperature, with areas of neutral or super-adiabatic stratification being shaded in grey. The position of the secondary circulation is indicated. Along-valley distance has an arbitrary origin at the town of Bellinzona (Fig. 4.1).*

secondary circulation, it is even shallower (50-100 m). The same qualitative picture holds on 21 and 25 August. Due to its high spatial variability, the thickness of the well-mixed layer, as measurable from radiosondes (i.e. at a given location), is thus not a representative length scale for the atmospheric boundary layer in the entire valley.

4.5   Total heat budget

4.5.1   Time evolution of the valley heat budget

Finally, we examine the processes which contribute to the heating of the Riviera Valley atmosphere as a whole, and thus ultimately determine the onset and strength of valley winds (if we assume them to be purely thermally driven). We therefore extend our analysis to a larger volume on the 350 m simulation grid which contains the major part of the Riviera Valley. We have chosen volume V350, as outlined in Fig. 4.1a, for the integration volume. The east and west boundaries of the volume are chosen such that they approximately follow the two ridge-lines which frame the valley. On the 350 m grid, the altitude of these two ridges varies between approximately 2000 m and 2500 m. The depth of volume V350 extends from the valley floor up to an altitude of 2000 m. The north and south boundaries of V350 are set locally perpendicular to the valley axis.

The volume-averaged and density-weighted heat budget components are calculated accord-

ing to following equation, which is based on Eq. 4.1:

$$
\underbrace{\frac{1}{M_V} \cdot \iiint_{V350} \rho \cdot \frac{\partial \theta}{\partial t}\, dV}_{\text{net heating rate}} = \underbrace{-\frac{1}{M_V} \cdot \iiint_{V350} \rho \left(u\frac{\partial \theta}{\partial x} + v\frac{\partial \theta}{\partial y} + w\frac{\partial \theta}{\partial z} \right) dV}_{\text{total advection}} +
$$

$$
\underbrace{-\frac{1}{M_V} \cdot \iiint_{V350} \rho \cdot T\, dV}_{\text{turb. heat flux div.}} - \underbrace{\frac{1}{M_V} \cdot \iiint_{V350} \rho \cdot R\, dV}_{\text{radiation flux div.}} .
$$

$$(4.2)$$

M_V is the total mass of air in V350, and ρ is the density. The time-series of the heat budget components in volume V350 on 21 August are shown in Fig. 4.15. Similar to earlier plots, the individual advection components in the valley coordinate system are displayed separately. In Fig. 4.15a, it can be seen that the dominant source of heating is turbulent heat flux divergence. This result is plausible, because turbulent flux divergence has to balance the total surface heat flux, but it appears to be contradictory to the findings of Section 4.4.3, where the shallowness of the TFDL and the large vertical advective heating over the valley base were emphasized. The paradox can be understood by recalling that the valley side-walls are not contained in slices S150 and N150, but are included here in V350. Over the slopes, turbulent heat flux divergence is consistently strong and positive (not shown), while the heat budget contribution of vertical advection is mainly negative (due to up-slope winds). This means that, averaged over V350, turbulent heat flux divergence gains in importance with respect to vertical advective heating.

The daytime evolution of turbulent heat flux divergence smoothly follows the pattern of incoming solar radiation. The maximum ($1.5 \cdot 10^{-4}$ K s^{-1}) occurs at around 1230 UTC. Radiation flux divergence, on the other hand, is almost negligible. Total advection, finally, is only the dominant source of heating until about 0900 UTC. After that, it quickly decreases and changes sign at about 1100 UTC. Its maximum is only half the magnitude of the maximum turbulent flux divergence. The advection components in the valley coordinate system (Fig. 4.15b) show that vertical and along-valley advection are of considerable magnitude, while cross-valley advection is relatively small. Vertical advection is a constant source of heating until about 1600 UTC, while along-valley advection continuously cools the valley. Net cooling begins at approximately 1600 UTC.

The results obtained for 22 August (Fig. 4.16) and 25 August (Fig. 4.17) generally follow 21 August apart from a few details. On 22 August, the magnitude of turbulent flux divergence is larger than on 21 August (achieving a maximum value of $2 \cdot 10^{-4}$ K s^{-1}), while total advection is comparatively weak. It dominates over turbulent flux divergence only until about 0800 UTC and does not exceed a maximum heating rate of $0.5 \cdot 10^{-4}$ K s^{-1}. On 25 August, on the other hand, advection is very strong and dominant (on the order of $1.5 \cdot 10^{-4}$ K s^{-1}) until about 0900 UTC before it drops sharply and changes sign.

An analysis of the along-valley variability of the heat budget components (not shown) reveals that the observed characteristics are relatively independent of the circulation regime in the lower valley atmosphere. This means that the overall valley heat budget is not significantly affected by the sense of rotation of the underlying cross-valley circulation, i.e. on whether the circulation is thermally driven or curvature-induced.
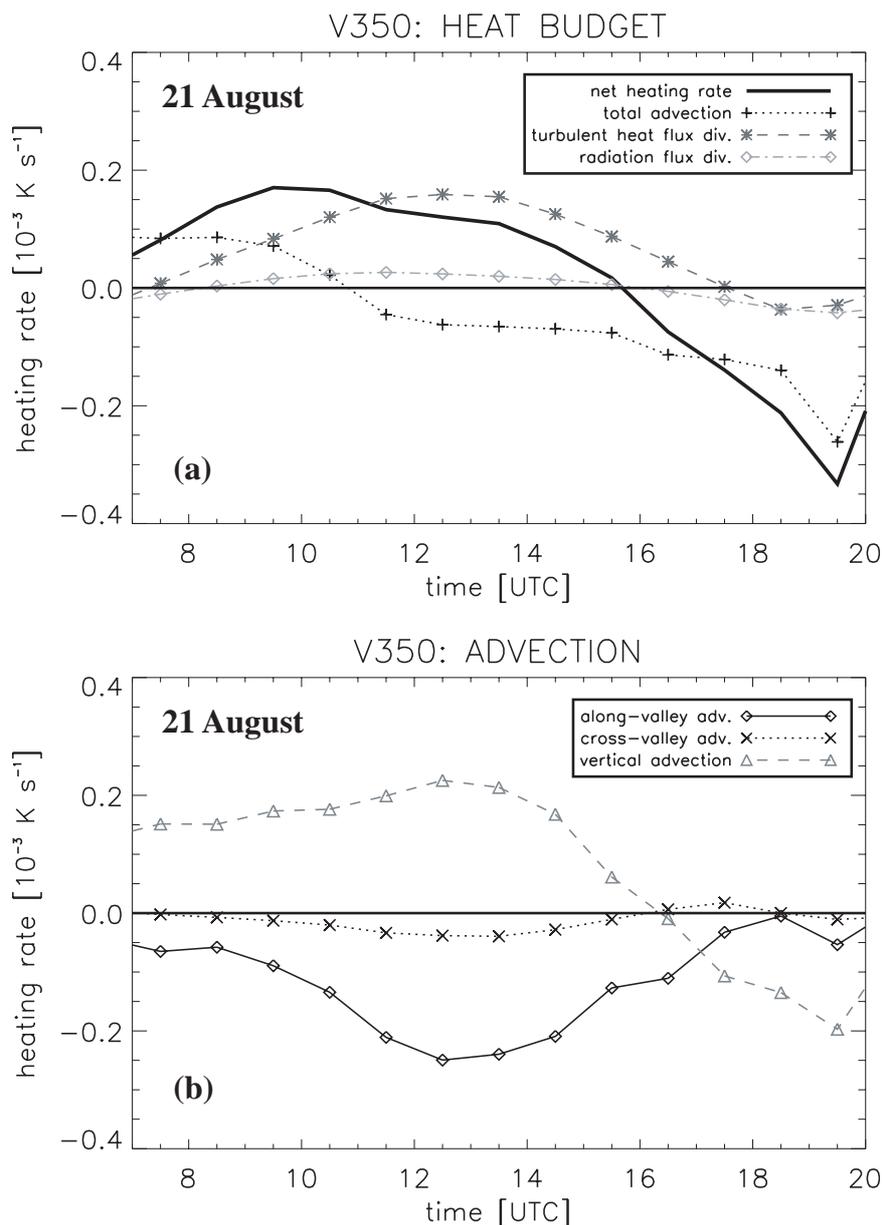
Figure 4.15: *Time-series from simulations of (a) the heat budget components and (b) the advection components on 21 August, averaged over V350 on the 350 m grid (see Fig. 4.1b).*

4.5.2 Discussion

The volume argument of the TAF concept implies that no heat is exchanged with the free atmosphere above the valley, meaning that the valley atmosphere heats entirely due to turbulent heat flux divergence, because advection would only redistribute heat within a closed circulation. If we assume negligible variation of density with time (justified in the frame of the shallow motion approximations, Mahrt, 1986), and if we assume the volume argument to hold, then the sum of vertical and cross-valley advection must be zero. The heat budget analysis has shown that turbulent flux divergence (averaged over V350) is indeed an important contributor to the overall heating rate. Vertical advection, however, is also consistently positive (until about 16-17 UTC) and has a magnitude which is on the order of or even larger than the effect of turbulent heat flux divergence. Cross-valley advection is negative, but has only a comparatively small magnitude, meaning that the sum of vertical and cross-valley advection is positive and clearly
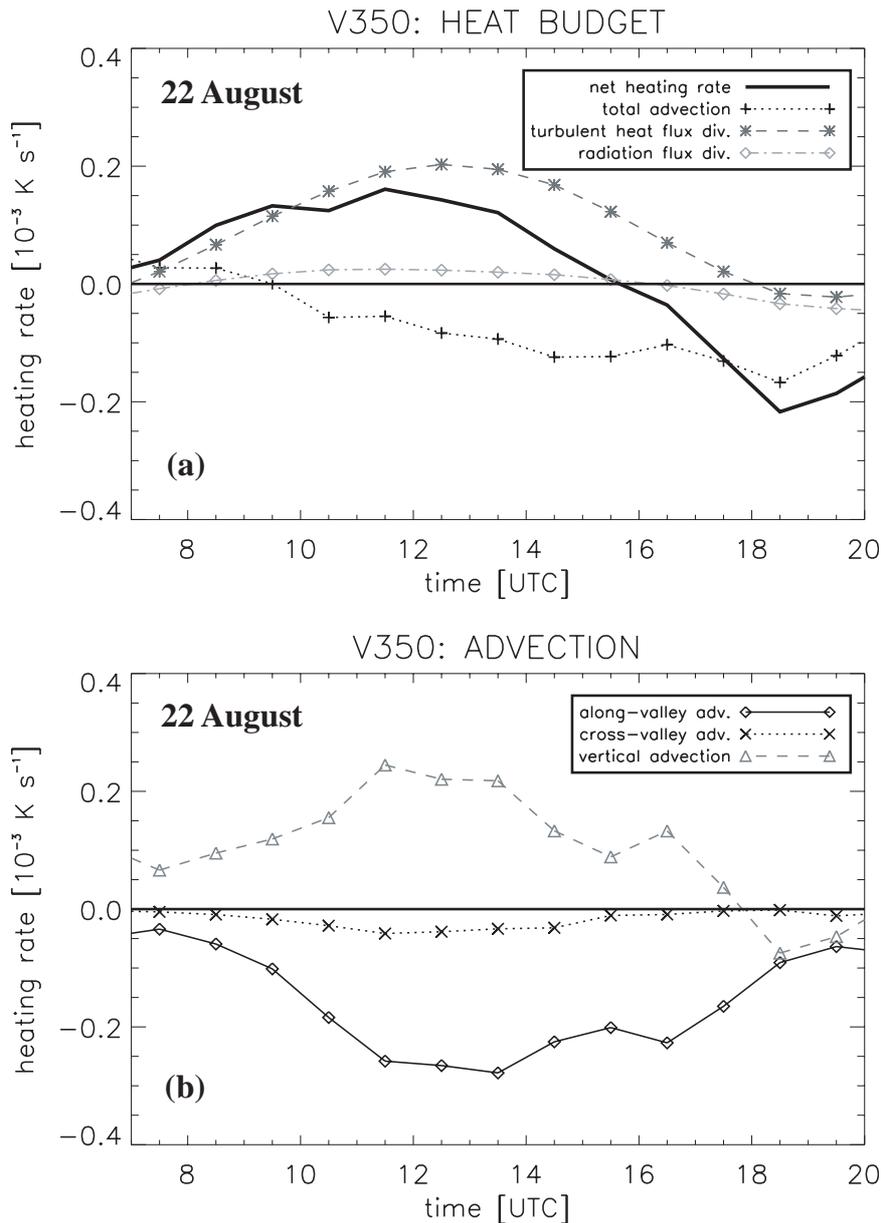
Figure 4.16: *As Fig. 4.15, but for 22 August.*

non-zero. This can only be explained by subsidence of potentially warmer air from the free atmosphere through the valley top (as proposed in Section 4.4.3), which violates the volume argument of the TAF concept. Given the strong cooling due to along-valley advection, the net heating rate and thus the valley temperature would be lower without the effect of subsidence heating. This would lead to a reduced valley-plain temperature gradient and thus weaker up-valley winds.

In the case of significant net vertical export of valley air through the upper boundary of V350, the vertical advection term in the heat budget becomes negative. This is for example the case on 21 August after 1630 UTC, when a mass budget analysis (not shown) reveals strong vertical mass fluxes on the order of 0.07 kg s^{-1} m^{-2}. North of the Riviera Valley, i.e. closer towards the central Alps, the valleys become smaller and are characterized by significantly sloped floors and decreasing widths. Consistent with classical valley flow theory, strong rising motions can be expected in such narrowing valleys during up-valley flow periods, connecting
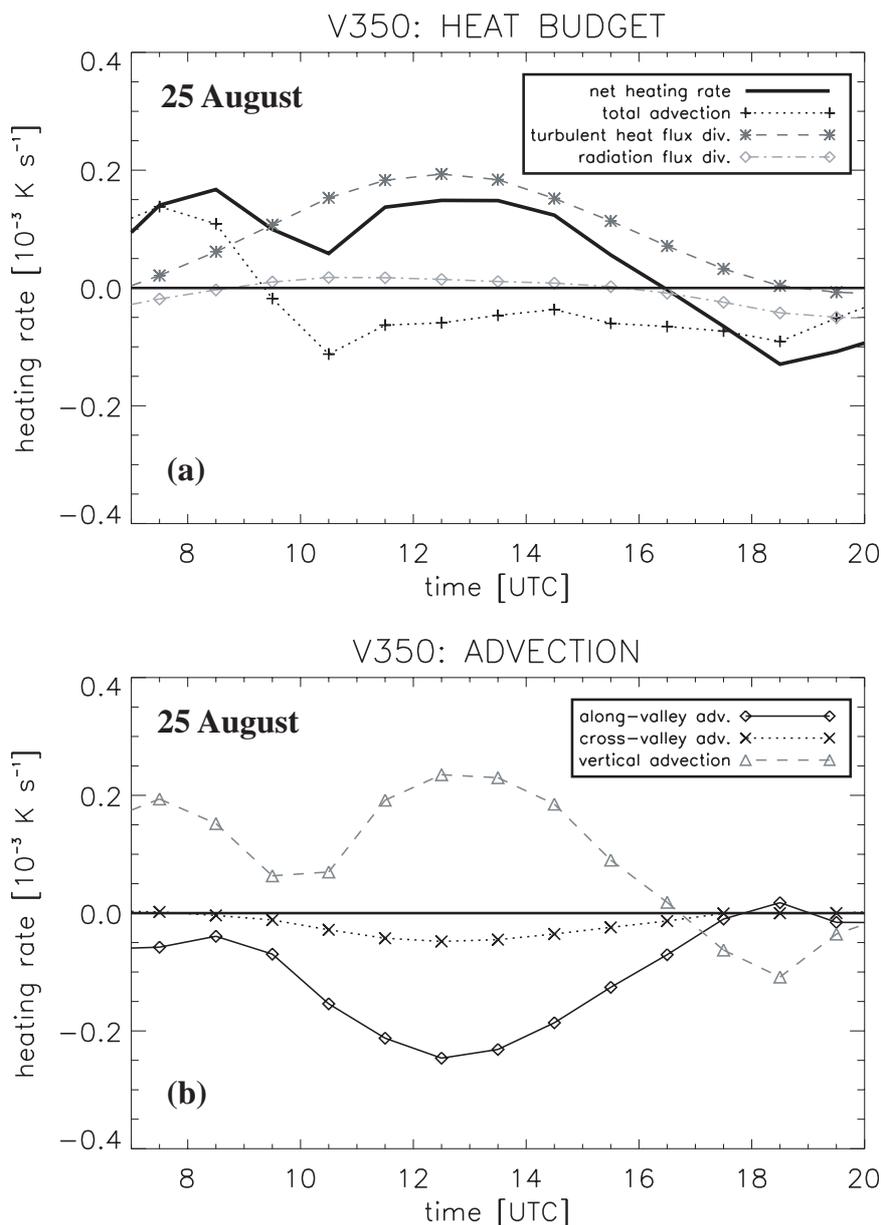
Figure 4.17: *As Fig. 4.15, but for 25 August.*

the flow layer within the valleys with a larger-scale return flow layer above. This means that once valley winds have started, the heat budgets in those valleys may well be different from our Riviera Valley observations.

We now evaluate the structure of the heat budget in the hours before the onset of up-valley winds in the morning, i.e. before 0900-1000 UTC. On 21 and 25 August, advective heating (solely due to subsidence) rather than turbulent flux divergence is the dominant contributor to the net heating rate during this time. Therefore, on these two days the warming of the Riviera atmosphere appears to support the concept of Rampanelli et al. (2004), according to which subsidence leads to the heating necessary for the development of thermally driven up-valley winds. On the morning of 22 August, the situation is less clear, as subsidence is relatively low and turbulent flux divergence dominates over net advective heating from about 0730 UTC. This means that on this day the up-valley winds are probably initiated due to a combination of subsidence heating and turbulence heating.

The strength of subsidence heating itself is determined by two factors: the subsidence velocity and the stratification of the valley atmosphere. On 21 and 22 August, the average gradients of potential temperature in the valley atmosphere at 0800 UTC are of comparable magnitude (around 0.004 $K\,m^{-1}$), but the subsidence velocity is higher on 21 August (0.05 $m\,s^{-1}$) than on 22 August (0.03 $m\,s^{-1}$), explaining the stronger subsidence heating on 21 August. Comparable subsidence velocities are found on 22 and 25 August, but 25 August is much more stably stratified (0.0066 $K\,m^{-1}$). Due to the larger vertical gradient of potential temperature, 25 August experiences more subsidence heating than 22 August. To quantify the effect of subsidence heating in the general case, it would be necessary to analyze the factors determining the strength of the slope flows and thus of subsidence velocity. This has not been done here, but aspects such as Bowen ratio, stability (Whiteman et al., 2004) and the mixing of momentum from the top of the valley (Egger, 1990) are expected to be of importance in this context.

4.6 Summary and conclusions

The LES-code 'ARPS' has been applied to simulate and investigate the daytime atmosphere in the Riviera Valley on three summer days with fair weather conditions and pronounced thermally driven up-valley winds. The performance of the code has been evaluated with comparisons to data from the MAP-Riviera field campaign. From our work, we can conclude that ARPS is able to reproduce both the thermal and dynamic features of the atmosphere over topography as steep and complex as the Riviera Valley. This not only refers to the stratification and surface winds (shown in Part I by Chow et al., 2005b), as the model also captures very distinct circulation patterns. These patterns have been identified from airborne measurements and include thermally driven cross-valley circulations as well as a curvature-induced secondary circulation at the southern valley mouth (summarized in Fig. 4.8). Given the good performance of ARPS, the components contributing to the heat budgets have been investigated. The major findings can be summarized as follows:

(i) The growth of a well-mixed layer in the Riviera Valley is suppressed (Fig. 4.9). Despite positive surface heat fluxes, the valley atmosphere has a tendency to stabilize. Turbulent heat flux divergence as a source of heating is restricted to a shallow layer of only 100-300 m depth above the ground and the slopes. These observations are due to the combined effect of cold-air advection in the up-valley direction and subsidence of warm air from the free atmosphere aloft (Fig. 4.12b). The subsidence is a consequence of thermally driven slope winds.

(ii) The existence of a curvature-induced secondary circulation in the southern half of the valley further stabilizes the near-surface valley atmosphere compared to the northern valley half. Consequently, the well-mixed layer can vary considerably in depth along the valley, depending on the geographic position and the overlying circulation pattern (Fig. 4.14). Therefore, the mixed-layer depth, as obtained from point measurements (e.g. from radiosondes), is not a representative length scale for the atmospheric boundary layer of the entire valley.

(iii) Subsidence of warm air from the free atmosphere above the valley is one of the main heating sources in the heat budget of the entire valley atmosphere (Figs. 4.15, 4.16, 4.17). Subsidence heating typically reaches about $2 \cdot 10^{-4}\ K\,s^{-1}$ in mid-afternoon and is of comparable or even larger magnitude than turbulent heat flux divergence. It compensates for most of the cooling due to along-valley advection. Therefore, a positive net heating rate can be maintained throughout the afternoon. This is a prerequisite for the persistence of valley-plain temperature gradients and thus of strong thermally driven up-valley winds until the evening.

(iv) On the mornings of two out of the three observation days, subsidence has been identified

as the *only* major heating source of the valley atmosphere prior to the onset of valley-winds (Figs. 4.15 and 4.17). Thus, the build-up of a valley-plain temperature gradient cannot be explained by the 'topographic amplification factor' concept alone, at least not in the Riviera Valley. Our observations support the subsidence concept of Rampanelli et al. (2004) as an essential mechanism of valley warming.

These conclusions are solely drawn from an analysis of the processes in the Riviera Valley, which is part of a large and widely branched valley system. As the Riviera Valley is located in the center of this valley system and is of medium size, the processes observed in the Riviera Valley are likely to be similar to those found in other valleys of the system, as long as the flow conditions are comparable. Nevertheless, it would be desirable to carry out a comparable heat budget analysis on the entire valley system. Moreover, in order to quantify and generalize the relevance of subsidence heating, a thorough analysis of the factors determining the strength of cross-valley circulations under real conditions is necessary. LES has been shown to be a useful tool in this context.

Acknowledgments

Chapter 5

TKE production in the Riviera Valley

5.1 Introduction

In Section 2.5 we have described the turbulence characteristics of the Riviera Valley as obtained from aircraft measurements on clear-sky days. We saw that profiles of turbulent kinetic energy (TKE) scale surprisingly well if (i) a TKE threshold criterion (TKE > 0.5 m^2s^{-2}) is employed as a definition of the boundary layer height and (ii) if the surface fluxes from the sun-lit slope sites are used rather than those from directly beneath the profile considered (see Fig. 2.14). An explanation of this phenomenon, however, was not provided. While it is well-known that the dominant forcing mechanisms can have a big impact on the turbulence structure (e.g. Deardorff, 1972; Mason, 1992), from the observation data presented in Section 2.5 it remained unclear how turbulence is produced in the Riviera Valley and whether the turbulence structure is only *related to* or actually *determined by* the surface heat fluxes on the eastern slope. This chapter addresses these open questions by evaluating ARPS output data for August 21, 22 and 25, the three simulation days previously described in Chapters 3 and 4.

In the next section, the model TKE results are presented and compared to the corresponding airborne measurement data. In Section 5.3, the TKE budget is evaluated and the mechanisms of TKE production in the Riviera Valley are elaborated and discussed.

5.2 TKE from ARPS output data

5.2.1 Resolved TKE and subgrid-scale TKE

The calculation of turbulence quantities from LES output data requires a distinction between parameterized subgrid-scale (SGS) turbulence and resolved turbulence. While SGS turbulence is directly obtained from the LES closure, resolved turbulence needs to be explicitly calculated from the output velocity fields. The latter requires the definition of a cut-off length scale or time scale.

In our simulations, a 1.5-order TKE closure (Deardorff, 1980; Moeng, 1984) is used, meaning that a prognostic (SGS) TKE equation is solved. Resolved TKE, on the other hand, is determined by a procedure similar to that used for the evaluation of the airborne data (see Section 2.5.1). Space-series of the three velocity components are extracted from ARPS output data along the valley axis and filtered with the recursive low-pass filter of McMillen (1988) in order to obtain the turbulent fluctuations of the velocity field. Resolved turbulence is then calculated by means of eddy-correlation. For the evaluation of the aircraft measurements, a filter constant

of $\tau_a = 24$ s was chosen (Section 2.5.1). Given a typical aircraft velocity of 50 m s^{-1}, this corresponds to a length scale of 1200 m. Therefore, to be consistent with the aircraft measurements, the simulated space-series are filtered using a filtering-width of 1200 m.

Fig. 5.1 shows typical profiles of TKE from the model output at 1200 and 1500 UTC on the three simulation days. Both SGS TKE and total TKE (= SGS TKE + resolved TKE) are displayed. All profiles reveal a qualitatively similar behavior with very pronounced maxima at an altitude of 300–700 m. The magnitude of these maxima, however, exhibits a distinct day-to-day variability, with 25 August revealing the lowest TKE values (about 0.6 m^2 s^{-2}) and 22 August the highest ones (up to 2.1 m^2 s^{-2} at 1500 UTC). Above these maxima, TKE decreases sharply and approaches zero at altitudes between 700 m (25 August) and 2000 m (22 August). Both on 21 and 22 August, TKE is larger at 1500 UTC than at 1200 UTC. On 25 August, the magnitudes remain relatively constant.

SGS TKE makes up approximately 50-80% of total TKE. On all three days, the vertical structure of total TKE, particularly the pronounced maximum, is mainly determined by the shape of the profiles of SGS TKE, while resolved TKE, i.e. the difference between total TKE and SGS TKE, shows less variation with height.

5.2.2 Comparison to measurements

Simulated profiles of total TKE are compared to airborne measurements in Fig. 5.2. The measurement data are obtained from flight-paths no. 1-6 (in ascending order) as described in Table 2.2. Note that each flight-path had a duration of typically 60-90 minutes. The simulated profiles are extracted from ARPS output data at the times indicated in the header to each panel, i.e. well within the time-intervals of the corresponding flight-paths. The measured profiles of TKE differ significantly from the ARPS output. Their magnitudes are larger, particularly in elevations above 1000 m. This is most evident in Fig. 5.2d, where the simulated TKE at 1500 m is on the order of 0.1 m^2 s^{-2}, while the measurements show a value of approximately 1.6 m^2 s^{-2}.

However, a one-to-one agreement between airborne TKE measurements and simulated TKE cannot be expected because several simplifying assumptions and thus potential error-sources are involved in the comparison. First, as mentioned above, the accomplishment of one flight-path necessary to obtain a TKE-profile is on the order of an hour, i.e. the observed profiles can only be regarded as 'instantaneous' if the turbulence structure is sufficiently stationary. Second, measurements of wind speed during a flight-leg are neither a time-series nor a space-series but a mixture of both. The conversion into a pure space-series requires the assumption of Taylor's frozen eddy-hypothesis (Taylor, 1938), the validity of which cannot be taken for granted in complex and mountainous terrain. Third, the modeled SGS TKE values are dependent on the respective parameterization scheme. As shown in Figs. 3.12 and 3.22, for example, turbulence obtained from the dynamic reconstruction model of Chow et al. (2005a) experiences less damping due to stable stratification than does turbulence from a 1.5-order TKE closure.

Despite these differences in the observed and simulated profiles there are also similarities. Both have their maximum at an elevation below 800 m. Above this maximum, both modeled and measured TKE decrease almost linearly with altitude (though with different gradients). And as in the simulations, the depth of the turbulent active layer is largest on 22 August and smallest on 25 August. Given these similarities, we proceed by investigating whether or not the simulated profiles of TKE reveal the same scaling behavior as the measured airborne TKE-profiles.

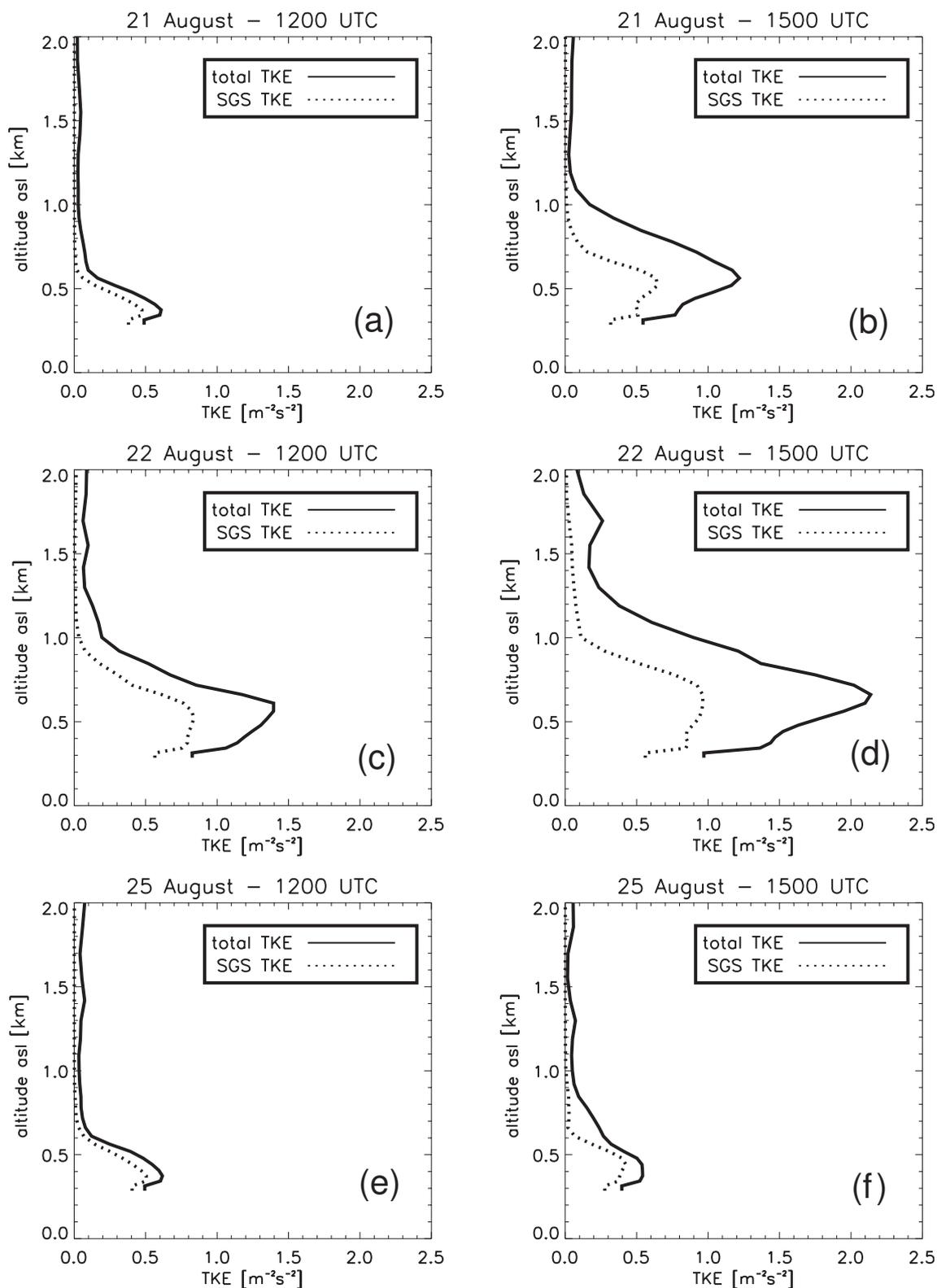***Figure 5.1:*** *Profiles of SGS-TKE and total (= SGS + resolved) TKE on the three days of simulation at 1200 and 1500* UTC.
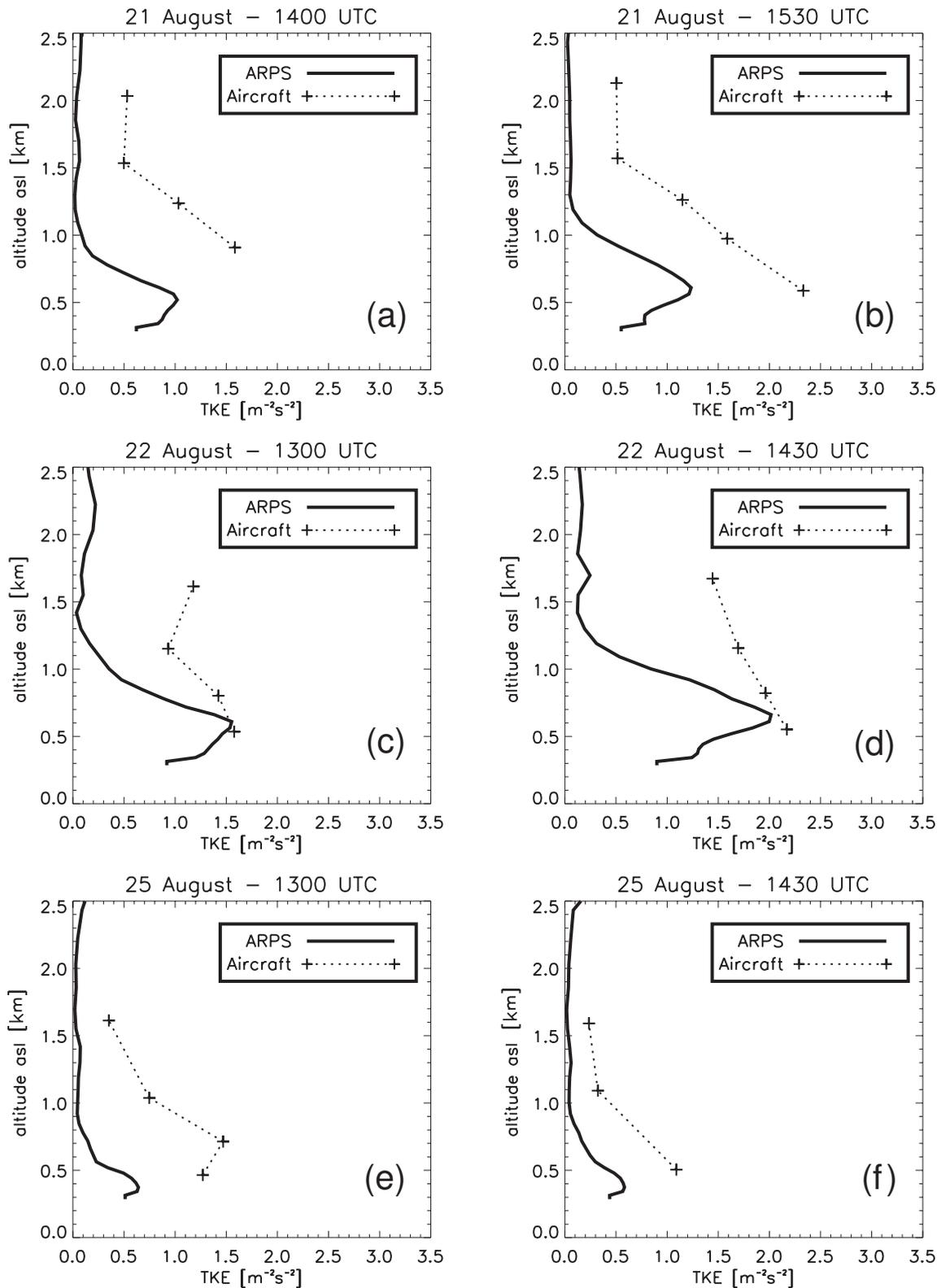
Figure 5.2: *Profiles of TKE as obtained from ARPS (total TKE) and airborne measurements at the times given in the header to each panel on the three days of simulation. The measurement data are obtained from flight-paths no. 1-6 (see Table 2.2) in ascending order.*

5.2.3 Scaling

Like in Section 2.5.2, profiles of simulated total TKE are scaled with the square of the convective velocity scale $w_*(= \{(g/\overline{\theta_0}) \cdot \overline{w'\theta'_0} \cdot z_i\}^{1/3}$, with $\overline{w'\theta'_0}$ = surface turbulent sensible heat flux, $\overline{\theta_0}$ = surface potential temperature, z_i = boundary layer thickness). As in Section 2.5.2, z_i is obtained from a TKE threshold criterion. The threshold has been lowered from 0.5 m^2 s^{-2} to 0.3 m^2 s^{-2} to account for the generally lower magnitudes of simulated TKE compared to the airborne measurements (Fig. 5.2). The results are shown in Fig. 5.3. All three panels display the same profiles of total TKE, extracted from model output data in hourly intervals between 1100 and 1600 UTC on all three days of simulation. In Fig. 5.3a, the TKE profiles are scaled with w_*^2 calculated from the surface heat fluxes on the location of the valley floor site 'A1' (see Fig. 2.1b and Table 2.1), while the profiles in Figs. 5.3b and 5.3c are scaled with w_*^2 from the locations of stations 'B' and 'E1' on the eastern slope.

Fig. 5.3a shows that scaling TKE with w_*^2 from the valley floor, i.e. from the surface directly underneath the profiles considered, yields very poor results: The profiles are scattered and do not collapse on one single curve. However, extraordinarily good scaling is achieved if w_*^2 from the eastern slope is used (Figs. 5.3b and particularly 5.3(c)). The simulated turbulence thus reveals the same surprising scaling characteristics as TKE observed from the aircraft (Section 2.5.2).

5.3 The TKE budget

The good scaling results shown in the previous section indicate that both modeled and measured TKE - despite considerable differences in their magnitudes - have a similar structure and are equally related to the surface processes on the eastern slope. It can therefore be assumed that TKE obtained from ARPS is produced by the same mechanisms as the 'real' turbulence observed from the aircraft. We try to identify these processes by investigating the TKE budget.

5.3.1 The TKE equation

Let $\overline{e}$ be the turbulent kinetic energy. The rate of change in $\overline{e}$ can be described by a budget equation of the following form (e.g. Stull, 1988, p. 152):

$$\underbrace{\frac{\partial \overline{e}}{\partial t}}_{\mathbf{I}} = \underbrace{-\overline{u}\left(\frac{\partial \overline{e}}{\partial x}\right) - \overline{v}\left(\frac{\partial \overline{e}}{\partial y}\right) - \overline{w}\left(\frac{\partial \overline{e}}{\partial z}\right)}_{\mathbf{II}} - \underbrace{(\overline{u'w'})\left(\frac{\partial \overline{u}}{\partial z}\right) - (\overline{v'w'})\left(\frac{\partial \overline{v}}{\partial z}\right)}_{\mathbf{III}} +$$

$$+ \underbrace{\frac{g}{\overline{\theta}}(\overline{w'\theta'})}_{\mathbf{IV}} - \underbrace{\frac{1}{\rho}\frac{\partial}{\partial z}(\overline{w'p'})}_{\mathbf{V}} - \underbrace{\frac{\partial}{\partial z}(\overline{ew'})}_{\mathbf{VI}} - \underbrace{\epsilon}_{\mathbf{VII}} . \tag{5.1}$$

The three velocity components in this coordinate system are u, v and w. θ is a reference potential temperature, ρ a reference density and p the pressure. The rate of change in $\overline{e}$ (I) is balanced by advection of turbulent kinetic energy (II), by TKE production due to shear (III) and buoyancy (IV), by pressure transport (V), turbulent transport (VI) and viscous dissipation ϵ (VII). Note that in terms (III) to (VI) the horizontal contributions have been neglected for greater readability.
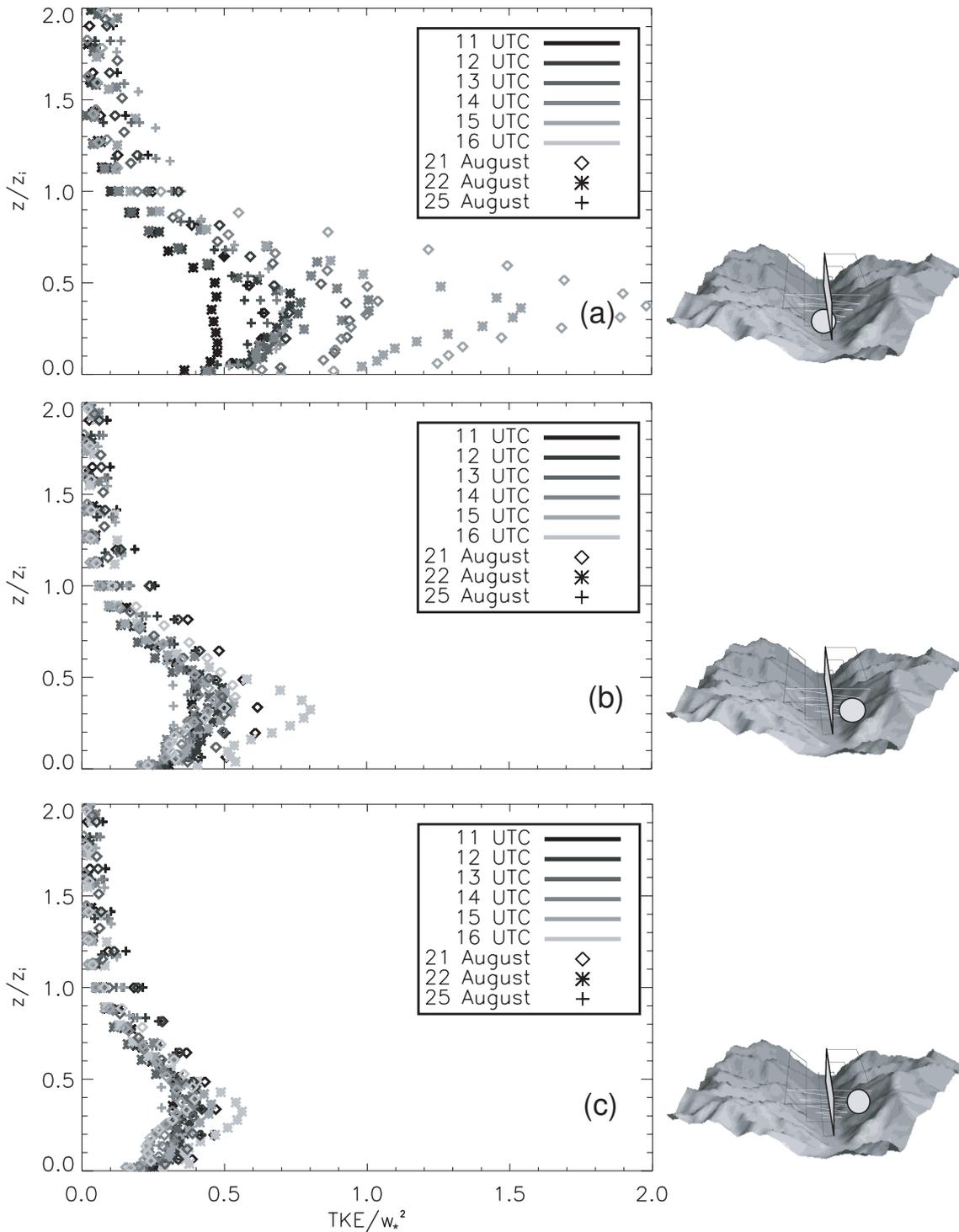
Figure 5.3: *Scaled profiles of TKE, obtained from ARPS output data in the center of the valley along the valley axis on the three days of simulation. Each plot displays the same TKE profiles, but scaled with different values of w_*^2 calculated from ARPS surface heat fluxes: (a) at the site of the valley floor station A1, (b) at the site of station B on the eastern slope and (c) at the site of station E1 on the eastern slope. Details of the measurement sites are given in Table 2.1.*

The 1.5-order TKE closure used by ARPS solves a prognostic TKE equation which is based on Eq. 5.1. The details of the parameterizations applied are given in Xue et al. (1995). Pressure transport and turbulent transport are treated as a single 'diffusion' term as introduced by Moeng (1984).

To identify the dominant TKE production mechanisms in the Riviera Valley, the components of the TKE budget equation are analyzed. We are aware that the TKE equation solved by ARPS only describes the structure of SGS turbulence and not total TKE. However, as can be seen from Fig. 5.1, SGS turbulence is generally of larger or at least comparable magnitude than resolved TKE. Moreover, SGS TKE determines the shape of the profiles of total TKE. The production mechanisms of SGS TKE are therefore assumed to be representative for total TKE.

5.3.2   The generation of TKE in the Riviera Valley

In Fig. 5.4, profiles of the (SGS) TKE budget components at the southern valley mouth (at the southern boundary of volume 'V350' in Fig. 4.1a) are displayed. The profiles are averages over the valley base width and obtained from model output on 22 August, the day with strongest turbulence activity. In the late morning, at 1000 UTC, TKE production is entirely determined by buoyancy (up to 0.0035 m^2s^{-3}). Shear production and advection of TKE are negligible, while diffusion and dissipation act as sink terms. This is consistent with the picture of a convectively growing boundary layer without wind shear (Moeng and Sullivan, 1994). At 1300 UTC, however, the dominating TKE production mechanism is wind shear with a maximum of 0.012 m^2s^{-3}. Note that shear production has its maximum in about 500 m altitude rather than at the surface. Buoyancy is an important source of TKE only in the lowest 200 m. By 1600 UTC buoyant production has totally ceased, while shear production is even stronger (exceeding 0.015 m^2s^{-3} at 400 m asl).

Fig. 5.5 shows the contours of buoyant TKE production at (a) 1000 UTC and (b) 1400 UTC in a vertical cross-section at the same location as the profiles of Fig. 5.4. The corresponding contour plots of shear production are displayed in Fig. 5.6. The pictures are consistent with the results of Fig. 5.4. At 1000 UTC, buoyancy is a positive production term on the valley floor and along the heated slopes (Fig. 5.5a), while shear production is negligible (Fig. 5.6a). By 1400 UTC, buoyant production has significantly increased along the eastern, sun-exposed slope, but its effect is restricted to a shallow layer of only 100–200 m depth (Fig. 5.5b). Above the valley floor, the vertical extent of the buoyant TKE production layer has decreased compared to the situation at 1000 UTC. Shear production, on the other hand, is much stronger than buoyancy at 1400 UTC (Fig. 5.6b), and it is effective over a larger part of the valley atmosphere, revealing a distinct maximum in the western valley half at 200–700 m.

Fig. 5.7 shows profiles of the TKE budget components in the northern valley half (at the location of the northern face of volume 'V350' in Fig. 4.1a). They appear qualitatively similar to those observed in the southern slice (Fig. 5.4), with shear production dominating over buoyant production in the later afternoon. The magnitudes of TKE, however, are considerably lower. At 1600 UTC, for example, shear production is lower than 0.003 m^2s^{-3}, i.e. only about a fifth of the corresponding production rate in the southern slice.

The turbulence structure on 21 and 25 August (not shown here) reveals similar characteristics as 22 August, although less pronounced. This is consistent with the observation of generally lower TKE values in the profiles of Fig. 5.1.
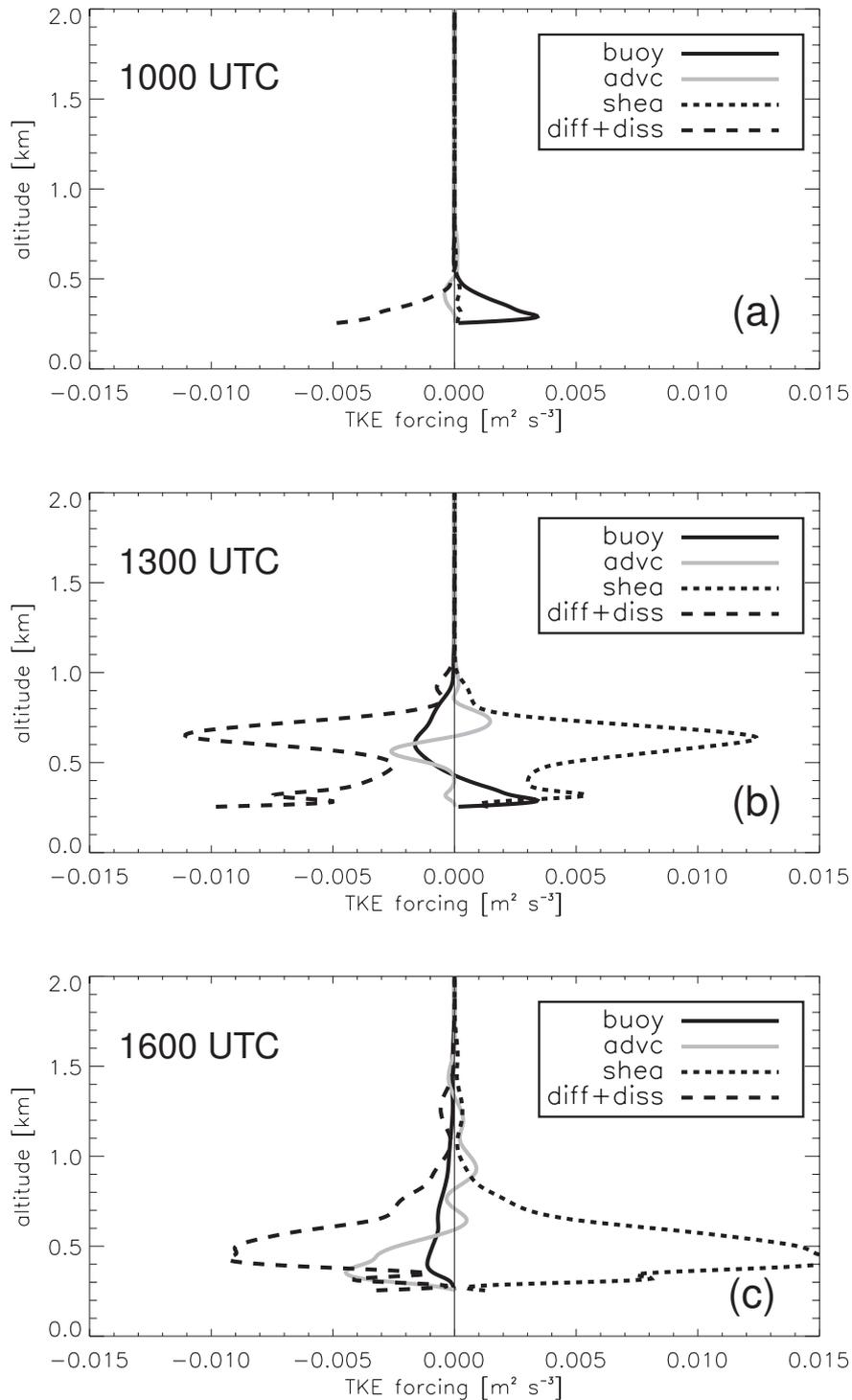
Figure 5.4: *Profiles of the TKE budget terms at (a) 1000* UTC, *(b) 1300* UTC *and (c) 1600* UTC *in a slice close to the southern valley mouth. "Buoy" and "shea" denote the production of TKE by buoyancy and wind shear, "advc" is the advection of TKE, and "diff" and "diss" are diffusion and dissipation, respectively.*
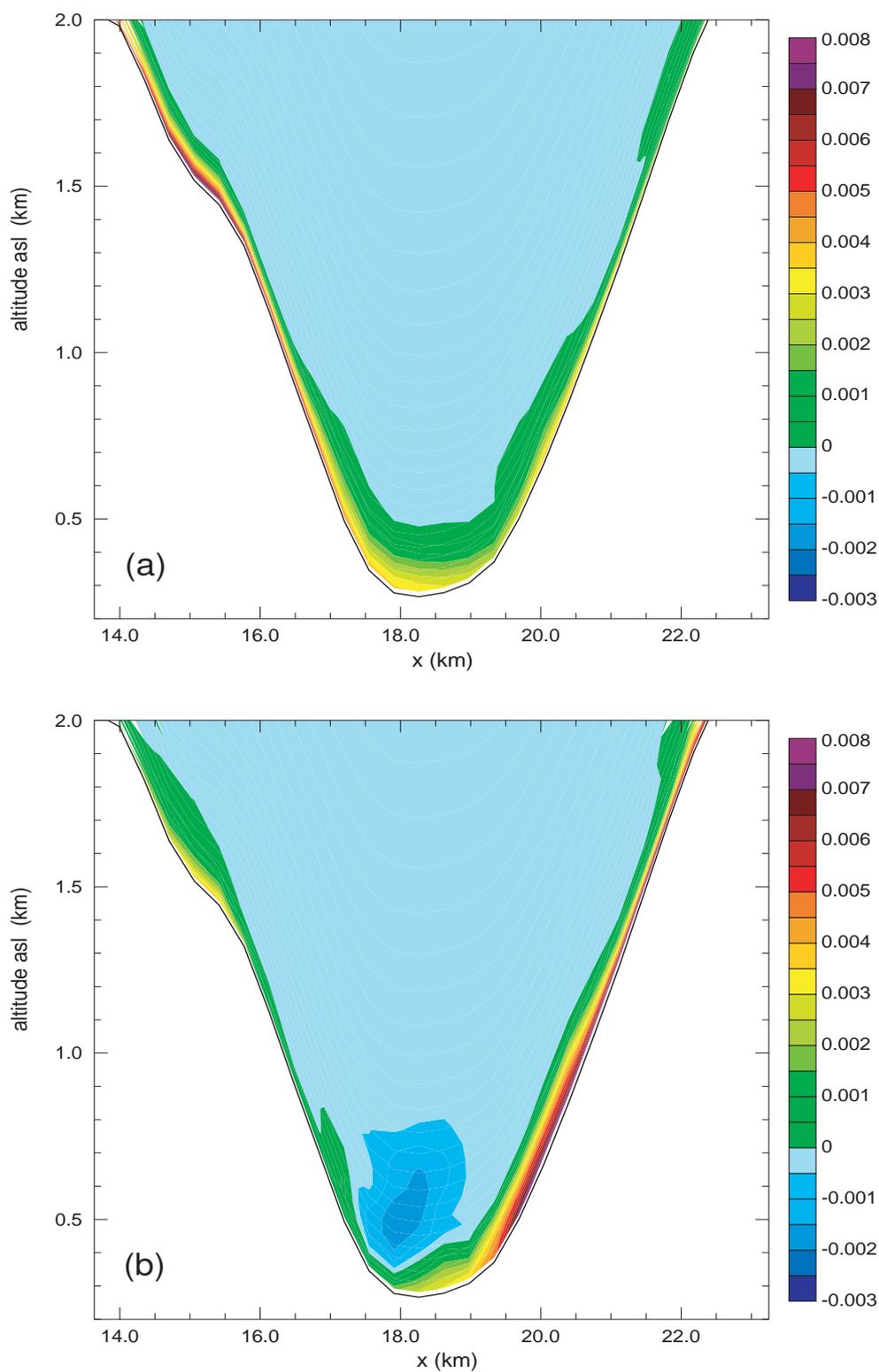
Figure 5.5: *Vertical cross-sections of the TKE production rate by buoyancy in [m² s⁻³] at (a) 1000* UTC *and (b) 1400* UTC *in a slice close to the southern valley entrance. The horizontal position is in kilometers with respect to an arbitrary origin.*
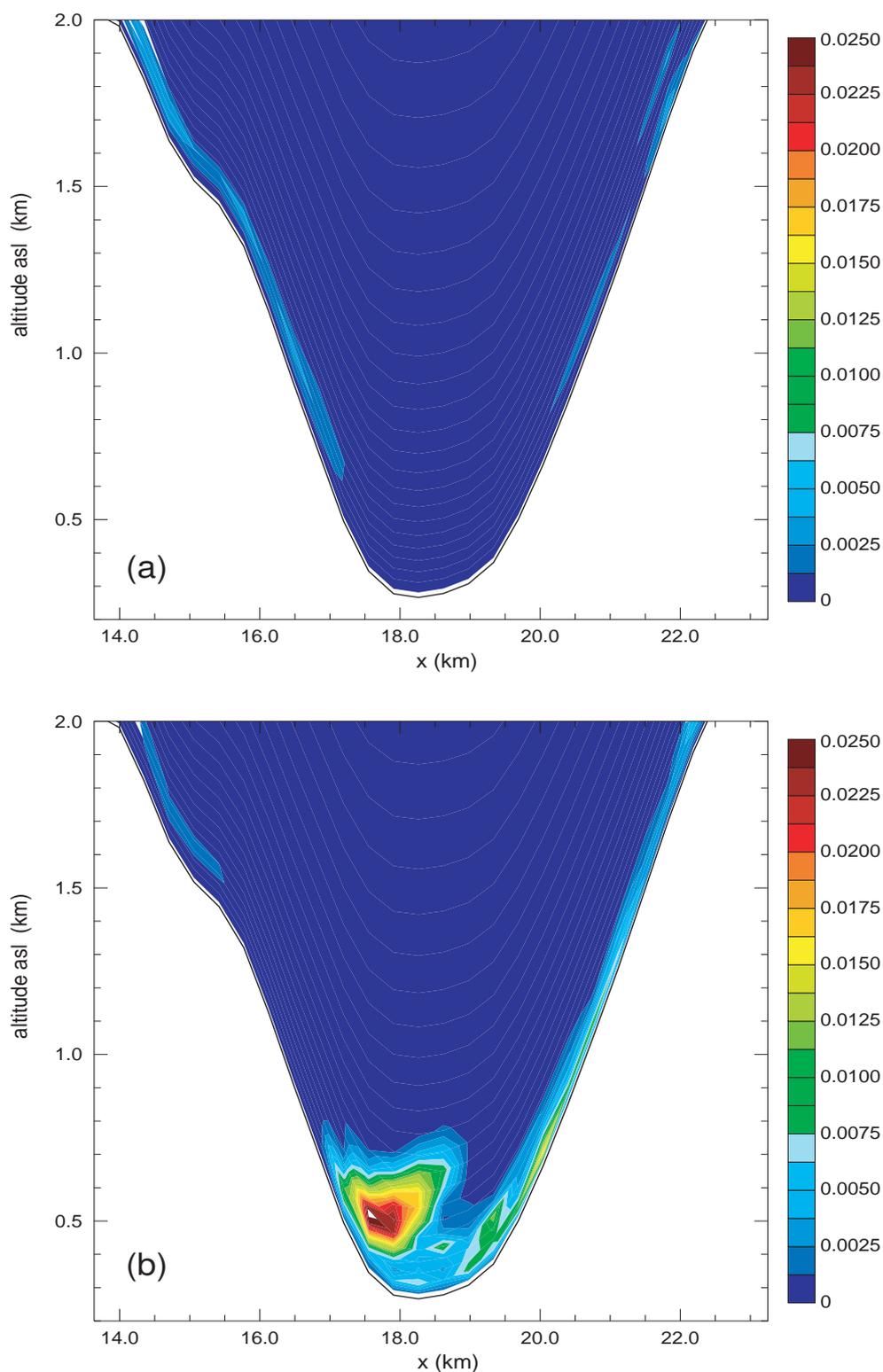
Figure 5.6: *Vertical cross-sections of the TKE production rate by wind shear in [m² s⁻³] at (a) 1000* UTC *and (b) 1400* UTC *in a slice close to the southern valley entrance. The horizontal position is in kilometers with respect to an arbitrary origin. Note that the colorbar is assigned with values different from Fig. 5.5.*
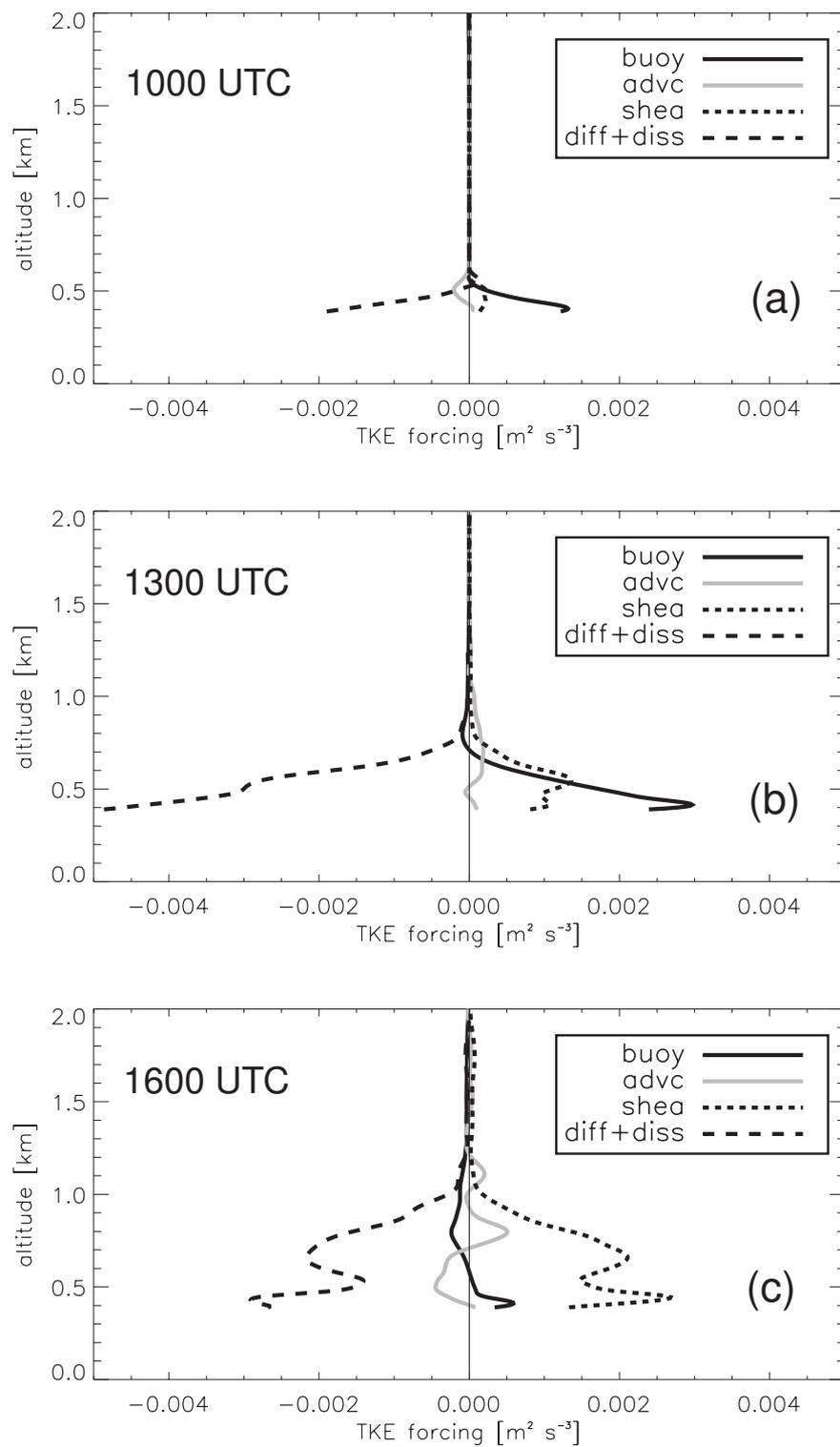
Figure 5.7: *As in Fig. 5.4, but in a slice in the northern part of the valley.*

5.3.3   Discussion

From the observations described in the previous subsection, it is apparent that the turbulence structure of the afternoon atmosphere is mainly determined by wind shear and only to a limited degree by buoyancy effects. In Section 2.3.2 we have shown that the Riviera atmosphere is characterized by a slightly stable stratification on all sunny days, which is due to subsidence of potentially warmer air from above. The growth of a well-mixed layer is consistently suppressed. The surprisingly small and sometimes even negative contribution of buoyancy to the TKE budget can be understood in the light of these observations: in the TKE equation, the buoyancy term (term IV in Eq. 5.1) depends on the turbulent heat fluxes. This means that in the case of stable stratification, when turbulent heat fluxes are negative, buoyancy is a sink term rather than a production term. More striking is the strong TKE production due to wind shear and the location of its maximum well above the valley surface. Over flat terrain, one would rather expect a pronounced maximum on the surface and only a secondary maximum at the upper boundary of the well-mixed layer (Pino et al., 2003). This means that shear production must be primarily a consequence of different interacting flow patterns in the valley atmosphere rather than of direct friction on the surface. This observation becomes plausible by considering the complicated flow structure in the Riviera Valley (Sections 2.4.2 and 4.3.2). Particularly in the valley entrance region, three different flow patterns are simultaneously present, giving rise to wind shear: a jet-like up-valley wind which is shifted towards the eastern slope, a strong mechanically induced clock-wise secondary circulation and, third, thermally induced slope winds. Further north, the valley winds are spread over the entire valley cross-section and the secondary circulation is 'replaced' by a weaker thermally induced anti-clockwise cross-valley circulation. While wind shear and the associated production of TKE in the northern valley half are consequently lower than at the southern valley mouth, wind shear still appears to be strong enough to be the dominant source of turbulence in the afternoon.

Given the comparatively small contribution of buoyancy as a source of TKE, the excellent scaling behavior with the convective velocity scale w_* based on the eastern slope (Fig. 5.3) is very surprising. The dominance of shear production would, at first sight, rather imply a scaling approach based on a friction velocity u_*, or at least a combination of w_* and u_* (Moeng and Sullivan, 1994; Khanna and Brasseur, 1998; Pino et al., 2003). Advection of turbulent boundary layer air from the eastern slope into the valley center cannot be an explanation, either, because advection does not contribute much to the total TKE budget (Figs. 5.4 and 5.7).

Therefore, despite the apparent close relationship to w_*^2 on the eastern slope, TKE cannot be *determined* by w_*^2, at least not directly. Scaling with the square of a surface friction velocity u_*, on the other hand, turns out to yield very poor results (not shown); this is plausible because shear production has been observed to have its maximum not on the surface but higher up in the valley atmosphere, i.e. it is a consequence of the direct interaction between the strong jet-like up-valley winds and the local slope winds and cross-valley circulations. This implies that the strength of up-valley winds is a key variable in this context rather than w_*^2 or u_*^2. In Fig. 5.8, time-series of the up-valley wind speed $\langle v \rangle$ (averaged over the entire valley volume up to an altitude of 2000 m) are displayed, together with time-series of w_*^2 at the locations of surface station A1 and of the slope site E1. It can be seen that w_*^2 on site E1 correlates very well with $\langle v \rangle$, in contrast to w_*^2 on site A1. This is even more apparent in Fig. 5.9, where values of $\langle v \rangle$ are plotted against the corresponding w_*^2 on site A1 (correlation coefficient R = 0.528; regression line *does not* intersect the origin) and w_*^2 on site E1 (R = 0.935; regression line *does* intersect the origin). Thus, if our hypothesis holds and $\langle v \rangle$ is indeed the key variable determining the production of TKE, the observed good scaling with w_*^2 at E1 may be understood as
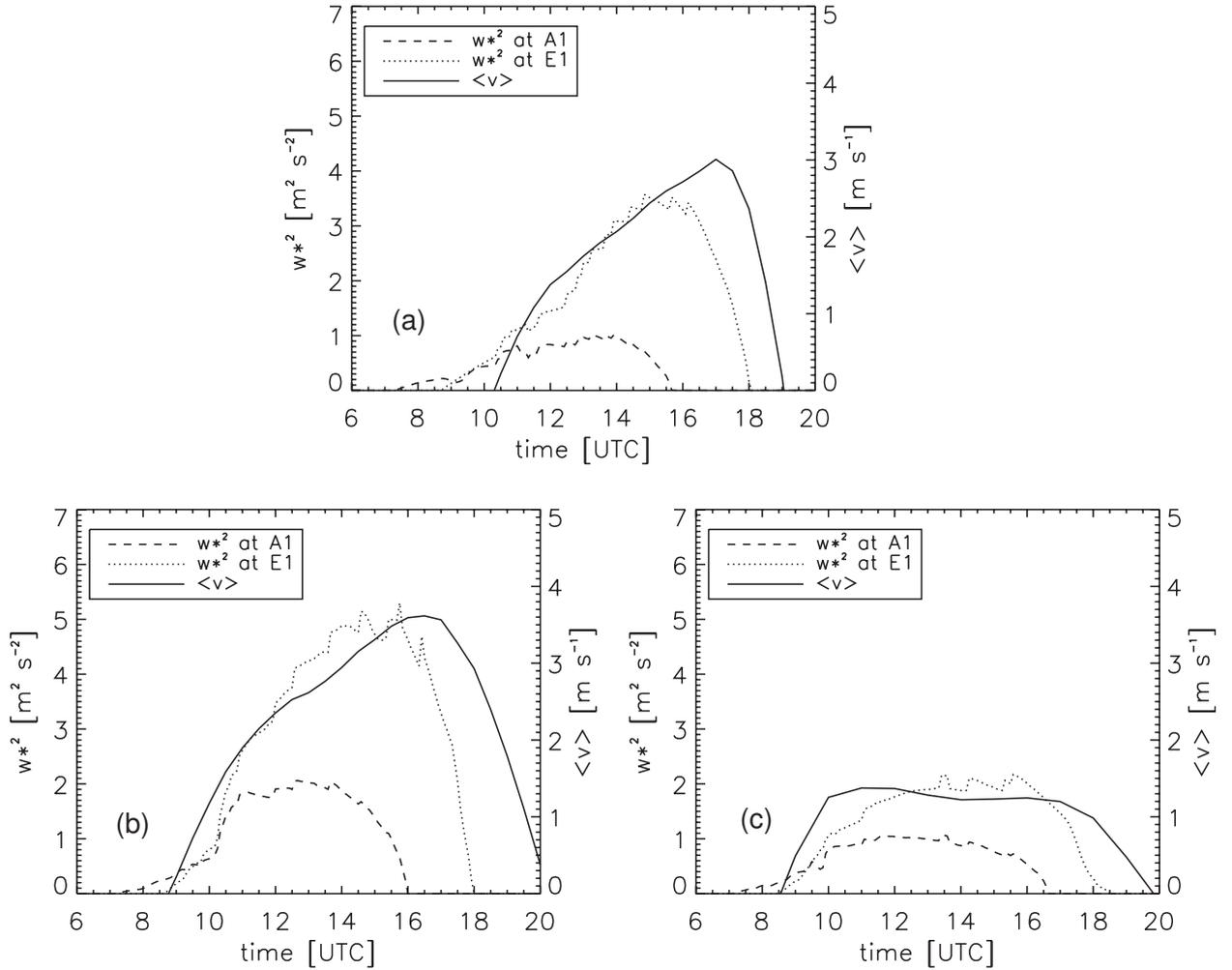
Figure 5.8: *Time series of w_*^2, obtained from ARPS output data at the locations of surface sites A1 and E2, and of the valley-averaged up-valley wind speed $\langle v \rangle$ on (a) 21 August, (b) 22 August and (c) 25 August. Note that the evening transition of $\langle v \rangle$ is delayed by 30-60 minutes with respect to the local flow on the valley floor (plotted in Fig. 2.4).*

a consequence of their direct proportionality. Of course, it is yet too early to propose a new general similarity theory for the atmospheric boundary layer in steep and complex topography. For dimensional reasons, one cannot simply use $\langle v \rangle$ as a new scaling variable instead of w_*^2. It is well possible, that a second velocity scale must be included which is associated with the cross-valley flow. However, this is still subject to future research.

The cause for the surprising agreement between up-valley wind speed and w_*^2 on the eastern slope is another aspect yet to be investigated. It is certainly plausible that the surface heat fluxes, and thus w_*, are essential for the heating of the valley atmosphere, either directly by heat flux divergence, or indirectly via thermally-driven cross-valley circulations. Therefore, one can expect w_* to have a direct impact on the magnitude of diurnal valley-plain temperature gradients and thus on the strength of the resulting valley winds. As the up-valley winds are strongest in the afternoon, it also appears plausible that the surface heat fluxes on the energetically active side, i.e. on the sun-exposed westward facing slope, are to be considered. However, a quantitative evaluation of the nature and characteristics of the relationship between w_* and the corresponding up-valley winds is still to be carried out.
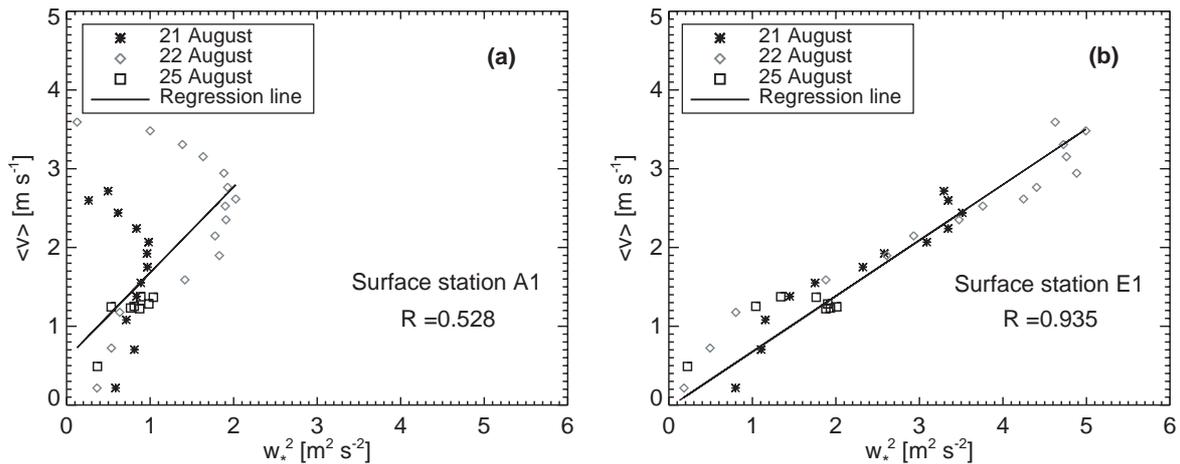
Figure 5.9: *Valley-averaged up-valley wind speed $\langle v \rangle$ plotted against the corresponding w_*^2 at the location of (a) the valley floor site A1 and (b) the slope site E1 between 0900 and 1600 UTC. R is the correlation coefficient. Note that the regression line in (b) intersects the origin, i.e. $\langle v \rangle$ is directly proportional to w_*^2.*

5.4 Summary and conclusions

In this chapter we have investigated the turbulence structure of the Riviera Valley as obtained from ARPS simulation output data. A 1.5-order TKE scheme has been applied for subgrid-scale (SGS) closure. The main results can be summarized as follows:

(i) On all three days of simulation, the profiles of TKE reveal qualitatively similar shapes with a very pronounced maximum at 300–700 m elevation.

(ii) The shape of the profiles of total TKE, particularly of the pronounced maximum, is mainly determined by the shape of SGS TKE, while resolved TKE shows less variation with height.

(iii) Simulated TKE has lower magnitudes and is confined to a shallower layer over the valley surface than TKE observed from the airborne measurements. The qualitative structure of the profiles, however, is similar. Moreover, as in the measurements, the simulated profiles scale very well with the square of the convective velocity scale w_* obtained from the surface fluxes on the eastern slope.

(iv) The simulations show that TKE is mainly produced by wind shear, while buoyancy appears to be an almost negligible production mechanism, at least during the afternoons. The maximum of shear production is not on the valley surface but further up in the valley atmosphere, indicating that wind shear is mainly produced by the interaction of the up-valley wind with the local cross-valley circulations rather than by surface friction.

(v) The paradox of a good scaling behavior with w_*^2 despite dominant shear production can possibly be explained by the observation of w_*^2 having a similar diurnal pattern as the averaged up-valley wind speed $\langle v \rangle$. This means that TKE may well be directly determined by $\langle v \rangle$, and a scaling with w_*^2 on the eastern slope nevertheless works. The reasons for the high correlation between $\langle v \rangle$ and w_*^2 on the eastern slope have not yet been investigated.

A general similarity theory for the structure of TKE over steep and mountainous topography cannot be proposed from this case-study, but the high correlation between $\langle v \rangle$ and w_*^2 suggests a direction for future studies. All in all, our measurements and simulations show that despite the complexity of the terrain and despite the apparent differences from a 'normal' convective boundary layer, the turbulence structure reveals reproducible patterns and scaling characteris-

tics. A generalization of these findings requires the investigation of other valley geometries and different topographic orientations. In particular, the functional dependence of up-valley wind speed on the surface fluxes must be elaborated.

Chapter 6

Export of mass and moisture from the valley into the free atmosphere

6.1 Introduction

Numerical weather and climate prediction models are known to be sensitive to surface moisture fluxes (e.g. Beljaars et al., 1996; Viterbo and Betts, 1999). These fluxes are often obtained from Land Surface Models as for example reviewed by Pitman (2003). If no such model is included, the kinematic surface moisture flux L_s is typically calculated with an equation of the following form:

$$L_s = C_{dq} \cdot V \cdot \Delta q \; . \tag{6.1}$$

V is the horizontal surface velocity and Δq the difference in specific humidity between the ground and the first model level above the ground. C_{dq} is the bulk aerodynamic coefficient for the moisture flux and is derived from similarity functions as formulated by, e.g., Businger et al. (1971) and Deardorff (1972).

While the validity of such similarity functions over complex topography is questionable in principle (Rotach, 1995), there are additionally many indications that microscale turbulence is not the only mechanism responsible for the vertical transport of moisture into the free atmosphere over steep and mountainous terrain. The same applies for the transport of other quantities such as heat, momentum and pollutants. Meso-gamma-scale motions - which are still on the subgrid-scale for typical weather and climate models - appear to be an additional component to be considered and parameterized. For example, Noppel and Fiedler (2001) identified mountain venting, i.e. overshooting slope winds, as an important process transferring heat into the free atmosphere. With a conceptual model they showed that the effect of this mechanism has a magnitude which is comparable to the impact of micro-scale turbulent fluxes alone. Clearly, coarse numerical climate models, which do not resolve the topography of narrow valleys, are not able to capture this process. Another example is given by the measurements of Henne et al. (2004) in the Leventina and Mesolcina Valleys in southern Switzerland. They observed a considerable export of valley air (and thus of moisture and pollutants) into the free atmosphere and attribute this effect to mountain venting. According to their estimate, valley air is exported into the free atmosphere at a surprisingly high rate of 33% of the entire valley air volume per hour. The observation of elevated moisture layers in the lower troposphere on the leeward side of the Alpine arc can perhaps only be explained by such non-turbulent processes of moisture export (Henne et al., 2005), emphasizing the importance of these transport mechanisms also for climatological considerations.

117

In this short chapter we use the output of our model runs to evaluate the daytime export of mass and moisture from the Riviera Valley into the free atmosphere aloft, and we try to identify and quantify the underlying mechanisms. Three days with fair weather conditions (August 21, 22 and 25) have been simulated. The results are compared to the parameterized turbulent surface fluxes, i.e. to those fluxes a coarse numerical atmospheric model not resolving the Riviera Valley would see as the only form of vertical moisture flux from the ground.

6.2 Mass fluxes

The vertical transfer of mass and moisture between the valley atmosphere and the free atmosphere is obtained from the output data of model simulations on the 350 m grid (Fig. 3.2b). We calculate the fluxes of mass and moisture through a horizontal interface S_{2km} intersecting the valley sidewalls at an altitude of $z_0 = 2.0$ km asl (graphically illustrated in Fig. 6.1). This interface is chosen such that it is identical to the upper boundary of volume 'V350' used in Section 4.5 (see Fig. 4.1a). The altitude of 2 km corresponds approximately to the level at which daytime winds transition from the up-valley direction to the direction of the large-scale flow. The net vertical flux of air mass through this interface from the valley into the free atmosphere, M_{net}, is given by

$$M_{net}(z_0) = \frac{1}{|S_{2km}|} \iint\limits_{S_{2km}} w(x, y, z_0) \cdot \rho(x, y, z_0) \, dx \, dy \ . \tag{6.2}$$

w is the vertical velocity component, ρ the density of air and $|S_{2km}|$ the area of interface S_{2km}. Positive fluxes are directed upwards. Fig. 6.2 displays the time-series of M_{net} between 0600 and 2000 UTC (solid lines). The magnitude of this flux reveals both a distinct diurnal pattern and pronounced day-to-day differences. On all three days, M_{net} is negative in the morning (on 21 August until about 0930 UTC, on 22 August until 1130 UTC and on 25 August until 0830 UTC), meaning that air is transported downward into the valley. The afternoon fluxes differ significantly on the three days. On 21 August, M_{net} continuously increases up to a peak value of about 0.22 kg s^{-1} m^{-2}. On 22 August, the afternoon mass flux is significantly lower and relatively constant (on the order of 0.03 kg s^{-1} m^{-2}), and on 25 August it is close to zero, partially even slightly negative. Averaged over the typical period of thermally driven up-valley flow (1000-1900 UTC), the net vertical export of air into the free atmosphere amounts, on 21 August, to 186% of the entire valley air mass. This is of comparable magnitude to the estimates reported by Henne et al. (2004) for a similar valley. On 22 August, net export is considerably lower at 84%, and it is almost negligible on 25 August at 7%.

If we neglect the thermal expansion of air, two processes can lead to vertical mass fluxes through S_{2km} out of the valley. (i) As in most Alpine valleys, the cross-sectional area of the Riviera Valley decreases in the up-valley direction, i.e. the valley becomes narrower. Mass conservation then requires either the along-valley flow to be accelerated or valley air to be vertically "squeezed out" of the valley. (ii) Spatial variations in the along-valley acceleration can lead to local zones of flow convergence or divergence. This could for example be due to abrupt changes in surface roughness (as investigated for water-land-transitions by Samuelsson and Tjernström, 2001) or due to variations in the local horizontal pressure gradients. For example, if the local along-valley pressure gradients north of the Riviera valley are significantly smaller than those south of the Riviera, up-valley winds would be decelerated in the Riviera Valley and vertical mass fluxes would be the consequence.
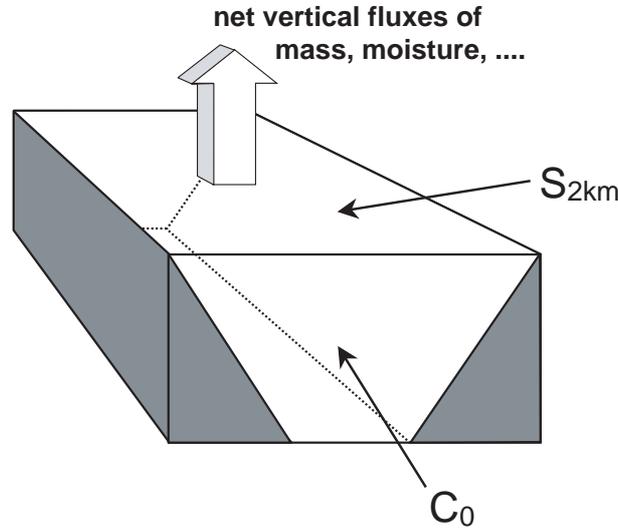
Figure 6.1: *Schematic representation of the interfaces C_0 and S_{2km}, which are used for the flux calculations.*

An upper boundary for the vertical mass flux due to the narrowing-effect, M_{narrow}, is estimated in the following way. Let M_{along} be the air flux in the along-valley direction (velocity v) at the southern valley mouth (at $y_0 = 0$), and let C_0 be the corresponding valley cross-sectional area (see Fig. 6.1), i.e. the southern vertical boundary of V350 in Fig. 4.1a. M_{along} can then be expressed by:

$$M_{along} = \frac{1}{|C_0|} \int_{C_0} v(x, y_0, z) \cdot \rho(x, y_0, z)\, dx\, dz \; . \tag{6.3}$$

The cross-section of the Riviera Valley decreases by about 18% from the southern to the northern valley mouth. If we assume that the flow does not accelerate, mass conservation requires 18% of the along-valley flow to be vertically exported through S_{2km}. This means, a rough estimate of M_{narrow} is given by

$$M_{narrow} = \frac{|C_0|}{|S_{2km}|} \cdot M_{along} \cdot 0.18 \; . \tag{6.4}$$

Time-series of M_{narrow} are shown in Fig. 6.2 (dashed lines). On 25 August, M_{narrow} is much larger than M_{net}, thus not providing a good estimate of the net vertical air flux. This is probably due to the relatively stable stratification (lapse rate 0.005 K m^{-1}) observed in the valley on that day (see Section 2.3.2). Under such conditions, the narrowing effect appears to favor a flow acceleration in the along-valley direction rather than vertical export of air. On 21 August and 22 August, on the other hand, the valley atmosphere is less stably stratified (lapse rate 0.001-0.002 K m^{-1}), and by and large, M_{narrow} is of a magnitude comparable to M_{net}. In the evening of 21 August (after 1600 UTC), however, M_{net} sharply exceeds M_{narrow}. This is due to a local convergence of horizontal flow in the Riviera Valley, as the valley winds north of the Riviera Valley turn to the down-valley direction earlier than do those south of the Riviera (not shown). The reasons for such an asymmetric evening transition of the valley winds have
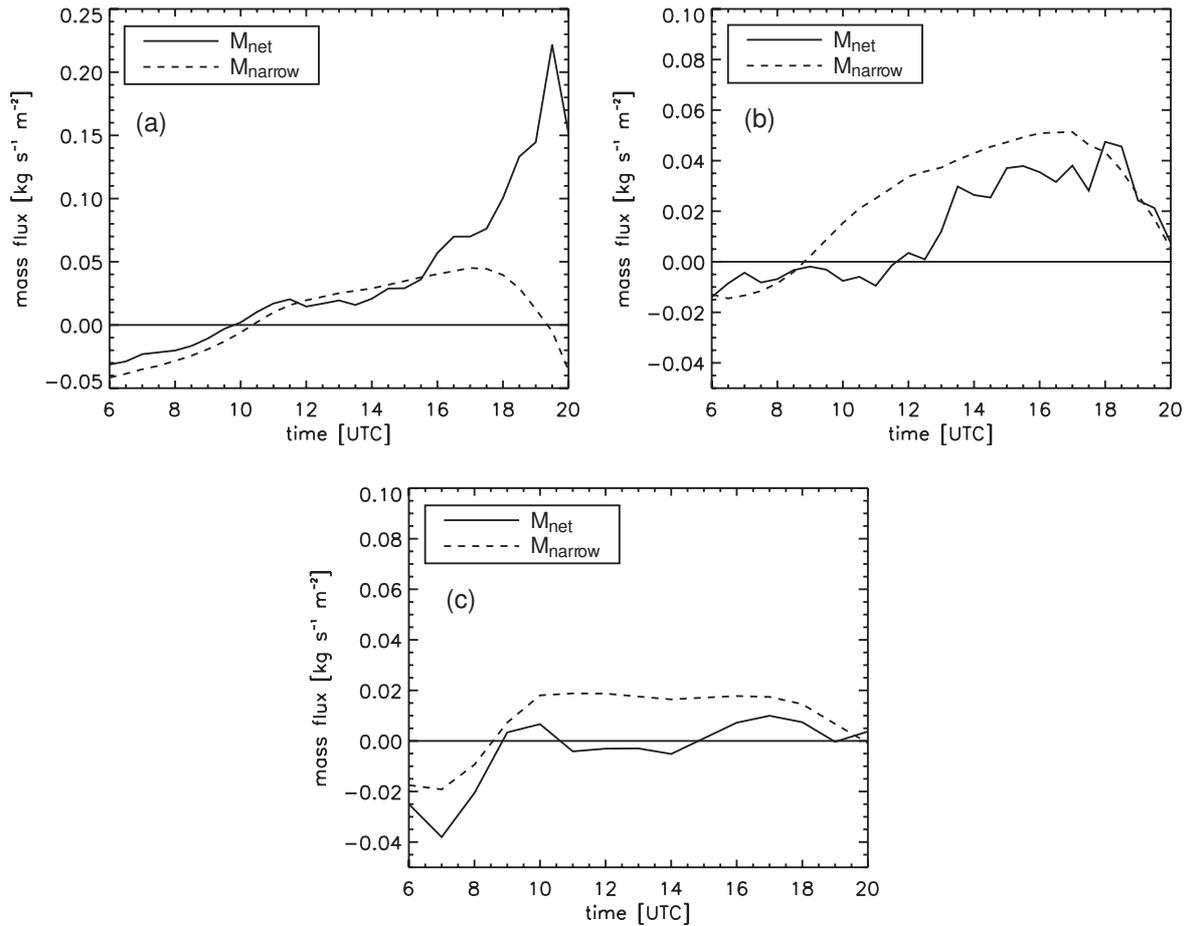
Figure 6.2: *Vertical mass fluxes through S_{2km}. The plots show the time-series of M_{net} (net vertical mass flux) and M_{narrow} (estimate of the vertical mass flux due to the narrowing effect) on (a) 21 August, (b) 22 August and (c) 25 August. Note the different scale in (a).*

not been investigated. Outside this transition period, however, the narrowing effect and the associated mass flux M_{narrow} appear to give a reasonable approximation of the vertical export of valley air, as long as the stratification is not too stable.

6.3   Moisture transport

The considerable vertical fluxes of air, which have been described in the previous section, carry moisture from the valley directly into the atmosphere aloft. The moisture flux associated with this mean vertical flow, L_{flow}, is

$$L_{flow} = \rho \langle w \rangle \langle q \rangle \ . \tag{6.5}$$

The brackets denote the spatial average over S_{2km}. Superimposed on the mean vertical mass flow are thermally or mechanically driven cross-valley circulations. These can be associated with an additional vertical moisture flux, as they lead to export of moist air up the slopes and subsidence of dryer air over the valley center (Kuwagata and Kimura, 1995, 1997; Weigel et al., 2004b). Finally, a third mechanism of moisture transport is given by resolved-scale (RS) and sub-grid scale (SGS) turbulence. As the scales of RS-turbulence overlap with those of the cross-valley circulations, the two processes will henceforth be treated jointly as one transport
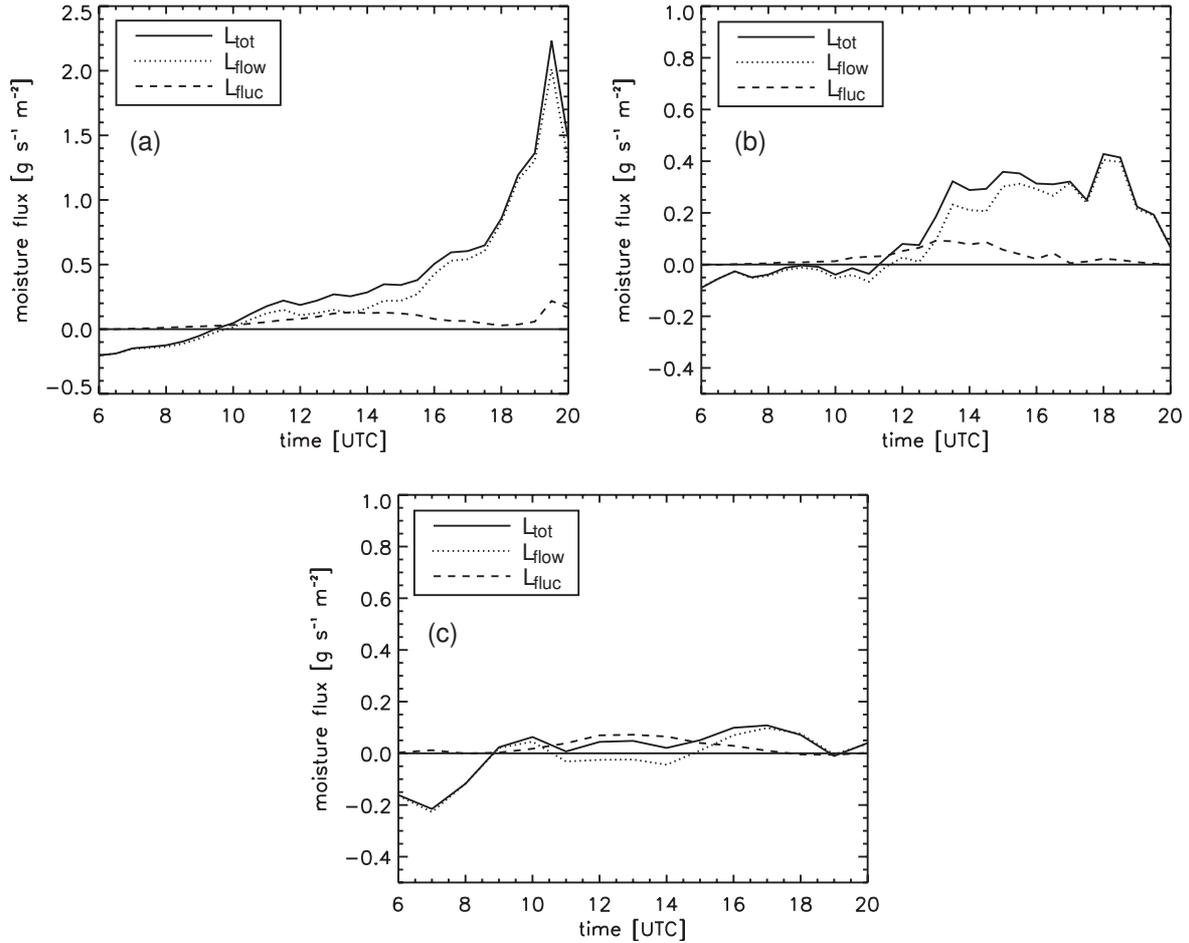
Figure 6.3: *Vertical moisture fluxes through S_{2km}. The plots show the time series of L_{tot} (total vertical moisture flux), L_{flow} (moisture flux due to vertical export of air) and L_{fluc} (moisture flux due to valley circulations and resolved-scale turbulence) on (a) 21 August, (b) 22 August and (c) 25 August. Note the different scale in (a).*

mechanism. Let w' and q' be the circulation-related and RS-turbulent fluctuations in vertical velocity and specific humidity, such that $\langle w' \rangle = 0$ and $\langle q' \rangle = 0$. The associated moisture flux L_{fluc} can then be written as $L_{fluc} = \rho \langle w'q' \rangle$. As SGS turbulent transport of moisture through S_{2km} is negligible (not shown), the total vertical moisture flux L_{tot} can be expressed by:

$$L_{tot} = \rho \langle wq \rangle = L_{flow} + L_{fluc} \tag{6.6}$$

Time series of L_{tot}, L_{flow} and L_{fluc} are shown in Fig. 6.3. L_{tot} and L_{flow} have been calculated from model output data, while L_{fluc} is obtained as residual from Eq. 6.6. On all three days, L_{fluc} reveals a similar diurnal pattern, reaching a maximum of about 0.05–0.1 g s^{-1} m^{-2} at around 13 UTC. While L_{fluc} is the dominating moisture transport term on 25 August, it appears to be of negligible magnitude compared to L_{flow} when strong vertical mass fluxes are present. On 22 August, a relatively constant moisture flux of 0.3–0.4 g s^{-1} m^{-2} is observed in the afternoon, and on 21 August L_{flow} peaks in a sharp maximum of 2 g s^{-1} m^{-2}, which is associated to the corresponding peak in the time series of M_{net} (Fig. 6.2).

As indicated in the introduction to this chapter, typical numerical weather and climate prediction models do not resolve valleys of the Riviera scale. The vertical moisture fluxes in such models are entirely determined by the parameterized turbulent surface fluxes. Moisture fluxes
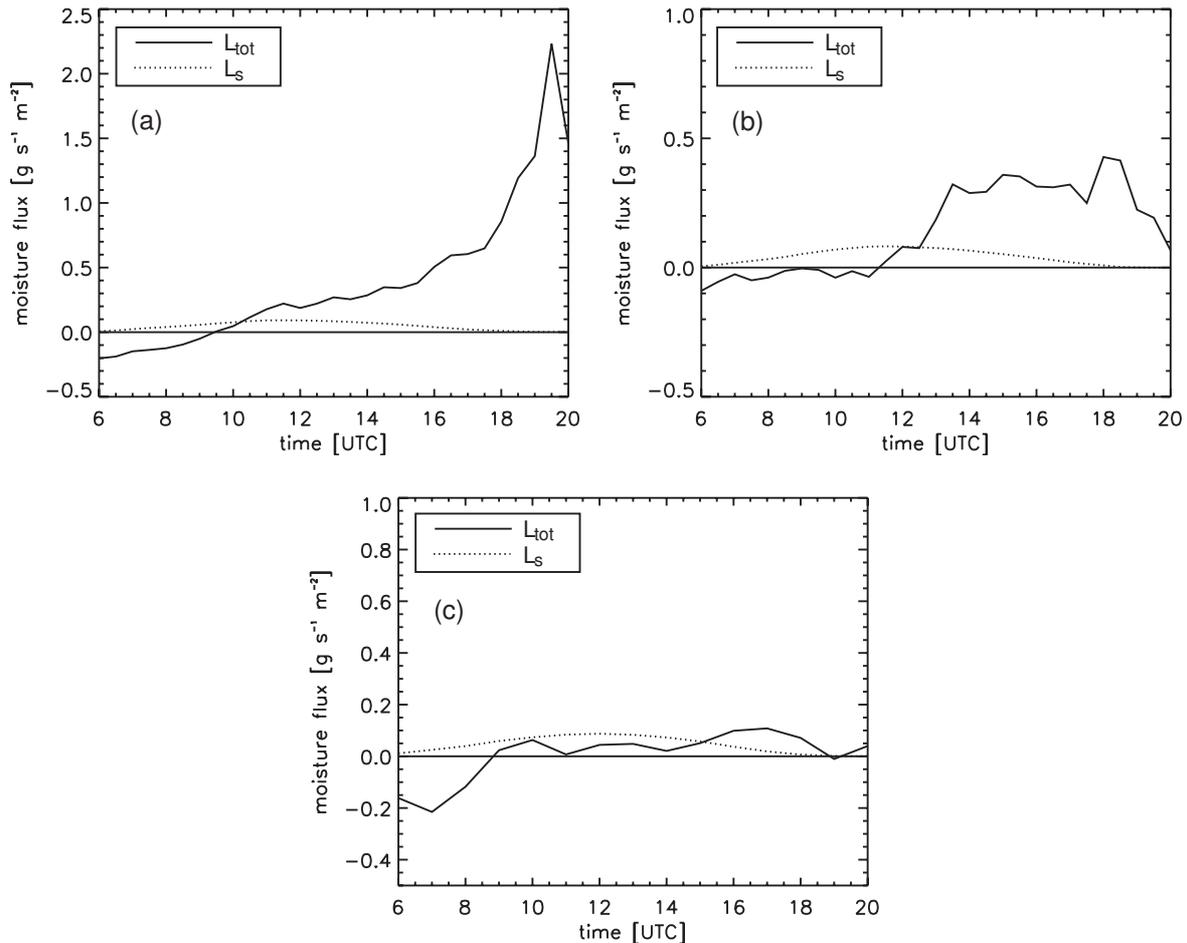
Figure 6.4: *Total vertical moisture flux L_{tot} through S_{2km} and turbulent surface moisture flux L_s on the valley surface underneath S_{2km} on (a) 21 August, (b) 22 August and (c) 25 August. Note the different scale in (a).*

which are related to the valley topography, i.e. L_{fluc} and L_{flow}, are not considered. In Fig. 6.4 we compare the total vertical mass flux L_{tot} to the corresponding turbulent surface moisture fluxes L_s, which are obtained from the ARPS land surface model (averaged over the entire valley surface underneath S_{2km}). Similarly to L_{fluc} in Fig. 6.3, the time series of L_s show the same behavior on all three days. The maximum (around 0.1 g s^{-1} m^{-2}) occurs at around 12 UTC. The magnitude of L_s is comparable to the magnitude of L_{fluc} (Fig. 6.3), which is plausible as the moisture content of the (overshooting) slope winds is directly related to the underlying surface fluxes. In the case of strong vertical mass fluxes (21 and 22 August), however, L_s and L_{tot} are highly uncorrelated. Averaged over the entire period of positive surface moisture fluxes (6-18 UTC), the net moisture transport into the free atmosphere exceeds the water evaporated from the surface by a factor of 3.8 on 21 August and a factor of 2.7 on 22 August. Advection by the up-valley flows supplies this extra moisture flux.

6.4   Summary and conclusions

In this chapter we presented an evaluation of the daytime vertical mass and moisture fluxes from the Riviera Valley to the free atmosphere aloft. Three days with fair weather conditions have been simulated. The results can be summarized as follows:
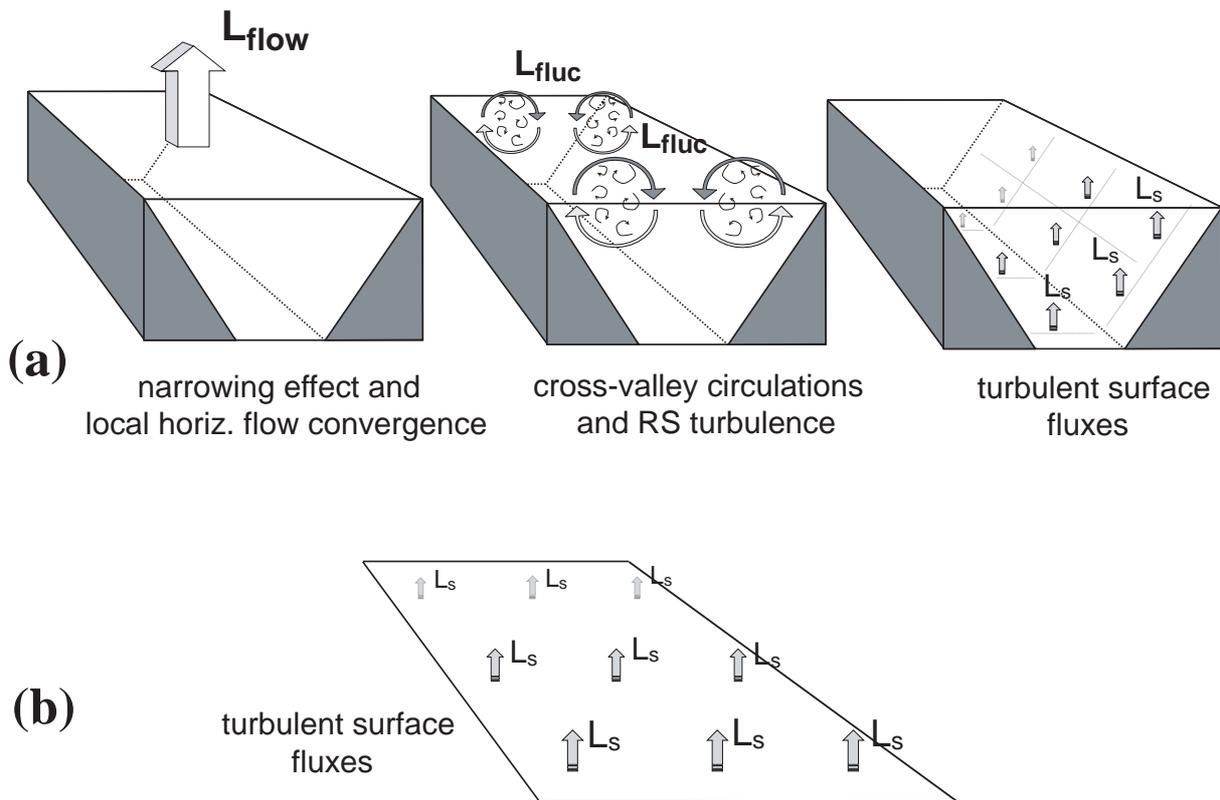
Figure 6.5: *Schematic representation of the processes responsible for vertical moisture fluxes over a steep valley: (a) as observed in reality and (b) as seen by a coarse numerical model not resolving the valley.*

(i) Depending on the stability of the valley atmosphere, considerable vertical mass fluxes out of the valley with magnitudes of up to 0.4–$2\ \mathrm{g\,s^{-1}\,m^{-2}}$ can be observed. These appear to be due to the narrowing of the valley cross-section and, in the evening of 21 August, due to an asymmetric valley-wind transition leading to horizontal flux convergence in the Riviera Valley.

(ii) Vertical mass fluxes transport moisture into the free atmosphere. In the daytime average, the amount of moisture carried out of the valley by these fluxes can be about 3-4 times larger than the amount of moisture evaporated from the surface underneath (if the stratification is not too stable).

(iii) Under very stable conditions in the valley atmosphere, vertical mass fluxes are suppressed. The export of moisture then seems to be mainly due to the effect of cross-valley circulations and resolved-scale turbulence. The associated moisture fluxes are of comparable magnitude to the turbulent surface fluxes.

Our findings indicate that classical subgrid-scale parameterizations in coarse atmospheric models can be far off reality if applied over highly mountainous terrain, at least when the stratification is only slightly stable or even neutral. Fig. 6.5 schematically summarizes the discrepancy between the 'real' moisture transport processes in a valley and those a coarse model not resolving the valley considers. Realistic parameterizations particularly need to include the mean vertical export of valley air. Our model simulations suggest that a simple valley-

narrowing argument may be helpful to provide a first estimate of the air carried out of the valley. From this net vertical mass flux, the corresponding fluxes of moisture (as well as pollutants, aerosols, and other scalars) can be easily obtained, if the specific humidity (pollutant concentration, aerosol concentration, etc.) of the air is known.

Chapter 7

Conclusions and outlook

7.1   Conclusions

This study has focused on the daytime atmosphere of a typical U-shaped Alpine valley under fair-weather conditions. Both the mean structure and the turbulence characteristics have been investigated. The methodology applied in this work is based on two pillars: On the one hand on the evaluation of measurement data from the MAP-Riviera field campaign, on the other hand on high-resolution large-eddy simulations with the Advanced Regional Prediction System (ARPS), which has been used in a one-way nesting mode with resolutions as fine as 150 m. Thus, the benefits of high-resolution numerical modeling have been combined with the "truth" provided by measurement data. The following conclusions can be drawn:

(i)   ARPS is able to accurately reproduce the flow structure and the boundary layer development observed in a steep and narrow Alpine valley. Even the scaling characteristics of measured profiles of turbulent kinetic energy (TKE) can be confirmed with the model. However, this success requires that the grid nesting configuration is carefully chosen and that high-resolution surface datasets are used to provide accurate lower boundary conditions. The soil moisture initialization on the 1 km grid, where the entire Riviera Valley system is resolved, is found to be one of the most important parameters for a successful simulation of the valley winds. Other aspects, such as topographic shading or the choice of sub-grid turbulence closure, have less impact on the mean structure of the valley atmosphere. The central conclusion is that simply increasing model resolutions without incorporating high-resolution surface datasets gives unsatisfactory results. This may be particularly important in the face of current research initiatives which aim at the application of operational atmospheric models with resolutions on the order of 2 km [Rotach, personal communication].

(ii)   On all days of observation, a pronounced thermally-driven valley wind system develops. The up-valley currents assume wind speeds of up to $10\,\mathrm{m\,s^{-1}}$ and reveal a jet-like flow structure. In the larger part of the valley, a cross-valley circulation pattern is observed which is consistent with classical slope-flow theory: Air rises along the sun-exposed heated slopes and subsides in the valley center. In the afternoons, this symmetric double-circulation degenerates to a simple cross-valley circulation with air subsiding on the shaded western side. However, this 'textbook' behavior is not observed along the entire valley. In the southern valley entrance region, the streamlines of the inflowing up-valley winds are highly curved, inducing a secondary circulation with strong subsidence along the sun-exposed and heated eastern slope. This demonstrates that the flow induced by local topographic peculiarities, such as a valley

bend, can dominate over and totally hide thermally-driven mountain winds. As the mechanism of the proposed secondary circulation is quite general, it should be observed elsewhere, when sharp curvature in the valley topography is present.

(iii)   The daily development of temperature profiles in the valley consistently shows a different pattern from that expected over flat terrain: A shallow well-mixed layer develops in the morning but stops growing by noon. On afternoons with strong valley winds, the stratification even stabilizes almost down to the valley floor. This behavior is due to the combined effect of cold-air advection in the up-valley direction and subsidence of warm air from above. Moreover, the well-mixed layer depth shows considerable variability in the along-valley direction. It is particularly shallow under the influence of the curvature-induced secondary circulation, where warm-air subsidence has its maximum. Given this high degree of heterogeneity, the results demonstrate that great caution is required when using point-measurements to characterize an entire valley atmosphere.

(iv)   The valley atmosphere directly interacts with the free atmosphere above: Overshooting slope winds inject valley air into the free atmosphere ("mountain venting") and induce subsidence over the valley center. Numerical simulations show that this subsidence of potentially warmer air contributes considerably to the valley heating. Its effect is of comparable, sometimes even larger, magnitude than heating due to turbulent heat flux convergence. This result indicates that the classical "topographic amplification factor" idea of valley heating may be too simplistic, because it is based on a volume argument forbidding interaction with the free atmosphere aloft. The observations in the Riviera Valley rather imply that a general theory or parameterization of valley heating, and thus of thermally-driven valley flow, must include and quantify the effects of mountain venting and subsidence heating.

(v)   A mass budget analysis of the valley atmosphere shows that, if the stratification is not too stable, subsidence does not fully compensate for the effect of mountain venting, i.e. a net vertical export of air mass is observed. This appears to be partially due to a narrowing of the valley cross-section, which is typical for Alpine valleys. The exported air carries a considerable amount of moisture from the valley into the atmosphere aloft. These moisture fluxes, which can exceed surface evaporation by a factor of 3-4, are not considered in classical subgrid-scale (SGS) parameterizations. Thus, the SGS fluxes assumed by a coarse atmospheric model can be unrealistic if applied over complex topography, not only due to potentially erroneous turbulence parameterizations, but also due to the neglect of non-turbulent mountain-induced SGS transport mechanisms.

(vi)   The turbulence structure of the valley atmosphere is different from that typically observed over flat and homogenous topography. First of all, turbulence activity is not restricted to the well-mixed layer but can be observed well above, even if the stratification is stable. Secondly, profiles of wind shear reveal a surprisingly strong lateral component. Thirdly, the classical convective TKE scaling approach of Deardorff (1970), which is based on the surface heat fluxes from directly underneath the TKE profile considered, does not work. And finally, TKE is mainly produced by wind shear instead of buoyancy, implying that turbulence in the Riviera Valley is not *directly* determined by the surface heat fluxes but probably *indirectly* via the thermally-driven valley winds. Despite these fundamental differences, a solution has been found to modify the Deardorff scaling approach so that it can be applied over the steep topography of the Riviera Valley. The TKE profiles scale surprisingly well if (i) a TKE-threshold

criterion is employed as a definition of the boundary layer height and (ii) if the surface fluxes from the sun-exposed westward facing slope sites are used for the calculation of the convective velocity scale. Thus, the turbulence structure in a steep and narrow valley is not as 'arbitrary' as one may have anticipated. On the contrary, it reveals consistent and reproducible patterns, indicating that suitable similarity functions can also be found for the atmospheric boundary layer in complex mountainous topography.

From these results and conclusions, six points can be crystallized which we consider to be generally applicable to other valley topographies:

1. High-resolution large-eddy simulations, if carefully initialized and configured, are able to reproduce atmospheric boundary layer flows over steep and complex terrain. However, accurate knowledge of the surface properties is necessary for successful simulations.

2. Thermally-driven valley flows and circulations can be heavily modified and complicated by topographic peculiarities such as valley bends. A combination of measurements and LES allows a quantitative description of such complex flow patterns and an understanding of the underlying physical processes.

3. Atmospheric boundary layers in steep and narrow Alpine valleys evolve differently from classical CBLs over flat terrain. In particular, the growth of a well-mixed layer is hindered. These differences can be fully understood by considering the effects of valley winds and circulation flows.

4. A general theory of thermally-driven valley winds should not be based solely on the application of a volume argument. It must also account for the interaction between the valley atmosphere and the free atmosphere aloft, which can be very important for the build-up of along-valley temperature gradients.

5. The vertical export of moisture and other scalars from a valley into the free atmosphere can significantly exceed the surface fluxes. To a large degree, this export is effected by terrain-related mechanisms, which are not considered in classical SGS parameterizations.

6. The turbulence characteristics of valley boundary layers are very different from those of CBLs over flat terrain. TKE is produced mainly by wind shear rather than by buoyancy. Nevertheless, even over very steep and complex topography, profiles of turbulence variables reveal consistent patterns, and scaling approaches can be found.

Given the highly complex and heterogeneous characteristics of typical valley atmospheres, it may still be a very long trek from the Riviera case-study to general parameterizations of SGS processes over mountainous topography. However, this dissertation has shown that there is a path, and that this path is accessible.

7.2   Outlook

Based on the findings of this study, several recommendations can be made for future research:

➠ *Generalization to other weather conditions.* As this study has "only" focused on sunny clear-sky days, one of the next logical steps is the generalization to other weather conditions. As a first move, this should be directly done on the basis of MAP-Riviera data, because the measurement periods also cover overcast and rainy days. Questions of interest include the following: How does the turbulence structure in an alpine valley behave under neutral or very stable conditions? How does the valley atmosphere "communicate" with the free atmosphere aloft when thermally-driven valley and slope winds are absent? How well can state-of-the-art high-resolution models simulate such a case? This latter aspect appears to be particularly challenging, as the system is more complex than on clear-sky days due to the existence of micro-physical processes.

➠ *Generalization to other valleys.* While the Riviera Valley can be regarded as a fairly typical and representative Alpine valley, it is nevertheless uncertain whether the presented results apply in exactly the same manner to other valley topographies. For instance, the TKE scaling approach presented in Sections 2.5.2 and 5.2.3 probably needs to be modified in the case of east-west oriented valleys, which reveal different insolation patterns. Therefore, to generalize the Riviera observations, more case-studies are needed with valleys of different size, shape, climate, surface structure and geographic orientation. They should be undertaken in a similar way as presented here, i.e. using a combination of field measurements and high-resolution LES. Even though it may appear tempting to just rely on simulations, measurement data are still urgently needed to evaluate and optimize model configurations, as has been shown in Chapter 3.

➠ *Evaluation of SGS parameterizations in coarse models.* Data from the Riviera simulations as well as from other (future) case-studies of this type can be used to evaluate the performance of numerical weather and climate prediction models in complex terrain. From high-resolution model output, vertical fluxes of heat, moisture and momentum can be directly calculated and averaged over an entire valley domain (as has been done for moisture in Chapter 6); comparisons can then be made to the parameterized SGS fluxes a coarse atmospheric model produces on the grid points corresponding to the valley domain. That way, an estimate could be obtained of the errors numerical weather and climate prediction models may generate over mountainous topography.

➠ *Idealized and semi-idealized simulations.* A systematic and quantitative evaluation of the key variables determining the structure of alpine boundary layers and valley wind systems should be carried out on the basis of idealized simulations. Such a study could follow the proposal of Schmidli (2005), who suggests systematic large-eddy simulations in idealized valleys of varying topology, surface properties and atmospheric conditions. This should also include 'semi-idealized' simulations, i.e. simulations over idealized valley topographies that are embedded into a real case environment and thus allow for direct comparisons to a 'true' reference. Further information on this method is given in Appendix B. Such idealized and semi-idealized simulations would improve the physical understanding of valley atmospheres. This would contribute to the development of parameterizations of valley flows and the associated vertical fluxes of momentum, heat and moisture into the free atmosphere.

➠ *Improvement of simulation tools*. The performance of high-resolution large-eddy simulations over complex topography needs further evaluation. The effect of different turbulence models over mountainous terrain is not yet clear. Their evaluation requires larger high-resolution domains than used in this study, as the dominating effect of lateral boundary forcing needs to be reduced. Another aspect to be investigated is the choice of grid-nesting technique. For example, two-way nesting is often considered as being preferable to one-way nesting approaches, but its superiority in complex topography has not yet been proven (Lozej and Bornstein, 1999; Soriano et al., 2001). Finally, improved radiation schemes need to be included in future model versions. In particular, incoming nocturnal longwave radiation is still treated in a very simplistic one-dimensional manner and does not account for the effect of, say, heated valley sidewalls. More advanced radiation models must consider the surrounding topography and sky-view corrections.

➠ *Soil moisture*. One of the central conclusions of Chapter 3 is that a detailed knowledge of soil moisture is essential for accurate simulations of valley wind systems. Particularly with respect to future operational applications, this points to the need for accurate soil moisture datasets in high resolutions over large domains (such as the entire Alps). As soil moisture has been shown to vary on very small scales, an operational network of measurement stations would have to be unrealistically dense. Rather, a combined approach may be useful, consisting of soil moisture measurements, the application of hydrological models and the use of remote sensing techniques.

Appendix A

ARPS - The Advanced Regional Prediction System

The Advanced Regional Prediction System (ARPS) was developed and tested at the Center for Analysis and Prediction of Storms (CAPS) at the University of Oklahoma. Version 5.1.0 of this freely available code[1] has been chosen as the simulation tool for this study. The model is particularly designed for the simulation of mesoscale and microscale phenomena, such as individual thunderstorms, snow bands and downslope windstorms. A detailed description of the model structure and numerics can be found in the ARPS User's manual (Xue et al., 1995) as well as in the papers of Xue et al. (2000, 2001). Here, only a very brief summary of the main model features is given.

A.1 Model dynamics

ARPS solves prognostic equations for velocity, pressure, potential temperature, atmospheric water substance, and, depending on the choice of subgrid-scale turbulence closure, for turbulent kinetic energy (TKE). The underlying physical equations include the three-dimensional, compressible non-hydrostatic Navier-Stokes equations, the equation of state of moist air and conservation equations of heat, mass and water substance. The equations are solved in a terrain-following, curvilinear and horizontally orthogonal coordinate-system, which can be stretched in the vertical (so-called σ-z-coordinates). As is typical for non-hydrostatic numerical models, the mode-splitting technique of Klemp and Wilhelmson (1978) is used for the integration of the dynamic equations. This means, the acoustically active terms are integrated at a smaller time step than the slower modes. The small time-step integration of the horizontal velocity components is done with an explicit forward-in-time scheme, while the equations of vertical velocity and pressure are treated implicitly. The large time-steps are integrated by means of the leapfrog scheme. For the calculation of the advection terms, ARPS provides the choice between second-order and fourth-order accurate centered formulations. The finite differences are thereby solved on a staggered Arakawa C-grid (Arakawa and Lamb, 1977).

Several options are available for the subgrid-scale turbulence model. If not stated differently, the 1.5-order TKE closure of Deardorff (1980) and Moeng (1984) is applied in this study. Small-scale noise, which builds up due to non-linear interactions, is removed by adding fourth-order computational mixing to the prognostic equations. Atmospheric radiation transfer is calculated with the models of Chou (1990, 1992) for short-wave radiation and the model of Chou

---

[1]http://www.caps.ou.edu/ARPS/index_flash.html

131

and Suarez (1994) for the long-wave part of the spectrum. Additionally, topographic shading of incoming direct solar radiation is considered using the model of Colette et al. (2003). The choice of microphysics scheme is irrelevant for the Riviera study, as only dry clear-sky days are considered.

A.2   Boundary conditions

(i)   Top and lateral boundary conditions.   As an upper boundary condition, a Rayleigh damping layer is applied. It damps out upward propagating waves in order to avoid reflection by the upper lid. The lateral boundary conditions are determined by a one-way nesting procedure: output data of simulations on a larger, coarser-scale domain are used as time-dependent boundary forcing (see Fig. A.1 and Section 3.3 for more details on the nesting levels used in this study). This is done by interpolating coarse-grid model results to a Davies-type (1983) relaxation zone on the edges of the finer grid.

(ii)   Bottom boundary conditions.   The surface exchange of momentum, heat and moisture is quantified by means of a drag coefficient approach (Businger et al., 1971) and stability-dependent similarity laws (based on Monin Obukhov similarity theory). This requires information on the land surface characteristics, such as roughness length and vegetation coverage, which is obtained from external datasets. Details of the datasets used in this study are presented in Section 3.3.5. Additionally, knowledge of soil temperature, soil moisture and canopy water is needed. These time-dependent surface properties are predicted with the help of a two-layer soil model that solves the surface energy and moisture budget equations (Noilhan and Planton, 1989; Jacquemin and Noilhan, 1990; Pleim and Xiu, 1995; Boone et al., 1999). By default, ARPS distinguishes between 14 vegetation classes and 13 soil types. In the presented high-resolution simulations, "rock" is considered as an additional soil type which is characterized by the absence of latent heat fluxes. We refined the ARPS vegetation classes to a new set of 30 land use categories. Partially following De Wekker's (2002) approach, each of these categories is assigned with values for leaf area index, fractional converage of vegetation, roughness length and other vegetation-specific quantities, which are summarized in Table A.1.
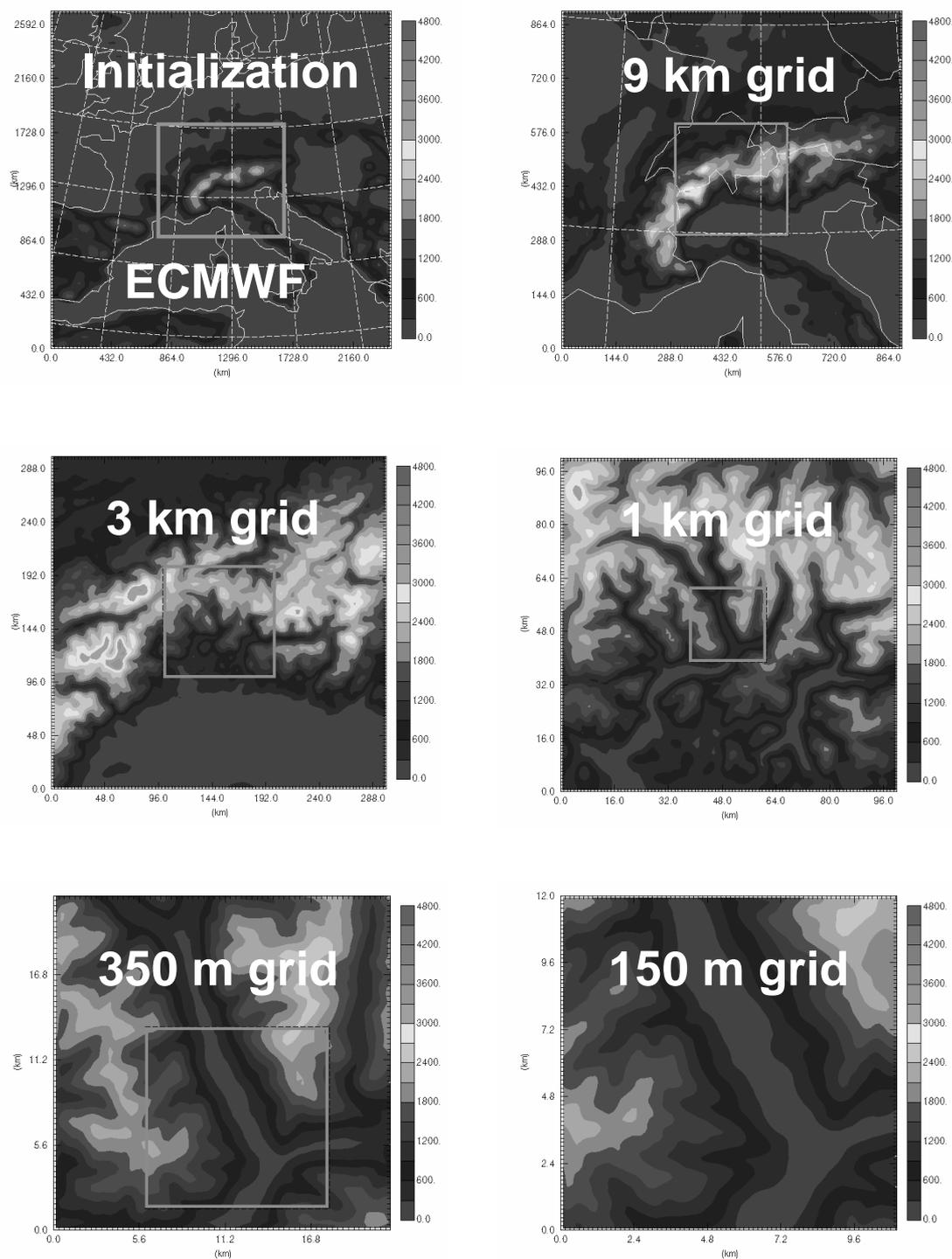
Figure A.1: *Nesting levels applied in this study. Starting from ECMWF analysis data (grid spacing of 0.5°, corresponding to approximately 60 km), five nested grids with resolutions of 9 km, 3 km, 1 km, 350 m and 150 m are used. The boxes within the panels show the position of the next finer grid.*

Table A.1: *The refined 30 vegetation categories used in the high-resolution simulations of this study. Each of these vegetation types is assigned with values for leaf area index (LAI), fractional vegetation coverage (veg), roughness length (z_0), minimum surface resistance (rsmin) and a species-dependent threshold value of incoming radiation (rgl) as shown in this table. More details on these parameters can be found in Xue et al. (1995).*

No.	Description	LAI	veg	z_0 [m]	rsmin [s/m]	rgl [W/m^2]
1	Evergreen needleleaf tree	6 (d)	0.8 (b)	1 (b)	175 (d)	30 (c)
2	Deciduous needleleaf tree	5 (d)	0.8 (b)	1 (b)	175 (d)	30 (c)
3	Deciduous broadleaf tree	5 (d)	0.8 (b)	0.8 (b)	200 (d)	30 (c)
4	Evergreen broadleaf tree	5 (d)	0.9 (b)	2 (b)	120 (d)	30 (c)
5	Short grass	2 (b)	0.8 (b)	0.02 (b)	40 (a)	100 (c)
6	Tall grass	3 (x)	0.8 (b)	0.1 (b)	83 (d)	100 (c)
7	Desert	0 (b)	0.01 (x)	0.05 (b)	999 (a)	100 (c)
8	Semi-desert	1.5 (x)	0.1 (b)	0.1 (b)	300 (a)	100 (c)
9	Ice	0 (b)	0.1 (a)	0.005 (a)	999 (a)	100 (c)
10	Tundra	1 (d)	0.2 (d)	0.04 (b)	500 (a)	100 (c)
11	Evergreen shrub	3 (d)	0.8 (b)	0.1 (b)	200 (d)	30 (c)
12	Deciduous shrub	3 (d)	0.8 (b)	0.1 (b)	200 (d)	30 (c)
13	Mixed woodland	5 (d)	0.8 (b)	0.8 (b)	200 (d)	30 (c)
14	Water	0 (b)	0 (a)	0.001 (a)	0 (E-30) (a)	100 (c)
15	Crop/mixed farming	3 (d)	0.85 (b)	0.06 (b)	70 (d)	100 (c)
16	Irrigated crop	3 (d)	0.8 (b)	0.06 (b)	60 (d)	100 (c)
17	Bog or marsh	4.5 (x)	0.8 (b)	0.03 (b)	5 (a)	100 (c)
18	Evergreen needleleaf forest	6 (d)	0.8 (b)	0.98 (b)	175 (d)	30 (c)
19	Evergreen broadleaf forest	5 (d)	0.9 (b)	2.2 (b)	120 (d)	30 (c)
20	Deciduous needleleaf forest	5 (d)	0.8 (b)	0.92 (b)	175 (d)	30 (c)
21	Deciduous broadleaf forest	5 (d)	0.8 (b)	0.91 (b)	200 (d)	30 (c)
22	Mixed cover	5 (d)	0.8 (b)	0.87 (b)	175 (e)	30 (c)
23	Woodland	5.7 (e)	0.8 (b)	0.83 (b)	174 (e)	30 (c)
24	Wooded grassland	5 (e)	0.8 (b)	0.51 (b)	169 (e)	30 (c)
25	Closed shrubland	5 (e)	0.6 (b)	0.14 (b)	175 (e)	30 (c)
26	Open shrubland	3 (x)	0.2 (b)	0.08 (b)	179 (e)	100 (c)
27	Grassland	2.6 (e)	0.8 (x)	0.04 (b)	83 (d)	100 (c)
28	Cropland	3 (x)	0.8 (b)	0.11 (b)	65 (x)	100 (c)
29	Bare ground	0.1 (x)	0.07 (b)	0.05 (b)	999 (x)	100 (c)
30	Urban and built up	2 (d)	0.4 (d)	0.8 (b)	150 (d)	100 (c)

(a) = ARPS values

(b) = LEAF-2 biophysical paramateres as used in RAMS (see DeWekker 2002)

(c) = Noilhan and Planton (1989)

(d) = Xiu and Pleim (2001)

(e) = LDAS-data, http://ldas.gsfc.nasa.gov/LDASnew/LDAS8th/MAPPED.VEG/web.veg.table.html

(x) = estimates based on comparison of various sources

Appendix B

Semi-idealized simulations

Semi-idealized simulations, as carried out by Rucker (2003) in the Wipp Valley in Austria, could provide a helpful tool for the investigation of the impact of terrain and surface conditions on the valley atmosphere. The idea is to apply controlled modifications to topography or surface characteristics while preserving real-case boundary forcing and initialization configurations. In contrast to fully idealized simulations, the model output can thus be directly compared to 'real' reference cases. In this appendix, two semi-idealized test simulations of the Riviera Valley atmosphere are presented, with the aim to motivate more comprehensive and systematic studies of this type.

In the first simulation, a straightened and smoothed 'version' of the Riviera Valley is used (from now on referred to as T1). The second simulation employs a topography which is similar to T1 except that the valley is additionally widened (topography T2). The terrain modifications are only considered on the 1 km grid and the 350 m grid, because the Riviera Valley is not resolved at all on the coarser nesting levels. The implementation of T1 and T2 on these two grids is shown in Figs. B.1 and B.2. For comparison, Fig. B.3 displays the unmodified topography (REF). Note that both in T1 and T2 the tributaries of the Riviera Valley are removed. As an example, the 22 August case is simulated, using these two modified topographies. The initialization and grid nesting configurations are equivalent to those used in the real-case simulations of Section 4.2.

Fig. B.4 shows the diurnal cycles of simulated surface potential temperature in the three topographies REF, T1 and T2 at the location of measurement site 'A1' (see Fig. 4.1). The corresponding measurement data are displayed in Fig. 4.2b. Interestingly, all three cases reveal similar daytime surface temperatures, while at night the T1 and T2 cases are about 2–3 °C warmer than when the original topography is used. From measurements in the Bush Creek Valley, Colorado, Porch et al. (1989) suggest that tributaries are essential for the production of nocturnal cold air flow. This might explain the observed warm bias in T1 and T2. Further evaluation of this phenomenon is not provided here.

Comparisons of surface wind speeds are presented in Fig. B.5a. With respect to the unmodified REF case, daytime wind speeds are higher in T1 and lower in T2. This observation is plausible: in the straightened and smoothed topography of T1, less resistance and friction oppose the up-valley winds, i.e. they can accelerate to higher velocities than in REF. In T2, on the other hand, the valley diameter is widened. The up-valley winds can spread over a larger cross-sectional area and thus do not need to flow as fast as in REF or T1 in order to effect comparable mass transport. Interestingly, the transition times between up-valley and down-valley flow are hardly influenced by the topographic modifications (Fig. B.5b). This indicates that
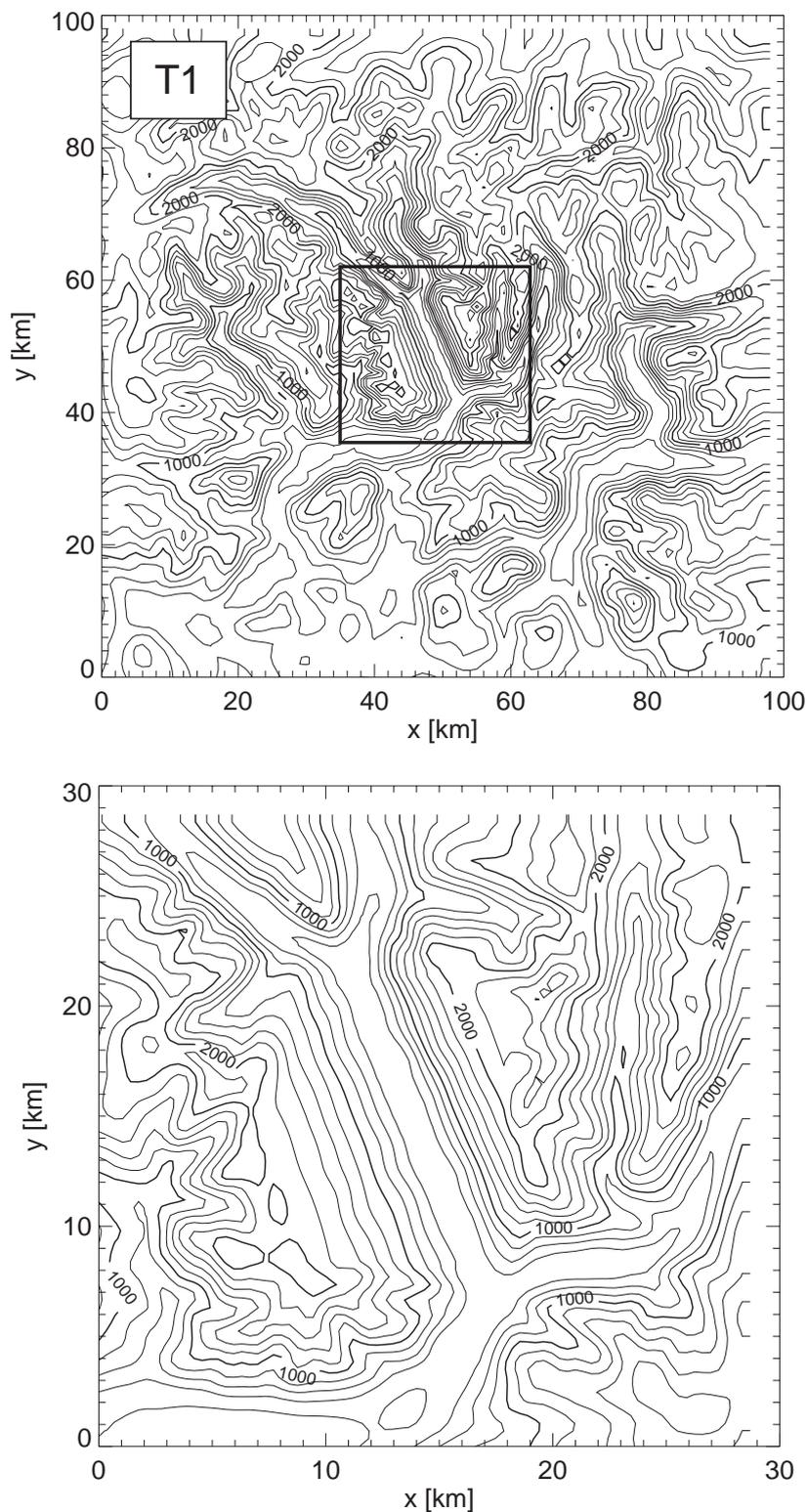
Figure B.1: *Modified Riviera topography ('T1') on the 1 km grid (upper panel) and the 350 m grid (lower panel). The Riviera Valley is straightened and smoothed, and the tributaries are removed. The black box in the upper panel indicates the location of the 350 m domain. For comparison, the unmodified Riviera Valley is shown in Fig. B.3.*

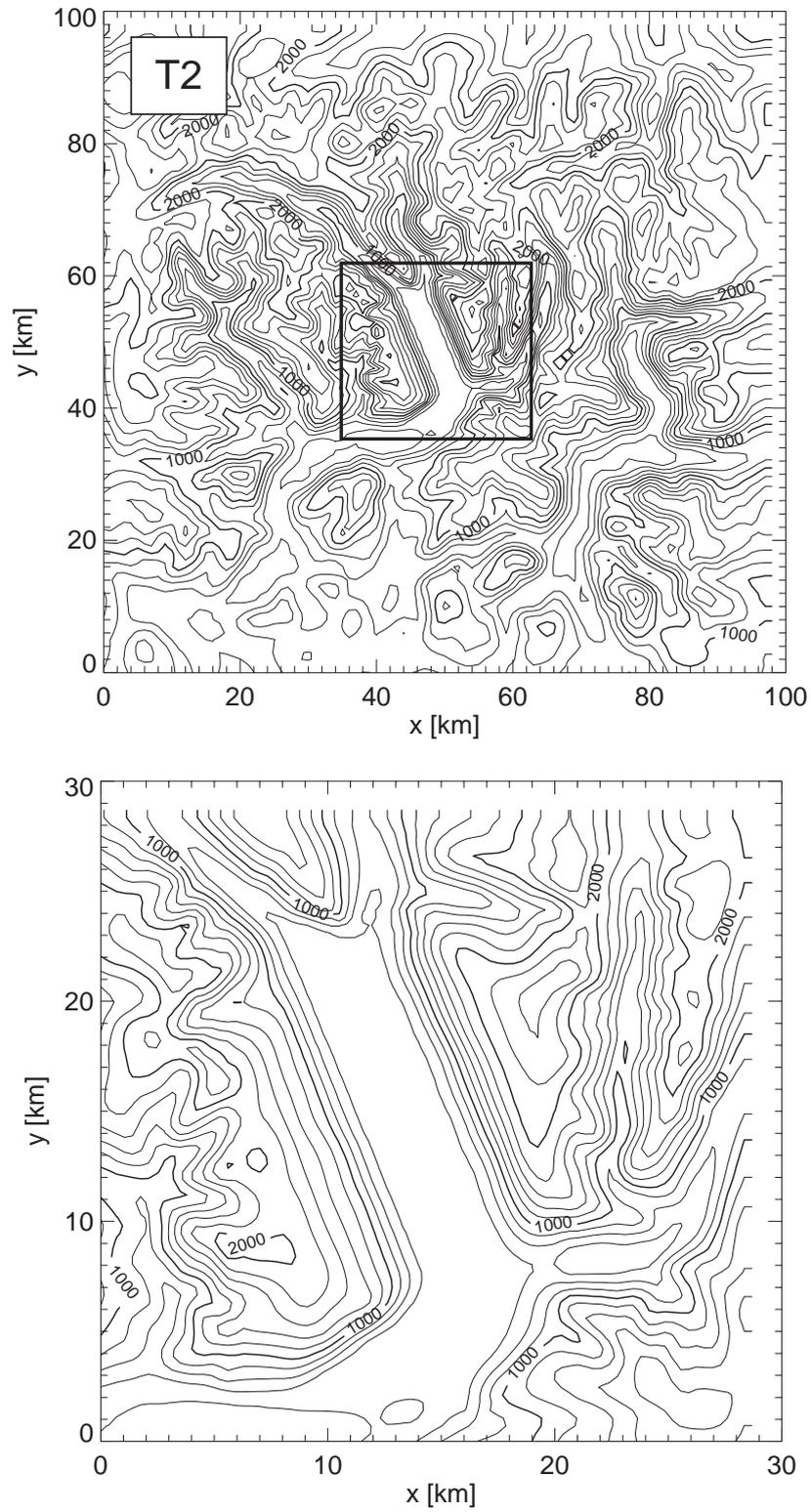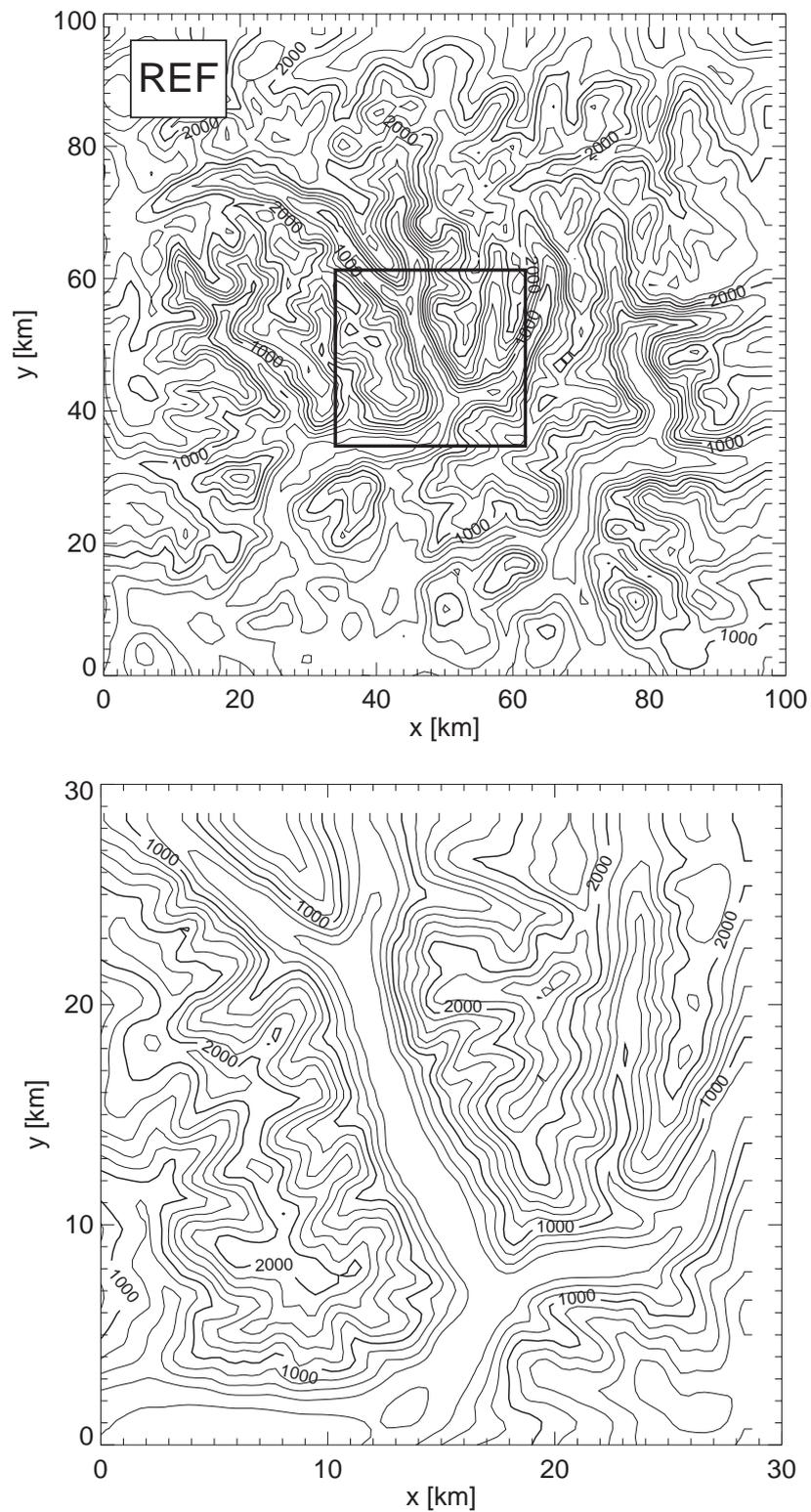**Figure B.2:** *As Fig. B.1, however with the Riviera Valley being additionally widened ('T2').*

Figure B.3: *Unmodified Riviera topography ('REF') on the 1 km grid (upper panel) and the 350 m grid (lower panel).*
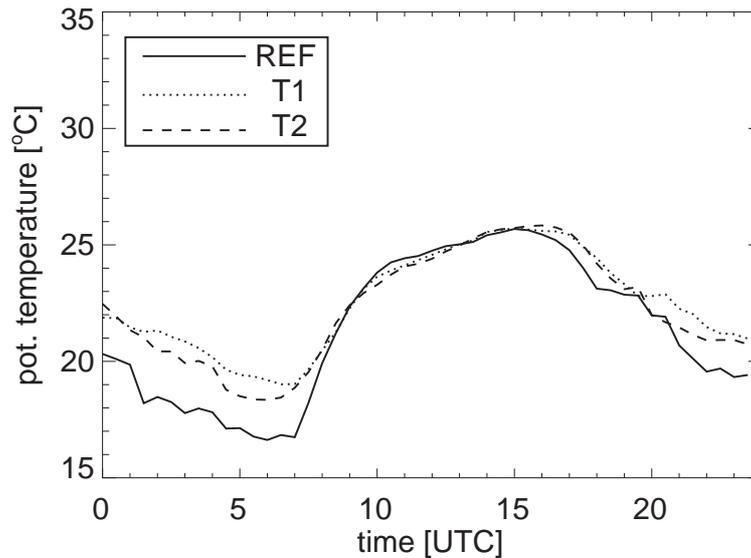
Figure B.4: *Surface potential temperature time series at the coordinates of measurement site A1 (see Fig. 4.1), using the unmodified topography REF and the two modified topographies T1 and T2.*

up-valley winds are produced on a scale which extends well beyond the Riviera Valley; i.e. in order to see an effect, it may be necessary to additionally alter the topographies of the upstream Magadino Valley and the downstream Leventina Valley.

Not only the up-valley currents are affected by topographic modifications. In Sections 2.4.3 and 4.3.2, for example, a curvature-induced secondary circulation at the southern valley mouth is described. Such a circulation also develops in the modified topographies T1 and T2, as is shown in Fig. B.6. However, with a subsidence velocity not exceeding 0.5 m s^{-1}, the circulation in T2 is much weaker than in T1, where air subsides with up to 1.4 m s^{-1}. The reason is the direct dependance of secondary circulation strength on the along-valley flow speed (Kalkwijk and Booij, 1986), which is lower in T2. Note that in T1 the circulation is strong enough to suppress the development of up-slope winds on the sun-exposed eastern side, while in T2 a shallow up-slope layer can persist. Given the conclusions presented in Chapter 4, the weaker secondary circulation of T2 implies reduced subsidence of warm air from the free atmosphere aloft. Following the argumentation of Section 4.4, one would thus expect the well-mixed layer to grow deeper in T2 than in T1. Fig. B.7 shows that this is indeed the case. While the mixed layer in T1 assumes a maximum depth of only about 200 m, which is comparable to the REF case in Fig. 4.9a, it grows twice as deep in T2.

In summary, these tests demonstrate the feasibility and the potential of semi-idealized simulations for the investigation of valley atmospheres. It has been shown that controlled variations in the valley topography directly affect flow structure and boundary layer characteristics in a way that is consistent with the observations presented in this dissertation. The success of these test simulations encourages more extensive and more systematic studies of this semi-idealized type, which should also encompass modifications in vegetation structure and soil type. This would allow a further generalization of our Riviera findings and facilitate the quest for valley boundary layer parameterizations.
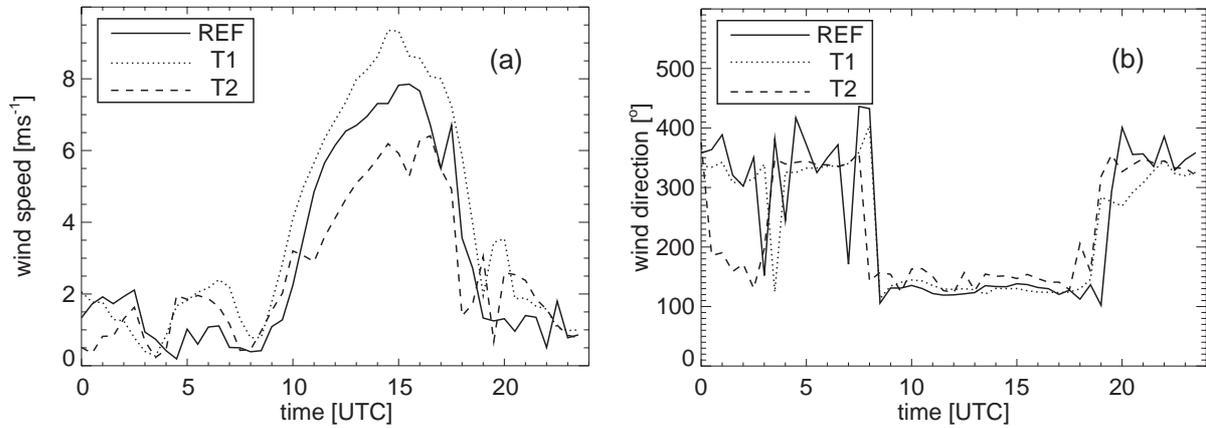
Figure B.5: *Time series of surface wind speed (a) and direction (b) at the coordinates of measurement site A1 (see Fig. 4.1) on 22 August, using the unmodified topography REF and the two modified topographies T1 and T2.*
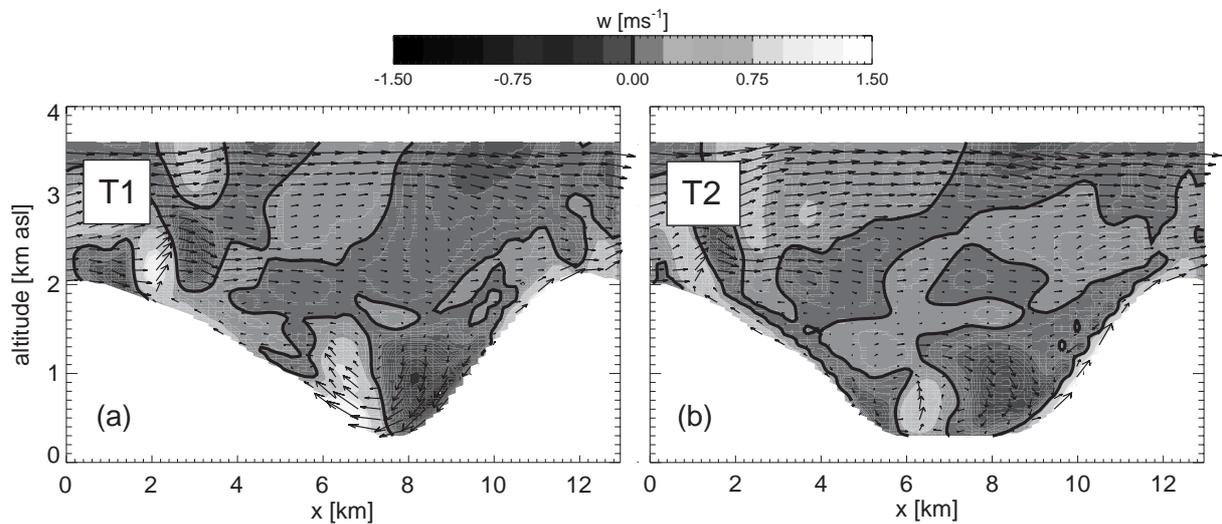
Figure B.6: *Cross-valley wind vectors on 22 August at 1430 UTC in a slice close to the southern valley mouth (same position as in Fig. 4.6d). Panel (a) is with topography T1, panel (b) with T2. The shading indicates vertical wind velocity, and the black line is the contour of zero vertical velocity.*
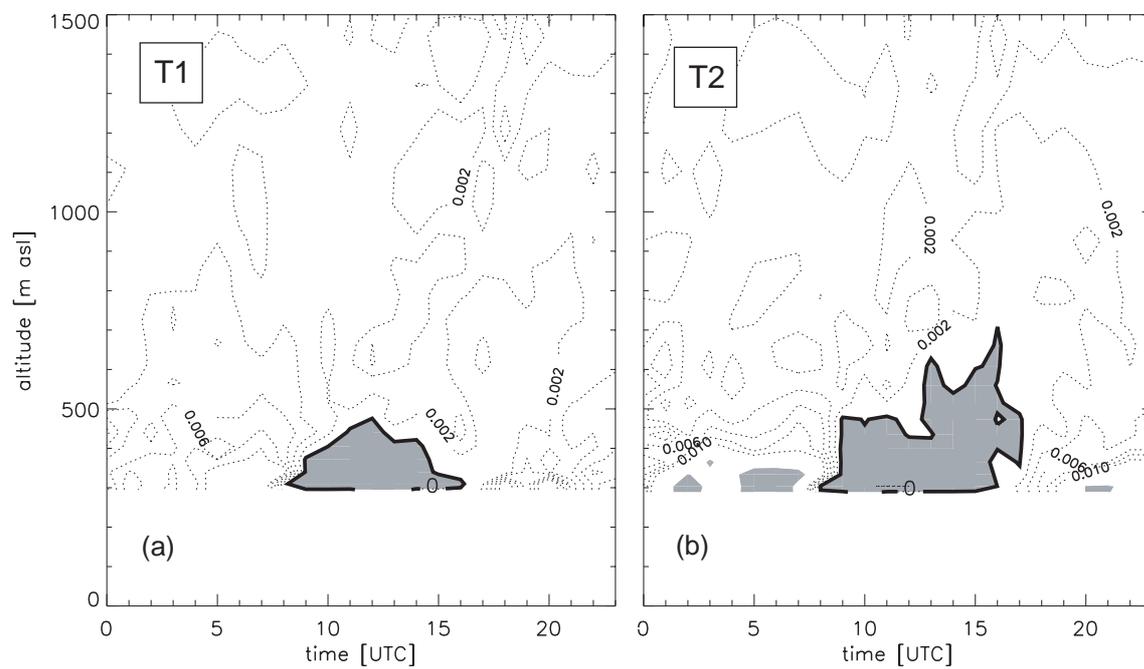
Figure B.7: *Time-height plots of simulated lapse rate on 22 August (contours labeled in $K\,m^{-1}$). The shading indicates neutral to super-adiabatic stratification. (a) is in topography T1 and (b) in T2.*

References

Andretta, M., A. Weiss, N. Kljun, and M. W. Rotach, 2001: Near-surface turbulent momentum flux in an Alpine valley: observational results. *MAP-Newsletter*, **15**, 122–125.

Andretta, M., S. Zimmermann, M. W. Rotach, and P. Calanca, 2000: Investigation of the near-surface boundary layer in an Alpine valley. *MAP-Newsletter*, **13**, 68–69.

Arakawa, A. and V. R. Lamb: 1977, Computational design of the basic dynamical processes of the UCLA general circulation model. *Methods in Computational Physics*, J. Chang, ed., Academic Press, New York, volume 17, 173–265.

Atkinson, B. W. and A. N. Shahub, 1994: Orographic and stability effects on daytime, valley-side slope flows. *Bound.-Layer Meteor.*, **68**, 275–300.

Attié, J.-L., A. Druilhet, B. Bénech, and P. Durand, 1999: Turbulence on the lee side of a mountain range: Aircraft observations during PYREX. *Quart. J. Roy. Meteor. Soc.*, **125**, 1359–1381.

Bader, D. C. and T. B. McKee, 1985: Effects of shear, stability and valley characteristics on the destruction of temperature inversions. *J. Clim. Appl. Meteor.*, **24**, 822–832.

Bader, D. C., T. B. McKee, and G. J. Tripoli, 1987: Mesoscale boundary-layer evolution over complex terrain. Part I: Numerical simulation of the diurnal cycle. *J. Atmos. Sci.*, **44**, 2823–2838.

Bader, D. C. and C. D. Whiteman, 1989: Numerical simulation of cross-valley plume dispersion during the morning transition period. *J. Appl. Meteor.*, **28**, 652–664.

Banta, R. M.: 1990, The role of mountain flows in making clouds. *Atmospheric processes over complex terrain*, W. Blumen, ed., American Met. Soc., 229–283.

Banta, R. M. and P. T. Gannon, 1995: Influence of soil-moisture on simulations of katabatic flow. *Theor. Appl. Climatol.*, **52**, 85 – 94.

Barr, S. and M. M. Orgill, 1989: Influence of external meteorology on nocturnal valley drainage winds. *J. Appl. Meteor.*, **28**, 497–517.

Barry, R. G.: 1992, *Mountain weather and climate*, Routledge, London and New York. 2nd edition.

Bathurst, J. C., C. R. Thorne, and R. D. Hey, 1977: Direct measurements of secondary currents in river bends. *Nature*, **269**, 504–506.

Baumann-Stanzer, K. and I. Groehn, 2004: Alpine radiosoundings - feasible for mixing height determination? *Meteorol. Z.*, **13**, 131–142.

Beljaars, A. C. M., P. Viterbo, M. J. Miller, and A. K. Betts, 1996: The anolamous rainfall over the United States during July 1993: Sensitivity to land surface parameterization and soil moisture. *Mon. Wea. Rev.*, **124**, 362–383.

Benoit, R., C. Schär, P. Binder, S. Chamberland, H. C. Davies, M. Desgagne, C. Girard, C. Keil, N. Kouwen, D. Lüthi, D. Maric, E. Müller, P. Pellerin, J. Schmidli, F. Schubiger, C. Schwierz, M. Sprenger, A. Walser, S. Willemse, W. Yu, and E. Zala, 2002: The real-time ultrafinescale forecast support during the Special Observing Period of the MAP. *Bull. Amer. Met. Soc.*, **83**, 85 – 109.

Binder, P. and C. Schär, 1996: MAP design proposal. *Available from the MAP Programme Office, MeteoSwiss, CH 8044, Zürich, Switzerland*.

Blumen, W., 1990: *Atmospheric processes over complex terrain*. American Meteorological Society, Boston.

Boone, A., J.-C. Calvet, and J. Noilhan, 1999: Inclusion of a third soil layer in a land surface scheme using the force-restore method. *J. Appl. Meteor.*, **38**, 1611–1630.

Bougeault, P., P. Binder, A. Buzzi, R. Dirks, R. Houze, J. Kuettner, R. B. Smith, R. Steinacker, and H. Volkert, 2001: The MAP Special Observing Period. *Bull. Amer. Met. Soc.*, **82**, 433–462.

Businger, J. A., J. C. Wyngaard, Y. Izumi, and E. F. Bradley, 1971: Flux-profile relationships in the atmospheric surface layer. *J. Atmos. Sci.*, **28**, 181–189.

Cairns, M. M. and J. Corey, 2003: Mesoscale model simulations of high-wind events in the complex terrain of western Nevada. *Wea. Forecast.*, **18**, 249–263.

Caughey, S. J. and S. G. Palmer, 1979: Some aspects of turbulence structure through the depth of the convective boundary-layer. *Quart. J. Roy. Meteor. Soc.*, **105**, 811–827.

Cederwall, R. T., 2001: *Large-eddy simulation of the evolving stable boundary layer over flat terrain*. Ph.D. thesis, Stanford University.

Chen, F., T. T. Warner, and K. Manning, 2001: Sensitivity of orographic moist convection to landscape variability. A study of the Buffalo Creek, Colorado, flash flood case of 1996. *J. Atmos. Sci.*, **58**, 3204 – 3223.

Chen, Y., F. L. Ludwig, and R. L. Street, 2004: Stably stratified flows near a notched transverse ridge across the Salt Lake Valley. *J. Appl. Meteor.*, **43**, 1308–1328.

Chou, M.-D., 1990: Parameterization for the absorption of solar radiation by O_2 and CO_2 with application to climate studies. *J. Climate*, **3**, 209–217.

— 1992: A solar radiation model for use in climate studies. *J. Atmos. Sci.*, **49**, 762–772.

Chou, M.-D. and M. J. Suarez, 1994: An efficient thermal infrared radiation parameterization for use in general circulation models. NASA Tech Memo 104606, 85 pp, NASA Center for Aerospace Information, 800 Elkridge Landing Road, Linthicum Heights, MD 21090-2934.

Chow, F. K., 2004: *Subfilter-scale turbulence modeling for large-eddy simulation of the atmospheric boundary layer over complex terrain*. Ph.D. thesis, Stanford University.

Chow, F. K. and R. L. Street, 2004: Evaluation of turbulence models for large-eddy simulations of flow over Askervein hill. Paper 7.11. *Amer. Meteor. Soc., 16th Symp. Bound. Layers Turb.*.

Chow, F. K., R. L. Street, M. Xue, and J. H. Ferziger, 2005a: Explicit filtering and reconstruction turbulence modeling for large-eddy simulation of neutral boundary layer flow. *J. Atmos. Sci.*, **in press**.

Chow, F. K., A. P. Weigel, R. L. Street, M. W. Rotach, and M. Xue: 2004, Paper 6.2: High-resolution large-eddy simulations of the Riviera Valley: Methodology and sensitivity studies. *Proceedings 11th Conference on Mountain Meteorology, Amer. Met. Soc.*, Bartlett, NH.

Chow, F. K., A. P. Weigel, R. L. Street, M. W. Rotach, and M. Xue, 2005b: High-resolution large-eddy simulations of flow in a steep alpine valley. Part I: Methodology, verification and sensitivity studies. *J. Appl. Meteor., **submitted for publication***.

Clements, W. E., J. A. Archuleta, and P. H. Gudiksen, 1989: Experimental design for the 1984 ASCOT field study. *J. Appl. Meteor.*, **28**, 405–413.

Colette, A., F. K. Chow, and R. L. Street, 2003: A numerical study of inversion-layer breakup and the effects of topographic shading in idealized valleys. *J. Appl. Meteor.*, **42**, 1255 – 1272.

Coppin, P. A., E. F. Bradley, and J. J. Finnigan, 1994: Measurements of flow over an elongated ridge and its thermal stability dependence: the mean field. *Bound.-Layer Meteor.*, **69**, 173–199.

Davies, H. C., 1983: Limitations of some common lateral boundary schemes used in regional NWP models. *Mon. Wea. Rev.*, **111**, 1002–1012.

Dayan, U., R. Shenhav, and M. Graber, 1988: The spatial and temporal behavior of the mixed layer in Israel. *J. Appl. Meteor.*, **27**, 1382–1394.

De Franceschi, M. and D. Zardi, 2003: Evaluation of cut-off frequency and correction of filter-induced phase lag and attenuation in eddy covariance analysis of turbulence data. *Bound.-Layer Meteor.*, **108**, 289–303.

De Wekker, S. F. J., 2002: *Structure and morphology of the convective boundary layer in mountainous terrain*. Ph.D. thesis, The University of British Columbia, Vancouver, Canada.

De Wekker, S. F. J., D. G. Steyn, J. D. Fast, M. W. Rotach, and S. Zhong, 2005: The performance of RAMS in representing the convective boundary layer structure in a very steep valley. *Environ. Fluid Mech.*, **5**, 35–62.

De Wekker, S. F. J., D. G. Steyn, and S. Nyeki, 2004: A comparison of aerosol-layer and convective boundary-layer structure over a mountain range during STAAARTE '97. *Bound.-Layer Meteor.*, **113**, 249–271.

Deardorff, J. W., 1970: Convective velocity and temperature scales for the unstable planetary boundary layer and for Rayleigh convection. *J. Atmos. Sci.*, **27**, 1211–1213.

— 1972: Numerical investigation of neutral and unstable planetary boundary layers. *J. Atmos. Sci.*, **29**, 91–115.

— 1980: Stratocumulus-capped mixed layers derived from a 3-dimensional model. *Bound.-Layer Meteor.*, **18**, 495–527.

Defant, F.: 1951, Local winds. *Compendium of Meteorology*, T. F. Malone, ed., Amer. Met. Soc, Boston, 655–672.

Doran, J. C., J. D. Fast, and J. Horel, 2002: The VTMX 2000 campaign. *Bull. Amer. Met. Soc.*, **83**, 537–551.

Doyle, J. D. and D. R. Durran, 2002: The dynamics of mountain-wave-induced rotors. *J. Atmos. Sci.*, **59**, 186–201.

Dudhia, J., 1993: A non-hydrostatic version of the Penn State/NCAR mesoscale model: Validation tests and simulation of an Atlantic cyclone and cold front. *Mon. Wea. Rev.*, **121**, 1493–1513.

Durran, D. R.: 1990, Mountain waves and downslope winds. *Atmospheric processes over complex terrain*, W. Blumen, ed., American Met. Soc., 59–82.

Durran, D. R. and J. B. Klemp, 1983: A compressible model for the simulation of moist mountain waves. *Mon. Wea. Rev.*, **111**, 2341–2361.

Eastman, J. L., R. A. Pielke, and D. J. McDonald, 1998: Calibration of soil moisture for large-eddy simulations over the FIFE area. *J. Atmos. Sci.*, **55**, 1131–1140.

Egger, J.: 1990, Thermally forced flows: Theory. *Atmospheric processes over complex terrain*, W. Blumen, ed., American Met. Soc., Boston, 43–58.

Egger, J., S. Bajrachaya, U. Egger, R. Heinrich, J. Reuder, P. Shayka, H. Wendt, and V. Wirth, 2000: Diurnal winds in the Himalayan Kali Gandaki Valley. Part I: Observations. *Mon. Wea. Rev.*, **128**, 1106–1122.

Fast, J. D., S. Zhong, and C. D. Whiteman, 1996: Boundary layer evolution within a canyonland basin. Part II: Numerical simulations of nocturnal flows and heat budgets. *J. Appl. Meteor.*, **35**, 2162–2178.

Ferziger, J. H.: 1996, Large eddy simulations. *Simulation and modeling of turbulent flows*, T. B. Gatski, M. Y. Hussaini, and J. L. Lumley, eds., Oxford University Press, chapter 3, 109–154.

Finnigan, J. J., M. R. Raupach, E. F. Bradley, and G. K. Aldis, 1990: A wind tunnel study of turbulent flow over a two-dimensional ridge. *Bound.-Layer Meteor.*, **50**, 277–317.

Freytag, C., 1985: MERKUR results: Aspects of the temperature field and the energy budget in a large alpine valley during mountain and valley wind. *Beitr. Phys. Atmosph.*, **58**, 458–475.

Fuhrer, O. and C. Schär, 2005: Embedded cellular convection in moist flow past topography. *J. Atmos. Sci., **in press***.

Furger, M., J. Dommen, W. K. Graber, L. Poggio, A. S. H. Prévôt, S. Emeis, G. Grell, T. Trickl, B. Gomiscek, B. Neininger, and G. Wotawa, 2000: The VOTALP Mesolcina Valley Campaign 1996 - concept, background and some highlights. *Atmos. Environ.*, **34**, 1395–1412.

Garratt, J. R., 1992: *The atmospheric boundary layer*. Cambridge University Press, Cambridge.

— 1994: Review: the atmospheric boundary layer. *Earth-Sci. Rev.*, **37**, 89–134.

Georgelin, M., E. Richard, M. Petitdidier, and A. Druilhet, 1994: Impact of subgrid-scale orography parameterization on the simulation of orographic flows. *Mon. Wea. Rev.*, **122**, 1509–1521.

Germano, M., 1996: A statistical formulation of the dynamic model. *Phys. Fluids*, **8**, 565–570.

Geyer, W. R., 1993: Three-dimensional tidal flow around headlands. *J. Geophys. Res.*, **98 (C1)**, 955–966.

Gohm, A., G. Zängl, and G. J. Mayr, 2004: South Foehn in the Wipp Valley on 24 October 1999 (MAP IOP 10): Verification of high-resolution numerical simulations with observations. *Mon. Wea. Rev.*, **132**, 78–102.

Gong, W. M. and A. Ibbetson, 1989: A wind tunnel study of turbulent flow over model hills. *Bound.-Layer Meteor.*, **49**, 113–148.

Grell, G. A., S. Emeis, W. R. Stockwell, T. Schoenemeyer, R. Forkel, J. Michalakes, R. Knoche, and W. Seidl, 2000: Application of a multiscale, coupled MM5/chemistry model to the complex terrain of the VOTALP valley campaign. *Atmos. Environ.*, **34**, 1435 – 1453.

Gronas, S. and A. D. Sandvik, 1999: Numerical simulations of local winds over steep orography in the storm over north Norway on October 12, 1996. *J. Geophys. Res.*, **104 (D8)**, 9107–9120.

Hanna, S. R. and R. X. Yang, 2001: Evaluations of mesoscale models' simulations of near-surface winds, temperature gradients, and mixing depths. *J. Appl. Meteor.*, **40**, 1095 – 1104.

Hart, K. A., W. J. Steenburgh, D. J. Onton, and A. J. Siffert, 2004: An evaluation of mesoscale-model-based model output statistics (MOS) during the 2002 Olympic and Paralympic Winter Games. *Wea. Forecast.*, **19**, 200–218.

Härtel, C.: 1996, Turbulent flows: direct numerical simulation and large-eddy simulation. *Handbook of Computational Fluid Mechanics*, R. Pegret, ed., Academic Press, 283–338.

Haugen, D. A., J. C. Kaimal, and E. F. Bradley, 1971: Experimental study of Reynolds stress and heat flux in the atmospheric surface layer. *Quart. J. Roy. Meteor. Soc.*, **97**, 168–180.

Henne, S., M. Furger, S. Nyeki, M. Steinbacher, B. Neininger, S. F. J. de Wekker, J. Dommen, N. Spichtinger, A. Stohl, and A. S. H. Prévôt, 2004: Quantification of topographic venting of boundary layer air to the free troposphere. *Atmos. Chem. Phys.*, **4**, 497–509.

Henne, S., M. Furger, and A. S. H. Prévôt, 2005: Climatology of mountain venting induced elevated moisture layers in the lee of the Alps. *J. Appl. Meteorol., **accepted for publication**.

Hennemuth, B., 1987: Heating of a small Alpine valley. *Meteor. Atmos. Phys.*, **36**, 287–296.

Hodur, R. M., 1997: The Naval Research Laboratory's Coupled Ocean/Atmosphere Mesoscale Prediction System (COAMPS). *Mon. Wea. Rev.*, **125**, 1414–1430.

Holtslag, A. A. M. and F. T. M. Nieuwstadt, 1986: Scaling the atmospheric boundary layer. *Bound.-Layer Meteor.*, **36**, 201–209.

Hunt, J. C. R. and D. J. Carruthers, 1990: Rapid distortion theory and the 'problems' of turbulence. *J. Fluid Mech.*, **212**, 497–532.

Hunt, J. C. R., H. J. S. Fernando, and M. Princevac, 2003: Unsteady thermally driven flows on gentle slopes. *J. Atmos. Sci.*, **60**, 2169–2182.

Hunt, J. C. R., S. Leibovich, and K. J. Richards, 1988a: Turbulent shear flows over low hills. *Quart. J. Roy. Meteor. Soc.*, **114**, 1435–1470.

Hunt, J. C. R., K. J. Richards, and P. W. M. Brighton, 1988b: Stably stratified shear flow over low hills. *Quart. J. Roy. Meteor. Soc.*, **114**, 859–886.

Jackson, P. S. and J. C. R. Hunt, 1975: Turbulent wind flow over a low hill. *Quart. J. Roy. Meteor. Soc.*, **101**, 929–955.

Jacobson, M. Z., 2001: GATOR-GCMM - 2. A study of daytime and nighttime ozone layers aloft, ozone in national parks, and weather during the SARMAP field campaign. *J. Geophys. Res.*, **106 (D6)**, 5403 – 5420.

Jacquemin, B. and J. Noilhan, 1990: Sensitivity study and validation of a land surface parameterization using the HAPEX-MOBILHY data set. *Bound.-Layer Meteor.*, **52**, 93–134.

Jasper, K., 2001: *Hydrological modelling of alpine river catchments using output variables from atmospheric models*. Published dissertation no. 14385, Swiss Federal Institute of Technology (ETH), Zurich, Switzerland.

Kaimal, J. C. and J. J. Finnigan: 1994, *Atmospheric boundary layer flows*, Oxford University Press, New York, Oxford.

Kaimal, J. C., J. C. Wyngaard, D. A. Haugen, O. R. Coté, Y. Izumi, S. J. Caughey, and C. J. Readings, 1976: Turbulence structure in the convective boundary layer. *J. Atmos. Sci.*, **33**, 2152–2169.

Kalkwijk, J. P. T. and R. Booij, 1986: Adaptation of secondary flow in nearly-horizontal flow. *J. Hydraul. Res.*, **24**, 19–37.

Kalnay, E., 2003: *Atmospheric modeling, data assimilation and predictability*. Cambridge University Press.

Kalthoff, N., V. Horlacher, U. Corsmeier, A. Volz-Thomas, B. Kolahgar, H. Geiß, M. Möllmann-Coers, and A. Knaps, 2000: Influence of valley winds on transport and dispersion of airborne pollutants in the Freiburg-Schauinsland area. *J. Geophys. Res.*, **105 (D1)**, 1585–1597.

Khanna, S. and K. G. Brasseur, 1998: Three-dimensional bouyancy- and shear-induced local structure of the atmospheric boundary layer. *J. Atmos. Sci.*, **55**, 710–743.

Kimura, F. and T. Kuwagata, 1995: Horizontal heat fluxes over complex terrain computed using a simple mixed-layer model and a numerical model. *J. Appl. Meteor.*, **34**, 549–558.

Klemp, J. B. and R. B. Wilhelmson, 1978: The simulation of three-dimensional convective storm dynamics. *J. Atmos. Sci.*, **35**, 1070–1096.

Kossmann, M., U. Corsmeier, S. F. J. de Wekker, F. Fiedler, N. Kalthoff, H. Güsten, and B. Neininger, 1999: Observation of handover processes between the atmospheric boundary layer and the free troposphere over mountainous terrain. *Contrib. Atmos. Phys.*, **72**, 329–350.

Kossmann, M. and F. Fiedler, 2000: Diurnal momentum budget analysis of thermally induced slope winds. *Meteor. Atmos. Phys.*, **75**, 195–215.

Kossmann, M. and A. P. Sturman, 2003: Pressure-driven channeling effects in bent valleys. *J. Appl. Meteor.*, **42**, 151–158.

Kossmann, M., A. P. Sturman, P. Zawar-Reza, H. A. McGowan, A. J. Oliphant, I. F. Owens, and R. A. Spronken-Smith: 2000, Paper J4.5: Analysis of the wind and temperature field in an alpine lake basin. *Proceedings 9th Conference on Mountain Meteorology. Amer. Met. Soc.*, Aspen, CO.

Kossmann, M., R. Vögtlin, U. Corsmeier, B. Vogel, F. Fiedler, H.-J. Binder, N. Kalthoff, and F. Beyrich, 1998: Aspects of the convective boundary layer structure over complex terrain. *Atmos. Environ.*, **32**, 1323–1348.

Kravchenko, A. G., P. Moin, and R. Moser, 1996: Zonal embedded grids for numerical simulations of wall-bounded turbulent flows. *J. Comput. Phys.*, **127**, 412–423.

Kuwagata, T. and F. Kimura, 1995: Daytime boundary layer evolution in a deep valley. Part I: Observations in the Ina Valley. *J. Appl. Meteor.*, **34**, 1082–1091.

— 1997: Daytime boundary layer evolution in a deep valley. Part II: Numerical simulation of the cross-valley circulation. *J. Appl. Meteor.*, **36**, 883–895.

Lenschow, D. H. and B. B. Stankov, 1986: Length scales in the convective boundary layer. *J. Atmos. Sci.*, **43**, 1198–1209.

Lenschow, D. H., J. C. Wyngaard, and W. T. Pennell, 1980: Mean fields and second moment budgets in a baroclinic convective boundary layer. *J. Atmos. Sci.*, **37**, 1313–1326.

Lilly, D. K., 1962: On the numerical simulation of buoyant convection. *Tellus*, **14**, 148–172.

Lorenz, E. N., 1993: *The essence of chaos*. University of Washington Press, Seattle.

Lozej, C. and R. D. Bornstein: 1999, Comparison of nesting techniques within a meteorological model. *Air pollution VII, Billerica. Comp. Mechanics Pub.*, C. A. Brebbia, M. Jacobsen, and H. Power, eds., 1009–1021.

Lu, R. and R. P. Turco, 1995: Air pollutant transport in a coastal environment – II. Three-dimensional simulations over Los Angeles basin. *Atmos. Environ.*, **29**, 1499 – 1518.

Mahrer, Y., 1984: An improved numerical approximation of the horizontal gradients in a terrain-following coordinate system. *Mon. Wea. Rev.*, **112**, 918–922.

Mahrt, L., 1986: On the shallow motion approximations. *J. Atmos. Sci.*, **43**, 1036–1044.

Mason, P. J., 1992: Large-eddy simulation of dispersion in convective boundary layers with wind shear. *Atmos. Environ.*, **26A**, 1561–1571.

Mason, P. J. and R. I. Sykes, 1979: Flow over an isolated hill of moderate slope. *Quart. J. Roy. Meteor. Soc.*, **105**, 383–395.

Matzinger, N., M. Andretta, E. Van Gorsel, R. Vogt, A. Ohmura, and M. W. Rotach, 2003: Surface radiation budget in an Alpine valley. *Quart. J. Roy. Meteor. Soc.*, **129**, 877–895.

McKee, T. B. and R. D. O'Neil, 1989: The role of valley geometry and energy budget in the formation of nocturnal valley winds. *J. Appl. Meteor.*, **28**, 445–456.

McMillen, R. T., 1988: An eddy correlation technique with extended applicability to non-simple terrain. *Bound.-Layer Meteor.*, **43**, 231–245.

Moeng, C.-H., 1984: A large-eddy simulation model for the study of planetary boundary-layer turbulence. *J. Atmos. Sci.*, **41**, 2052–2062.

Moeng, C.-H. and P. P. Sullivan, 1994: A comparison of shear- and buoyancy driven planetary boundary layer flows. *J. Atmos. Sci.*, **51**, 999–1022.

Monin, A. S. and A. M. Obukhov, 1954: Basic laws of turbulent mixing in the atmosphere near the ground. *Tr. Akad. Nauk., SSSR Geofiz. Inst.*, **24 (151)**, 1963–1987.

Neininger, B., 1982: Mesoklimatische Messungen im Oberwallis. *Int. Tagung für Alpine Meteorologie, Berchtesgaden, DWD, Ann. Meteor.*, **19**, 105–107.

Neininger, B., W. Fuchs, M. Bäumle, A. Volz-Thomas, A. S. H. Prévôt, and J. Dommen: 2001, Paper 5.7: A small aircraft for more than just ozone: MetAir's 'Dimona' after ten years of evolving development. *Proceedings of the 11th Symposium on Meteorological Observations and Instrumentation, Amer. Met. Soc.*, Albuquerque, NM, 123–128.

Noilhan, J. and S. Planton, 1989: A simple parameterization of land surface processes for meteorological models. *Mon. Wea. Rev.*, **117**, 536–349.

Noppel, H. and F. Fiedler, 2001: Mesoscale heat transport over complex terrain by slope winds - a conceptual model and numerical simulations. *Bound.-Layer Meteor.*, **104**, 73–97.

Nyeki, S., M. Kalberer, I. Colbeck, S. de Wekker, M. Furger, H. W. Gäggeler, M. Kossmann, M. Lugauer, D. Steyn, E. Weingartner, M. Wirth, and U. Baltensperger, 2000: Convective boundary layer evolution to 4 km asl over high alpine terrain: airborne lidar observations in the Alps. *Geophys. Res. Let.*, **27**, 689–692.

Ookouchi, Y., M. Segal, R. C. Kessler, and R. A. Pielke, 1984: Evaluation of soil moisture effects on the generation and modification of mesoscale circulations. *Mon. Wea. Rev.*, **112**, 2281 – 92.

Panofsky, H. A. and J. A. Dutton, 1984: *Atmospheric Turbulence*. Wiley-Interscience, New York.

Pielke, R. A., W. R. Cotton, R. L. Walko, C. J. Tremback, W. A. Lyons, L. D. Grasso, M. E. Nicholls, M. D. Moran, D. A. Wesley, T. J. Lee, and J. H. Copeland, 1992: A comprehensive meteorological modeling system – RAMS. *Meteor. Atmos. Phys.*, **49**, 69–91.

Pino, D., J. V.-G. de Arellano, and P. G. Duynkerke, 2003: The contribution of shear to the evolution of a convective boundary layer. *J. Atmos. Sci.*, **60**, 1913–1926.

Pitman, A. J., 2003: The evolution of, and revolution in, land surface schemes designed for climate models. *Int. J. Climatol.*, 479–510.

Pleim, J. E. and A. Xiu, 1995: Development and testing of a surface flux and planetary boundary layer model for application in mesoscale models. *J. Appl. Meteor.*, **34**, 16–32.

Pope, S. B., 2000: *Turbulent flows*. Cambridge University Press, Cambridge, UK, 770 pp.

Porch, W. M., R. B. Fritz, R. L. Coulter, and P. H. Gudiksen, 1989: Tributary, valley and sidewall air-flow interactions in a deep valley. *J. Appl. Meteor.*, **28**, 578–589.

Poulos, G., 1999: *The interaction of katabatic winds and mountain waves*. Ph.D. thesis, Colorado State University.

Prandtl, L.: 1942, *Führer durch die Ströhmungslehre*, F. Vieweg und Sohn, Braunschweig. 373–375.

Rampanelli, G., D. Zardi, and R. Rotunno, 2004: Mechanisms of up-valley winds. *J. Atmos. Sci.*, **61**, 3097–3111.

Revell, M. J., D. Purnell, and M. K. Lauren, 1996: Requirements for large-eddy simulation of surface wind gusts in a mountain valley. *Bound.-Layer Meteor.*, **80**, 333–53.

Richardson, L. F., 1922: *Weather Prediction by Numerical Process*. Cambridge University Press, Cambridge.

Ross, A. N., S. Arnold, S. B. Vosper, S. D. Mobbs, N. Dixon, and A. G. Robins, 2004: A comparison of wind-tunnel experiments and numerical simulations of neutral and stratified flow over a hill. *Bound.-Layer Meteor.*, **113**, 427–459.

Rotach, M. W., 1995: On the boundary layer over mountainous terrain - a frog's perspective. *MAP-Newsletter*, **3**, 31–32.

Rotach, M. W., P. Calanca, G. Graziani, J. Gurtz, D. G. Steyn, R. Vogt, M. Andretta, A. Christen, S. Cieslik, R. Connolly, S. F. J. De Wekker, S. Galmarini, E. N. Kadygrov, V. Kadygrov, E. Miller, B. Neininger, M. Rucker, E. van Gorsel, H. Weber, A. Weiss, and M. Zappa, 2004: The turbulence structure and exchange processes in an Alpine valley: The Riviera project. *Bull. Amer. Met. Soc.*, **85**, 1367–1385.

Rozovskii, I. L., 1957: Движение воды на повороте открытого русла. *Izd. Akad. Nauk. Ukr. SSR, Kiev (*English translation 1961: Flow of water in bends of open channels. *Israel Progr. Sci. Transl., Jerusalem)*.

Rucker, M., 2003: *Observational and numerical study of daytime flows in an Alpine valley*. Ph.d. thesis, The University of British Columbia, Vancouver, Canada.

Sakiyama, S. K., 1990: Drainage flow characteristics and inversion breakup in two Alberta mountain valleys. *J. Appl. Meteor.*, **29**, 1015–1030.

Samuelsson, P. and M. Tjernström, 2001: Mesoscale flow modification induced by land-lake surface temperature and roughness differences. *J. Geophys. Res.*, **106 (D12)**, 12419–12435.

Schmidli, J., 2005: Effects of valley geometry and land surface properties on the diurnal valley wind systems, turbulence structure and exchange processes. ASP Research Proposal, Institute for Atmospheric and Climate Science ETH.

Skamarock, W. C. and J. B. Klemp, 1992: The stability of time split numerical methods for the hydrostatic and non-hydrostatic elastic equations. *Mon. Wea. Rev.*, **120**, 2109–2127.

Smagorinsky, J., 1963: General circulation experiments with the primitive equations. *Mon. Wea. Rev.*, **91**, 99–164.

Soriano, C., O. Jorba, and J. M. Baldasano: 2001, Air pollution modelling and its application. *25th Int. Tech. Meeting of NATO-CCMS, Louvain la Neuve, Belgium*, C. Borrego and G. Schayes, eds., 177–185.

Steinacker, R., 1984: Area-height distribution of a valley and its relation to the valley wind. *Contrib. Atmos. Phys.*, **57**, 64–71.

Stull, R. B.: 1988, *An Introduction to Boundary Layer Meteorology*, Kluwer Academic Publishers, Dordrecht, Boston, London.

Taylor, G. I., 1938: The spectrum of turbulence. *Proc. Roy. Soc. of London*, **A164**, 476–490.

Taylor, P. A. and H. W. Teunissen, 1987: The Askervein hill project: Overview and background data. *Bound.-Layer Meteor.*, **39**, 15–39.

Tolkien, J. R. R., 1954: *The Fellowship of the Ring: being the first part of The Lord of the Rings*. George Allen and Unwin, London.

Van Gorsel, E., A. Christen, C. Feigenwinter, E. Parlow, and R. Vogt, 2003: Daytime turbulence statistics above a steep forested slope. *Bound.-Layer Meteor.*, **109**, 311–329.

Vergeiner, I. and E. Dreiseitl, 1987: Valley winds and slope winds - observations and elementary thoughts. *Meteor. Atmos. Phys.*, **36**, 264–286.

Viterbo, P. and A. K. Betts, 1999: The impact of the ECMWF reanalysis soil water on forecasts of the July 1993 Mississippi flood. *J. Geophys. Res.*, **104 (D16)**, 19361–19366.

Voke, P. R. and M. W. Collins, 1983: Large-eddy simulation - retrospect and prospect. *Physicochem. Hydrodyn.*, **4**, 119–161.

Volkert, H., 1990: An Alpine orography resolving major valleys and massifs. *Meteor. Atmos. Phys.*, **43**, 231–234.

von Hann, J.: 1932, *Handbuch der Klimatologie, I. Band: Allgemeine Klimatologie*, J. Engelhorns Nachf., Stuttgart. 4th edition, 308–321.

Vosper, S. B. and S. D. Mobbs, 1997: Measurement of the pressure field on a mountain. *Quart. J. Roy. Meteor. Soc.*, **123**, 129–144.

Vosper, S. B., S. D. Mobbs, and B. A. Gardiner, 2002: Measurements of the near-surface flow over a hill. *Quart. J. Roy. Meteor. Soc.*, **128**, 2257–2280.

Wagner, A., 1932a: Der tägliche Luftdruck- und Temperaturgang in der freien Atmosphäre und in Gebirgstälern. *Gerlands Beitr. Geophys.*, **37**, 315–344.

— 1932b: Neue Theorie des Berg- und Talwindes. *Meteorol. Z.*, **49**, 329–341.

— 1938: Theorie und Beobachtung der periodischen Gebirgswinde. *Gerlands Beitr. Geophys.*, **52**, 408–449.

Warner, T. T., R. A. Peterson, and R. E. Treadon, 1997: A tutorial on lateral boundary conditions as a basic and potentially serious limitation to regional numerical weather prediction. *Bull. Amer. Met. Soc.*, **78**, 2599 –2617.

Watson, D. F., 1992: *Contouring: A guide to the analysis and display of spatial data*. Pergamon Press, Oxford.

Weigel, A. P., F. K. Chow, M. W. Rotach, and R. L. Street: 2004a, EGU04-A-03496: Assessment of large-eddy simulations of the atmospheric boundary layer in a steep and narrow Alpine valley. *Geophys. Res. Abstr., Europ. Geophys. Union: First General Assembly*, Nice, France.

Weigel, A. P., F. K. Chow, M. W. Rotach, R. L. Street, and M. Xue: 2004b, Paper 6.4: High-resolution large-eddy simulations of the Riviera valley: Assessment of the flow structure and the heat and moisture budgets. *Proceedings 11th Conference on Mountain Meteorology, Amer. Met. Soc.*, Bartlett, NH.

Weigel, A. P., F. K. Chow, M. W. Rotach, R. L. Street, and M. Xue, 2005: High-resolution large-eddy simulations of flow in a steep alpine valley. Part II: Flow structure and heat budgets. *J. Appl. Meteor., **submitted for publication***.

Weigel, A. P. and M. W. Rotach: 2003, Paper P2.10: On the turbulence structure in a daytime alpine valley atmosphere. *Proceedings 26th International Conference on Alpine Meteorlogy (ICAM)*, Brig, Switzerland.

Weigel, A. P. and M. W. Rotach, 2004: Flow structure and turbulence characteristics of the daytime atmosphere in a steep and narrow Alpine valley. *Quart. J. Roy. Meteor. Soc.*, **130**, 2605–2627.

Whiteman, C. D., 1982: Breakup of temperature inversions in deep mountain valleys: Part I. Observations. *J. Appl. Meteor.*, **21**, 270–289.

— 1989: Morning transition tracer experiments in a deep narrow valley. *J. Appl. Meteor.*, **28**, 626–635.

Whiteman, C. D.: 1990, Observations of thermally developed wind systems in mountainous terrain. *Atmospheric processes over complex terrain*, W. Blumen, ed., American Met. Soc., Boston, 5–42.

— 2000, *Mountain Meteorology. Fundamentals and applications*, Oxford University Press, New York, Oxford.

Whiteman, C. D., K. J. Allwine, L. J. Fritschen, M. M. Orgill, and J. R. Simpson, 1989a: Deep valley radiation and surface energy budget microclimates. Part I: Radiation. *J. Appl. Meteor.*, **28**, 414–426.

— 1989b: Deep valley radiation and surface energy budget microclimates. Part II: Energy budget. *J. Appl. Meteor.*, **28**, 427–437.

Whiteman, C. D., X. Bian, and J. L. Sutherland, 1999a: Wintertime surface wind patterns in the Colorado River valley. *J. Appl. Meteor.*, **38**, 1118–1130.

Whiteman, C. D. and J. C. Doran, 1993: The relationship between overlying synoptic-scale flows and winds within a valley. *J. Appl. Meteor.*, **32**, 1669–1682.

Whiteman, C. D. and T. B. McKee, 1982: Breakup of temperature inversions in deep mountain valleys: Part II. Thermodynamic Model. *J. Appl. Meteor.*, **21**, 290–302.

Whiteman, C. D., T. B. McKee, and J. C. Doran, 1996: Boundary layer evolution within a canyonland basin. Part I: Mass, heat and moisture budgets from observations. *J. Appl. Meteor.*, **35**, 2145–2161.

Whiteman, C. D., B. Pospichal, S. Eisenbach, P. Weihs, C. B. Clements, R. Steinacker, E. Mursch-Radlgruber, and M. Dorninger, 2004: Inversion breakup in small Rocky Mountain and Alpine basins. *J. Appl. Meteor.*, **43**, 1069–1082.

Whiteman, C. D., S. Zhong, and X. Bian, 1999b: Wintertime boundary layer structure in the Grand Canyon. *J. Appl. Meteor.*, **38**, 1084–1102.

Whiteman, C. D., S. Zhong, X. Bian, J. D. Fast, and J. C. Doran, 2000: Boundary layer evolution and regional-scale diurnal circulations over the Mexico Basin and Mexican plateau. *J. Geophys. Res.*, **105 (D8)**, 10081–10102.

Wong, V. C. and D. K. Lilly, 1994: A comparison of two dynamic subgrid closure methods for turbulent thermal-convection. *Phys. Fluids*, **6**, 1016 – 1023.

Wyngaard, J. C., 2004: Toward numerical modeling in the "Terra Incognita". *J. Atmos. Sci.*, **61**, 1816–1826.

Wyngaard, J. C. and O. R. Coté, 1974: The evolution of a convective planetary boundary layer - a higher order closure model study. *Bound.-Layer Meteor.*, **7**, 289–308.

Xue, M., K. K. Droegemeier, and V. Wong, 2000: The Advanced Regional Prediciton System (ARPS) - A multi-scale nonhydrostatic atmospheric simulation and prediction model. Part I: Model dynamics and verification. *Meteor. Atmos. Phys.*, **75**, 161–193.

Xue, M., K. K. Droegemeier, V. Wong, A. Shapiro, and K. Brewster: 1995, *ARPS Version 4.0 user's guide. Center for Analysis and Prediction of Storms (CAPS)*, Norman, OK.

Xue, M., K. K. Droegemeier, V. Wong, A. Shapiro, K. Brewster, F. Carr, D. Weber, Y. Liu, and D. Wang, 2001: The Advanced Regional Prediction System (ARPS) - A multi-scale nonhydrostatic atmospheric simulation and prediction tool. Part II: Model physics and applications. *Meteor. Atmos. Phys.*, **76**, 143–165.

Xue, M., D. H. Wang, J. D. Gao, K. Brewster, and K. K. Droegemeier, 2003: The Advanced Regional Prediction System (ARPS), storm-scale numerical weather prediction and data assimilation. *Meteor. Atmos. Phys.*, **82**, 139–170.

Young, G. S. and R. A. Pielke, 1983: Application of terrain height variance spectra to mesoscale modeling. *J. Atmos. Sci.*, **40**, 2555–2560.

Zängl, G., B. Chimani, and C. Häberli, 2004: Numerical simulations of the foehn in the Rhine Valley on 24 October 1999 (MAP IOP 10). *Mon. Wea. Rev.*, **132**, 368–389.

Zängl, G., J. Egger, and V. Wirth, 2001: Diurnal winds in the Himalayan Kali Gandaki Valley. Part II: Modeling. *Mon. Wea. Rev.*, **129**, 1062–1080.

Zappa, M. and J. Gurtz, 2003: Simulation of soil moisture and evapotranspiration in a soil profile during the 1999 MAP-Riviera campaign. *Hydrol. Earth Sys. Sci.*, **7**, 903–919.

Zawar-Reza, P., H. McGowan, A. Sturman, and M. Kossmann, 2004: Numerical simulations of wind and temperature structure within an Alpine lake basin, Lake Tekapo, New Zealand. *Meteor. Atmos. Phys.*, **86**, 245–260.

Zhong, S. and J. Fast, 2003: An evaluation of the MM5, RAMS, and Meso-Eta models at subkilometer resolution using VTMX field campaign data in the Salt Lake Valley. *Mon. Wea. Rev.*, **131**, 1301–1322.

Zhong, S. and C. D. Whiteman: 2004, Paper 10.6: The dynamics of drainage flows developed on a low angle slope in a large valley. *Proceedings 11th Conference on Mountain Meteorology, Amer. Met. Soc.*, Bartlett, NH.

List of acronyms and abbreviations

ABL	atmospheric boundary layer
agl	above ground level
aLMo	Alpine Model
AL	aerosol layer
ARPS	Advanced Regional Prediction System
asl	above sea level
AVFP	along-valley flight path
COAMPS	Coupled Ocean/Atmosphere Mesoscale Prediction System
CBL	convective boundary layer
CVFP	cross-valley flight path
DRM	Dynamic Reconstruction Model
ECHAM	European Centre / Hamburg model
ECMWF	European Centre for Medium-Range Weather Forecasts
ETH	Eidgenössische Technische Hochschule Zürich
IAC	Institute for Atmospheric and Climate Science
IOP	intensive observation period
LES	large-eddy simulations
LM	Lokalmodell
MAP	Mesoscale Alpine Program
MM5	Mesoscale Model, Version 5
msl	mean sea level
NCAR	National Center for Atmospheric Research
NSF	National Science Foundation
RADM2	Regional Acid Deposition Model, Version 2
RAMS	Regional Atmospheric Modeling System
RANS	Reynolds-averaged Navier Stokes
rmse	root-mean-square error
RL	residual layer
RS	resolved scale
RSFS	resolved subfilter-scale
SFS	subfilter-scale
SGS	subgrid-scale
TAF	topographic amplification factor
TFDL	turbulent flux divergence layer
TKE	turbulent kinetic energy
USGS	United States Geological Survey
UTC	Coordinated Universal Time
WaSiM	Water Flow and Balance Simulation Model

Curriculum Vitae

Andreas Weigel, Saatlenstrasse 9, 8051 Zürich, Switzerland;
born on 9 October 1975 in Kempten, Germany; German citizen.

EDUCATION AND PROFESSIONAL TRAINING

09/01 - 03/05	PhD student in the group of Prof. A. Ohmura at the Institute for Atmospheric and Climate Science, ETH Zürich, Switzerland. PhD Defense: 15 March 2005.
01/03 - 07/03	Visiting researcher in the group of Prof. R. L. Street at the Environmental Fluid Mechanics Laboratory, Stanford University, USA.
11/95 - 06/01	Studies in Physics at the University of Munich, Germany. Specialization in Medical Physics and Meteorology. Diploma thesis at the Institute for Clinical Radiology under guidance of Prof. K.E.G. Löbner and Dr. M. Peller. Topic: "In vivo temperature measurement by means of T1-relaxation in magnetic resonance tomography". Graduation: Dipl.-Phys. (Univ.)
07/99 - 08/99	Internship at the Alfred-Wegener-Institute for Polar and Marine Research, Bremerhaven, Germany.
09/98 - 06/99	Study abroad (ERASMUS program) at the School of Physics and Astronomy, University of Nottingham, UK.
03/98 - 04/98	Internship at the Geohazard Research Group of Munich Re, Munich.
09/86 - 07/95	Secondary and highschool education at the Allgäu-Gymnasium school in Kempten, Germany. Majors in Mathematics, Physics, German and Geography. Graduation: Abitur.

INTERNATIONAL CONFERENCES AND WORKSHOPS

EMS Annual Meeting 2004, Nice, France; AMS Conference on Mountain Meteorology 2004, Bartlett, NH, USA; EGU General Assembly 2004, Nice, France; International Conference on Alpine Meteorology 2003, Brig, Switzerland; Summer school on Mountain Meteorology 2002, Trento, Italy; EGS General Assembly 2002, Nice, France; Summer Academy of the German National Academic Foundation 2000, St. Johann, Italy.